Unattended Design of Wideband Planar Filters Based on Stepped Impedance Resonators (SIRs) through Aggressive Space Mapping (ASM)

Marc Sans Soler

Escola d'Enginyeria

Departament d'Enginyeria Electrònica

Unattended Design of Wideband Planar Filters Based on Stepped Impedance Resonators (SIRs) through Aggressive Space Mapping (ASM)

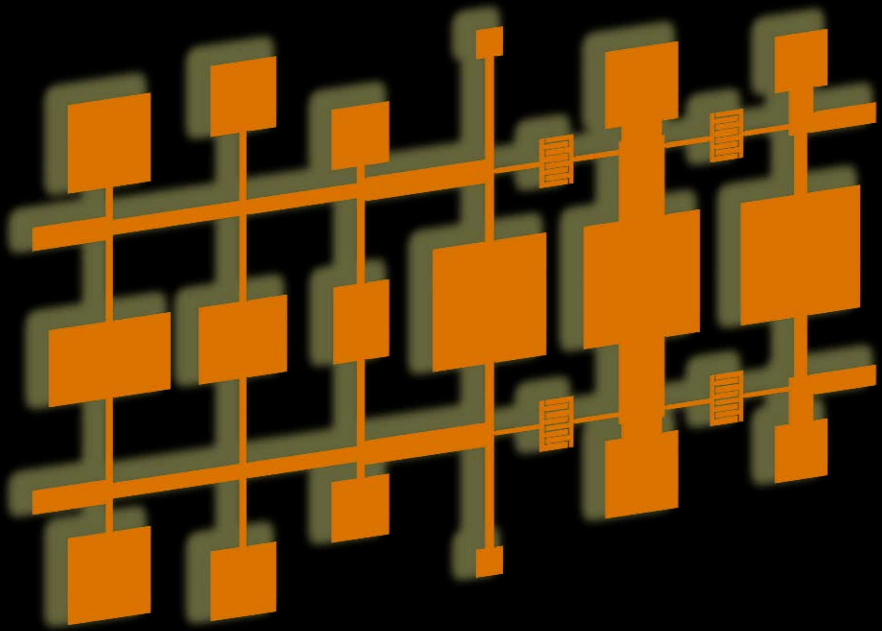

Ph.D. Thesis written by
Marc Sans Soler

Under the supervision of
Ferran Martín Antolín

Universitat Autònoma de Barcelona

Universitat Autònoma de Barcelona

UAB CEI
CAMPUS OF INTERNATIONAL EXCELLENCE

Unattended Design of Wideband Planar Filters based on Stepped Impedance Resonators (SIRs) through Aggressive Space Mapping (ASM)

Ph.D. Thesis written by

Marc Sans Soler

Under the supervision of

Ferran Martín Antolín

cimitec

Bellaterra (Cerdanyola del Vallès), July 2018

The undersigned, **Ferran Martín Antolín**, Professor of the Electronics Engineering Department (Engineering School) of the Universitat Autònoma de Barcelona,

CERTIFIES:

That the thesis entitled "Unattended Design of Wideband Planar Filters based on Stepped Impedance Resonators (SIRs) through Aggressive Space Mapping (ASM)" has been written by **Marc Sans Soler** under his supervision.

And hereby to acknowledge the above, sign the present.

Signature: Ferran Martín Antolín

Programa de Doctorat d'Enginyeria Electrònica i de Telecomunicació
Departament d'Enginyeria Electrònica - Escola d'Enginyeria
Universitat Autònoma de Barcelona

Bellaterra (Cerdanyola del Vallès), July 2018.

Contents

Acknowledgements

I would like to express my gratitude to all who participated directly or indirectly to the realization of this work, without whom it would had never come true. This thesis is also yours.

My most special thanks to my supervisor, Prof. Ferran Martín, for supporting me during this long journey. I really appreciate your mentoring, guidance and the fruitful discussions we had along the way.

I would also like to thank to Prof. Vicente Boria and Ana Rodríguez, from Universitat Politècnica de València, who have always brought solid contributions to the thesis, for these years of collaborative work, advices and shared knowledge.

Not to forget my acknowledgments to the CIMITEC members. Specially to Jordi Boanche, this thesis would have never begun without your initial support. Many thanks as well to Paris Vélez and Cristian Herrojo for your always altruistic and invaluable help.

Special words to you, Jordi Selga, for your unquantifiable contribution to this work. Thank you for being always eager to help, for our endless discussions, for your wise suggestions and ideas. And thank you as well for helping me to solve uncountable paperwork issues, without your aid it would be almost impossible to manage this work from abroad.

To my parents. To my sister. To my grandparents. To my uncles. To all my friends. For all the love and support you have always showed to me.

For all you do, for who you are, I will be forever grateful you are in my life, Elisenda.

Summary

The synthesis of planar microwave circuits able to satisfy a set of given specifications has been a subject of interest in the microwave community for years. Despite the fact that most commercially available computer aided design tools and electromagnetic solvers include optimizers, obtaining the circuit topologies that satisfy the design requirements is generally cumbersome. Convergence to the optimum solution is not always guaranteed unless the seeding layout is already very close to the one providing the target response, and designer experience plays a key role in such optimization process as long as the circuit complexity increases.

On the other hand, single-ended and, more specially, balanced microwave filters have become essential devices with the recent advances in the development of wireless communication technologies, where higher levels of integration and more complex microwave systems are key requirements. Therefore, a systematic procedure able to provide the filter layout satisfying the required specifications would be very welcomed by microwave engineers.

This thesis is focused on the automatic synthesis of single-ended and balanced planar microwave filters providing wideband bandpass responses. Such filter structures are based on semi-lumped resonant elements, implemented by a combination of high and low impedance transmission line sections, also known as Stepped Impedance Resonators (SIRs). The optimization approach, based on the Aggressive Space Mapping (ASM) technique, is aimed to generate the filter layout from design specifications following a completely unattended scheme. Therefore, such filter optimization scheme can represent the first step towards an optimization tool for this type of SIR-based filters suitable to be part of any commercially available engineering software focused on microwave design.

To this end, specific ASM-based algorithms are developed in order to automatically synthesize multiple single-ended and balanced filter topologies based on SIRs. The proposed automatic design procedures are thoroughly detailed and validated through its application to generate several filter layouts starting from different sets of practical specifications. The

reported procedures and the results obtained reveal that this optimization methodology can be extended to many other filter structures, and have lead this research work to contribute to the state of the art with innovative strategies in the ASM formulation as well as with novel synthesized passband filter topologies.

Chapter 1

Motivation and Objectives

The synthesis of planar microwave circuits able to satisfy a set of given specifications is a subject of interest for the microwave community. Despite the fact that most commercially available computer aided design (CAD) tools and electromagnetic (EM) solvers include optimizers, obtaining the circuit topologies that satisfy the design requirements is not always straightforward. This design difficulty increases with circuit complexity, and convergence to the optimum solution is not always guaranteed (for instance due to limitations related to local minima), unless the seeding layout is already very close to the one providing the target response.

This thesis is focused on a specific type of planar circuits, of interest in many different microwave applications, whose design requires significant computational effort: single-ended and balanced wideband bandpass filters. There are many approaches for the design of wideband planar microwave filters [1], [2]. The interest in this thesis is the design of wideband bandpass filters, based on semi-lumped (i.e., electrically small and planar) resonant elements coupled through admittance inverters. More specifically, such resonators are implemented by a combination of high and low impedance transmission line sections and are also known as Stepped Impedance Resonators (SIRs), while the admittance inverters typically consist of quarter-wavelength transmission lines. However, deviations from the ideal responses are caused by the limited functionality of the inverters and by the distributed effects of the planar resonators at sufficiently high frequencies. These deviations are more pronounced if the filter is broadband, mainly because the required phase shift of the inverters is not preserved over the whole filter pass band.

A systematic design procedure of different filter structures based on SIRs, able to provide the filter layout satisfying the required specifications, is the main focus of this research work. The main purpose of this EM optimization approach, based on the

Aggressive Space Mapping (ASM) technique, is to generate the filter layout from the specifications following a completely unattended scheme. Therefore, such filter optimization scheme can represent the first step towards an optimization tool suitable to be embedded in any engineering CAD software focused in microwave design.

To this end, the main purpose of this thesis is to develop specific ASM-based algorithms which are able to automatically synthesize different filter topologies: high order (and hence highly selective) single-ended filters as well as more complex balanced filter structures with common-mode suppression. The implemented optimization schemes will be aimed to overcome the aforementioned inherent bandwidth limitations of the admittance inverters which, in turn, will lead this research work to contribute to the state of the art with innovative strategies in the ASM formulation and with novel synthesized filter topologies.

This thesis is written in the basis of a compendium of articles. The research has already been published in international journals, conference proceedings and a book chapter. The articles included in this thesis are found in the **PhD Thesis Main Articles** Section and have been differentiated between **Fundamental Articles** and **Non-Fundamental Articles**. The superscript * following the corresponding Articles references denotes that such Articles do not belong to the set of fundamental Articles of this thesis, but they are included for completeness. All the author's publications, contributions to conferences and the book chapter are listed in the **PhD Thesis Author Publications** Section. The thesis is organized as follows:

Chapter 1 corresponds to the present introduction and it is aimed to provide the motivations and the main objectives of the thesis, as well as an overview of the arrangement of the chapters.

Chapter 2 is addressed to the theoretical formulation of the Space Mapping optimization techniques, paying special attention to the Aggressive Space Mapping, widely used along this work. The classical single-ended microwave filter synthesis theory and the fundamentals of the balanced microwave filters are both presented as well. Next, an extensive overview of the state of the art of the ASM technique applied to the microwave filter optimization is conducted. Finally, the most recent advances in the balanced microwave filter synthesis are reviewed in detail, and the competitiveness of the balanced filters based on SIRs is justified. This analysis will be helpful in order to put into context the filter ASM-based optimization strategy applied throughout this work, which is presented at the end of this chapter.

Chapter 3 is devoted to the automatic synthesis of single-ended planar wideband bandpass filters based on SIRs through ASM. The entire optimization process is described and supported by examples in order to prove the validity of the concept. The flow of the implemented ASM algorithm is detailed in depth, and the analysis of the topology of the synthesized filters based on SIRs is also conducted. Moreover, an innovative *Two-Step ASM* concept is introduced at the end of this chapter in order to solve the issue of the narrowband limitations of the quarter-wavelength admittance inverters.

Chapter 4 addresses the ASM-based automatic synthesis of balanced planar wideband bandpass filters based on SIRs. In a similar manner than Chapter 3, the entire optimization flow is described which, in this case, is applied to different balanced topologies, so that the particularities of the ASM algorithm implemented for each structure are also emphasized. The analysis of the different topologies is also conducted and the validity of the concept is supported by the corresponding examples in all cases. In addition, a novel balanced filter topology (where the admittance inverters are replaced with semi-lumped elements) is presented, so that the ASM algorithm is simplified by avoiding the *Two-Step ASM* scheme.

Chapter 5, summarizes the most relevant results and contributions reported in this thesis. Future lines based on the results obtained in this work are also proposed.

This thesis has been conducted in the GEMMA (Grup d'Enginyeria de Microones, Metamaterials i Antenes) / CIMITEC (Centre d'Investigació en Metamaterials per a la Innovació en Tecnologies Electrònica i de Comunicacions) group, that belongs to the Electronics Engineering Department of the Universitat Autònoma de Barcelona.

CIMITEC is one of the centers of the Technological Innovation Network of TECNIO of the Catalan Government, created with the objective of promoting the transference of technology to industry in the field of Information and Communication Technology and has been recognized as a Consolidated Group by the Catalan Government (AGAUR).

The most relevant projects and different institutions that have supported this research activity can be highlighted as follows:

- Recognition as a consolidated group of research from the Generalitat de Catalunya: Agència de Gestió y Ajuts Universitaris y de Recerca (AGAUR). Period: 2014-2016. File 2014SGR-157.

- Project TEC2013-40600-R. From the Spanish government: Dirección General de Investigación Científica (Ministerio de Economía y Competitividad). Period: 2013-2016. Title: "*Diseño y sintesis de componentes de RF/microondas basados en conceptos avanzados y su aplicacion a circuitos de comunicaciones, sensores y RFID*".

- Project TEC2013-49221-EXP, under the Explora Ciencia y Tecnologia program, from the Spanish government: Dirección General de Investigación Científica (Ministerio de Economía y Competitividad). Period: 2014-2016. Title: "*Herramienta CAD para la síntesis desasistida y automatitzada de circuitos complejos de RF/Microondas en tecnologia plana*".

- Project TEC2016-75650-R, under the I+D+i Orientada a los Retos de la Sociedad program. From the Spanish government: Dirección General de Investigación Científica (Ministerio de Economía y Competitividad). Period: 2017-2019. Title: "*Diseño y sintesis de componentes de RF/microondas basados en conceptos avanzados y su aplicacion a circuitos de comunicaciones, sensores y RFID (II)*".

- Recognition as a consolidated group of research from the Generalitat de Catalunya: Agència de Gestió y Ajuts Universitaris y de Recerca (AGAUR). Period: 2017-2019. File 2017SGR-1159.

Chapter 2

Introduction and State of the Art

The Space Mapping (SM) technique applied to the design and optimization of microwaves devices is introduced in Section 2.1. The concept behind this effective optimization technique is explained together with its mathematical formulation, which provides the basic insights prior to the presentation of the Aggressive Space Mapping (ASM), by far the most widely used Space Mapping design optimization approach up to now [3], [4]. The ASM algorithm can be understood as an improvement of the original Space Mapping scheme by making it more general, robust and efficient while the algorithm complexity is not increased significantly.

The main theoretical aspects about single-ended and balanced microwave filters used throughout this thesis are reviewed in Section 2.2. To this end, an overview about the fundamentals of the classical filter synthesis theory and the theoretical background of the balanced microwave networks will be thoroughly provided.

Finally, in Section 2.3, a review of the state of the art regarding the ASM algorithm and its applications is presented, as well as the most recent advances with regards to the balanced microwave filters synthesis, paying special attention to those based on planar structures, since it is the technology used for the filter topologies implemented in this work. Last but not least, the basis of the strategy followed in this work about the unattended design of wideband bandpass filters by means of ASM is detailed, while emphasizing its most novel aspects.

2.1 Space Mapping Algorithms in Microwave Device Optimization

Optimization techniques have been widely used by engineers in the last decades with the aim to satisfy certain design specifications for specific microwave devices. The main target is to determine the optimum values for a set of physical parameters linked to the device structure to be optimized. Traditionally, general-purpose optimization algorithms were proposed for computer-aided design (CAD), being effective through specialized iterative techniques based on utilizing the simulated responses and their derivatives if available. The simulation is fast in this context, where analytical solutions and exact derivatives can be found, but at expenses of accuracy in the circuit model. Hence, in order to improve the accuracy of the solution, the idea of employing EM solvers, mainly used for design verification, for direct optimal design was attractive to the microwave community. However, EM solvers are by far more CPU-intensive and, originally, they presented some drawbacks like non-differentiable response evaluation and non-parametrized design variables. The interest in the microwave optimization software increased at the same pace as the complexity of the microwave circuits increased, and it was in 1990 when Bandler introduced the first microwave optimization engine incorporating state-of-the-art microwave circuit simulation and optimization algorithms, named OSA90. Nevertheless, since EM simulation remained CPU-intensive, the link between EM solvers and optimization techniques did not solve the EM-based design bottleneck, so that the automated EM-based design optimization was not (and still it is not) satisfying the ambitions of the microwave community.

One of the main purposes of this thesis is to present a novel strategy applied to the automatic and unattended optimization of microwave circuits in the EM domain, with the aim to show the most recent advances in this field as well as proving its feasibility and effectiveness with regards the current and most common optimization techniques existing nowadays.

2.1.1 The Space Mapping (SM) Concept

In 1994, Bandler et al. [5], in order to get the efficiency of circuit optimization with the accuracy of EM solvers, proposed an optimization technique based on mapping designs from optimized circuit models to corresponding EM models. That methodology was named Space Mapping. The principle of Space Mapping is to utilize a coarse model, i.e. analytical approximation of the physics of the device, to obtain a near-to-optimal design for the fine model, i.e., the EM model, following an iterative optimization process. The main goal is to obtain the fine model optimal design without direct optimization of the fine model, but using the coarse model instead, so that the iterative optimization steps are fast and computationally efficient. In planar microwave circuits, the coarse model might be the device equivalent circuit defined in a simulator such as Keysight® ADS, whereas the fine model typically corresponds to the device layout, implemented in an EM-based simulator like Keysight® Momentum or Ansys® HFSS, for instance. Therefore, a link, or mapping, between the fine and coarse models is stablished through a *parameter extraction* process, and the values of the relevant parameters of these mappings are updated during each iteration in order to obtain the best matching possible between the coarse model and the fine model. At each iteration, the coarse model is optimized generating a new design. Such new design will also be evaluated at the fine model space for verification purposes, and also to provide data to be used in the next iteration of the algorithm. A vital characteristic of Space Mapping is that both coarse and fine models describe the same physical phenomena of the device, but with less and more accuracy respectively. Hence, if the coarse model is accurate enough, the Space Mapping optimization process is expected to converge after few iterations.

Space Mapping Formulation

The coarse and fine model parameters are defined as the vectors $\mathbf{x_c}$ and $\mathbf{x_f}$ respectively, whereas $\mathbf{R_c(x_c)}$ and $\mathbf{R_f(x_f)}$ are their corresponding coarse and fine model responses. The Space Mapping concept is illustrated in Figure 2.1, where the correspondence between both spaces is shown.

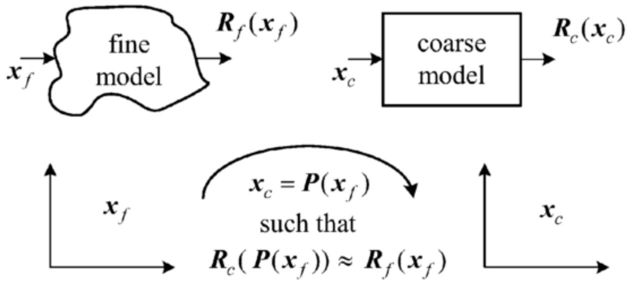

Figure 2.1. Space Mapping concept. Reprinted from [6].

Let us assume that the fine and coarse model vectors are linked by a linear mapping function **P**:

$$\mathbf{x_c} = \mathbf{P(x_f)} \tag{2.1}$$

and therefore, in the region of interest, the fine and coarse responses can be expressed as:

$$\mathbf{R_c(P(x_f))} \approx \mathbf{R_f(x_f)} \tag{2.2}$$

The optimal solution for the coarse model is denoted as $\mathbf{x_c}^*$, while $\mathbf{x_f}^{(M)}$ is the optimal solution for the fine model vector (found at the Mth iteration). Hence, the direct fine model optimization can be avoided by solving (2.1):

$$\mathbf{x_f}^{(M)} = \mathbf{P^{-1}}(\mathbf{x_c}^*) \tag{2.3}$$

In the original SM approach, it is needed to obtain an initial approximation of the mapping $\mathbf{P}^{(0)}$ by performing at least a preselected set of m_0 fine model analyses, where $m_0 > k+1$ and k is the number of the fine and coarse design parameters. One initial point in the fine space is taken as the optimal solution in the coarse space, $\mathbf{x_f}^{(1)} = \mathbf{x_c}^*$, and the remaining m_0 - 1 points are obtained through perturbations of $\mathbf{x_f}^{(1)}$. Next, the corresponding coarse model points are obtained through the *parameter extraction* process by means of the first linear mapping function approximation $\mathbf{P}^{(0)}$, enabling the first algorithm iteration by applying (2.1).

In general terms, the *parameter extraction* process is formulated as an optimization subproblem based on minimizing differences between the coarse and fine model space at the i-th iteration:

$$\mathbf{x_c}^{(i)} = \arg\min_{x_c} \left\| \mathbf{R_f}\left(\mathbf{x_f}^{(i)}\right) - \mathbf{R_c}(\mathbf{x_c}) \right\| \tag{2.4}$$

At the i-th iteration, the sets of points in both spaces will be expanded to contain m_i points so that a more accurate mapping $\mathbf{P}^{(i)}$ can be found. The parameter extraction function $\mathbf{P}$ update process is essential in the Space Mapping algorithm since the analytical form of $\mathbf{P}$ is not available. Hence, Space Mapping uses the current approximation $\mathbf{P}^{(i)}$ to estimate $\mathbf{x_f}^*$ at the i-th iteration as follows:

$$\mathbf{x_f}^{(m_i+1)} = \left(\mathbf{P}^{(i)}\right)^{-1}(\mathbf{x_c}^*) \tag{2.5}$$

The iterative process will continue until the M^{th} iteration is reached, where $M = m_i + 1$ and $\mathbf{R_f}(\mathbf{x_f}^{(M)})$ is matching in a good approximation $\mathbf{R_c}(\mathbf{x_c}^*)$. In this case, $\mathbf{P}^{(i)}$ is also assumed to be close enough to the desired $\mathbf{P}$, and $\mathbf{x_f}^{(M)}$ is considered to be the solution vector for the fine space. This solution is called the *final space-mapped* solution:

$$\mathbf{R_f}\left(\mathbf{x_f}^{(M)}\right) = \mathbf{R_f}(\mathbf{x_f}^{(m_i+1)}) \approx \mathbf{R_c}(\mathbf{x_c}^*) \tag{2.6}$$

Although the simplicity of the Space Mapping is notable, several limitations can be pointed out. First, m_0 fine model CPU-intensive model simulations are needed in advance to be able to find $\mathbf{P}^{(0)}$ and start the iterative process. Second, a linear mapping might not be useful in situations where the coarse model is notably misaligned with the fine model. Third, non-uniqueness of the *parameter extraction* process might provide algorithm non-convergence and oscillation issues due to an erroneous mapping.

2.1.2 The Aggressive Space Mapping (ASM) Approach

The ASM algorithm [7] is a significant improvement of the SM strategy for EM optimization. Its main advantage with respect the original SM approach is that in this case there is no need to perform a preselected set of m_0 fine model analyses, so that the iterative optimization scheme starts from the very first EM analysis performed. ASM utilizes a quasi-Newton type iteration by exploiting first-order derivatives approximations updated by means of the classical Broyden formula [8].

ASM Flow Diagram

The ASM flow diagram is described in Figure 2.2. It consists of an *initializing stage* followed by an *iterative stage*. In the *initializing stage*, the starting point is finding the optimal coarse model vector $\mathbf{x_c}^*$ that gives the target coarse model response $\mathbf{R_c}^* = \mathbf{R_c}(\mathbf{x_c}^*)$.

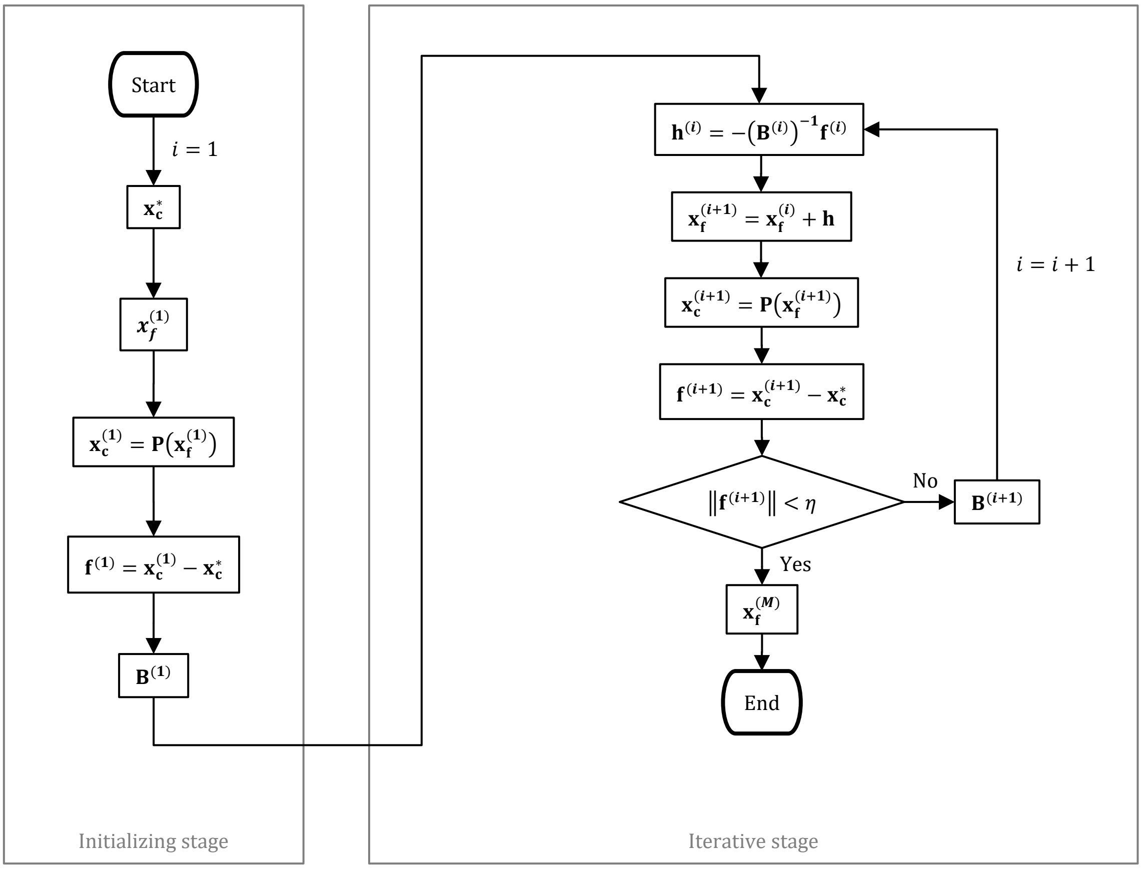

Figure 2.2. Generic flow diagram of the ASM algorithm.

The optimal coarse model response can be obtained by direct optimization of the coarse model by means of available classical optimization methods or by means of classical design methods. The second strategy is the one used in this work, where classical filter synthesis methods are used to obtain the ideal coarse model.

Next step is to initialize the initial fine model vector, $\mathbf{x}_f^{(1)}$, which contains the fine model design parameters, and proceed with the parameter extraction process $\mathbf{P}(\mathbf{x}_f^{(1)})$ through the corresponding *parameter extraction* function $\mathbf{P}$, so that the initial difference, $\mathbf{f}^{(1)}$, between the fine model extracted parameters and the optimal coarse model can be calculated. $\mathbf{f}$ is known as the error vector function. Indeed, the aim of the ASM is to minimize this difference by solving the following non-linear system for $\mathbf{x}_f$:

$$\mathbf{f}(\mathbf{x}_f) = \mathbf{P}(\mathbf{x}_f) - \mathbf{x}_c^* = 0 \tag{2.7}$$

At this point the first Broyden matrix, $\mathbf{B}^{(1)}$, is initialized. Note that when the design parameters in both models have the same nature (i.e. $\mathbf{x}_c$ and $\mathbf{x}_f$ contain geometrical dimensions), $\mathbf{B}$ should be initialized by the identity matrix, that is, $\mathbf{B}^{(1)} = \mathbf{I}$. Conversely, if the natures of $\mathbf{x}_c$ and $\mathbf{x}_f$ differ, as it does in most of the cases in this work, $\mathbf{B}$ might be initialized by estimating the Jacobian of $\mathbf{x}_c$ with respect $\mathbf{x}_f$ by finite differences as follows:

$$\mathbf{B}^{(1)} = \begin{pmatrix} \frac{\delta x_{c1}}{\delta x_{f1}} & \frac{\delta x_{c1}}{\delta x_{f2}} & \cdots & \frac{\delta x_{c1}}{\delta x_{fk}} \\ \frac{\delta x_{c2}}{\delta x_{f1}} & \frac{\delta x_{c2}}{\delta x_{f2}} & & \frac{\delta x_{c2}}{\delta x_{fk}} \\ \vdots & & \ddots & \vdots \\ \frac{\delta x_{ck}}{\delta x_{f1}} & \frac{\delta x_{ck}}{\delta x_{f2}} & \cdots & \frac{\delta x_{ck}}{\delta x_{fk}} \end{pmatrix} \tag{2.8}$$

where $\delta x_{fi} \approx \Delta x_{fi}$ and $\delta x_{ci} \approx \Delta x_{ci}$. Δx_{fi} can be obtained by applying a small perturbation to the initial fine model design parameters while Δx_{ci} can be obtained through the *parameter extraction* function **P**. Therefore, the Broyden matrix linearly approximates the relationship between both design parameter spaces.

The ASM *initializing stage* ends at this moment leading into the ASM *iterative stage*. The updated *i*-th + 1 solution for the fine space $\mathbf{x}_\mathrm{f}^{(i+1)}$ is defined as:

$$\mathbf{x}_\mathbf{f}^{(i+1)} = \mathbf{x}_\mathbf{f}^{(i)} + \mathbf{h}^{(i)} \tag{2.9}$$

where $\mathbf{x}_\mathrm{f}^{(i+1)}$ is then able to be calculated by solving **h** in the following linear system:

$$\mathbf{B}^{(i)}\mathbf{h}^{(i)} = -\mathbf{f}^{(i)} \tag{2.10}$$

and by the *parameter extraction* process the updated fine space solution, $\mathbf{x}_\mathrm{f}^{(i+1)}$, can be mapped into the coarse model so that the updated error vector can be computed as follows:

$$\mathbf{f}^{(i+1)} = \mathbf{P}\left(\mathbf{x}_\mathbf{f}{}^{(i+1)}\right) - \mathbf{x}_\mathbf{c}^{*} \tag{2.11}$$

Next, the stopping criteria is tested, which typically is based on obtaining the normalized error function $\|\mathbf{f}^{(i)}\|$:

$$\|\mathbf{f}^{(i)}\| = \sqrt{\left(\frac{x_{c1}{}^{(i)} - x_{c1}^{*}}{x_{c1}^{*}}\right)^2 + \left(\frac{x_{c2}{}^{(i)} - x_{c2}^{*}}{x_{c2}^{*}}\right)^2 + \cdots + \left(\frac{x_{ck}{}^{(i)} - x_{ck}^{*}}{x_{ck}^{*}}\right)^2} \tag{2.12}$$

and comparing it with a predefined, and sufficiently small, target convergence error, η. The iterative process will end only if the stopping criteria is fulfilled. Otherwise, the iterative process will continue by obtaining the Broyden matrix update, $\mathbf{B}^{(i+1)}$, which will be calculated based on the data from the previous iterations [8]:

$$\mathbf{B}^{(i+1)} = \mathbf{B}^{(i)} + \frac{\mathbf{f}^{(i+1)}\mathbf{h}^{(i)\mathbf{T}}}{\mathbf{h}^{(i)\mathbf{T}}\mathbf{h}^{(i)}} \tag{2.13}$$

and the iterative process starts again. Such optimization process will finish at the M^{th} iteration, when the solution vector for the fine space, $\mathbf{x}_\mathrm{f}^{(M)}$, that fulfils the stopping condition $\|\mathbf{f}^{(M)}\| < \eta$, is found.

ASM Approach in this Thesis

It is important to note that, in the generic ASM formulation, the iterative optimization of the *parameter extraction* function **P** has still to be considered as an independent problem focused on minimizing (2.4) at each iteration step [5], [6]. However, in this work a different strategy will be used in order to avoid the iterative optimization of **P**. As it is shown in Figure 2.3, in this work the coarse model space will be defined by the device electrical equivalent circuit while the fine model space will be defined by the device layout. Therefore, the design parameters defined in the coarse space, $\mathbf{x_c}$, will correspond to circuit parameters, whereas the variables defined in the fine space, $\mathbf{x_f}$, will correspond to geometrical dimensions. In addition, the *parameter extraction* function **P** will be defined by a set of available closed-form analytical formulas, which link the fine model response with the coarse model design parameters.

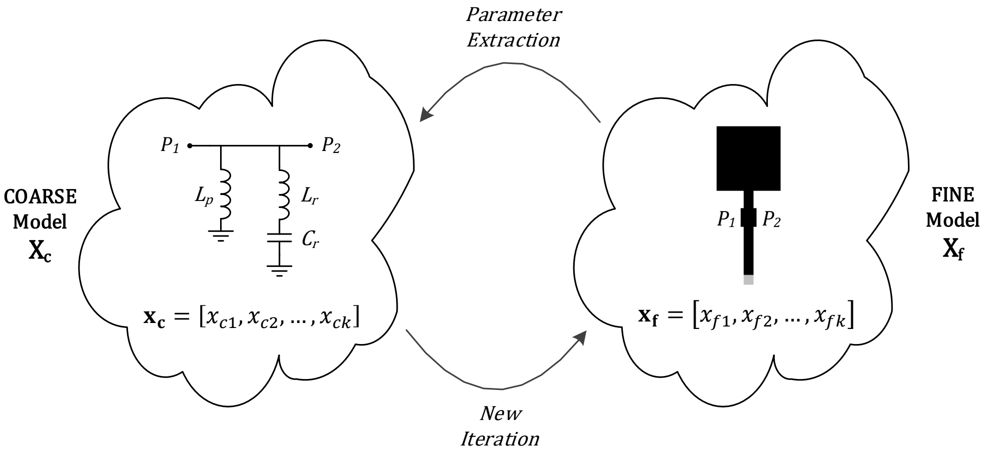

Figure 2.3. Aggressive Space Mapping design spaces definition in this work.

Therefore, in this particular approach, the *parameter extraction* process consists on inferring the values of the coarse model circuit parameters from the S-parameter response of the fine model, obtained by its corresponding EM simulation. The *parameter extraction* analytical functions are strictly dependent on the device topology. Since several filter structures are reported in this work, such formulas are specifically detailed for each case in the corresponding section.

2.2 Single-Ended and Balanced Wideband Microwave Filters

The foundations of the synthesis of microwaves filters are briefly discussed in this section, providing the basis with which the bandpass filter structures synthesized in this work are based on. The description of the lowpass filter prototype, the frequency and impedance transformation in order to obtain the canonical bandpass filter circuit and the generalized bandpass filter definition are presented next.

2.2.1 Fundamentals of Single-Ended Filters Synthesis

In this thesis, the classical filter theory is used in order to synthesize bandpass filters providing Chebyshev-like responses, with wide bandwidths and good out-of-band rejection, among other characteristics, and according to given specifications. Therefore, the filter theory is used to obtain the ideal filter circuit, based on ideal lumped elements such as inductances and capacitances, which provides the desired response over the frequency range of interest. To this end, the normalized lowpass filter prototype with Chebyshev response as well as the frequency and impedance transformations to be applied in order to obtain the desired passband filter circuit are briefly reviewed. Next, the generalized bandpass filter structure based on impedance or admittance inverters and generic resonators is introduced, which is the basis of most of the passband filter structures synthesized throughout this work.

Lowpass Filter Prototype

The lowpass filter circuits presented in Figure 2.4 are capable of synthesizing canonical responses like Chebyshev or Butterworth. The values of the elements of such circuits are normalized in impedance, so that the source resistance or conductance is equal to the unity, i.e. $g_0 = 1$, as well as in frequency, so that the angular cut-off frequency is also $\Omega_c = 1$.

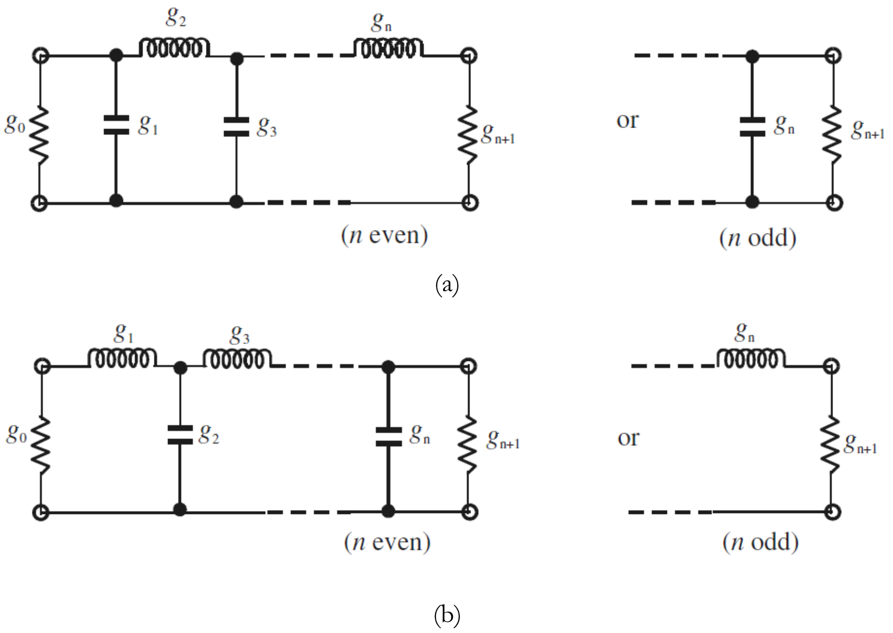

Figure 2.4. Lowpass prototype filter structure (a) and its dual (b). Reprinted from [9].

The normalized elements g_i strictly depend on the response to be synthesized. For instance, for a Chebyshev response, such elements are defined as [9]:

$$
\begin{aligned}
g_0 &= 1 \\
g_1 &= \frac{2}{\gamma}\sin\left(\frac{\pi}{2N}\right) \\
g_i &= \frac{1}{g_{i-1}}\frac{4\sin\left[\frac{(2i-1)\pi}{2N}\right]\sin\left[\frac{(2i-3)\pi}{2N}\right]}{\gamma^2+\sin^2\left[\frac{(i-1)\pi}{N}\right]} \qquad \text{for } i = 2,3,\dots N \\
g_{N+1} &= \begin{cases} 1 & \text{for } N \text{ odd} \\ \coth^2\left(\frac{\beta}{4}\right) & \text{for } N \text{ even} \end{cases}
\end{aligned}
\tag{2.14}
$$

where

$$\beta = \ln\left[\coth\left(\frac{L_{Ar}}{17.37}\right)\right]$$

$$\gamma = \sinh\left(\frac{\beta}{2N}\right)$$

N is the order of the filter and L_{Ar} corresponds to the equal ripple passband level, a parameter that is defined by nature in the Chebyshev response, as it can be seen in Figure 2.5.

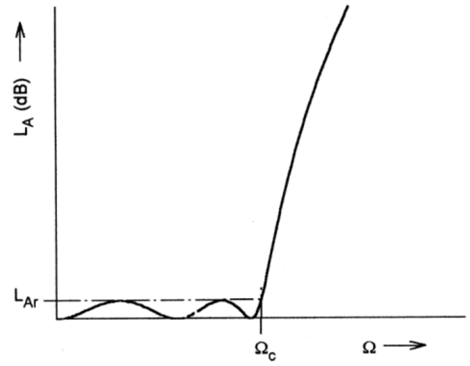

Figure 2.5. Chebyshev response of a lowpass prototype filter. *Ω* is the normalized frequency and L_A correspond to the response insertion loss. Reprinted from [9].

Note that for a lossless two-port network filter, the minimum passband return loss, *RL* in *dB* (where *RL* > 0), is related to the passband ripple, L_{Ar}, as follows:

$$L_{Ar} = -10\log(1 - 10^{-0.1RL}) \tag{2.15}$$

Next, in the case of a bandpass filter design subjected to certain specifications, the corresponding frequency and impedance transformations must be applied to the lowpass filter prototype in order to obtain the filter Chebyshev response at the required center frequency, f_0, and port impedance, Z_0 (which typically corresponds to 50 Ω).

Bandpass Filter Transformation

The required frequency and element transformation to obtain from the lowpass prototype a filter with a bandpass response is shown in Figure 2.6:

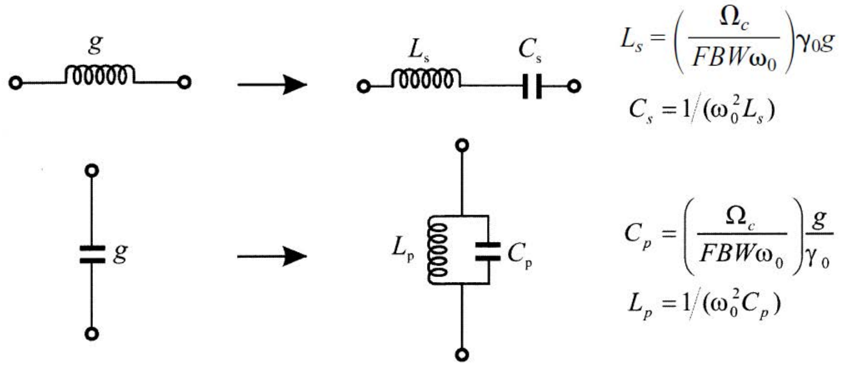

Figure 2.6. Lowpass prototype to bandpass elements transformation. Reprinted from [9].

where ω_0 denotes the center angular frequency, γ_0 is the impedance scaling factor and the *FBW* corresponds to the fractional bandwidth. The center angular frequency ω_0 is defined as follows:

$$\omega_0 = \sqrt{\omega_1\omega_2} \tag{2.16}$$

where ω_2 and ω_1 indicate the passband edge angular frequencies. On the other hand, the fractional bandwidth, *FBW,* is defined as the ratio between the passband frequency range, delimited by ω_2-ω_1, and the center angular frequency ω_0:

$$FBW = \frac{\omega_2 - \omega_1}{\omega_0} \tag{2.17}$$

Generalized Bandpass Filter

A more general filter structure can be obtained by replacing the lumped LC resonators of Figure 2.6 by distributed circuits such as microwave cavities, coaxial or microstrip resonators, etc. Ideally, the reactances or susceptances of the distributed circuits should equal those of the lumped resonators at all frequencies but, in practice, they approximate the reactances or susceptances of the lumped resonators only near the resonance frequency. Therefore, the synthesis of filters by means of distributed components implies bandwidth limitations whose effects might be negligible for narrowband filters, but that directly have a negative impact in the design of wideband filters as it is discussed later in Chapters 3 and 4.

By convenience, regardless of the resonator topology, the reactance or susceptance slope of such resonators needs to coincide with the one of the ideal LC resonator, in order to mimic its behavior nearby the resonance frequency. The reactance slope for resonators having null reactance, $X(\omega_0) = 0$, at center frequency ω_0 is defined as:

$$x_i = \frac{\omega_0}{2}\frac{dX_i(\omega)}{d\omega}\bigg|_{\omega=\omega_0} \tag{2.18}$$

Whereas the susceptance slope for resonators having null susceptance, $B(\omega_0) = 0$, at center frequency ω_0 is defined as:

$$b_i = \frac{\omega_0}{2}\frac{dB_i(\omega)}{d\omega}\bigg|_{\omega=\omega_0} \tag{2.19}$$

For instance, in its simplest form, it can be shown that the reactance and susceptance slope parameters of the ideal lumped LC series and shunt resonators are $x = \omega_0 L$ and $b = \omega_0 C$ respectively [9].

On the other hand, it is often desirable to use only series or shunt elements when synthesizing a filter with a particular resonator technology. To this end, the impedance or admittance inverters can be used, in order to transform a series resonator to a shunt resonator or viceversa. An ideal impedance inverter provides the inverse of the impedance load, Z_L, at its input, Z_{in}:

$$Z_{in} = \frac{K^2}{Z_L} \tag{2.20}$$

Similarly, an ideal admittance inverter provides the inverse of the admittance load, Y_L, at its input, Y_{in}:

$$Y_{in} = \frac{J^2}{Y_L} \tag{2.21}$$

These ideal inverters are frequency independent and introduce a phase shift of ±90º and they also have the property to shift the impedance or admittance levels depending on the choice of the characteristic impedance, *K*, or admittance, *J*. In practice, such inverters are frequency dependent so that the ±90º phase shift will be set at the design center frequency, and typically they are implemented by means of quarter-wavelength transmission lines. Hence, note that such inverters implemented with transmission lines present a narrowband functionality by nature due to their inherent frequency dependence.

Therefore, by combining the properties of the impedance or admittance inverters with the generic reactance or susceptance slope definitions of the resonators, a more suitable form for microwave bandpass filters implementation can be derived, leading to the so called generalized bandpass filter structures, depicted in Figure 2.7.

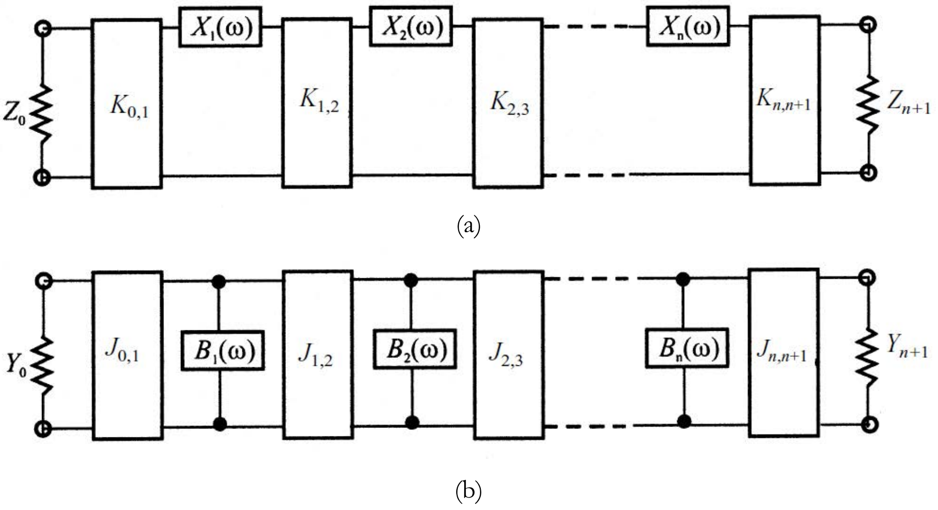

Figure 2.7. Generalized bandpass filters. (a) Using impedance inverters. (b) Using admittance inverters. Reprinted from [9].

The equations corresponding to the generalized bandpass filter structure based on impedance inverters are detailed as follows [9]:

$$K_{0,1} = \sqrt{\frac{Z_0 FBW x_1}{\Omega_c g_0 g_1}}\,, \qquad K_{i,i+1} = \frac{FBW}{\Omega_c}\sqrt{\frac{x_i x_{i+1}}{g_i g_{i+1}}}\Bigg|_{i=1\text{ to }N-1}\,, \qquad K_{N,N+1} = \sqrt{\frac{Z_{N+1} FBW x_N}{\Omega_c g_N g_{N+1}}} \tag{2.22}$$

whereas the equations for the generalized bandpass filter structure based on admittance inverters are the following:

$$J_{0,1} = \sqrt{\frac{Y_0 FBW b_1}{\Omega_c g_0 g_1}}\,, \qquad J_{i,i+1} = \frac{FBW}{\Omega_c}\sqrt{\frac{b_i b_{i+1}}{g_i g_{i+1}}}\Bigg|_{i=1\text{ to }N-1}\,, \qquad J_{N,N+1} = \sqrt{\frac{Y_{N+1} FBW b_N}{\Omega_c g_N g_{N+1}}} \tag{2.23}$$

2.2.2 Microstrip Balanced Microwave Networks

In the last years, differential or balanced systems have been increasingly penetrating in the RF and microwave domain, typically dominated by single-ended systems. Traditionally, differential circuits have been applied to low-frequency analog and also to high-speed digital systems. Main advantages of the differential circuits in comparison with single-ended circuits are higher immunity to electromagnetic noise and crosstalk and lower electromagnetic interference (EMI). However, special attention needs to be paid to the presence of common-mode noise, an undesired effect originated by an external source or by mode conversion. Therefore, in order to prevent the negative effects of the common-mode noise (mainly radiation), the most optimal solution for a balanced circuit design is to suppress the common-mode while preserving the integrity of the differential-mode in the frequency range of interest.

In modern communication systems, where signal integrity and higher signal-to-noise ratio (SNR) are key figures of merit, balanced circuits sound to be a better option than the single-ended counterparts. Conversely, the design and fabrication of differential circuits is obviously more complex due to the need to deal with balanced signals interconnects, which is the main reason why unbalanced circuits are still leading in the RF and microwave field. In any case, the inherent properties of the balanced circuits make them very suitable for current digital communications systems, and together with recent technological advances, the research activity in this topic has increased very rapidly in the last decade. More specifically, the research oriented to the design of balanced filters has raised significantly, since these devices have a key role on such systems [10].

Most of the content of this work is focused on the unattended design and optimization of wideband balanced microstrip filter structures, where the main objective is to provide the required differential-mode response subjected to certain specifications and increase the common-mode rejection ratio (CMRR) in the differential-mode passband frequency range, as well as in the out-of-band frequencies if possible. As it will be described later in Chapter 4, the common-mode rejection is typically achieved by using circuit elements which are insensitive to the differential-mode but that provide controllable transmission zeros for the common-mode.

Topology and Propagation Modes

The balanced filters reported in this work are implemented by using differential microstrip lines. The equivalent schematic (the so-called three-wire balanced line) and the microstrip implementation of such lines is depicted in Figure 2.8.

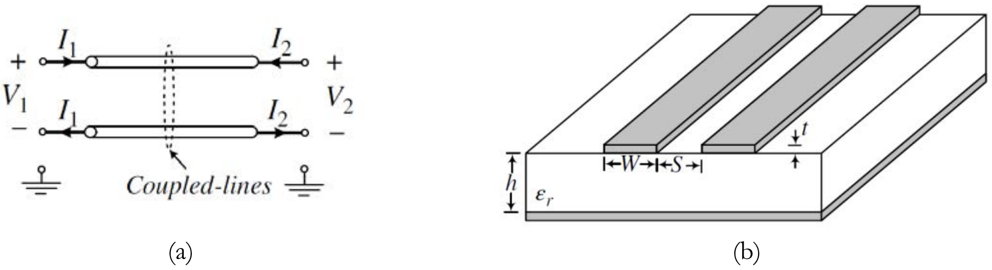

(a) (b)

Figure 2.8. Schematic of three-wire balanced line (a) and its microstrip implementation (b). Reprinted from [11].

This topology is the most common in practical implementations, and it is composed of a pair of coupled lines over a ground plane. Considering that such structure is perfectly balanced, the two active wires have equal potential with respect to ground but with a 180º phase shift, so that they carry equal but opposite currents because the impedances of each conductor to ground is the same.

The three-wire transmission lines propagate the balanced-mode as well as the unbalanced- or common-mode (the latter is due to the existence of the ground plane). The balanced-modes propagate when the pair of coupled lines are driven differentially, whereas for the unbalanced-mode equal signals in magnitude and phase propagate for each line. Since the distance between the ground plane and the lines is set by the substrate thickness, so that it is small in comparison with the wavelength, both balanced- and common-modes propagate quasi-TEM modes [12]. The differential- and common-modes are equivalent, but not equal, to the odd and even modes, respectively, and the difference between such modes comes from signal definitions [11]. In the differential- and common-modes, two single-ended ports are driven as a pair, leading to the so-called composite port. Therefore, any balanced circuit, which propagates both the differential- and common-modes, can be decomposed into its differential- and common-mode portions as it is shown in Figure 2.9.

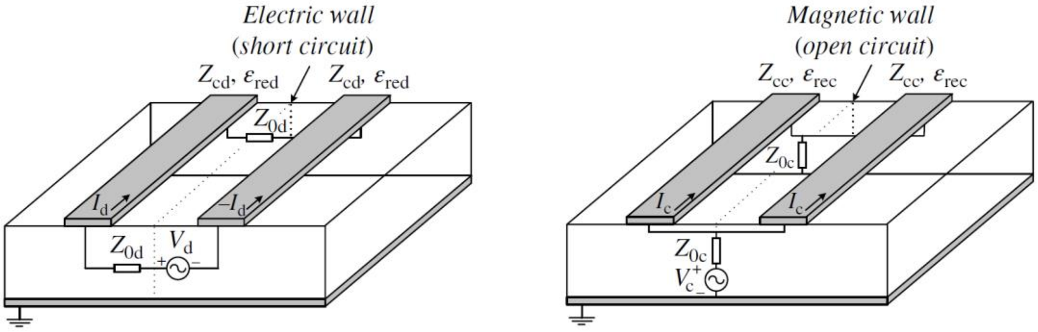

(a) (b)

Figure 2.9. Generation of the differential-mode (a) and the common-mode (b) in a differential microstrip line. Reprinted from [11].

Assuming that the lines are perfectly matched with Z_{0d} for the balance-mode and with Z_{0c} for the common-mode, only forward waves will be present in the lines. In this situation, the differential voltage and current between the pair of lines are defined as [13]:

$$V_d = V_1 - V_2 \tag{2.24}$$

$$I_d = \frac{1}{2}(I_1 - I_2) \tag{2.25}$$

where V_1, V_2 and I_1, I_2 are the voltages and currents present on the corresponding lines of the differential pair. On the other hand, the common-mode voltage and current are given by [13]:

$$V_c = \frac{1}{2}(V_1 + V_2) \tag{2.26}$$

$$I_c = I_1 + I_2 \tag{2.27}$$

and therefore the differential-mode and common-mode characteristic impedances can be derived as follows:

$$Z_{cd} = \frac{V_d}{I_d} = \frac{2(V_1 - V_2)}{I_1 - I_2} \tag{2.28}$$

$$Z_{cc} = \frac{V_c}{I_c} = \frac{V_1 + V_2}{2(I_1 + I_2)} \tag{2.29}$$

Mixed-Mode S-parameters

The S-parameters are used for the linear analysis of microwave networks, i.e. in the small signal region [14]. They give relative information about the amplitude and phase of the transmitted and reflected wave with regards to the incident wave. Such scattering parameters, typically used in any arbitrary single-ended networks, can be defined as well for the differential networks, but with some particularities. In this case, the simultaneous propagation of the differential- and common-modes, known as the mixed-mode propagation [13], needs to be considered, leading to the definition of the mixed-mode S-parameters. By convenience, in a two-port differential network, these mixed-mode S-parameters can be seen as a four port single-ended network, where the two ports are driven as a pair as it is shown in Figure 2.10.

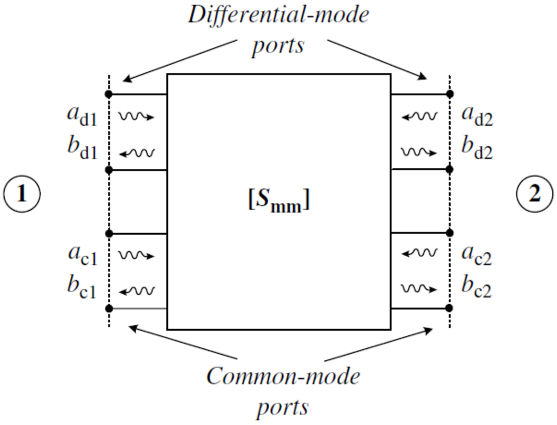

Figure 2.10. Diagram of mixed-mode S-parameters in a differential two-port circuit. Reprinted from [11].

Therefore, the mixed-mode S-parameter matrix can be arranged as:

$$\mathbf{b_{mm}} = \mathbf{S_{mm}}\mathbf{a_{mm}} = \begin{pmatrix} b_{d1} \\ b_{d2} \\ b_{c1} \\ b_{c2} \end{pmatrix} \begin{pmatrix} S_{11}^{dd} & S_{12}^{dd} & S_{11}^{dc} & S_{12}^{dc} \\ S_{21}^{dd} & S_{11}^{dd} & S_{21}^{dc} & S_{22}^{dc} \\ S_{11}^{cd} & S_{12}^{cd} & S_{11}^{cc} & S_{12}^{cc} \\ S_{21}^{cd} & S_{22}^{cd} & S_{21}^{cc} & S_{22}^{cc} \end{pmatrix} \begin{pmatrix} a_{d1} \\ a_{d2} \\ a_{c1} \\ a_{c2} \end{pmatrix} \tag{2.30}$$

where a_{di} and a_{ci} are the normalized differential- and common-mode voltage incident waves of the two-port differential network whereas b_{di} and b_{ci} are the reflected ones. In order to calculate the S-parameters, all ports except the stimulus port must be terminated with the port reference impedance, Z_{0d} and Z_{0c}, for the differential- and common-mode respectively. The mixed-mode S-matrix can be expressed as:

$$\mathbf{S_{mm}} = \begin{pmatrix} \mathbf{S^{dd}} & \mathbf{S^{dc}} \\ \mathbf{S^{cd}} & \mathbf{S^{cc}} \end{pmatrix} \tag{2.31}$$

where $\mathbf{S}^{\mathrm{dd}}$ and $\mathbf{S}^{\mathrm{cc}}$ correspond to the differential- and common-mode S-parameter matrices, which can be seen as the S-parameters obtained by analyzing the decomposed differential- and common-mode conceptual two-port circuits depicted in Figure 2.11.

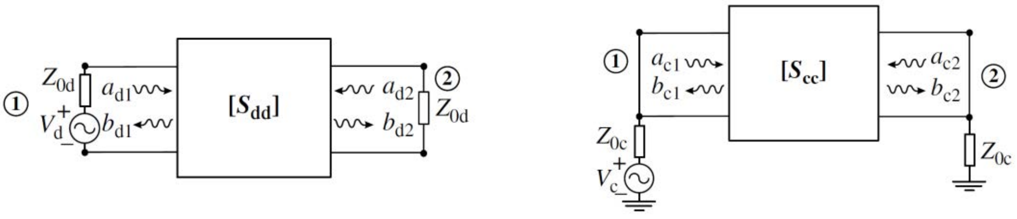

(a) (b)

Figure 2.11. Differential-mode (a) and common-mode (b) S-parameters in a differential two-port circuit. Reprinted from [11].

On the other hand, $\mathbf{S}^{\mathrm{dc}}$ describe the conversion of common-mode inputs into the differential-mode outputs, while $\mathbf{S}^{\mathrm{cd}}$ describe the conversion of differential-mode inputs into the common-mode outputs. Since actual devices are not perfectly symmetric (i.e. due to manufacturing imperfections), perfect balance cannot be achieved and therefore, mode conversion effects will occur. In addition, mixed-mode S-parameters can be related to the single-ended S-parameters by means of the following expressions:

$$
\begin{aligned}
\mathbf{S}^{\mathbf{dd}} &= \frac{1}{2}\begin{pmatrix} S_{11}-S_{13}-S_{31}+S_{33} & S_{12}-S_{14}-S_{32}+S_{34} \\ S_{21}-S_{23}-S_{41}+S_{43} & S_{22}-S_{24}-S_{42}+S_{44} \end{pmatrix} \\
\mathbf{S}^{\mathbf{cc}} &= \frac{1}{2}\begin{pmatrix} S_{11}+S_{13}+S_{31}+S_{33} & S_{12}+S_{14}+S_{32}+S_{34} \\ S_{21}+S_{23}+S_{41}+S_{43} & S_{22}+S_{24}+S_{42}+S_{44} \end{pmatrix} \\
\mathbf{S}^{\mathbf{dc}} &= \frac{1}{2}\begin{pmatrix} S_{11}+S_{13}-S_{31}-S_{33} & S_{12}+S_{14}-S_{32}-S_{34} \\ S_{21}+S_{23}-S_{41}-S_{43} & S_{22}+S_{24}-S_{42}-S_{44} \end{pmatrix} \\
\mathbf{S}^{\mathbf{cd}} &= \frac{1}{2}\begin{pmatrix} S_{11}-S_{13}+S_{31}-S_{33} & S_{12}-S_{14}+S_{32}-S_{34} \\ S_{21}-S_{23}+S_{41}-S_{43} & S_{22}-S_{24}+S_{42}-S_{44} \end{pmatrix}
\end{aligned}
\tag{2.32}
$$

and therefore the mixed-mode S-parameters of a balanced circuit can be easily obtained through the corresponding single-ended S-parameters measurement, which is very useful for the analysis and characterization of such balanced circuits.

Symmetry Properties in Balanced Circuits

Symmetry properties of balanced circuits bring some advantages in the S-parameter analysis of such circuits. First, it is important to mention that if a differential two-port network is symmetric, the single-ended S-parameters for the odd- and even-mode networks are identical to the S-parameters for the differential- and common-mode networks, that is, $\mathbf{S}^{\mathrm{dd}} = \mathbf{S}_{\mathrm{o}}$ and $\mathbf{S}^{\mathrm{cc}} = \mathbf{S}_{\mathrm{e}}$. Moreover, the analysis of symmetric two-port differential lines driven by single-ended four ports can be reduced to the analysis of two single-ended two-port networks as it is described in Figure 2.12.

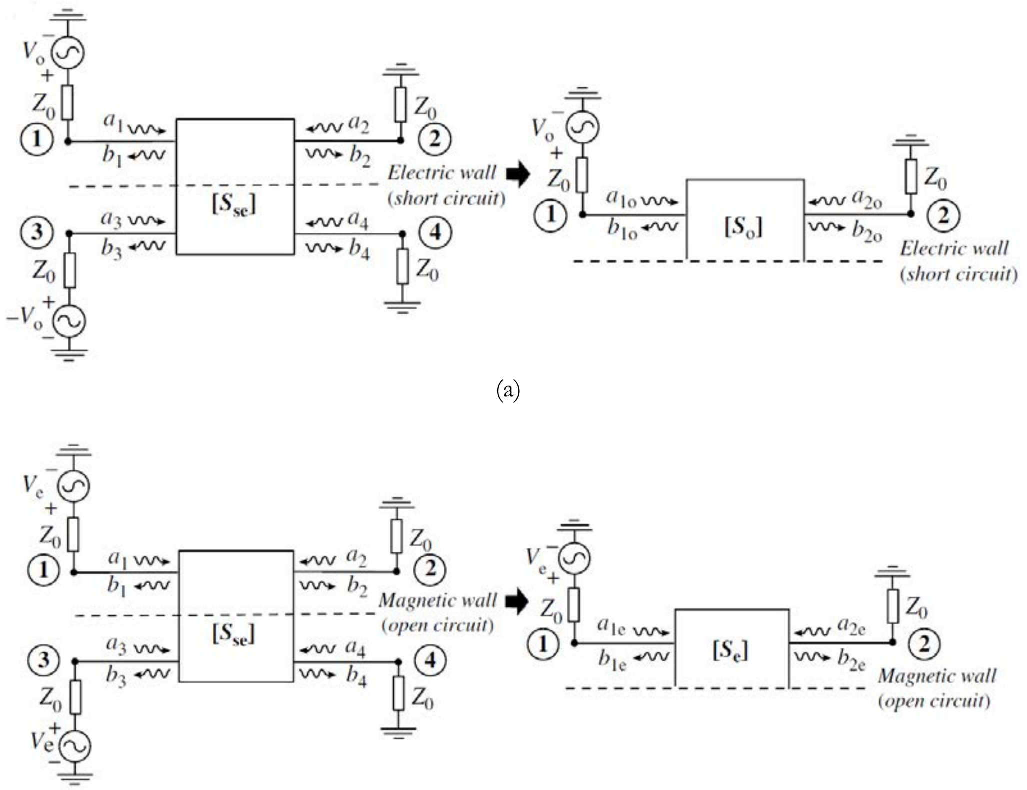

(a)

(b)

Figure 2.12. Symmetric single-ended four-port network (a) odd- and (b) even-mode S-parameters analysis. The four-port network is simplified in two two-port networks. Reprinted from [11].

When an odd, or differential, excitation is applied to the network, the symmetry plane behaves as an electric wall or E-wall (short circuit), and the two halves become the same two-port network. Similarly, when an even, or common, excitation is applied to the network, the symmetry plane behaves as a magnetic wall or H-wall (open circuit), and the two identical halves constitute the same two-port network. Hence, the symmetry properties of the differential circuits, previously highlighted in Figure 2.9, allow to simplify the S-parameter analysis of such networks.

2.3 State of the Art

In this section the recent advances in the ASM technique applied to single-ended and balanced filters are discussed. Moreover, the reasons for the continuous growing interest in balanced microwave filters are explained and well supported by some of the most novel publications in the field. Last, the approach used in this work by combining the ASM optimization technique with the single-ended and balanced filter structures based on SIRs is presented, and the most relevant and innovative contributions to the current state of art in these topics are emphasized.

2.3.1 ASM Advances in Microwave Filters Optimization

Since Bandler et al. proposed the ASM for the first time in 1995 [7], [15], the research about the optimization of microwave devices by means of ASM has become a hot topic in the last decades. More especially, the works focused on the usage of ASM for the optimization of microwave filters has increased very rapidly, mainly in the design of waveguide filters as well as microstrip filters, although ASM has also been applied in some other areas like LTCC technology filter and diplexer designs [16], dielectric resonator filters [17], [18], and even in some other technical fields, out of the original scope of ASM [19], [20], [21], [22], [23], reinforcing the vast usefulness of this optimization method.

With regard to waveguide filter design, ASM techniques are applied in order to automate the design process and improve the design robustness and the post-manufacturing tuning processes [24], [25], and in the most recent works the ASM has been also applied to the design of substrate integrated waveguide (SIW) bandpass filters [26]. To this end, specific theoretical contributions to the ASM concept have been proposed in some of these works, like statistical approaches to the *parameter extraction* function [27], minimize the fine model frequency points [28], model geometrical segmentation and hybrid optimization methods for coarse model and *parameter extraction* function [24], [29], and multiple coarse models generation with gradual increase in accuracy [30].

On the other hand, extensive research has been done in the ASM-based microstrip filter design, most likely because microstrip technology is widely used in the industry and the manufacturing process is inexpensive and fast, which makes it very suitable for proof of concept purposes. Without going any further, ASM first proof of concept was done by Bandler by means of a high temperature superconductor microstrip bandpass filter design [7], [15]. Many researchers followed his steps from then on, leading to a wide variety of microstrip filter designs based on ASM. Interdigital bandpass filters [31], [32], double-folded stub bandstop filters [33], [34], [35], bandstop filters based on open stubs [36] and bandstop filters based on mitered bends [37], cross-coupled bandpass filters [38], bandstop filters based on complementary split ring resonators (CSRR) [39], parallel coupled lines bandpass filters [40], bandpass hairpin filters [41], bandpass filters based on open complementary split ring resonators (OCSRR) [42], and, more recently, bandpass filters based in slow-wave structures [43], [44], reflect the wide research activity on this type of filter technology. These research publications brought also numerous theoretical contributions to the ASM formulation: structural decomposition of the fine model to build accurate coarse models [31], trust-region ASM with multipoint *parameter extraction* [35], trust-region ASM combined with direct optimization [33], surrogate enhancement by means of additional fine data [34], partial space mapping exploiting fine model sensitivities [36] and heuristically constrained ASM [37], to mention some of them.

In recent years, SIR-based lowpass filters optimized through ASM have also been reported [45], [46], [47], [48], which have proved the effectiveness of optimizing such resonators by means of the ASM technique. Conversely, before this work, the ASM optimization method applied to the synthesis of bandpass filters based on SIRs has not been reported yet. The semi-lumped nature of the SIRs, very compact in size and functional for wide bandwidths, combined with their inherent flexibility to synthesize complex resonator structures, enables the feasibility of the synthesis of compact and wideband microstrip bandpass filters with very competitive responses. Such filter topologies, automatically synthesized in combination with the ASM technique from design specifications, leads this work as one of the pioneers in this topic. Note that a fully automated and unattended optimization process has been developed for the different filter structures analyzed in this thesis, so that the optimization process starts from the filter design specifications (inputs), and ends with the filter layout (output) that fulfil such specifications, with no further manual interaction throughout the entire process. Therefore, those developed ASM algorithms can be understood as software engineering tools for automatic filter synthesis[1].

In addition, in this work the ASM coarse and fine spaces have different nature, corresponding to lumped elements and geometrical dimensions, respectively, and the *parameter extraction* function, **P**, that links both spaces is based in closed-form analytical formulas. This ASM strategy was first reported in [49], and it has become widely used since then [39], [44], [50]. In this case, **P** is known in advance, so that it is no longer treated as an ASM optimization subproblem. The effectiveness of fitting **P** to closed-form formulas is directly linked to the coarse model accuracy with regards the fine model to be optimized. In this work, it is demonstrated that the coarse models used for the SIRs, all based on lumped components [51], are accurate enough to let the ASM algorithm converge in few iterations.

2.3.2 Planar Balanced Microwave Filters Optimization

In the last years, the interest in the design of microwave balanced filters with high common-mode rejection has increased very sharply within the RF and microwave community, since their inherent properties makes them very suitable for the modern communication systems [10], [11]. Many publications have been reported recently presenting different strategies in order to provide balanced bandpass filters with the desired differential-mode response and, at the same time, good common-mode rejection levels in the frequency range of interest. Conversely, with regard to the automatic optimization by means of ASM of planar balanced microwave filters, to the best of our knowledge, no publications have been reported so far. This fact places this work in a privileged position to address this topic.

Both single-ended and balanced filter topologies based on SIRs are reported in this work. More precisely, Articles **IMS14*** and **TMTT14** (Chapter 3) are focused on the ASM-based automated synthesis of single-ended wideband bandpass filters, whereas Articles **TMTT15**, **EUMC15***, **IJMWT16**, **NEMO17*** and **TMTT18** (Chapter 4) are devoted to the automatic synthesis of wideband balanced bandpass filters. Therefore, ASM-based optimization of balanced filters with intrinsic common-mode suppression is widely explored in this research work, becoming one of its most relevant topics.

---

[1] Most of the ASM-based works reported so far are oriented to prove the validity of this technique or to provide novel theoretical contributions to the ASM concept. Contrarily, in this work, the usage of ASM pretends to be application-oriented, similarly as Bandler proposed in [72], and entirely developed in Matlab®, being focused on proving the validity of ASM as a practical engineering tool for automatic filter synthesis.

Different approaches to obtain balanced bandpass filters with wide (or even ultra-wide[2]) bandwidths have been recently published, and the most relevant ones are also simultaneously providing common-mode rejection at least in the differential-mode bandpass frequency range. As it is clearly demonstrated in Chapter 4, the results obtained for the balanced filter structures based on SIRs synthesized by means of ASM are very competitive with regard to other balanced filter topologies, considering their size and the differential- and common-mode performances achieved. Some of the balanced structures automatically optimized in this work were already previously reported [52], [53], which successfully proved the usage of SIRs in the design of wideband balanced bandpass filters with intrinsic common-mode suppression. Several other works of balanced filters synthesis by means of SIRs have been published recently [54], and even an UWB and ultra-compact balanced filter has been demonstrated [55].

Other state-of-the-art topologies for the synthesis of wideband balanced passband filters are, for instance, metamaterial-inspired balanced filter topologies based on open split ring resonators (OSRR) and OCSRR, which are able to provide wide bandwidths and good CMRR with a very compact outline [56], [57]. Structures using coupled line sections [58], [59], [60], [61], [62], T-shaped structures [63], [64], and branch line topologies [65], [66], [67], are also good examples of filter designs with competitive performances. Such structures are easy to implement since they are based on microstrip single-layer structures, but at expenses of occupying more effective area. On the other hand, some other useful strategies but more complex to manufacture are the multilayer defected ground structures (DGSs), based on the multilayer microstrip-to-slotline mechanism (the slotline pattern is etched in the ground layer) [68], [69]. These structures have inherent wideband common-mode suppression characteristics and thus have the potential to be used in UWB differential filter designs [70].

In Articles **TMTT15**, **EUMC15***, **IJMWT16**, **NEMO17*** and **TMTT18**, focused on the synthesis of balanced filters, the corresponding comparisons with the most relevant publications about the different balanced filter topologies mentioned previously are presented. Through this analysis, it is demonstrated that the synthesis of filter structures based on SIRs by means of ASM are very competitive in size and performance. Furthermore, in this work the synthesis of such structures has been carried out in an unattended manner, considering the filter design specifications as the input of each algorithm developed specifically for each structure. These ASM-based algorithms have been developed entirely with Matlab®, which has been linked to an independent EM solver, in this case Agilent®[3] Momentum, in order to perform the layout EM simulations when needed and to obtain their corresponding S-parameter data. This connection between those commercially available software packages is carried out automatically, so that there's no need for any kind of manual interaction during the whole optimization process.

---

[2] Ultra-Wide Band (UWB) filters are typically defined as those which are able to provide a passband response that covers a frequency range from 3.1GHz to 10.6GHz [73]. The Federal Communications Commission (FCC) authorized its unlicensed usage on 14th February 2002.

[3] Currently Keysight®.

2.3.3 Unattended Design of Wideband Bandpass Filters from Specifications by means of ASM

In this work, the combination between the ASM technique with the classical filter synthesis is explored. The main idea consists of automatically synthesizing the optimum layout of single-ended or balanced microstrip wideband bandpass filters based on Stepped-Impedance Resonators (SIRs). Such SIRs act as shunt resonators with a particular susceptance $B_i(\omega)$ and susceptance slope b_i, and two different strategies are followed in order to obtain the desired filter structures that meet the proposed design specifications. In Articles **IMS14***, **TMTT14**, **EUMC15*** and **TMTT15**, the SIRs are coupled to quarter-wavelength transmission lines, acting as admittance inverters, so that the filter structure is based in the one depicted in Figure 2.7 (b). On the other hand, in Articles **IJMWT16**, **NEMO17*** and **TMTT18**, the shunt SIRs are combined with interdigital capacitors acting as series resonators, leading to a novel filter topology not reported so far. In this case, the frequency and impedance transformations reported in Figure 2.6 must be applied in both SIRs and interdigital capacitors in order to obtain the desired bandpass filter topology.

The main principle behind the completely unattended ASM-based optimization scheme of these filter topologies is based on the independent optimization of each section or cells layout the filter is composed by. Once each filter cell layout is successfully optimized by means of the corresponding ASM algorithm, the optimum filter layout is obtained by simply cascading such optimized sections. The different filter structures reported in this work are based on specific resonators and/or admittance inverter topologies, so that a dedicated ASM algorithm must be specifically developed for each particular filter cell. Depending on the complexity of the filter cell topology, the ASM optimization process might also contain several ASM sub-stages.

Moreover, in this work the Space Mapping concept has also been applied beyond its standard definition. Widely discussed in Section 2.1.1, Space Mapping and its derivatives like ASM is mainly conceived in order to efficiently optimize a fine model (i.e. layout), computationally expensive, by means of a computationally more efficient coarse model (i.e. equivalent circuit). In this work, the ASM technique has also been successfully applied to overcome the narrowband limitations of the admittance inverters. As already pointed out in Section 2.2.1, in the design of wideband bandpass filters it is clear that the usage of such inverters based on quarter-wavelength transmission lines impact negatively the overall filter bandwidth, thus the synthesized filter will not satisfy the bandwidth requirements. In order to overcome this problem, this original ASM optimization scheme is formulated with the aim to obtain the optimum filter schematic which compensates the narrowband effects of such inverters. To this end, both coarse and fine spaces are defined by the filter circuit schematic, but with some differences. The coarse model is based on the ideal bandpass filter structure depicted in Figure 2.7 (b), where the admittance inverters are considered ideal and so frequency invariant. Conversely, the fine model considers a more practical model for such inverters, frequency dependent, so that the bandwidth limitation effects are then introduced in this model. Therefore, the optimization process will try to find the optimum fine model filter schematic which matches the target Chebyshev response of the ideal filter schematic defined in the coarse space. Such optimized fine model filter schematic, known as the optimum filter schematic, will compensate the narrowband effects of the inverters by modifying the resonator values. Therefore, it is expected that the response obtained from the filter synthesis based on this optimum schematic satisfies the entire filter design specifications, including bandwidth. Next, once the optimum schematic is known, the optimum layout ASM is performed in order to obtain the filter layout that fulfils the specifications. Hence, the complete optimization filter optimization process is based on a *Two-Step ASM* scheme, consisting of the combination of those two independent ASM stages. The *Two-Step ASM* scheme has been successfully applied in Articles **TMTT14**, **TMTT15** and **EUMC15***. On the other hand, as previously mentioned, the topologies reported in Articles **IJMWT16**, **NEMO17*** and **TMTT18** solve the narrowband limitations of the quarter-wavelength inverters by using interdigital capacitors instead, so that the usage of the *Two-Step ASM* is no longer needed, leading to a simplified optimization algorithm based in one ASM stage only.

Chapter 3

Planar Wideband Single-Ended Filters based on SIRs

In this chapter the ASM-based optimization algorithm is applied to single-ended filters implemented by a combination of SIRs. The optimization process will enable the automatic and unattended optimization of the filter layout, which will be provided ready for fabrication and meant to fulfil a predefined set of specifications once the complete optimization process is finished, with no further interaction during the entire process.

In Section 3.1 the topology used for the synthesis of the filter as well as the flow diagram of the optimization algorithm are presented. The key aspects and limitations of using this topology are emphasized, which are well supported by the results obtained that are also shown.

Section 3.2 introduces an improved optimization algorithm based on a *Two-Step ASM* process, developed in order to overcome some limitations inherent to the filter topology under analysis. The modified optimization flow is presented and proved as well with the results obtained.

3.1 Design of Wideband Bandpass Filters based on ASM Algorithm

The analysis and the automatic layout synthesis of the planar wideband filters under study is presented in Article **IMS14***. The single-ended microstrip filters are based on shunt SIRs and grounded stubs coupled through admittance inverters implemented by means of $\lambda/4$ transmission lines [51], [71]. By virtue of the semi-lumped nature of the SIRs, the filter does not provide periodicity on its response and its size can be made smaller than the wavelength at the operation frequency (if the filter order is small), leading to a very compact structures. As it will be described later, the SIRs provide out of band controllable transmission zeros which are useful to improve the selectivity of the filter or attenuate any undesired spurious. Moreover, the resulting susceptance slope values of this resonator topology can be small enough, which allow to achieve high fractional bandwidths. Conversely, the admittance inverters are narrowband by nature, which brings a limitation on the maximum passband bandwidth that such filter topologies can achieve while keeping the passband return loss above an acceptable value (i.e. RL>10dB).

PCB technology constraints will have also impact on the overall wideband performance of these microstrip filters due to the design rules which have to be obeyed in the manufacturing process (for instance, a common design rule value for the minimum line width and gap between lines is 0.15mm for a cost-wise effective standard class 6 PCB process). Note that one clear advantage of this planar structure is that it can be easily implemented in a two-layer substrate, so that the manufacturing process is simple and cheap.

The layout representation of these filters and their equivalent electrical model is depicted in Figure 3.1, where a 3rd order filter is used as an example. The three main items which will be independently optimized during the ASM synthesis process i.e., the λ/4 inverter line width, the SIRs and the filter cell, are also illustrated in Figure 3.1 (a). Each filter cell is built with the corresponding -and already optimized- inverter line and SIR, whereas the complete filter layout is built by a combination of such *N* pre-optimized filter cells, where *N* corresponds to the order filter layout.

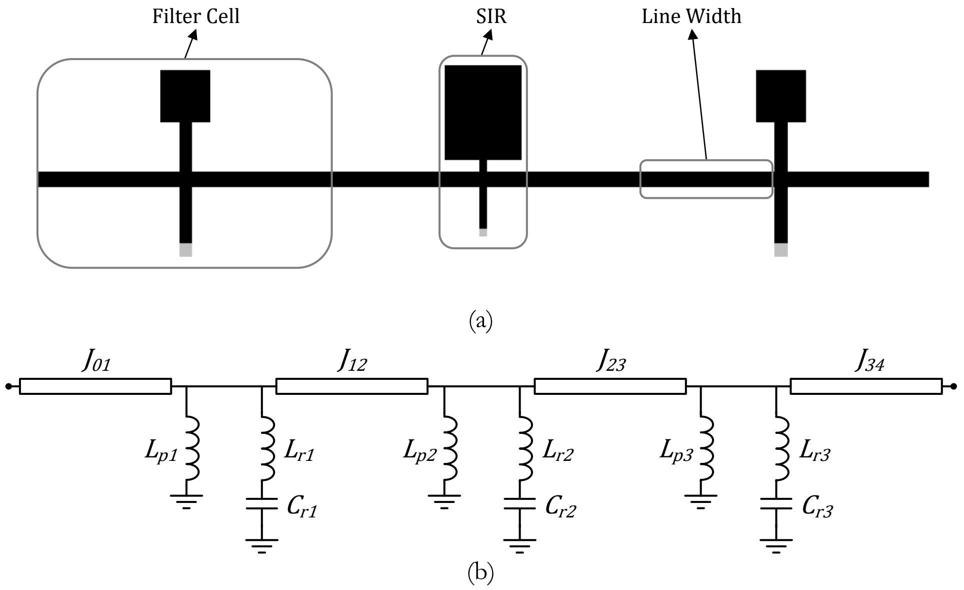

(a)

(b)

Figure 3.1. **IMS14*** 3rd order filter layout topology example (a) and equivalent circuit schematic (b).

A detailed description of the filter cell layout and its equivalent circuit are described in Figure 3.2, where all the variables that take part in the three different ASM stages are shown.

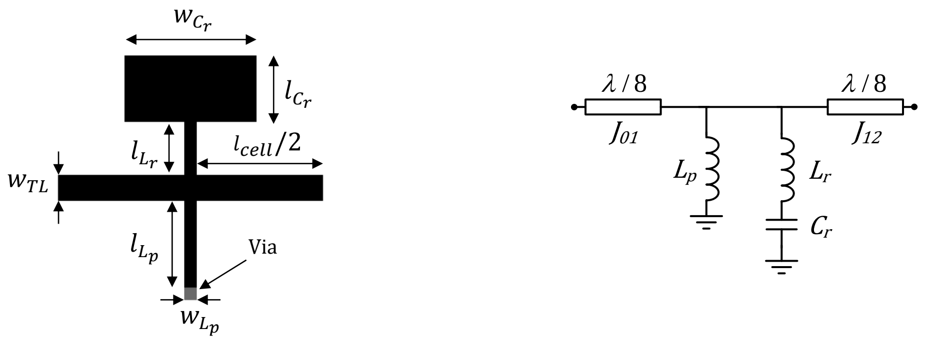

(a) (b)

Figure 3.2. Filter cell layout (a) and equivalent circuit model (b).

From the electrical model depicted in Figure 3.2 (b), the equations of the *parameter extraction* process of the shunt resonator can be defined. The SIR input susceptance B can be expressed as stated below:

$$B = \frac{\omega^2 C_r (L_p + L_r) - 1}{\omega L_p (-\omega^2 L_r C_r + 1)} \tag{3.1}$$

Hence, the transmission zero frequency, f_Z, the resonant frequency f_0, and the susceptance slope b at f_0 can be defined as follows:

$$f_Z = \frac{1}{2\pi\sqrt{L_r C_r}} \tag{3.2}$$

$$f_0 = \frac{1}{2\pi\sqrt{C_r (L_r + L_p)}} \tag{3.3}$$

$$b = \omega_0 \frac{C_r (L_r + L_p)^2}{{L_p}^2} \tag{3.4}$$

On the other hand, the $\lambda/4$ transmission lines that implement the filter's admittance inverters can be split as two $\lambda/8$ input and output transmission lines connected to the resonators input and output ports respectively, which will provide the desired admittance transformation when the values of the characteristic impedance, Z_0, and the phase shift, θ_{cell}, of each filter cell are correctly set.

3.1.1 Layout Generation by means of ASM

As mentioned previously, in order to determine the layout of the filter, each filter cell that compose the filter needs to be synthesized independently. The filter layout synthesis process involves three stages: 1) the *SIR ASM*, 2) the *Line Width ASM* and 3) the *Filter Cell (Line Length) ASM*. The flow diagram of the entire optimization process is presented in Figure 3.3.

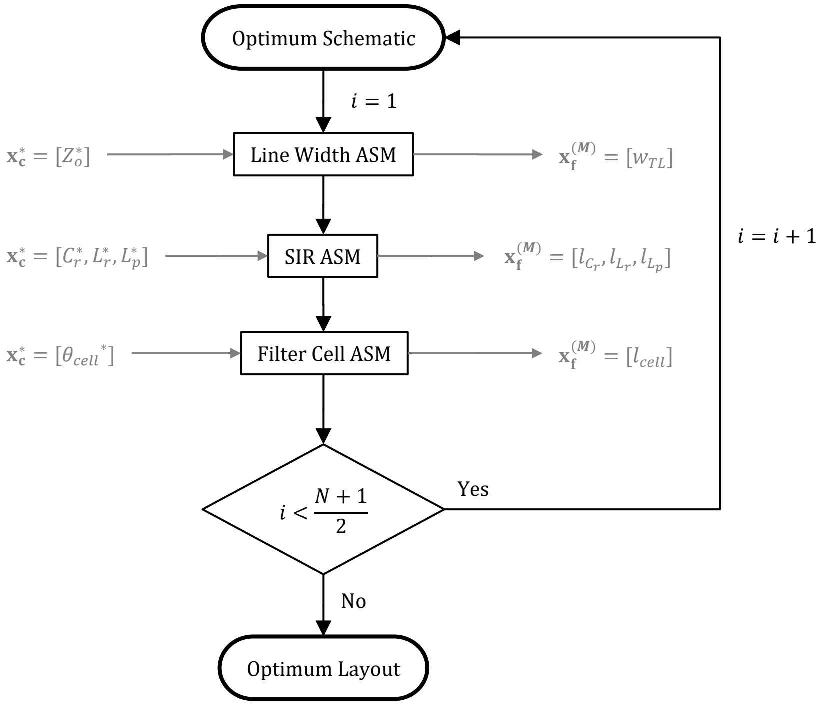

Figure 3.3. **IMS14*** wideband bandpass single-ended filter ASM flow diagram.

The complete three-stage cell optimization loop will be repeated as many times as different filter cells need to be optimized, which depends directly on the order N of the filter under synthesis. In the particular case of a synthesis of an odd N^{th} order Chebyshev response filter, the total number of cells to be optimized is reduced to $(N+1)/2$ since the cells i and $N+1-i$ are identical. However, this does not affect line width optimization since line width is identical for all filter stages.

It is important to note too that the main technology parameters, which basically are the dielectric permittivity ε_r and the thickness h of the substrate, as well as the minimum line width and gap between lines, will be fixed prior to the execution of the ASM scheme because the final dimensions of the filter layout will be directly linked to these parameters.

Line Width ASM

The optimization of the quarter-wavelength transmission line width involves one variable ASM, where in the coarse space is the transmission line characteristic impedance $\mathbf{x}_c = Z_0$, while in the fine space it corresponds to the width of such line $\mathbf{x}_f = w_{TL}$. To enable the ASM iterative process, the initial line width and the initial Broyden matrix need to be set. The initial line width value is derived from the microstrip analytical formulas [14] so that the initial fine model vector $\mathbf{x}_f^{(1)}$ is obtained. Next, by means of the *parameter extraction* process, the first coarse model vector $\mathbf{x}_c^{(1)}$ is inferred by direct inspection of the EM response. Similarly, the initial Broyden matrix $\mathbf{B}^{(1)}$ shown in equation (3.5) is inferred by perturbing the line width and obtaining the characteristic impedance from the EM simulation response.

$$\mathbf{B}^{(1)} = \left(\frac{\delta Z_0}{\delta w_{TL}}\right) \tag{3.5}$$

The *Line Width ASM* iterative loop will finish at the M^{th} iteration, when the normalized error function $\mathbf{f}^{(i)}$ between the target coarse model vector $\mathbf{x_c}^*$ and the final fine model vector $\mathbf{x_c}^{(M)}$ is lower than the specified target convergence error η so that the optimum values in the fine space will be given by $\mathbf{x_f}^{(M)}$.

SIR ASM

In the specific ASM process developed to carry out each resonator synthesis, the variables in the coarse space X_c correspond to the circuital elements of the resonator, $\mathbf{x_c} = [L_r, C_r, L_p]$ whose optimal values are obtained through the filter theory formulas [9], directly linked to the response specifications of the Chebyshev passband filter, i.e. the order, N, the fractional bandwidth, FBW, the central frequency, f_0, and the passband ripple L_{Ar}. On the other hand, the fine space X_f is defined by a set of variables that define the resonator layout, $\mathbf{x_f} = [l_{Lr}, l_{Cr}, l_{Lp}]$, which is forced to have the same number of variables than the coarse space, so that the remaining parameters that define the resonator layout are kept unaltered with a fixed value. By means of the well-known approximate formulas [14] for an electrically small narrow (inductive) and wide (capacitive) strip, the initial layout $\mathbf{x_f}^{(1)}$ of the shunt resonator can be determined. Next, $\mathbf{x_c}^{(1)}$ is inferred from the initial layout EM simulation by means of the *parameter extraction* process where equations (3.2)-(3.4) are used. In addition, by independently perturbing the lengths l_{Lr}, l_{Cr} and l_{Lp} defined in the fine model vector and obtaining after each perturbation the corresponding values for the coarse model vector L_r, C_r and L_p parameters through *parameter extraction*, the initial Broyden matrix $\mathbf{B}^{(1)}$ can be built.

$$\mathbf{B}^{(1)} = \begin{pmatrix} \frac{\delta L_r}{\delta l_{L_r}} & \frac{\delta L_r}{\delta l_{C_r}} & \frac{\delta L_r}{\delta l_{L_p}} \\ \frac{\delta C_r}{\delta l_{L_r}} & \frac{\delta C_r}{\delta l_{C_r}} & \frac{\delta C_r}{\delta l_{L_p}} \\ \frac{\delta L_p}{\delta l_{L_r}} & \frac{\delta L_p}{\delta l_{L_p}} & \frac{\delta L_p}{\delta l_{L_p}} \end{pmatrix} \tag{3.6}$$

At this point the *SIR ASM* loop is started, and it will end at the M^{th} iteration once the normalized error between the optimal coarse model vector $\mathbf{x_c}^*$ and the final coarse vector $\mathbf{x_c}^{(M)}$ is lower than the predefined target convergence error η so that the optimum values in the fine space will be defined in $\mathbf{x_f}^{(M)}$.

Filter Cell (Line Length) ASM

The main purpose of the *Filter Cell ASM* is to define the proper admittance inverters lines length in order to absorb the small -but not negligible- phase offset added by the shunt resonator at the center frequency of operation. A single-variable ASM is needed in order to optimize the line length of the filter cell, and the coarse model vector corresponds to the cell electrical length $\mathbf{x_c} = \theta_{cell}$, while the filter cell length is mapped in the fine model vector, $\mathbf{x_f} = l_{cell}$. The initial value for the fine model vector $\mathbf{x_f}^{(1)}$ is obtained by the formula that gives the line length as a function of the required phase (in this case $\theta_{cell} = 90^{\circ}$) and the operation frequency f_0 [14]. Then $\mathbf{x_c}^{(1)}$ can be inferred from the EM simulation of the initial inverter line layout. Similarly, the initial Broyden matrix $\mathbf{B}^{(1)}$ is inferred by perturbing the line length and obtaining the electrical length from the corresponding EM simulation response.

$$\mathbf{B}^{(1)} = \left(\frac{\delta\theta_{cell}}{\delta l_{cell}}\right) \tag{3.7}$$

The *Filter Cell ASM* iterative loop will finish at the M^{th} iteration, when the normalized error function $\mathbf{f}^{(i)}$ between the target coarse model vector $\mathbf{x}_c^*$ and the final coarse model vector $\mathbf{x}_c^{(M)}$ is lower than the specified target convergence error η so that the optimum values in the fine space will be defined in $\mathbf{x}_f^{(M)}$. Once each optimum filter cell has been synthesized, the cells are simply cascaded to generate the final filter layout.

Optimum Layout

A wideband bandpass filter example with Chebyshev response and predefined specifications i.e., order N, center frequency f_0, fractional bandwidth FBW_{-3dB} (where the cut-off frequencies are defined at -3dB of the bandpass response) and passband return loss RL (directly related to the passband ripple L_{Ar}), is next used as an example for the proof of concept of the ASM-based automatic synthesis applied to the filter topology under analysis.

A 7th order bandpass filter with f_0 = 3.87 GHz, FBW_{-3dB} = 52%, return loss RL > 10 dB (i.e., L_{Ar} < 0.46 dB) and transmission zero frequency f_z = 8 GHz (to provide good selectivity and spurious suppression) is synthesized by means of the presented ASM algorithm and fabricated using *Rogers RO3010* substrate with thickness h = 0.635mm, dielectric constant ε_r = 10.2 and tangent delta $tan\delta$ = 0.0022. The final layout obtained in a complete unattended process by combining the optimized filter cells is presented in Figure 3.4 (a), whereas the comparison between the target schematic response, the EM simulated response (without losses) and the measured response are compared in Figure 3.4 (b).

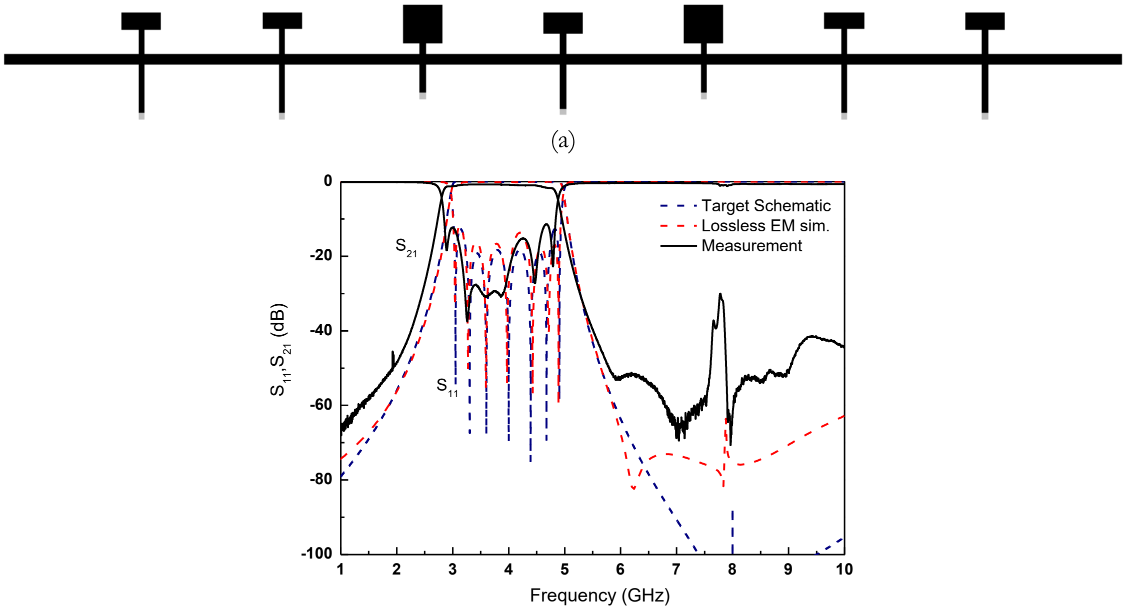

(a)

(b)

Figure 3.4. **IMS14*** 7th order wideband bandpass filter layout (a) and comparison between the filter target schematic, EM lossless simulation and measured response (b).

As can be seen, the agreement between the response of the circuit schematic, the electromagnetic simulation and the measurement is very good, which proves the validation of the synthesis methodology. Nevertheless, the deviation between the measured response and the target schematic response is in part related to the fact that the losses have not been considered in the optimization process, which was meant to automatically obtain the filter layout providing a lossless electromagnetic simulation able to satisfy the specifications.

Having said that, it is important to point the fact that the circuit schematic response shown in Figure 3.4 (b) deviates slightly from the ideal Chebyshev. The obtained quasi-Chebyshev response is due to the limited functionality in terms of bandwidth of the admittance inverters. One possibility to overcome this narrowing effect is to over-dimension the filter fractional bandwidth and the return loss specifications in advance at the design stage, in order to obtain a circuit schematic response which fulfils the predefined requirements. Even though that strategy is valid and proven in **IMS14***, it seems not to be the most efficient method since it consists in a trial and error process to get the over-dimensioned values for the filter specifications which provide the expected circuit response that meets the requirements. In the next section, a systematic procedure implemented through a *Two-Step ASM* process which solves this inefficient manual iterative method is presented.

3.2 Wideband Bandpass Filter Design by means of Two-Step ASM Technique

In the Article **TMTT14** and the Book Chapter **SPMS16*** a systematic ASM-based design procedure able to get the optimum filter schematic which overcomes the narrowband limitations of the admittance inverters is presented. With this approach, the filter automatic design can be arranged in a two-step optimization process: in the first step the optimum filter schematic that satisfies the filter design requirements is obtained, whereas in the second step the filter layout which matches the optimum schematic is determined. The two-step design process can in principle be applied to the automated synthesis of any type of wideband bandpass filter implemented by means of semi-lumped shunt resonators coupled through admittance inverters. The flow diagram about the proposed *Two-Step ASM* process is described in Figure 3.5.

As mentioned previously, the filters to be synthesized in this chapter are based on shunt resonators coupled through admittance inverters, so that they follow the network analysis applied to the generalized bandpass filter schematic based on ideal admittance inverters reported in many textbooks [9], which are able to provide the well-known Chebyshev response, among others.

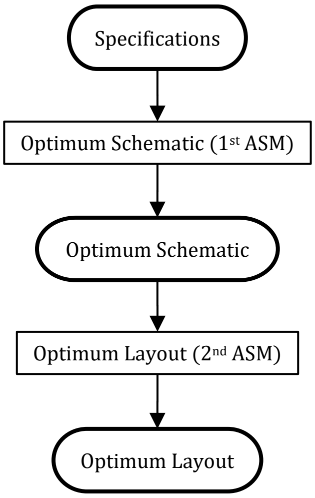

Figure 3.5. *Two-Step ASM* block diagram.

In Figure 3.6 (a) such schematic is shown for a 3rd order filter example, and it is compared in (b) with a more practical approach which replaces the frequency-invariant ideal admittance inverters with the frequency-dependent quarter-wavelength transmission lines. Such frequency dependence characteristic inherent to the quarter wavelength transmission line inverters is the one that brings the narrow-band nature to that structures, which in turn degrades the overall response of the entire filter. However, that fact does not mean that the intended filter response (or at least a very good approximation in the region of interest) cannot be achieved with the filter schematic shown in Figure 3.6 (b).

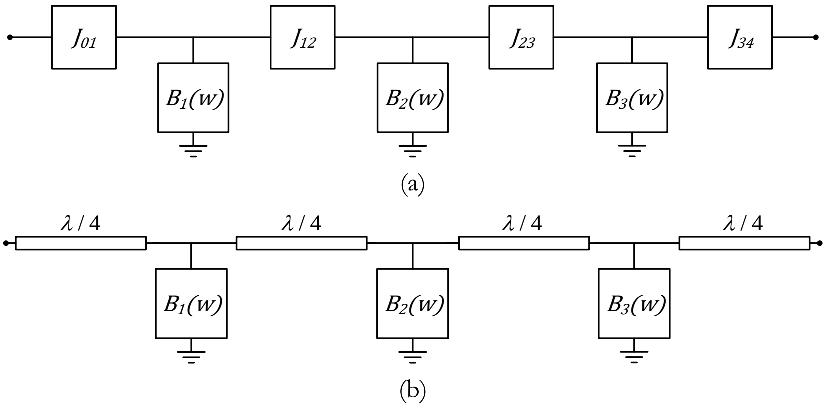

Figure 3.6. 3rd order ideal bandpass generalized filter schematic based on ideal admittance inverters (a) and based on quarter-wavelength transmission line inverters (b).

Planar resonant elements such as split rings, Stepped Impedance Resonators (SIRs) and combinations of inductive/capacitive stubs, etc. can be considered as semi-lumped resonators used in this design filter approach, and will be represented by their corresponding equivalent circuital susceptance B in the filter circuit schematic. For simplicity, the equivalent circuit of filter depicted in Figure 3.1, based on the shunt resonator analyzed in Figure 3.2, will be considered in next section in order to explain the *Optimum Schematic ASM* algorithm functionality.

3.2.1 Optimum Schematic Generation by means of ASM

The main hypothesis in the development of the iterative ASM algorithm able to provide the optimum filter schematic is to assume that there is a set of filter specifications, different than the target, that leads to a filter schematic (inferred by substituting the ideal admittance inverters with quarter-wavelength transmission lines), whose response satisfies the filter specifications. The ASM process will consist in a single optimization stage, as it is shown in Figure 3.7.

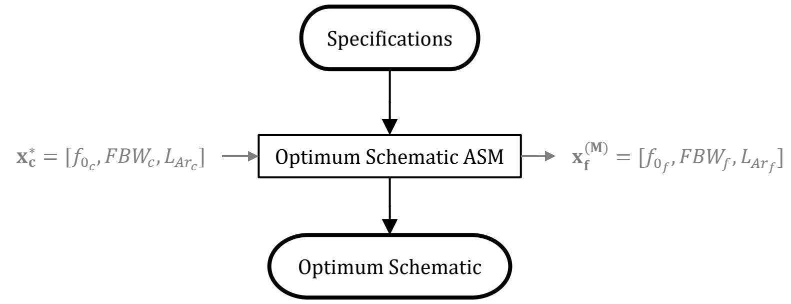

Figure 3.7. *Optimum Schematic ASM* block diagram (1st ASM).

In this particular case, the ASM coarse model vector is defined based on the filter target specifications $\mathbf{x_c} = [f_{0c}, FBW_c, L_{Arc}]$ that are linked to the ideal schematic presented in Figure 3.6 (a), so that generates the ideal Chebyshev target response. On the other hand, the fine model vector is constituted by the same variables and therefore $\mathbf{x_f} = [f_{0f}, FBW_f, L_{Arf}]$, but its response is inferred from the schematic of Figure 3.6 (b) which corresponds to the schematic where the admittance inverters are implemented by $\lambda/4$ transmission lines. Therefore, the definitions of the coarse and fine spaces in this particular ASM scheme can be described as follows:

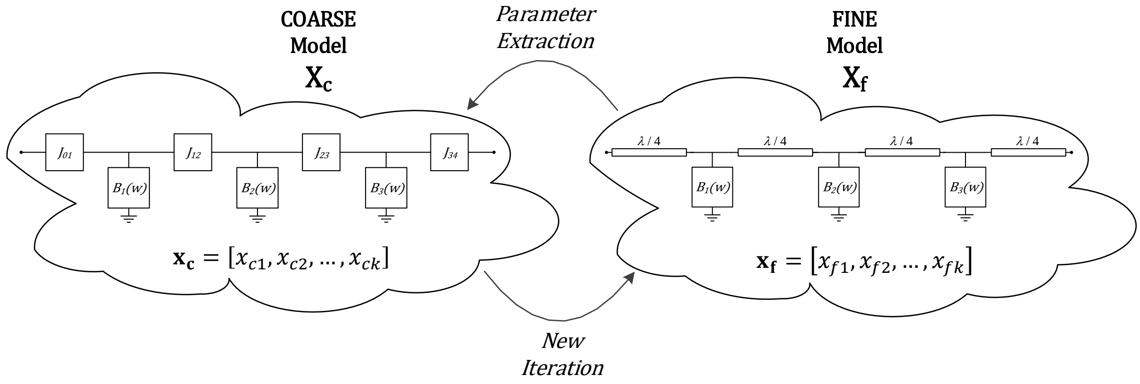

Figure 3.8. *Optimum Schematic ASM* coarse and fine spaces definition.

As an example, let us assume that the Chebyshev target response corresponds to the one depicted in Figure 3.9, which satisfies the following filter specifications: $N = 5$, $f_0 = 2.4$ GHz, $FBW_{-3dB} = 44\%$ and $L_{Ar} = 0.2$dB (RL=13.45dB). The correspondence between the response and the parameters defined in the specifications is also shown in this figure. These parameters are the ones used in the *parameter extraction* process of the *Optimum Schematic ASM* scheme.

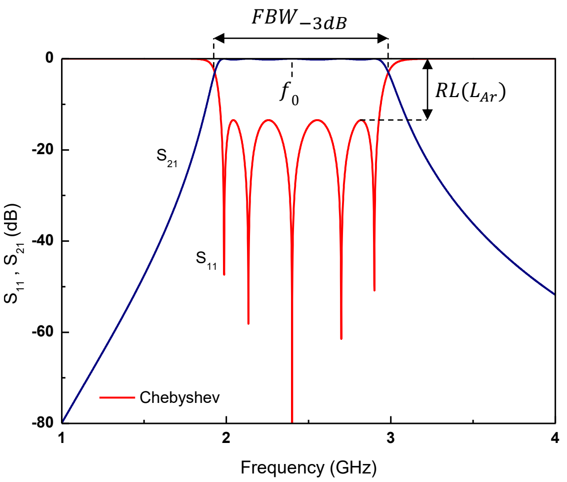

Figure 3.9. 5th order ideal filter schematic Chebyshev response and its correspondence with the parameters defined in the filter specifications (f_0, FBW_{-3dB}, L_{Ar}).

In Figure 3.10 the ideal Chebyshev response is compared with the one obtained from the schematic based on $\lambda/4$ inverters. As expected, the response based on $\lambda/4$ inverters deviates notably from the target Chebyshev response, affecting all three parameters f_0, FBW_{-3dB}, L_{Ar}. This fact confirms the assumption about the limited behavior of the transmission line inverters mentioned previously.

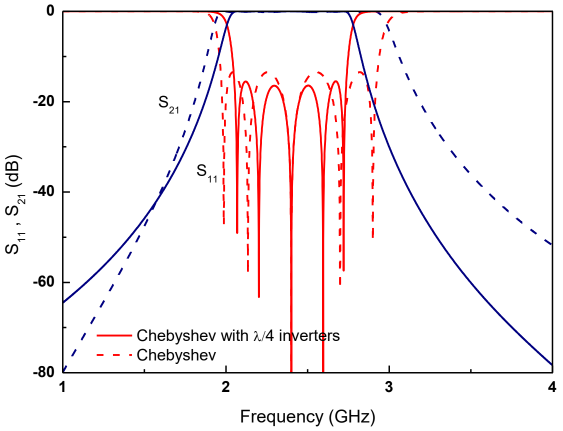

Figure 3.10. 5th order Chebyshev response comparison: filter schematic based on ideal admittance inverters and filter schematic based on $\lambda/4$ inverters.

Following the standard procedure in ASM, the first step before starting the iterative process is to make an estimation of the initial vector in the fine space $\mathbf{x}_\mathbf{f}^{(1)}$ and to obtain the initial Broyden matrix $\mathbf{B}^{(1)}$. For simplicity, since the variables in both spaces are the same, the initial fine space vector is forced to be the optimal coarse space vector $\mathbf{x}_\mathbf{f}^{(1)} = \mathbf{x}_\mathbf{c}^*$, which is the one that provides the deviated Chebyshev response shown in Figure 3.10. Next, the initial Broyden matrix $\mathbf{B}^{(1)}$ is calculated by independently applying a slight perturbation to each fine model variable, whose effect on the (same) variables of the coarse space is inferred by proper inspection of the response.

$$\mathbf{B}^{(1)} = \begin{pmatrix} \dfrac{\delta f_{0_c}}{\delta f_{0_f}} & \dfrac{\delta f_{0_c}}{\delta FBW_f} & \dfrac{\delta f_{0_c}}{\delta L_{Ar_f}} \\ \dfrac{\delta FBW_c}{\delta f_{0_f}} & \dfrac{\delta FBW_c}{\delta FBW_f} & \dfrac{\delta FBW_c}{\delta L_{Ar_f}} \\ \dfrac{\delta L_{Ar_c}}{\delta f_{0_f}} & \dfrac{\delta L_{Ar_c}}{\delta FBW_f} & \dfrac{\delta L_{Ar_c}}{\delta L_{Ar_f}} \end{pmatrix} \tag{3.8}$$

At this point the *Optimum Schematic ASM* loop is started, and it will end at the M^{th} iteration once the normalized error between the optimal coarse model vector $\mathbf{x}_c^*$ and the final coarse model vector $\mathbf{x}_c^{(M)}$ is lower than the predefined target convergence error η, so that the optimum values in the fine space will be defined in $\mathbf{x}_f^{(M)}$. In the case of the example under discussion, in Figure 3.11 the final response obtained in the fine space is compared with the ideal Chebyshev response. As can be seen, after the optimization process, a quasi-Chebyshev response - very close to the target Chebyshev response in the frequency range of interest - is obtained for the filter schematic implemented by means of $\lambda/4$ admittance inverters, which proves the validity of the optimization process.

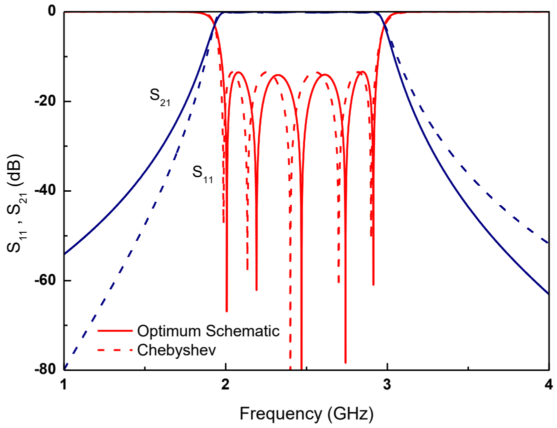

Figure 3.11. 5th order filter target Chebyshev response and optimum schematic response obtained after applying the *Optimum Schematic ASM*.

Once the optimum schematic is found, the next step is to determine the layout of the filter. To this end, the second ASM algorithm, firstly reported in Section 3.1.1 will be used. Hence, considering the current example, the main goal of this second ASM is to obtain the filter layout which matches the response of the optimum schematic presented in Figure 3.11, which fulfils the specifications mentioned before. As it is deeply detailed in the Article **TMTT14**, the resulting optimized filter layout is presented in Figure 3.12 (a) whereas the results obtained for the EM simulated (considering losses) and the optimum schematic responses are shown in Figure 3.12 (b). To prove the validity of the *Two-Step ASM* scheme concept, the filter layout was fabricated using *Rogers RO3010* with dielectric constant ε_r = 10.2, thickness h = 0.635mm and tangent delta $tan\delta$ = 0.0022, and the measured response of the filter is also plotted in the same figure.

It can be observed that the measured response is in good agreement with the electromagnetic simulation and hence the filter specifications are satisfied, proving the validity of the optimization process, which has been carried out in a fully unattended way, without any manual interruption.

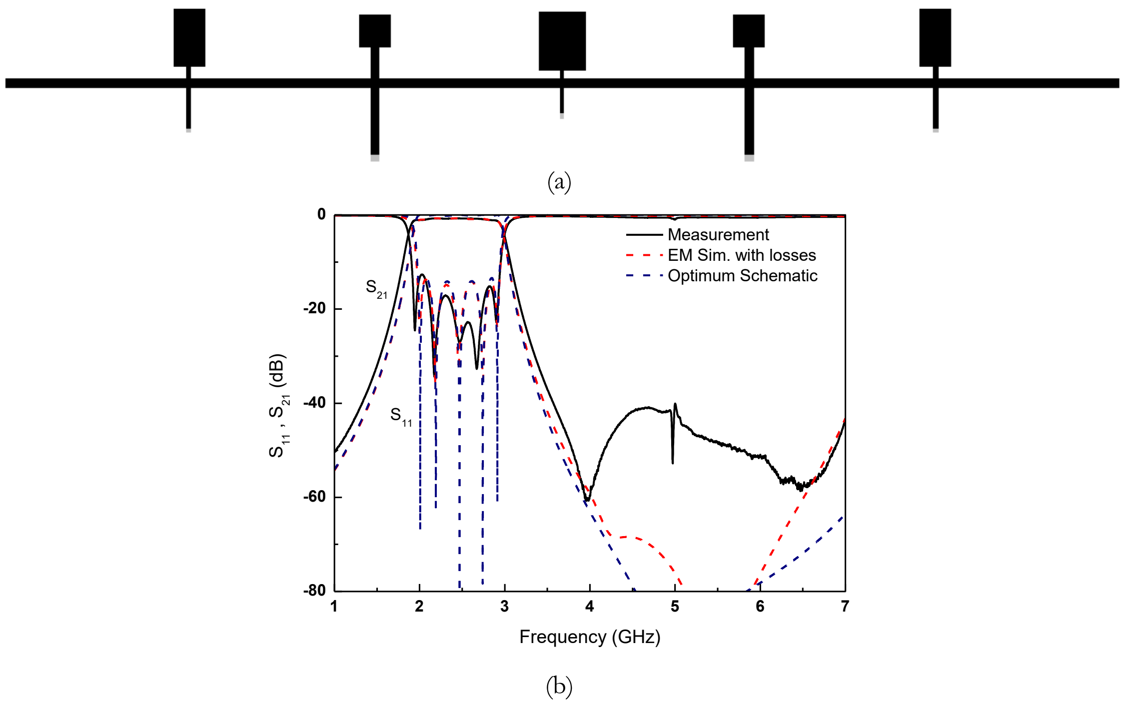

Figure 3.12. **TMTT14** 5th order wideband bandpass filter layout (a) and comparison between the filter optimum schematic, EM simulation with losses and measured response (b).

Further examples of filters based on the same topology and automatically synthesized using the *Two-Step ASM* algorithm can be found in the Article **TMTT14** and in the Book Chapter **SPMS16***, which include a 9th and 7th order filter synthesis respectively, using the same methodology.

Chapter 4

Planar Wideband Balanced Filters based on SIRs

This chapter is focused on the application of the ASM algorithm to several balanced filter structures, all of them based on SIRs, which will provide different types of Chebyshev-like responses. Each particular structure will be best suited to fulfil a specific set of predefined requirements. In the same way as Chapter 3 for the case of the single-ended filter structures, since all these balanced structures are synthesized through ASM, the optimization process is in all cases carried out by a fully automatic and unattended process. The key aspects and limitations of each topology used in this chapter are analyzed and proved with the necessary simulation and measurement results.

The balanced filter structures analyzed in Section 4.1 are based on shunt SIRs coupled through $\lambda/4$ transmission lines inverters and are meant to provide very high common-mode rejection ratio (CMRR) in the filter passband frequency range.

On the other hand, the structure used in Section 4.2 is based on a combination of shunt SIRs and series interdigital capacitors. The main advantage with regard to the previous ones is to improve the layout compactness while keeping the CMRR at an acceptable level in the filter passband frequency range. In addition, the optimization scheme is also simplified leading to a more efficient automatic synthesis process.

Finally, in Section 4.3 the previous structure based on shunt SIRs and series interdigital capacitors is improved in order to give more versatility to the filter response, which leads to better performance in the passband, as well as in the stopband regions for both differential- and common-mode responses.

4.1 Balanced Wideband Filters with High CMRR

The Articles **EUMC15*** and **TMTT15** are focused on the automated and unattended design of planar balanced wideband bandpass filters based on mirrored SIRs coupled through admittance inverters. Such inverters are based on $\lambda/4$ transmission lines, so they will suffer from the same limitations than the single-ended counterparts, mainly leading to bandwidth degradation. To overcome this undesired phenomena, the *Two-Step ASM* optimization scheme reported in Section 3.2 will applied here as well to synthesize the optimum layout for such filter structures, with the aim to obtain the responses that fulfil the specifications defined in each case.

In Section 4.1.1 the SIRs are based on shunt resonators coupled through $\lambda/4$ inverters for the differential-mode, while for the common-mode the SIRs behave as a shunt connected series resonator which provides a transmission zero. On the other hand, in Section 4.1.2, the resonator structure is slightly modified by adding a series inductance to the shunt capacitance which provides a transmission zero also in the differential-mode, while keeping the transmission zero for the common-mode.

4.1.1 Two-Step ASM Applied to Balanced Filters based on Shunt SIRs Coupled through $\lambda/4$ Inverters

The filter structures implemented in Article **EUMC15***, firstly reported in [52], are based on mirrored SIRs coupled through admittance inverters whose layout and equivalent circuit for a 3rd order filter example are described in Figure 4.1.

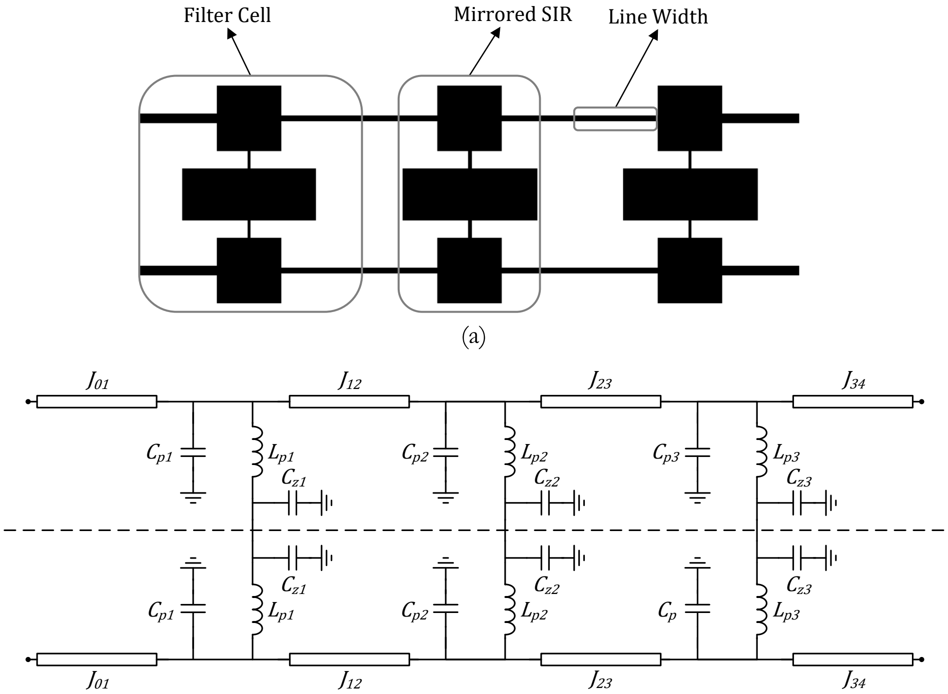

(a)

(b)

Figure 4.1. **EUMC15*** 3rd order balanced wideband bandpass filter layout (a) and equivalent circuit (b).

The mirrored SIRs can be described as a combination of capacitances and inductances as can be observed in Figure 4.1 (b), where the symmetry plane behaves as an E-wall for the differential-mode so that the capacitances C_{zi}, the ones synthesized by the central patches, do not play any role for that mode because they are grounded. Hence, the resulting equivalent circuit for the differential-mode is the one shown in Figure 4.2 (a) which consists on the canonical L_{pi}-C_{pi} shunt resonator described in the generic bandpass filters theory. On the other hand, the symmetry plane for the common-mode behaves as an H-wall, which acts as an open circuit and allow the central patches of the SIRs add common-mode transmission zeros due to the L_{pi}-C_{zi} series resonators, useful for the suppression of the common-mode noise in the differential passband. The resulting equivalent circuit for the common-mode is the one shown in Figure 4.2 (b). Comparing the schematics from Figure 4.2 (a) and (b), it can be seen that the position of the transmission zeros does not affect the differential-mode response.

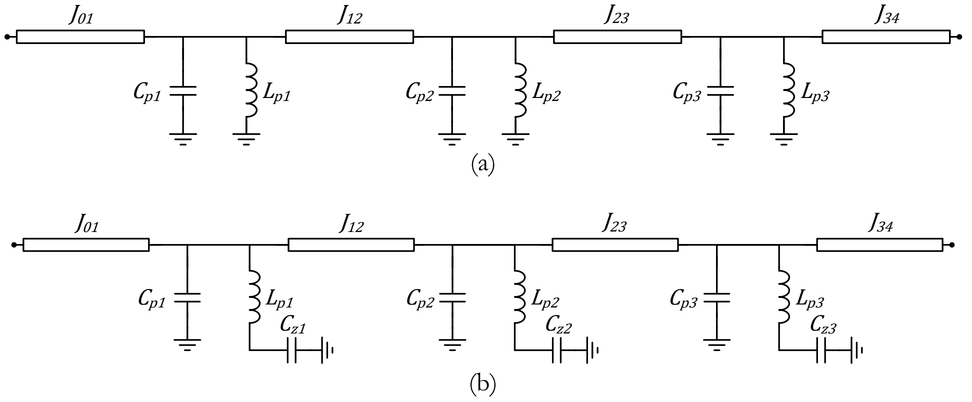

Figure 4.2. Differential- (a) and common- (b) mode circuit schematics of the **EUMC15*** filter structure.

The first step of the design process is the determination of the optimum filter schematic for the differential-mode, namely the one that satisfies the specifications. The *Optimum Schematic ASM* algorithm applied in this case is similar to the one reported in Section 3.2.1 for the single-ended filters, with the particularity that in this case the filter is composed by identical resonators, i.e. $L_{pi} = L_p$ and $C_{pi} = C_p$, but different admittance inverters. The inverters are synthesized with their corresponding optimum characteristic admittance to obtain the ideal Chebyshev filter response and, since they are implemented through $\lambda/4$ transmission lines, the filter response will be deviated from the target provoking, among other less critical effects, a substantial bandwidth degradation. Hence, the application of the *Optimum Schematic ASM* algorithm to overcome this problem is also justified for this filter topology.

In the same manner than in the single-ended filter structure described in Section 3.1, the second ASM step, that is, the *Optimum Layout ASM*, will consist of the independent optimization of the main three items that conform the filter structure, already emphasized in Figure 4.1: the $\lambda/4$ inverters line width, the SIRs and the filter cells. The layout and equivalent circuit of the filter cell is detailed in Figure 4.3, where all the variables that play a role in these three different *Optimum Layout ASM* stages are also highlighted (the other geometrical variables are set to fixed values and are not variables of the optimization process).

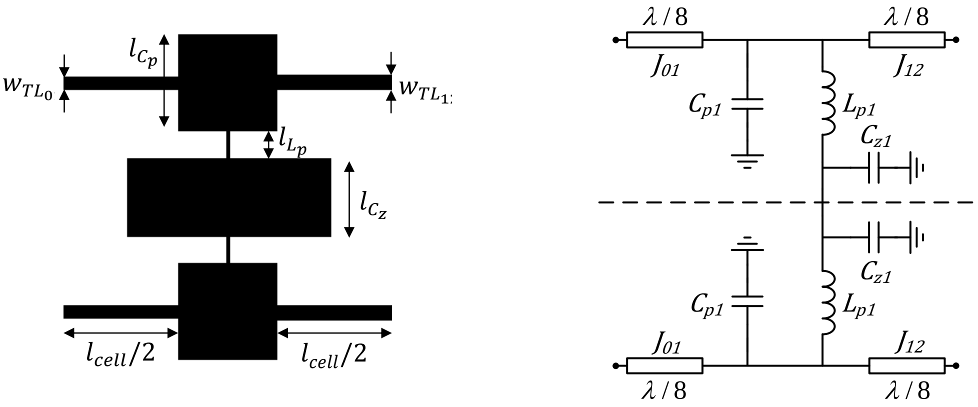

(a) (b)

Figure 4.3. Filter cell layout (a) and equivalent circuit model (b).

The equations of the *parameter extraction* process of the shunt resonator can be defined from the electrical model depicted in Figure 4.3 (b). Considering the differential-mode (L_p is grounded so C_z does not play any role), the SIR susceptance B_{dd} can be expressed as stated below:

$$B_{dd} = \frac{\omega^2 C_p L_p - 1}{\omega L_p} \tag{4.1}$$

Hence, the resonant frequency, f_0, and the susceptance slope, b_{dd}, at f_{0dd} can be defined as follows:

$$f_{0_{dd}} = \frac{1}{2\pi\sqrt{C_p L_p}} \tag{4.2}$$

$$b_{dd} = 2\pi f_{0_{dd}} C_p \tag{4.3}$$

and the transmission zero frequency, f_{Zcc}, in the common-mode is determined by:

$$f_{z_{cc}} = \frac{1}{2\pi\sqrt{L_p C_z}} \tag{4.4}$$

On the other hand, the $\lambda/4$ transmission lines that implement the admittance inverters are split in two $\lambda/8$ input and output transmission lines connected to the resonators input and output ports respectively. The characteristic impedance Z_0 and the phase shift θ_{cell} of each $\lambda/8$ transmission line will have to be tailored to the appropriate value in order to provide the desired admittance transformation to each filter cell that composes the filter structure.

Layout Generation by means of ASM

The layout synthesis process is similar than the one reported for the single-ended filter in Section 3.1.1 and it involves the same three ASM stages: 1) the *SIR ASM*, 2) the *Line Width ASM* and 3) the *Filter Cell (Line Length) ASM*. The flow diagram of the entire optimization scheme is presented in Figure 4.4.

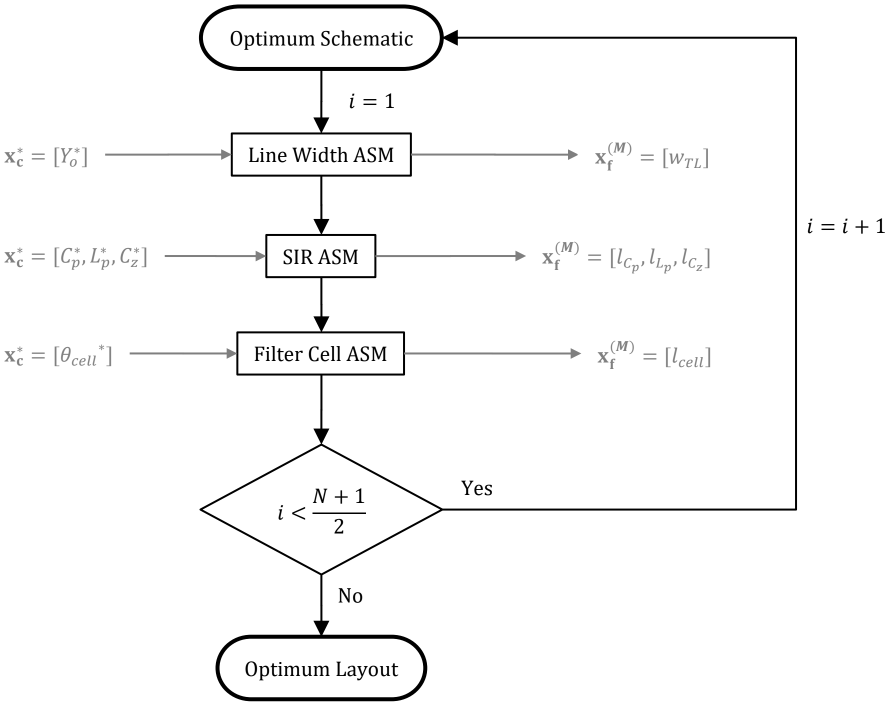

Figure 4.4. **EUMC15*** balanced wideband bandpass filter 2nd ASM flow diagram.

The *Line Width ASM* algorithm consists on obtaining the optimum width w_{TL} for each $\lambda/4$ transmission line, and this ASM must be repeated as many times as different admittance inverters are present in the filter. Its modus operandi has been previously described in Section 3.1.1.

On the other hand, concerning the *SIR ASM* process, the coarse model vector is defined as $\mathbf{x_c} = [C_p, L_p, C_z]$ whereas the fine model vector corresponds to $\mathbf{x_f} = [l_{Cp}, l_{Lp}, l_{Cz}]$. By means of the well-known approximate formulas [14] for an electrically small narrow and wide strips, the initial layout $\mathbf{x_f}^{(1)}$ of the shunt resonator can be determined, and next $\mathbf{x_c}^{(1)}$ is inferred from the initial layout EM simulation by means of the *parameter extraction* process where equations (4.2)-(4.4) are used. In this case, the initial Broyden matrix $\mathbf{B}^{(1)}$ can be defined as follows:

$$\mathbf{B}^{(1)} = \begin{pmatrix} \frac{\delta L_p}{\delta l_{L_p}} & \frac{\delta L_p}{\delta l_{C_p}} & \frac{\delta L_p}{\delta l_{C_z}} \\ \frac{\delta C_p}{\delta l_{L_p}} & \frac{\delta C_p}{\delta l_{C_p}} & \frac{\delta C_p}{\delta l_{C_z}} \\ \frac{\delta C_z}{\delta l_{L_p}} & \frac{\delta C_z}{\delta l_{C_p}} & \frac{\delta C_z}{\delta l_{C_z}} \end{pmatrix} \tag{4.5}$$

Considering this particular filter structure where all the resonators are equal, the *SIR ASM* process will provide exactly the same final fine model vector $\mathbf{x_f}^{(M)}$ -and therefore the same optimum layout- for all the resonators.

Concerning the *Filter Cell ASM* process, it is meant to calculate the optimum phase θ_{cell} for each filter cell that forms the filter structure. The functionality of this ASM process is described in Section 3.1.1. In this case, the line length θ_{cell} of each filter cell might not be 90° (as it was in the case of the single-ended filter topology) since now the cells might be composed by two $\lambda/8$ transmission lines with different characteristic admittances, leading to a total electrical length different than 90º. The optimum electrical length for each cell is inferred in advance from the response obtained by the differential-mode equivalent schematic shown in Figure 4.2 (a).

Optimum Layout

Let us consider the following balanced filter design specifications: $N = 5$, $f_0 = 2.4$ GHz, $FBW = 40\%$ (corresponding to a $FBW_{-3dB} = 44\%$) and $L_{Ar} = 0.2$dB ($RL = 13.45$dB). In addition, all the transmission zero frequencies in the common-mode have been set to the same value, i.e. $f_{Zcc} = 1.1 f_0$, which provides a good CMRR in the whole differential-mode pass band. After applying the *Two-Step ASM* scheme described in this section, the resulting filter layout is the one depicted in Figure 4.5 (a), whereas in Figure 4.5 (b) the optimum schematic, the lossless EM and the measured responses are plotted. The filter was fabricated using *Rogers RO3010* substrate with dielectric constant $\varepsilon_r = 10.2$, tangent delta $tan\delta = 0.0022$ and thickness $h = 0.635$mm.

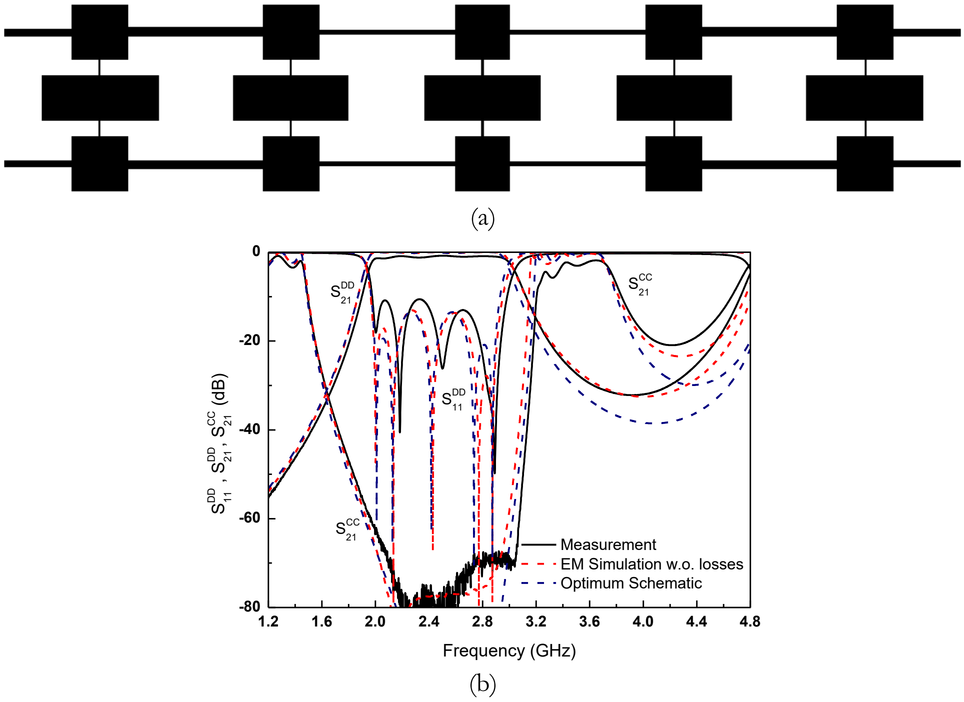
(a)

(b)

Figure 4.5. **EUMC15*** 5th order balanced wideband bandpass filter layout (a) and comparison between the optimum schematic, EM lossless simulation and measured responses (b).

The lossless electromagnetic response is very close to the response of the optimum schematic and hence to the target Chebyshev response. The fabricated device exhibits a frequency response in very good agreement to the lossless electromagnetic simulation. As for the single-ended filter synthesis reported in Chapter 3, the layout of the balanced filter has been determined from the specifications without the need of any further action during the optimization process. The results of this section demonstrate that the *Two-Step ASM* scheme is also useful for the synthesis of common-mode suppressed balanced filters based on resonators coupled through admittance inverters.

A deeper analysis about the synthesis of these balanced filter topologies through the *Two-Step AMS* scheme can be found in the Article **EUMC15*** and also in the Book Chapter **SPMS16***, where a 3rd order balanced filter synthesis is also carried out using the same methodology.

4.1.2 Two-Step ASM Applied to Balanced Filters based on Shunt SIRs and Grounded Stubs Coupled through $\lambda/4$ Inverters

The filter structures implemented in Article **TMTT15**, firstly reported in [53], are based on mirrored SIRs coupled through admittance inverters whose layout and equivalent circuit for a 3rd order filter example are described in Figure 4.1. The same *Two-Step ASM* strategy reported in Section 4.1.1 is used to obtain the optimum layout which satisfies the design specifications by means of a fully unattended process.

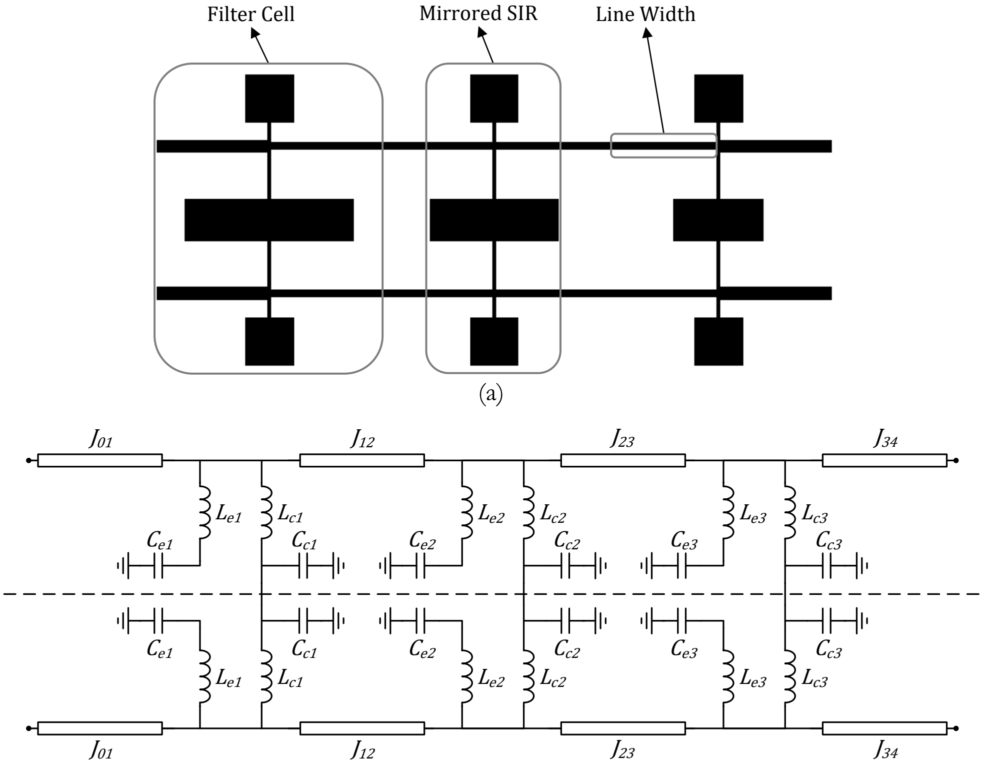

(a)

(b)

Figure 4.6. **TMTT15** 3rd order balanced wideband bandpass filter layout (a) and equivalent circuit (b).

The proposed balanced wideband bandpass filters are implemented by combining semi-lumped and distributed elements as it is shown in Figure 4.6 (a). The semi-lumped elements are transverse multi-section mirrored SIRs, described by means of a combination of capacitances and inductances while the distributed elements are $\lambda/8$ transmission lines acting as admittance inverters. In this case, both the SIRs and the inverters are different for each filter cell, which differentiates this filter structure from the one reported in Section 4.1.1, where the SIRs are always equal.

The circuit schematic of these filters is depicted in Figure 4.6 (b). The symmetry plane is an E-wall for the differential-mode and hence the capacitances C_{ci} do not play an active role for that mode since they are grounded. Thus, the equivalent circuit schematic for the differential-mode is the one depicted in Figure 4.7 (a). Conversely, the symmetry plane for the common-mode is an H-wall (open circuit) and the equivalent circuit schematic is the one depicted in Figure 4.7 (b). The resonators L_{ci}-C_{ci} provide transmission zeros that are useful for the suppression of the common-mode in the region of interest (differential filter pass band). According to the schematics of Figure 4.7 (a), the position of the common-mode transmission zeros does not affect the differential-mode response. Similarly, the resonators L_{ei}-C_{ei} provide transmission zeros for both the differential- and common-modes. This transmission zeros add more versatility in the filter response since allow to fulfil more stringent filter specifications with regards the filter topology reported in Section 4.1.1. By allocating these transmission zeros above the differential-mode pass band, frequency selectivity and stopband rejection for the differential-mode can be enhanced.

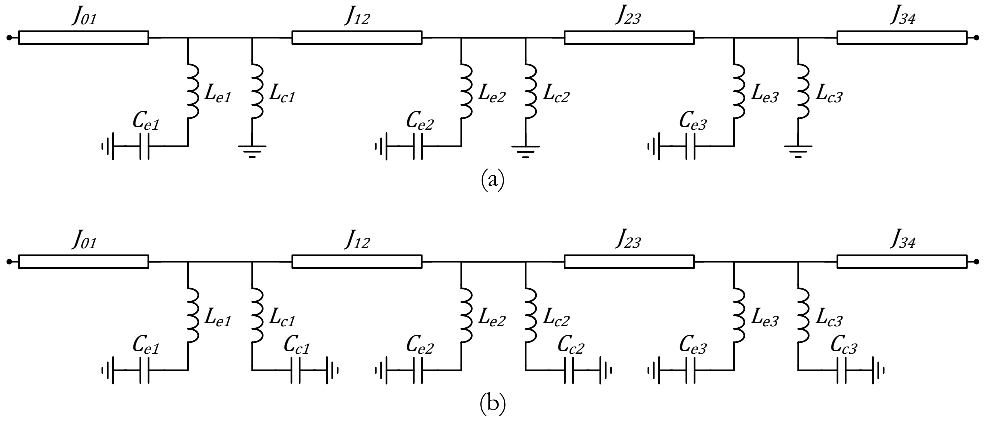

Figure 4.7. Differential- (a) and common- (b) mode circuit schematics of the **TMTT15** filter structure.

Due to the limited functionality in terms of bandwidth of the $\lambda/4$ transmission lines, in this filter topology the *Two-Step ASM* is applied in a similar way than it has been done in the balanced filter structure reported Section 4.1.1. Therefore, the first step of the design process is to use the *Optimum Schematic ASM* to determine of the optimum filter schematic for the differential-mode, based on given specifications. Once the optimum schematic is obtained, the second ASM step consists of the independent optimization of the main three items that form the filter structure which are highlighted in Figure 4.6 (a): the $\lambda/4$ inverters line width, the mirrored SIRs and the filter cells. The layout and equivalent circuit of the filter cell is detailed in Figure 4.8, where all the variables that play a role in these three different *Optimum Layout ASM* stages are shown (the other geometrical variables are set to fixed values and are not variables of the optimization process).

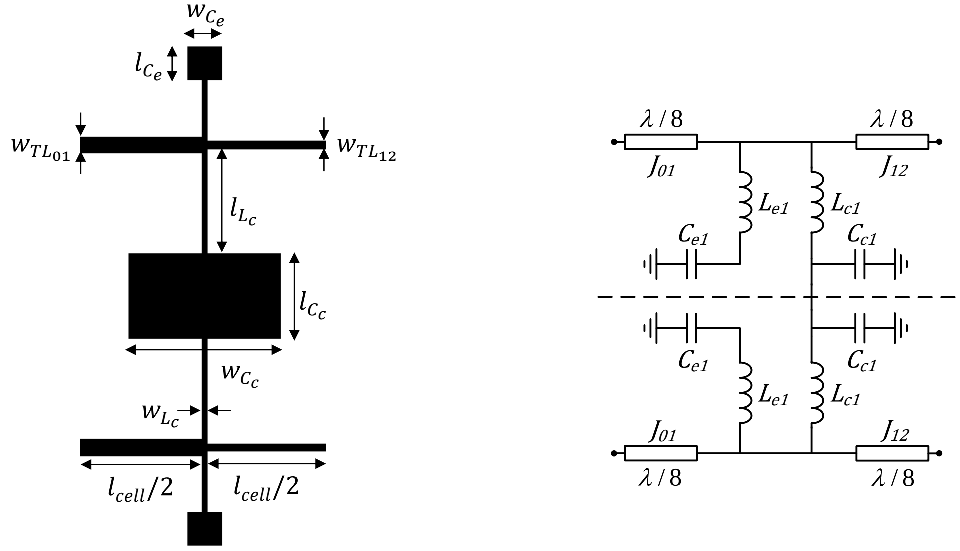

(a) (b)

Figure 4.8. Filter cell layout (a) and equivalent circuit model (b).

The equations for the *parameter extraction* process of the shunt SIRs can be obtained from its equivalent circuit shown in Figure 4.8 (b). Considering the differential-mode (L_c is grounded so C_c does not play any role), the SIRs susceptance B_{dd} can be expressed as stated below:

$$B_{dd} = \frac{\omega^2 C_e(L_e + L_c) - 1}{\omega L_c(-\omega^2 L_e C_e + 1)} \tag{4.6}$$

Hence, the resonant frequency, f_{0dd}, the transmission zero frequency, f_{Zdd}, and the susceptance slope, b_{dd}, at f_{0dd} can be defined as follows:

$$f_{0_{dd}} = \frac{1}{2\pi\sqrt{C_e(L_e + L_c)}} \tag{4.7}$$

$$f_{z_{dd}} = \frac{1}{2\pi\sqrt{L_e C_e}} \tag{4.8}$$

$$b_{dd} = 2\pi f_{0_{dd}} \frac{C_e(L_e + L_c)^2}{{L_c}^2} \tag{4.9}$$

and the transmission zero frequency, f_{Zcc}, in the common-mode is determined by:

$$f_{z_{cc}} = \frac{1}{2\pi\sqrt{L_c C_c}} \tag{4.10}$$

On the other hand, the $\lambda/4$ transmission lines that implement the admittance inverters are split in two $\lambda/8$ input and output transmission lines connected to the resonators input and output ports respectively. The characteristic impedance Z_0 and the phase shift θ_{cell} of each $\lambda/8$ transmission line will have to be tailored to the appropriate value in order to provide the desired admittance transformation to each filter cell that composes the filter structure.

Layout Generation by means of ASM

The layout synthesis process is similar to the one reported for the single-ended filter in Section 3.1.1 and it involves the same three ASM stages: 1) the *SIR ASM*, 2) the *Line Width ASM* and 3) the *Filter Cell (Line Length) ASM*. The flow diagram of the entire optimization scheme is presented in Figure 4.9.

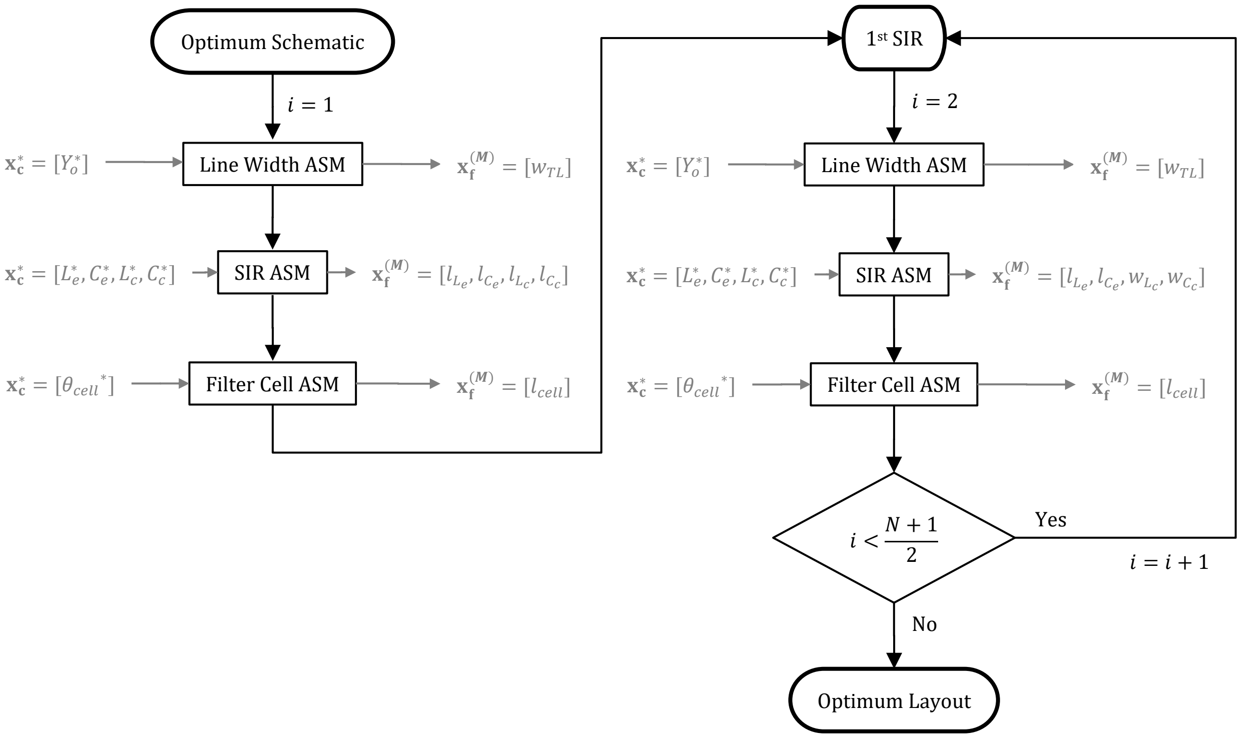

Figure 4.9. **TMTT15** balanced wideband bandpass filter 2nd ASM flow diagram.

As can be observed in the presented scheme, it is important to point out that in this flow diagram it is needed to differentiate the first three-stage ASM, concerning the first filter cell, from the rest. The reason for that is related to the SIRs topology, which might not be equal for each filter stage, so that special attention needs to be taken into account when connecting them in the layout construction phase. For a proper filter cells interconnection, it is clear that the distance in the vertical axis of the pair of inverter lines needs to be kept unaltered (see Figure 4.6 (a)) and therefore needs to be considered in the layout optimization process of the mirrored SIRs.

Regarding the *Line Width ASM* algorithm, it consists on obtaining the optimum width w_{TL} for each $\lambda/4$ transmission line, so it is based on a one-variable ASM procedure as explained in Section 3.1.1. However, it has to be noted that this ASM must be repeated as many times as different admittance inverters are present in the filter.

On the other hand, the ASM process devoted to the resonator synthesis, i.e. the *SIR ASM*, the coarse model vector for the mirrored SIRs is defined as $\mathbf{x_c} = [L_e, C_e, L_c, C_c]$ and its response is obtained through circuit simulation, whereas the fine model vector of the first mirrored SIR, i.e. $i = 1$, corresponds to $\mathbf{x_f} = [l_{Le}, l_{Ce}, l_{Lc}, l_{Cc}]$ and its response is obtained through electromagnetic simulation of the layout. By means of the approximate formulas [14] for an electrically small narrow and wide strips, the initial layout $\mathbf{x_f}^{(1)}$ of the shunt resonator can be determined, and next $\mathbf{x}_c^{(1)}$ can be inferred from the initial layout EM simulation by means of the *parameter extraction* process through the equations (4.7)-(4.10). In this case, the initial Broyden matrix $\mathbf{B}^{(1)}$ corresponding to the first resonator can be defined as follows:

$$\mathbf{B}^{(1)} = \begin{pmatrix} \frac{\delta L_e}{\delta l_{L_e}} & \frac{\delta L_e}{\delta l_{C_e}} & \frac{\delta L_e}{\delta l_{L_c}} & \frac{\delta L_e}{\delta l_{C_c}} \\ \frac{\delta C_e}{\delta l_{L_e}} & \frac{\delta C_e}{\delta l_{C_e}} & \frac{\delta C_e}{\delta l_{L_c}} & \frac{\delta C_e}{\delta l_{C_c}} \\ \frac{\delta L_c}{\delta l_{L_e}} & \frac{\delta L_c}{\delta l_{C_e}} & \frac{\delta L_c}{\delta l_{L_c}} & \frac{\delta L_c}{\delta l_{C_c}} \\ \frac{\delta C_c}{\delta l_{L_e}} & \frac{\delta C_c}{\delta l_{C_e}} & \frac{\delta C_c}{\delta l_{L_c}} & \frac{\delta C_c}{\delta l_{C_c}} \end{pmatrix} \tag{4.11}$$

The first *SIR ASM* process will be associated to the mirrored SIR providing the lower common-mode transmission zero (which will provide the wider central patch which synthesizes C_z). For the determination of the layout of the other resonant elements, the *SIR ASM* sub-process to be applied is based on the same principle than the first one, but considering as optimization variables of the validation space the widths for the inner sections (the ones between the pair of transmission lines), and the lengths for the outer sections. By this means, the distance between the pair of lines is kept unaltered. Therefore, the coarse model vector for the mirrored SIRs is still defined as $\mathbf{x}_c = [L_e, C_e, L_c, C_c]$, while the fine model vector of the other mirrored SIRs will correspond to $\mathbf{x}_f = [l_{Le}, l_{Ce}, w_{Lc}, w_{Cc}]$. The definition of the initial Broyden matrix for these resonators is defined as:

$$\mathbf{B}^{(1)} = \begin{pmatrix} \frac{\delta L_e}{\delta l_{L_e}} & \frac{\delta L_e}{\delta l_{C_e}} & \frac{\delta L_e}{\delta w_{L_c}} & \frac{\delta L_e}{\delta w_{C_c}} \\ \frac{\delta C_e}{\delta l_{L_e}} & \frac{\delta C_e}{\delta l_{C_e}} & \frac{\delta C_e}{\delta w_{L_c}} & \frac{\delta C_e}{\delta w_{C_c}} \\ \frac{\delta L_c}{\delta l_{L_e}} & \frac{\delta L_c}{\delta l_{C_e}} & \frac{\delta L_c}{\delta w_{L_c}} & \frac{\delta L_c}{\delta w_{C_c}} \\ \frac{\delta C_c}{\delta l_{L_e}} & \frac{\delta C_c}{\delta l_{C_e}} & \frac{\delta C_c}{\delta w_{L_c}} & \frac{\delta C_c}{\delta w_{C_c}} \end{pmatrix} \tag{4.12}$$

The iterative process will finish once the final fine model vectors $\mathbf{x}_{fi}^{(M)}$ corresponding to the $(N+1)/2$ resonators that conform the filter structure are found.

The *Filter Cell ASM* process will be used to determine the length of the inverters. To this end, the whole filter cell need to be considered, consisting of the resonator cascaded in between the inverter halves (not necessarily of the same width, or admittance). As it was pointed out in Section 3.1.1, the optimization of the whole filter cell is necessary since the resonators may introduce some (although small) phase shift. In Section 3.1.1, the whole filter cell was forced to exhibit a phase shift of 90° at the central frequency of the optimum schematic. However, the fact that the inverters at both sides of the resonator have different admittance means that the phase of S_{21} is no longer 90° at the central frequency of the optimum schematic. Nevertheless, the phase shift of the cell can be easily inferred from circuit simulation (through the corresponding optimum filter schematic depicted in Figure 4.7 (a)), and the resulting value is the goal of this third ASM sub-process. Thus, the *Filter Cell ASM* optimization consists of varying the length of the lines cascaded to the resonator until the required phase per filter cell is achieved (the other geometrical parameters of the cell are kept unaltered). The phase is directly inferred from the frequency response of the cell obtained from electromagnetic simulation at each iteration step. Once each filter cell is optimized, the cells are cascaded and no further optimization is required.

Optimum Layout

Let us consider the synthesis of a filter with the following design specifications: $N = 7$, $f_0 = 3$ GHz, $FBW = 60$ % (corresponding to $FBW_{-3dB} = 63.43\%$) and $L_{Ar} = 0.15$ dB ($RL = 14.69$ dB). Since the differential-mode bandwidth is wide, a single common-mode transmission zero does not suffice to completely reject this mode over the differential filter pass band. Thus, in this case, several transmission zeros for the common-mode are generated. Such transmission zeros must be (roughly) uniformly distributed along the differential-mode pass band for an efficient common-mode rejection over that band. Therefore, as many different capacitances C_{ci} as transmission zeros must be calculated by means of the expression (4.10) to completely determine the elements of the optimum filter schematic.

The application of the *Two-Step ASM* scheme to the described filter structure, considering the aforementioned 7th order filter example, using *Rogers RO3010* substrate with thickness $h = 635$ μm, dielectric constant $\varepsilon_r = 10.2$ and loss tangent $tan\delta = 0.0022$, provides the layout indicated in Figure 4.10 (a). The optimum schematic, the EM (with losses) and the fabricated filter differential-mode responses are compared in Figure 4.10 (b), while in Figure 4.10 (c) the same comparison is done for the common-mode responses.

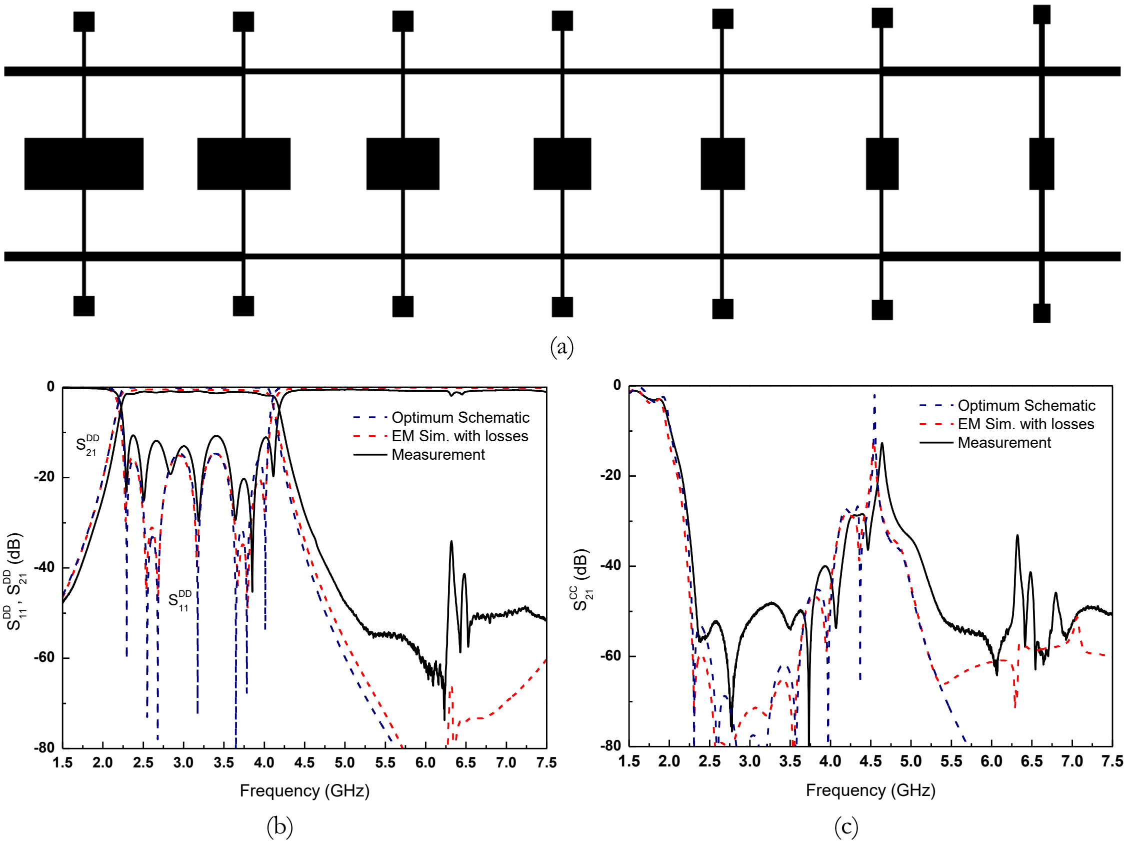

(a)

(b) (c)

Figure 4.10. **TMTT15** 7th order balanced wideband bandpass filter layout (a) and optimum schematic, EM simulation with losses and measured responses for the differential- (b) and common- (c) modes.

Very good agreement between the different responses can be observed, and it is found that the filter responses satisfy the considered specifications, including an efficient common-mode rejection over the differential filter pass band, with a common-mode rejection ratio (CMRR) better than 30 dB in the whole the differential filter pass band.

Thus, it is clear that balanced wideband bandpass filters with common-mode suppression are achievable by means of this optimization approach and filter design is simple since the determination of the filter layout does not need any external aid during the whole synthesis process.

In Article **TMTT15** a more detailed description is reported about the synthesis of these balanced filter topologies through the *Two-Step ASM* scheme, including the synthesis of a 5th order filter using the same topology, but with narrow differential-mode bandwidth requirements. In this case, applying the same value for all common-mode transmission zeros is enough to obtain good CMRR within the differential-mode pass band, leading to a bit simpler and faster optimization scheme.

4.2 Compact Semi-Lumped Balanced Wideband Filters

The balanced filters previously reported in Section 4.1 consist on a combination of semi-lumped elements, i.e. the SIRs, and distributed elements, i.e. the quarter-wavelength transmission lines, that act as admittance inverters. Despite the fact that these structures are able to fulfil the design specifications, their size is not fully optimized due to the distributed behavior of the inverters. Moreover, the limited narrowband functionality of the admittance inverters means that a method for bandwidth compensation is necessary to satisfy the filter specifications, and therefore the *Two-Step ASM* scheme is totally justified to automatically synthesize these filter structures.

However, this method complicates significantly the design of the filters, since the ASM-based tool used for this purpose must include an ASM algorithm able to determine the optimum schematic satisfying the specifications, which is different than the one directly inferred from the required Chebyshev filter response. In order to cope with this limitations, in Article **IJMWT16** is presented a novel filter structure based on replacing the inverters with interdigital capacitors, modelled as a series resonator with parasitic shunt capacitances, so that the structure can be roughly described by the canonical circuit of a bandpass filter. In addition, the filter size is reduced and its layout synthesis is carried out following a completely unattended scheme as well, with the added advantage that the first ASM algorithm is avoided since the resulting filter is composed of semi-lumped elements accurately described by their corresponding circuit models over a wide frequency range.

4.2.1 Design of Compact Balanced Filters based on Mirrored SIRs and Interdigital Capacitors by means of ASM

The novel differential-mode microstrip bandpass filters reported in Article **IJMWT16** are implemented by combining shunt connected mirrored SIRs and series connected interdigital capacitors. The filter topology and the lumped equivalent circuit is depicted in Figure 4.11 (a) and (b), respectively, for a 3rd order filter example.

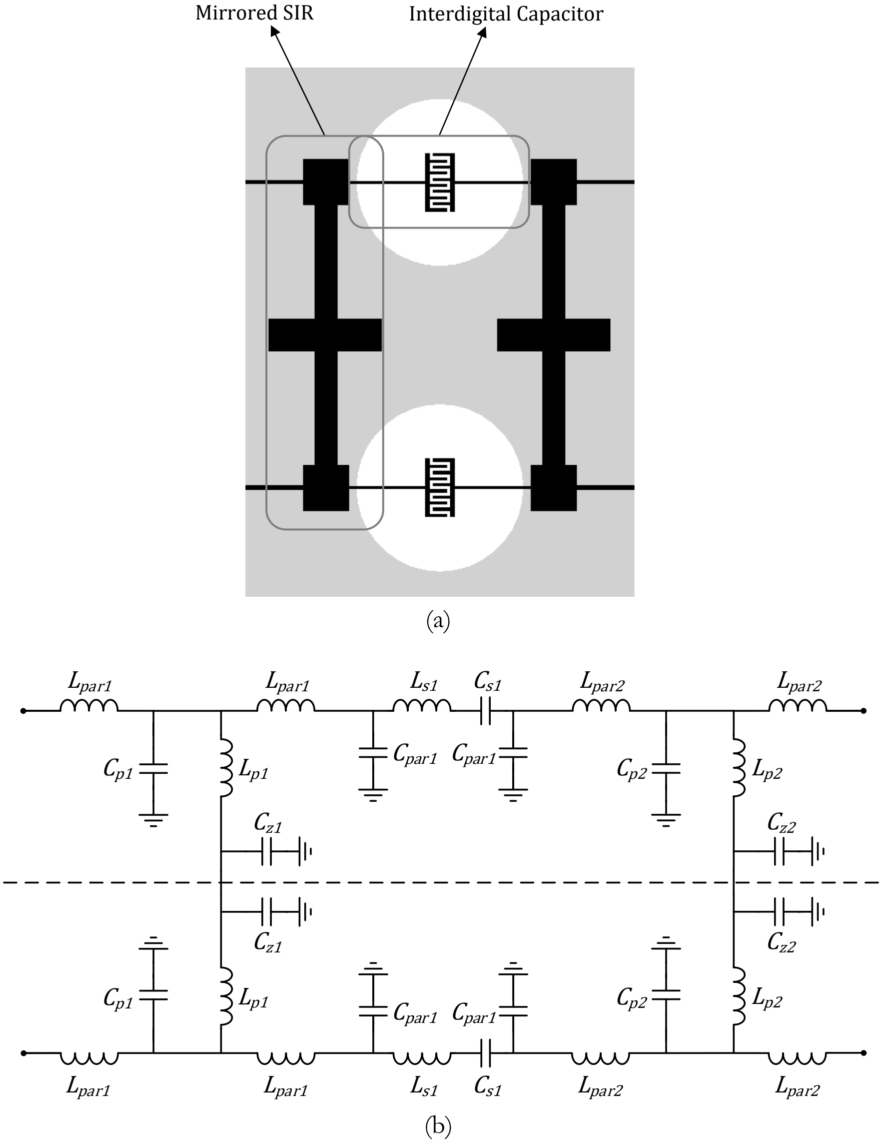

(a)

(b)

Figure 4.11. **IJMWT16** 3rd order balanced wideband bandpass filter layout (a) and equivalent circuit (b).

The shunt mirrored SIRs can be described as a T-network based on a combination of capacitances C_{pi} and C_{zi}, and inductances L_{pi} and L_{pari}, whereas the interdigital capacitors are modelled by a π-network with series resonators L_{si} and C_{si}, and shunt parasitic capacitors, C_{pari}. It is worth to mention that in the previous SIR structures reported in Sections 3.1.1 and 4.1.1, the parasitic inductance L_{pari} is omitted since it was supposed to be small enough to not alter the overall filter response. This assumption cannot be made for the current topology, even though L_{pari} is expected to be small as well, and needs to be included for an accurate description of the mirrored SIR in this case.

The symmetry plane of the filter is an E-wall for the differential-mode so that the capacitances C_{zi} do not play an active role for that mode since L_{pi} are grounded. Moreover, note that the circuit model of the differential-mode shown in Figure 4.12 (a) is approximately equivalent to the canonical circuit of a band pass filter if L_{par} is considered to be sufficiently small, so that the capacitance C_{pari} is directly connected in parallel with the capacitance C_{pi}. L_{pari} prevents of that filter canonicity, but as L_{par} is expected to be small, the resulting response of the topology shown in Figure 4.12 (a) can be assumed to be similar to those inferred from the canonical one. On the other hand, the symmetry plane for the common-mode is an H-wall which acts as an open circuit, and the equivalent circuit model is the one depicted in Figure 4.12 (b), where the resonators L_{pi}-C_{zi} provide transmission zeros that are useful for the suppression of the common-mode in the region of interest (differential filter pass band). From Figure 4.12 (a) it can be observed that the position of these common-mode transmission zeros does not affect the differential-mode response.

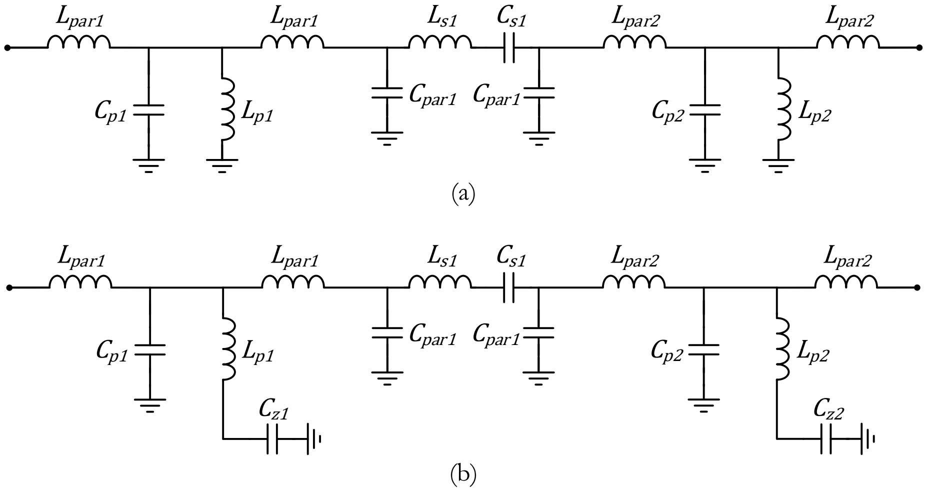

Figure 4.12. **IJMWT16** differential- (a) and common- (b) mode circuit schematics of the filter structure.

Since the equivalent circuit model for the differential-mode does not exactly match the canonical model of a bandpass filter, in order to automatically determine the filter layout from the specifications of such filter topology there is the need to find the elements of the equivalent circuit, including the parasitics, which provide a response as close as possible to the target canonical Chebyshev pass band filter. Therefore, the first step in this unattended optimization scheme is to find the optimum schematic of the structure depicted in Figure 4.11 (b), and to do so the values of the parasitic elements C_{par} and L_{par} need to be determined in advance. The parasitic elements are not design variables but they can be extracted and taken into account during the series and shunt resonators ASM synthesis processes. Once the optimum schematic is found, the next step is the generation of the layout.

Considering this filter topology as a combination of interdigital capacitors and mirrored SIRs, a two-level ASM will be used, where each ASM sub-process is dedicated to each resonator topology. The first ASM is focused on the layout optimization of the interdigital capacitors whereas the second one is focused on the layout optimization of the mirrored SIRs. It is also important to point out that the shunt parasitic capacitances of the interdigital capacitors, C_{par}, need to be extracted in advance from the corresponding series resonator EM response prior to start with the shunt SIRs ASM process, since C_{par} is needed to define the optimum equivalent circuit of such mirrored SIRs.

The layout and equivalent circuit of the interdigital capacitor resonator is depicted in Figure 4.13, where all the variables that take part on the ASM process are also highlighted in the same figure. Note that the window in the ground plane is necessary to enhance the inductance L_s and decrease the capacitance C_{par}, and it is circularly shaped in order to minimize the interaction with the mirrored SIR resonators connected on both ports.

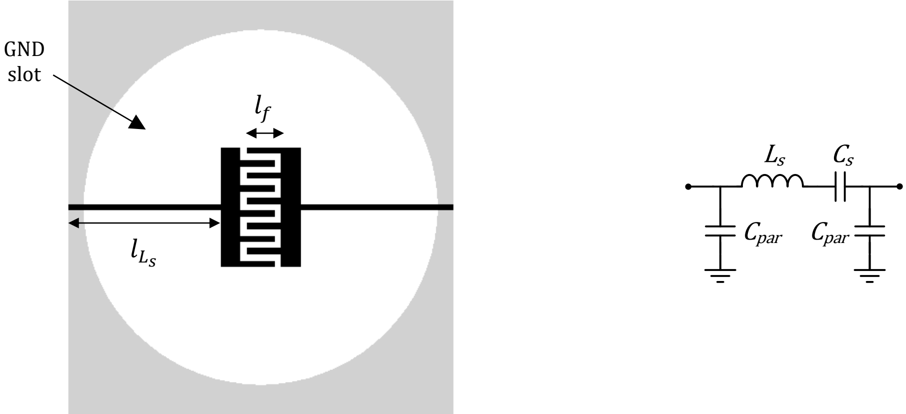

(a) (b)

Figure 4.13. Series interdigital capacitor layout (a) and equivalent circuit model (b).

The equations for the *parameter extraction* process of the interdigital resonator can be obtained from the equivalent circuit of Figure 4.13 (b). The series reactance, X_s, of the series resonator can be expressed as:

$$X_s = \frac{\omega^2 L_s C_s - 1}{\omega C_s} \tag{4.13}$$

Hence, the resonant frequency, f_0, and the reactance slope, x, at f_0 can be defined as follows:

$$f_0 = \frac{1}{2\pi\sqrt{C_s L_s}} \tag{4.14}$$

$$x = \omega_0 L_s \tag{4.15}$$

Moreover, the shunt impedance of the interdigital capacitor, Z_p, from where C_{par} can be found, can be extracted by proper inspection of the EM simulation response using the following expression, valid for a reciprocal π-network:

$$\mathrm{Z_p} = Z_0 \frac{(1 + \mathrm{S_{11}})^2 - \mathrm{S_{21}}^2}{\left(1 - \mathrm{S_{11}}^2\right) + \mathrm{S_{21}}^2 - 2\mathrm{S_{21}}} \tag{4.16}$$

so that the shunt parasitic capacitance C_{par} can be expressed as follows:

$$C_{par} = -\frac{1}{\omega_0 \mathrm{X_p}} \tag{4.17}$$

The value of C_{par} is relevant since it must be subtracted to the capacitance C_{pi} of the mirrored SIRs, as it will be justified later.

On the other hand, the layout and equivalent circuit of the mirrored SIRs is described in Figure 4.14. The resonator layout and all the physical variables that will be part of the ASM process are depicted in Figure 4.14 (a), while in Figure 4.14 (b) the resonator equivalent circuit is presented (the other geometrical variables are set to fixed values and are not variables of the optimization process).

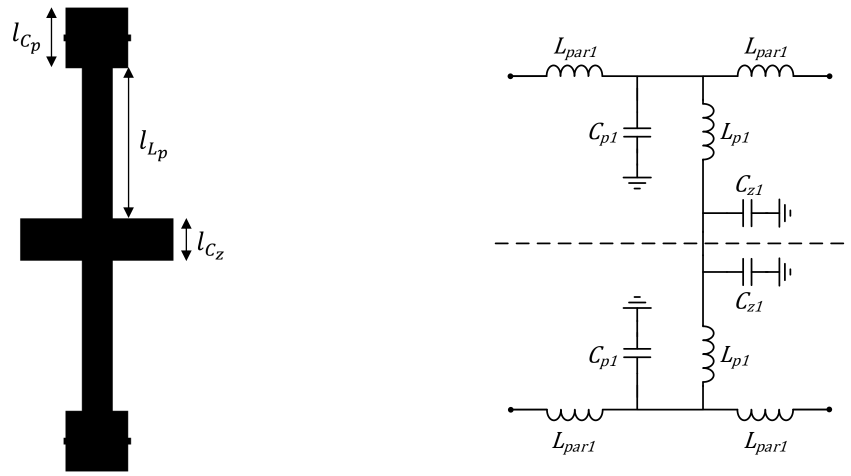

(a) (b)

Figure 4.14. Mirrored SIR layout (a) and equivalent circuit model (b).

As discussed previously, it can be noticed that the electrical model of the mirrored SIR depicted in Figure 4.14 (b) takes into account the series parasitic inductance L_{par}. In any case, the equations (4.2)-(4.4) presented for the mirrored SIR of Section 4.1.1 are also valid for the mirrored SIR model depicted in Figure 4.14 (b) and are the ones to be used in the *parameter extraction* process of such shunt resonator. In addition, the resonator series impedance, Z_s, from where L_{par} can be found, can be extracted by proper inspection of the EM simulation response using the following expression, valid for a reciprocal T-network:

$$\mathrm{Z_s} = Z_0 \frac{(1 - \mathrm{S_{11}}^2) + \mathrm{S_{21}}^2 - 2\mathrm{S_{21}}}{(1 - \mathrm{S_{11}})^2 - \mathrm{S_{21}}^2} \tag{4.18}$$

so that the series parasitic inductance L_{par} can be expressed as follows:

$$L_{par} = \frac{\mathrm{X_s}}{\omega_0} \tag{4.19}$$

The value of L_{par}, although it is expected to be small, will have impact in the overall circuit response and therefore is relevant enough to have it into consideration.

Layout Generation by means of ASM

The complete automatic layout synthesis process involves three ASM stages: 1) the *1st Interdigital Capacitor ASM*, 2) the *SIR ASM* and 3) the *2nd Interdigital Capacitor ASM*. The flow diagram of the entire optimization scheme is presented in Figure 4.15.

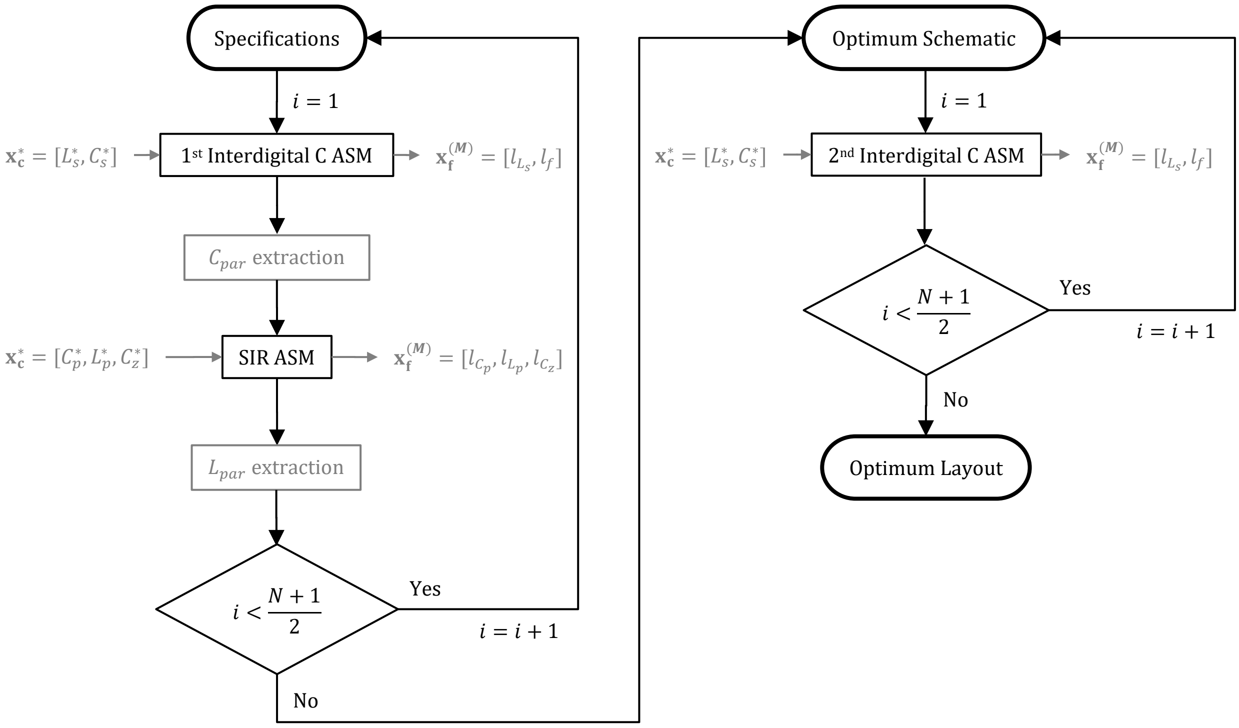

Figure 4.15. **IJMWT16** compact wideband balanced filter ASM flow diagram.

The elements of the series (L_s, C_s) and shunt (L_p, C_p) resonators of the differential-mode canonical bandpass equivalent circuit can be inferred from filter specifications through the well-known transformations from the low-pass filter prototype [9]. On the other hand, the capacitances C_{zi} are dictated by the position of the transmission zeros of the common-mode response as it is defined in equation (4.4). Once the elements of the series resonators of the interdigital capacitors are known, the specific ASM process for the determination of the layout giving such elements is necessary. In this ASM algorithm, that is, the *1st Interdigital Capacitor ASM*, the variables in the optimization (coarse) space are $\mathbf{x_c} = [L_{si}, C_{si}]$, whereas the variables in the validation (fine) space are the length of the inductive line, l_{Ls}, and the length of the fingers, l_f, i.e., $\mathbf{x_f} = [l_{Ls}, l_f]$. The other geometrical parameters are not modified during the optimization process and are set to a fixed value. The first vector of the validation space, $\mathbf{x_f}^{(1)}$, is estimated from approximate formulas providing the inductance of a narrow inductive strip and the capacitance of an interdigital capacitor [14]. Next, $\mathbf{x_c}^{(1)}$ is inferred from the initial layout EM simulation through the *parameter extraction* procedure carried out by means of equations (4.14) and (4.15). Finally, the first approach to the Broyden matrix $\mathbf{B}^{(1)}$, necessary to iterate the process as indicated above, is given by:

$$\mathbf{B}^{(1)} = \begin{pmatrix} \dfrac{\delta L_s}{\delta l_{L_s}} & \dfrac{\delta L_s}{\delta l_f} \\ \dfrac{\delta C_s}{\delta l_{L_s}} & \dfrac{\delta C_s}{\delta l_f} \end{pmatrix} \tag{4.20}$$

With this ASM scheme, the layout providing the target elements of the series branch is determined, and from this layout, the parasitic capacitance C_{par} is also inferred from the interdigital resonator EM response by using equations (4.16) and (4.17). The C_{par} *extraction* process, as indicated in Figure 4.15, is key for the optimum equivalent circuit definition of the mirrored SIR. The presence of such parasitic element forces to recalculate the mirrored SIR circuit schematic taking into account C_{par}: once the C_{par} value is obtained, it will be subtracted from the shunt capacitance C_p of the mirrored SIR, so that the final shunt capacitance value to be synthesized in the mirrored SIR will consider already the addition of C_{par} coming from the interdigital resonator when forming the complete filter structure, as can be envisioned in Figure 4.11 (b) assuming that L_{par} is sufficiently small.

The layout of the mirrored SIRs is then determined using the *SIR ASM* algorithm, where the coarse model vector is defined as $\mathbf{x_c} = [L_{pi}, C_{pi}, C_{zi}]$, whose variables correspond to the circuit schematic for the common-mode depicted in Figure 4.14 (b). On the other hand, the fine model vector is constituted by a set of variables describing the resonator layout and is defined as $\mathbf{x_f} = [l_{Lpi}, l_{Cpi}, l_{Czi}]$. Therefore, in order to deal with the same number of variables in both spaces, the remaining physical parameters of the layout are set to fixed values. The first vector of the validation space, $\mathbf{x_f}^{(1)}$, is estimated from the well-known approximate formulas providing the inductance and capacitance of a narrow and wide electrically small transmission line sections [14]. Since the shunt impedance of the mirrored SIR is equivalent than the one reported in Section 4.1.1, *parameter extraction* is carried out by using the same equations (4.2)-(4.4) and, similarly, the first approach to the Broyden matrix, $\mathbf{B}^{(1)}$, necessary to iterate the process, is defined as described in equation (4.5). With this ASM scheme, the layout providing the target elements of the shunt resonator is determined, and from this layout, the series parasitic inductance L_{par} is also inferred from the mirrored SIR EM response by using equations (4.18) and (4.19).

Optimum Schematic Definition Strategy

With the previous ASM algorithms, the layouts of the filter stages corresponding to the interdigital capacitors and mirrored SIRs can be determined. However, the presence of the parasitic elements forces us to recalculate the circuit schematic taking into account such parasitics. The hypothesis in the design process is to assume that the L_{par} and C_{par} values inferred as explained before will not vary significantly when applying slight changes in the corresponding resonators geometries. Hence, the next step is to set in the schematic the inferred values for the parasitics, and consider the remaining elements as variables that must be tuned at the circuit level in order to satisfy the filter specifications. However, as long as the inductance L_{par} is small, it can be expected that by subtracting the parasitic capacitance C_{par} to the capacitance of the mirrored SIR, C_p, the other variables in the filter equivalent circuit of Figure 4.11 (b) do not need to be modified that much, thus only the undesired L_{par}

effect needs to be compensated. Indeed, it has been verified that it is enough to automatically tune L_s to satisfy the filter specifications and hence to obtain the optimum filter schematic. Therefore, once Ls is tuned (and the optimum schematic is obtained) the layout of the interdigital capacitors must be recalculated again, leading to the *2nd Interdigital Capacitor ASM* stage, as it is shown in Figure 4.15. Next, the resulting layouts are cascaded and the entire filter layout is thus constructed.

Let us consider the synthesis of a 3rd order Chebyshev filter with central frequency f_0 = 2.4 GHz, fractional bandwidth *FBW* = 40% and ripple L_{Ar} = 0.15 dB. After applying the *1st Interdigital Capacitor ASM* and the *SIR ASM* schemes shown in Figure 4.15, C_{par} and L_{par} are inferred so that the optimum schematic can be obtained by tuning the interdigital capacitor series inductance, L_s, by means of an automatic procedure. This automatic tuning process is carried out in the circuit level space, and it is based in an iterative process where the value of L_s is slightly modified (reduced) until the differential-mode response of the filter equivalent schematic of Figure 4.12 fulfills the design specifications. In other words, the aim of the L_s tuning is to compensate the L_{par} undesired effect in order to obtain a filter response as close as possible to the canonical Chebyshev pass band filter response. Concerning this example, in Figure 4.16 the comparison between both responses after the application of the L_s tuning is shown.

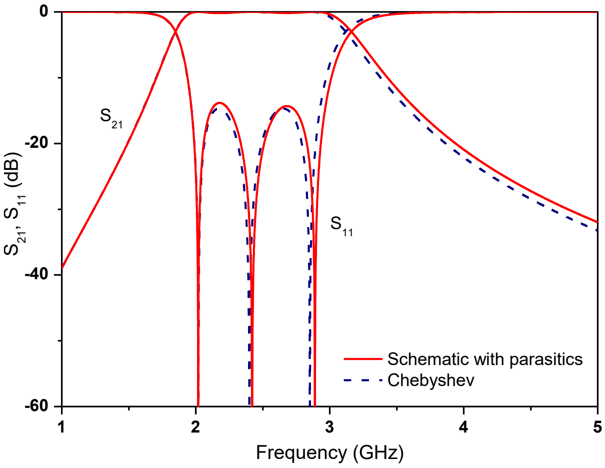

Figure 4.16. Comparison between the ideal Chebyshev response and the optimum filter schematic response including parasitic elements.

As can be seen, the responses are very similar, thus validating the approach based on the tuning of L_s only.

Optimum Layout

Once the new value of L_s is found and the optimum schematic is obtained, it is necessary to recalculate the new layout of the interdigital capacitor by means of the *2nd Interdigital Capacitor ASM* and next the optimum layout of the filter can be already built. Its final layout is presented in Figure 4.17 (a) whereas the frequency response of the filter, including the simulation of the optimum schematic, electromagnetic simulation and measurement is depicted in Figure 4.17 (b) and (c) for the differential-mode and the common-mode respectively. The filter is fabricated in a *Rogers RO3010* substrate with thickness h = 254 μm, dielectric constant ε_r = 10.2 and loss tangent tanδ = 0.0022.

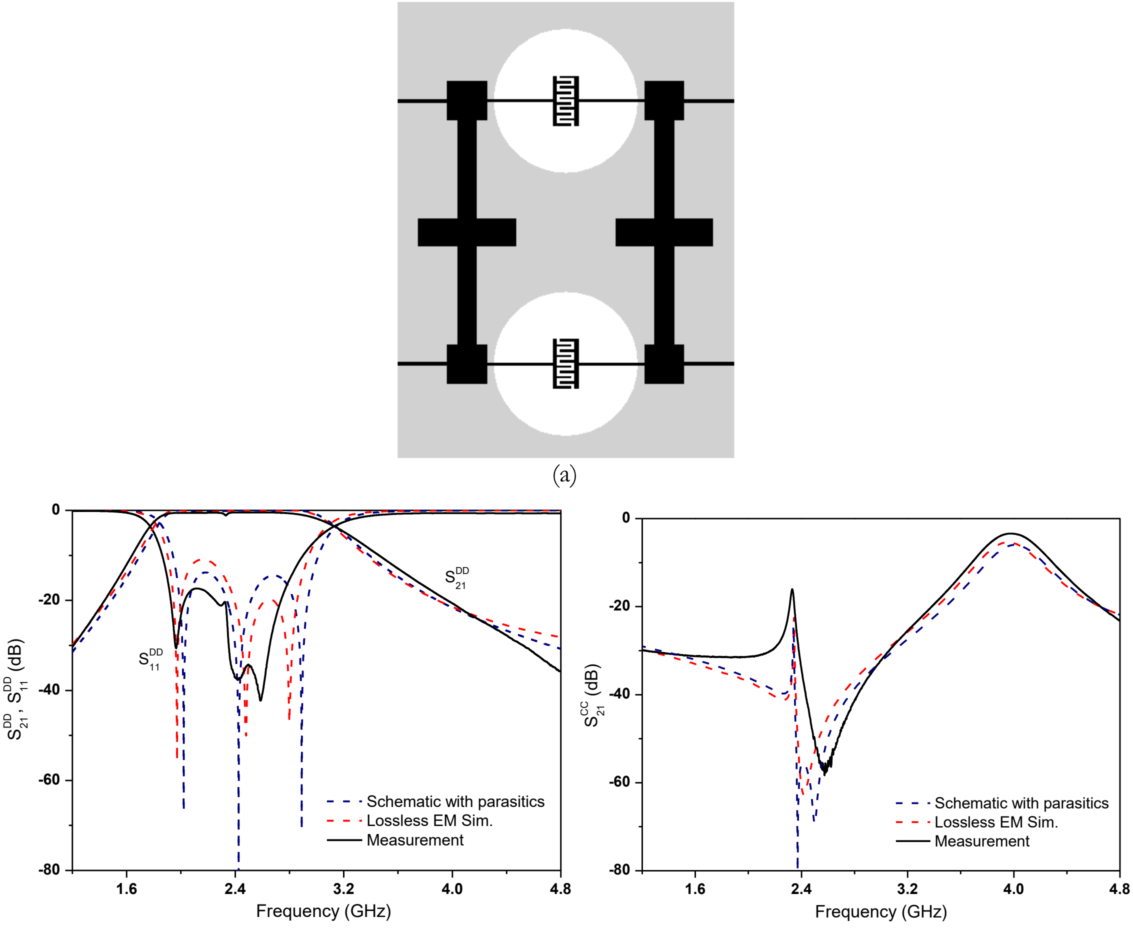

(a)

(b)

(c)

Figure 4.17. **IJMWT16** 3rd order compact balanced wideband bandpass filter layout (a) and comparison between the optimum schematic, EM lossless simulation and measured responses for the differential-mode (b) and for the common-mode (c).

The agreement between the electromagnetic simulation and circuit simulation for the differential-mode is reasonable as can be observed in Figure 4.17 (b), and discrepancies with the measurement can be attributed to the fabrication-related tolerances. Note that the synthesis of the interdigital capacitors requires narrow gaps between fingers in order to obtain the appropriate series capacitance C_s value, which makes them a bit sensitive due to their implementation is close to the limits of the standard PCB technology process. The common-mode response is reasonably predicted by the circuit model as depicted in Figure 4.17 (c) and the final dimensions are showing a compact outline with $0.48\lambda \times 0.35\lambda$, λ being the guided wavelength at the central filter frequency. In summary, this novel filter structure exhibits good balance between size and performance, with the added value that the design of the filter is carried out following a completely unattended procedure.

4.3 Compact Balanced Wideband Filters with Very Broad Common- and Differential-Mode Stop Bands

The balanced compact filter structure presented in Section 4.2 exhibits certain advantages compared with the balanced topologies described Section 4.1. The filter size reduction, leading to a more compact size, and the direct generation of the optimum schematic from design specifications, with no need of a dedicated *Optimum Schematic ASM* process, are the main beneficial aspects of this compact structures. However, as reported in Articles **NEMO17*** and **TMTT18**, these structures can be modified by adding controllable transmission zeros in both differential- and common-modes in a similar way to the structures of Section 4.1.2. By controlling these transmission zeros adequately, the differential- and common-mode stopbands can be extended up to significantly high frequencies. The filter is automatically synthesized by means of a dedicated ASM scheme and two pre- and post-optimization algorithms, necessary to accurately determine the transmission zero frequencies. Thus, the unattended layout synthesis, the compact size and the differential- and common-mode stopband performance are the main relevant characteristics of the proposed novel balanced filter structures.

4.3.1 Design of Compact Balanced Filters based on Mirrored SIRs and Interdigital Capacitors by means of ASM and Pre- and Post-Optimization Algorithms

The novel differential-mode microstrip bandpass filters reported in articles **NEMO17*** and **TMTT18** are implemented by combining shunt-connected mirrored SIRs and series-connected interdigital capacitors. The balanced filter topology is depicted in Figure 4.18 (a). Such topology corresponds to a 3rd order filter example and its corresponding balanced equivalent circuit is depicted in Figure 4.18 (b). That filter structure can be generalized to an arbitrary order by simply adding or removing filter stages.

As can be observed in Figure 4.18 (b), the series resonators are described by π-networks with series resonators C_{si}-L_{si} and parallel parasitic capacitances C_{par}, which coincides with the structure previously reported in Section 4.2.1. On the other hand, the mirrored SIRs are described by the inductances L_{ei} and L_{ci}, and by the capacitances C_{ei} and C_{ci}. Therefore, in this topology, the series parasitic inductance, L_{par}, included previously in the mirrored SIR equivalent circuit of Section 4.2.1, is omitted here since in this case it is assumed to be very small. The symmetry plane is an electric wall for the differential-mode and a magnetic wall for the common-mode. Therefore, the circuit models for these modes can be inferred from the model of Figure 4.18 (b) by grounding (differential-mode) or opening (common-mode) the nodes intersecting the symmetry plane, as it is shown in Figure 4.19 for the differential- (a) and common- (b) modes.

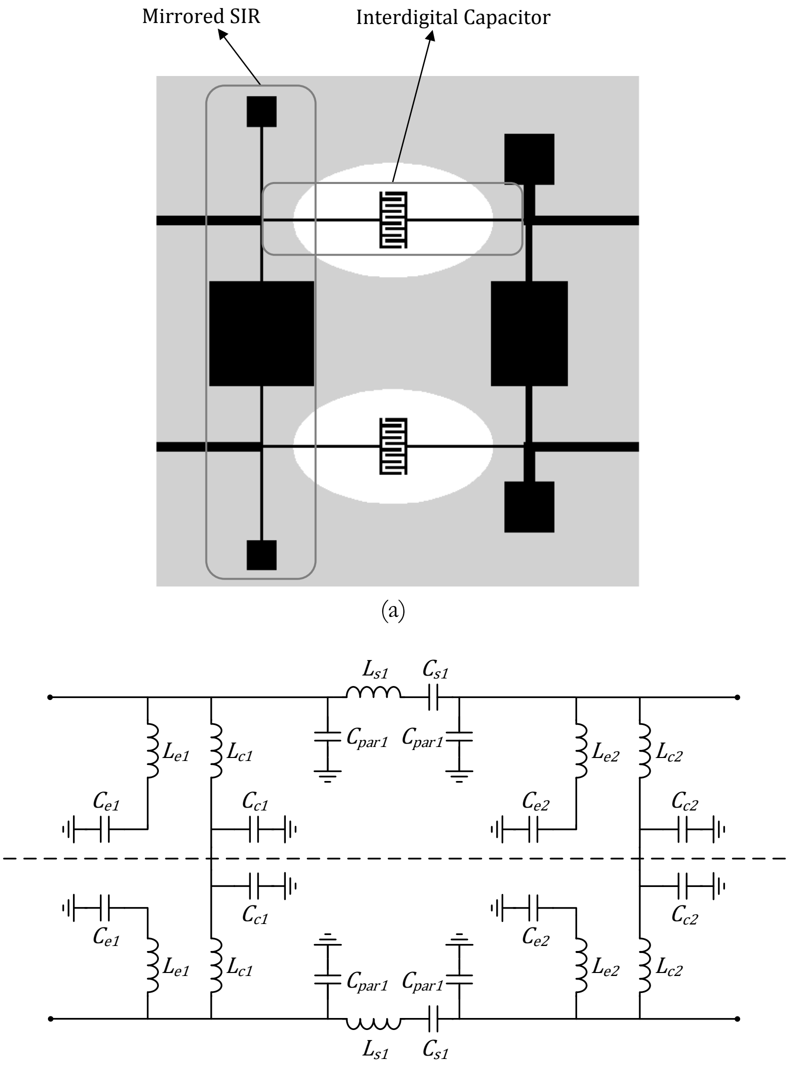

(a)

(b)

Figure 4.18. **NEMO17*** and **TMTT18** 3rd order compact wideband bandpass filter layout (a) and equivalent circuit (b).

For the differential-mode, the capacitances C_{ci} are short circuited and do not play an active role. Conversely, such capacitances and the inductances L_{ci} act as shunt-connected series resonators for the common-mode, providing transmission zeros at the resonance frequencies. The strategy to efficiently suppress the common-mode is to distribute these common-mode transmission zeros along the differential-mode pass band by varying the dimensions of the central patches (and hence the values of C_{ci}). The external resonators (L_{ei}-C_{ei}) provide transmission zeros for both modes, something that was not possible to achieve with the former topology reported in Section 4.2.1, due to the non-existence of L_{ei}. It must be noted that for both shunt-connected series resonators types (L_{ci}-C_{ci} and L_{ei}-C_{ei}), as many different transmission zeros can be controlled as shunt SIR stages are available in the filter structure, that is, $(N + 1)/2$, where N is the filter order. This fact gives added value to the current topology, which is able to generate differential- and common-mode transmission zeros above the pass band of interest, in order to broaden the stop band for both modes and efficiently reject out-of-band differential signals.

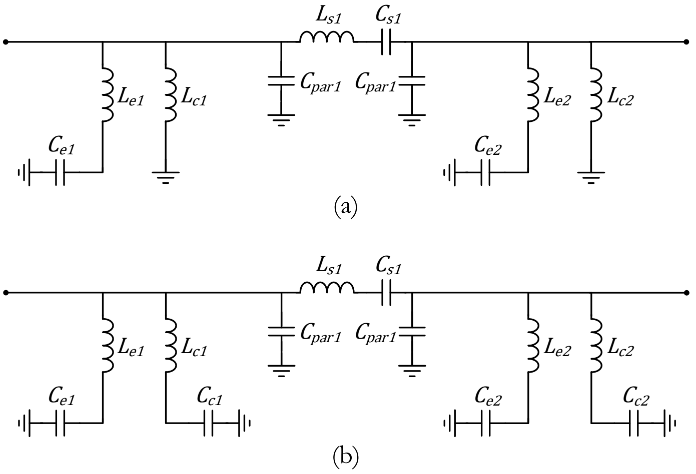

Figure 4.19. **NEMO17*** and **TMTT18** circuit schematic for the differential (a) and common (b) modes.

In the design of the filter, the first step is the determination of the elements of the circuit model from filter specifications and from the position of the differential- and common-mode transmission zeros (a pre-optimization process is used in order to obtain the optimum location of such transmission zeros, which will be described later). Once such elements are known, the second step is the determination of the filter layout by means of a dedicated two-level ASM scheme. The first ASM level is focused in the interdigital capacitors layout optimization whereas the second ASM level is focused in the mirrored SIRs layout optimization. Such optimization process will be active until all resonator stages that form the filter layout are properly optimized.

Since the interdigital capacitor structure is the same than the one reported in Section 4.2.1, its corresponding layout and equivalent circuit has been already reported in Figure 4.13. Therefore, the equations (4.14) and (4.15) will be used in the *parameter extraction* process when performing the ASM algorithm of such series resonator. Special attention needs to be paid to the interdigital capacitors shunt parasitic capacitances C_{pari}. Similarly as it has been done in Section 4.2.1, such capacitances will be considered as part of the shunt mirrored SIRs. They are not controllable parameters but they can be easily inferred once the layouts of the series resonators stages are known. Therefore, in the design flow, it is first necessary to determine the series elements, L_{si} and C_{si}, and then synthesize the layouts of the interdigital capacitor resonators. From such layouts, the values of capacitances C_{par} can be easily derived from proper inspection of the EM response by means of equations (4.16) and (4.17).

The layout and equivalent circuit of the multi-section mirrored SIRs is described in Figure 4.20. In Figure 4.20 (a) their layout and all the physical variables that are part of their optimization ASM process are indicated, while in Figure 4.20 (b) their equivalent circuit is presented (the other geometrical variables are set to fixed values and are not variables of the optimization process).

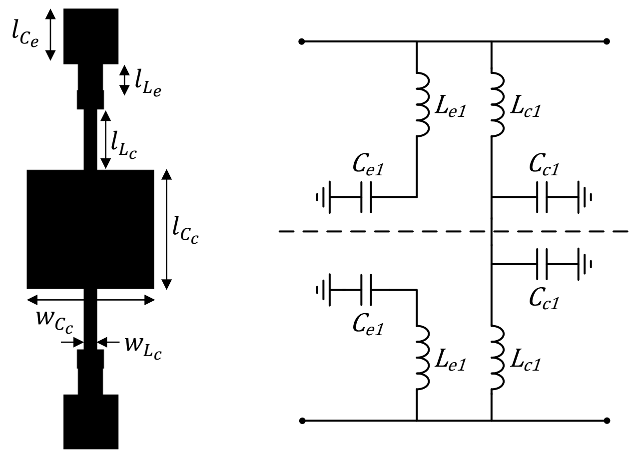

(a) (b)

Figure 4.20. Multi-section mirrored SIR layout (a) and equivalent circuit model (b).

Note that the circuit topology and equivalent circuit is the same than the former one reported in Section 4.1.2 but, in this case, the shunt parasitic capacitances C_{par} are directly considered as part of the SIR resonators, so that the SIRs equivalent shunt reactance, X_{sdd}, can be expressed by:

$$\chi_{s_{dd}} = \frac{(\omega^2 L_e C_e - 1) L_c}{\omega^3 C_{par} L_e C_e L_c - \omega\big(C_e(L_e + L_c) + C_{par} L_c\big)} \tag{4.21}$$

For the differential-mode, the filter central frequency, f_{0dd}, the transmission zero frequency, f_{0ZZ}, and the susceptance slope, b_{dd}, at the central angular frequency ω_0, are given by:

$$f_{0_{dd}} = \frac{1}{2\pi}\sqrt{\frac{C_e(L_e + L_c) + C_{par} L_c}{C_{par} L_c L_e}} \tag{4.22}$$

$$f_{z_{dd}} = \frac{1}{2\pi\sqrt{L_e C_e}} \tag{4.23}$$

$$b_{dd} = \frac{\omega_0 C_{par}}{2} + \frac{1}{2 L_c \omega_0} + \frac{C_e \omega_0 (1 + L_e C_e {\omega_0}^2)}{2(1 - L_e C_e {\omega_0}^2)^2} \tag{4.24}$$

while the transmission zero frequency, f_{Zcc}, can be defined as:

$$f_{z_{cc}} = \frac{1}{2\pi\sqrt{L_c C_c}} \tag{4.25}$$

Therefore, the four circuit variables L_e, C_e, L_c and C_e can be obtained from equations (4.22)-(4.25) by means of the corresponding *parameter extraction* process.

Optimization of the Transmission Zero Frequencies

In Article **TMTT18**, the zeros for the common-mode are distributed along the frequency range in order to achieve good common-mode rejection within the differential-mode pass band and beyond. With these transmission zeros, and those for the differential-mode, necessarily set above the pass band of interest (but also active for the common-mode), the common-mode can be significantly rejected beyond the differential-mode pass band, as will be shown later. In practice, it is difficult to a priori predict the optimum position of the transmission zeros (for the differential- and common- modes) necessary to optimize the differential- and common-mode rejection bands. The reason is that the filter design is focused on achieving a certain differential-mode response which fulfils the design specifications. However, the common-mode response is not linked to these specifications and typically exhibits non-desired transmission peaks. In order to reduce the level of such common-mode peaks, an iterative algorithm for the optimization of the transmission zero frequencies (for both the differential- and common- modes) has been developed. This algorithm is implemented in the equivalent lumped circuit space and it is meant to define the optimum schematic of the filter, including the optimum differential pass band response (linked to the design specifications) as well as the optimum location of the transmission zero frequencies. Thus, this algorithm can be understood as a pre-optimization process since it is going to be executed prior to the *Optimum Layout ASM* scheme, and its block diagram is described in Figure 4.21.

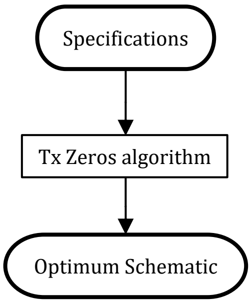

Figure 4.21. **TMTT18** *Transmission Zeros* optimization algorithm block diagram.

Let us illustrate the operation principle of this algorithm based on a specific filter example, corresponding to the following specifications: order $N = 5$, central frequency $f_0 = 1.8$ GHz, fractional bandwidth $FBW = 48\%$ (55.4% at 3-dB fractional bandwidth) and ripple level $L_{Ar} = 0.04$ dB ($RL = 20.4$ dB).

Initially, the location of all transmission zeros (differential- and common-mode) is set to an arbitrary single frequency, significantly above the upper cut-off frequency of the differential-mode pass band, e.g., $2.5f_0$. From filter specifications, we can infer the element values of the interdigital capacitors, i.e. L_s and C_s, corresponding to the series resonator stages, using well-known formulas [9]. Since the elements of the shunt SIRs depend on C_{par}, it is necessary to first synthesize the layout of the series branches, according to the ASM algorithm to be described later, and, from it, determine the value of C_{par}. Once this parasitic capacitance value is known, equations (4.22)-(4.25) can be used to determine L_e, L_c, C_e and C_c for the shunt resonator filter stages, and the response of the circuit (differential- and common- modes) at the schematic level can be inferred, as it is shown in Figure 4.22 (a). From this response, we can identify two common-mode transmission peaks, which in this case both fall inside the differential-mode passband frequency range.

In the second step, we reallocate two of the common-mode transmission zeros in those transmission peak frequencies (for that mode) and set the additional common-mode transmission zero to 1.5f_0. The differential-mode transmission zeros are kept unaltered in this second step. The new response is the one depicted in Figure 4.22 (b), where now we have three common mode transmission peaks, the former two, falling inside the differential-mode passband, plus a new one which appears outside.

According to the previous common-mode transmission peaks, in the next (third) iteration, we reallocate the same two common-mode transmission zeros in those transmission peak frequencies that fall within the differential passband, while the additional common mode transmission zero is kept to 1.5f_0. On the other hand, the third common-mode transmission peak (the one that falls outside the differential pass band) is cancelled by means of the first differential-mode transmission zero, while the two remaining differential-mode transmission zeros are kept at 2.5f_0. The new filter response is found to be the one depicted in Figure 4.22 (c), where it can be appreciated that the common-mode transmission peaks are significantly attenuated.

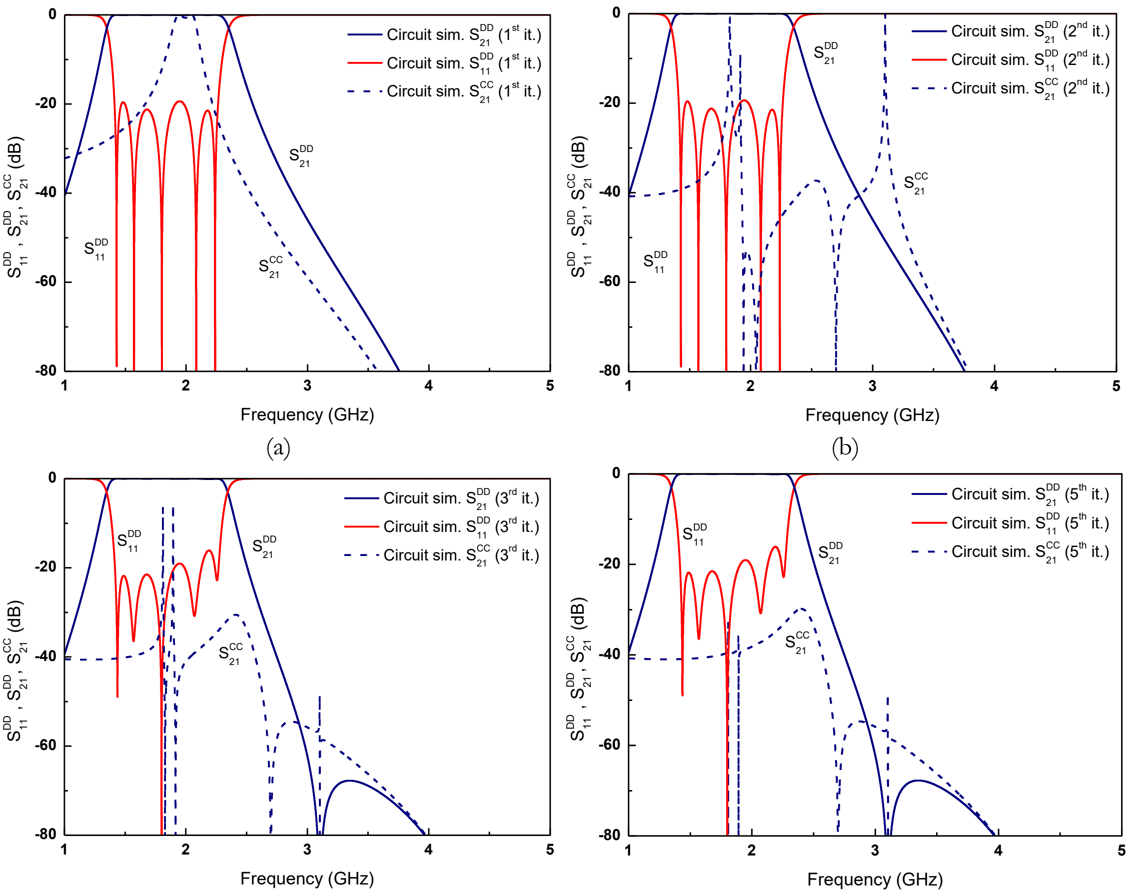

(a) (b)

(c) (d)

Figure 4.22. *Transmission Zeros* optimization algorithm example. (a) 1st iteration, (b) 2nd iteration, 3rd iteration(c) and (d) 5th iteration.

Nevertheless, in this iterative algorithm, the objective is to have an optimum common-mode rejection level within the differential-mode pass band. To this aim, the common-mode transmission peaks maximum level is specified to be below 25 dB in this case, so that some more iterations are needed to achieve that attenuation value for these common-mode peaks. Hence, a new set of transmission zeros is defined in the next iteration, using the same strategy defined in the previous iteration. This iterative process will continue until reach the specified common-mode rejection level, which in this case it has been set to be higher than 25 dB as mentioned before.

In this example, at the fifth iteration the filter response exhibits common-mode rejection above 25 dB up to at least 2.5f0, as it can be observed in Figure 4.22 (d). Therefore, the algorithm stops at this fifth iteration, and the optimum common-mode and differential-mode transmission zeros are found, so that the optimum filter equivalent circuit can be already defined.

The comparison between the obtained differential-mode response using the optimum filter schematic (after the *Transmission Zeros* optimization algorithm) and the theoretical (ideal) Chebyshev response is depicted in Figure 4.23.

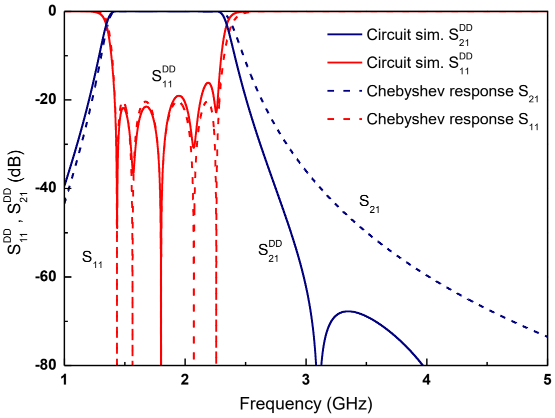

Figure 4.23. Comparison between the ideal Chebyshev response and the differential-mode response of the optimum schematic filter resulting from the *Transmission Zeros* optimization algorithm.

Although somehow degraded, the return loss in the pass band is acceptable on account of the improved filter selectivity beyond the upper cut-off frequency (upper transition band), and therefore the validity of this methodology, based on optimizing the location of the transmission zeros over the frequency band, is demonstrated.

Further information about this pre-optimization algorithm can be found in Article **TMTT18**, where this method is explained by following the same example but conducted in more detail.

Layout Generation by means of ASM

Once the optimum schematic is determined by the *Transmission Zeros* pre-optimization algorithm, the automatic filter layout generation from the lumped element values is carried out by means of two main ASM stages: 1) the *Interdigital Capacitor ASM* and 2) the *SIR ASM*. The flow diagram of the complete optimization scheme is presented in Figure 4.24.

At this point, the lumped elements of the interdigital capacitors are already known, and the specific ASM process for the determination of the layout giving such elements is necessary. As the interdigital capacitor topology used is equal to the one used in Section 4.2.1, the same coarse and fine spaces are defined in this ASM process. Hence, the variables in the optimization space are $\mathbf{x_c} = [L_{si}, C_{si}]$, whereas the variables in the validation space are the length of the inductive line, l_{Ls}, and the length of the fingers, l_f, i.e., $\mathbf{x_f} = [l_{Ls}, l_f]$. The first vector of the validation space, $\mathbf{x_f}^{(1)}$, providing the initial series resonator layout, is estimated from approximate formulas providing the inductance of a narrow inductive strip and the capacitance of an interdigital capacitor [14]. The following steps are to infer $\mathbf{x_c}^{(1)}$ from the initial layout EM simulation through the *parameter extraction* procedure carried out by means of equations (4.14) and (4.15), and to obtain the first approach to the Broyden matrix $\mathbf{B}^{(1)}$ by means of equation (4.20).

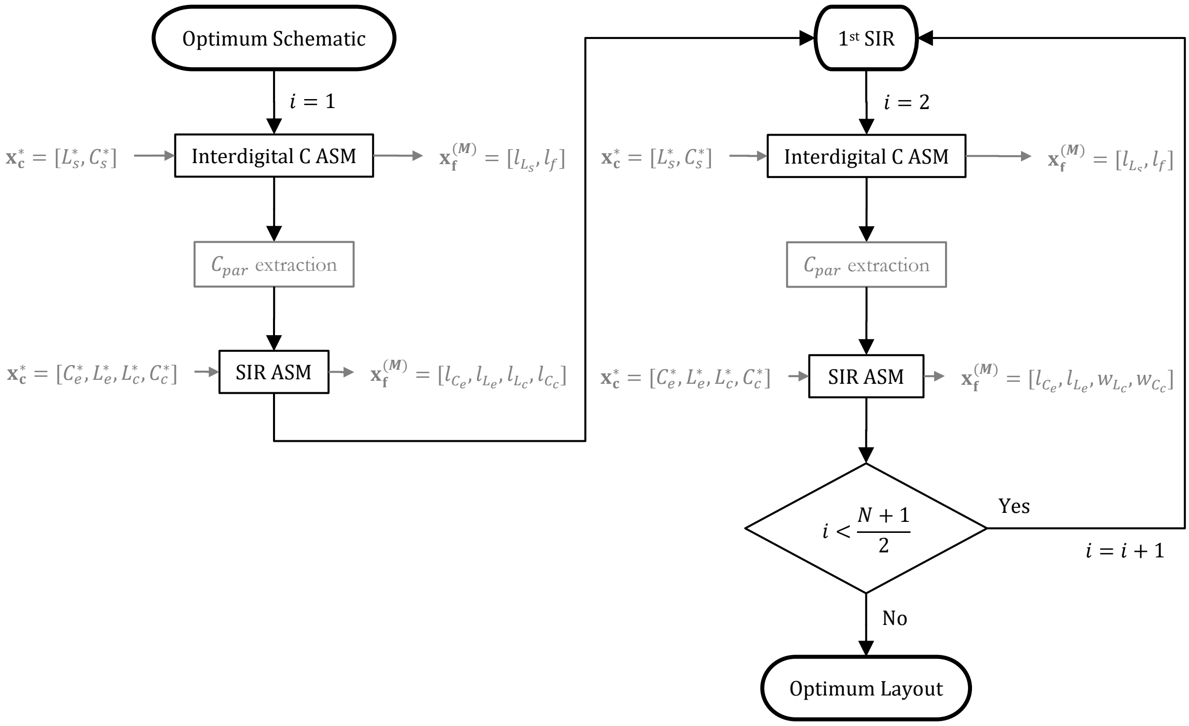

Figure 4.24. **NEMO17*** and **TMTT18** ASM block diagram.

Next, the layout of the multi-section mirrored SIRs is determined using an specific ASM algorithm where the coarse model vector is defined as $\mathbf{x_c} = [L_e, C_e, L_c, C_c]$, whose variables correspond to the circuit schematic for the common-mode depicted in Figure 4.20 (b). On the other hand, the fine model vector of the first mirrored SIR, i.e. $i = 1$, is constituted by a set of variables defining the resonator layout as detailed in Figure 4.20 (a) and it is defined as $\mathbf{x_f} = [l_{Le}, l_{Ce}, l_{Lc}, l_{Cc}]$. Therefore, in order to deal with the same number of variables in both spaces, the remaining physical parameters of the layout are set to fixed values.

On the other hand, since the mirrored SIR of this filter structure is equivalent to the one reported in Section 4.1.2, the first approach to the Broyden matrix, $\mathbf{B}^{(1)}$, necessary to iterate the process, is defined as described in equation (4.11), but uniquely for the first SIR. Similarly as previously described for the filter structure reported in Section 4.1.2, in the determination of the layout of the other mirrored SIRs, the *SIR ASM* sub-process to be applied will be based in the same principle than the first one, but considering as optimization variables of the validation space the widths for the inner sections (the ones between the pair of the interdigital capacitors inductive strips), and the lengths for the outer sections. By this means, the distance between the pair of interdigital capacitors is kept unaltered and allows the perfect alignment between all the layout resonator stages. Therefore, the coarse model vector of the rest of the mirrored SIRs is still defined as $\mathbf{x_c} = [L_e, C_e, L_c, C_c]$, but the fine model vector of these subsequent mirrored SIRs will correspond to $\mathbf{x_f} = [l_{Le}, l_{Ce}, w_{Lc}, w_{Cc}]$. Thus, the definition of the initial Broyden matrix for these resonators will be defined as shown previously in equation (4.12).

The initial SIR layout, corresponding to the first vector of the validation space, $\mathbf{x_f}^{(1)}$, is estimated in the same manner than reported previously, i.e. using approximate formulas providing the inductance and capacitance of a narrow and wide, respectively, electrically small transmission line sections [14]. Next, the four circuit elements can be extracted from the SIR layout electromagnetic response using the *parameter extraction* equations (4.22)-(4.25), and start the iterative process until find the final fine model vector $\mathbf{x_f}^{(M)}$ that describes the optimum SIR layout. This sequence will be repeated as many times as different resonators to be optimized, where for an odd-order Chebyshev response filter will correspond to $(N+1)/2$, being N the order of the filter.

Optimum Layout

To demonstrate the proposed approach, let us consider the same example presented previously when describing the *Transmission Zeros* optimization scheme, which consists on the synthesis of a balanced filter with the following specifications: $N = 5$, $f_0 = 1.8$ GHz, $FBW = 48\%$ (or 55.4% at 3-dB fractional bandwidth) and $L_{Ar} = 0.04$ dB. Once the optimum schematic is found by means of such *Transmission Zeros* optimization process and the ASM scheme shown in Figure 4.24 is executed, the optimum layouts for both the mirrored SIRs and the interdigital capacitors are obtained. Therefore, by cascading the five stages the complete filter layout is generated, worth to mention, by following a fully unattended process. The final layout is presented in Figure 4.25 (a) whereas the frequency response of the filter, including the simulation of the optimum schematic, electromagnetic simulation and measurement is depicted in Figure 4.25 (b) and (c) for the differential-mode and the common-mode respectively.

Despite the fact that the circuit model of the proposed filters provides a reasonable response in the region of interest, it can be appreciated in Figure 4.25 (c) that the common-mode resulting from lossy electromagnetic simulation (the response of interest) exhibits transmission peaks above -20 dB. The reason is that such peaks are very sensitive to the position of the transmission zeros, which may lead to some shift in the lossy electromagnetic simulation, as compared to the circuit response simulation. This phenomena has been already observed previously, during the description of the *Transmission Zeros* optimization scheme (see Figure 4.22).

Since common-mode rejection is not satisfactory enough, readjustment of the transmission zero positions is needed. To this end, a second *Transmission Zeros* optimization scheme has been developed, but this time the responses are not the circuit simulations of the resulting equivalent circuits, but the electromagnetic simulations (including losses) of the filter after the application of the ASM synthesis algorithm.

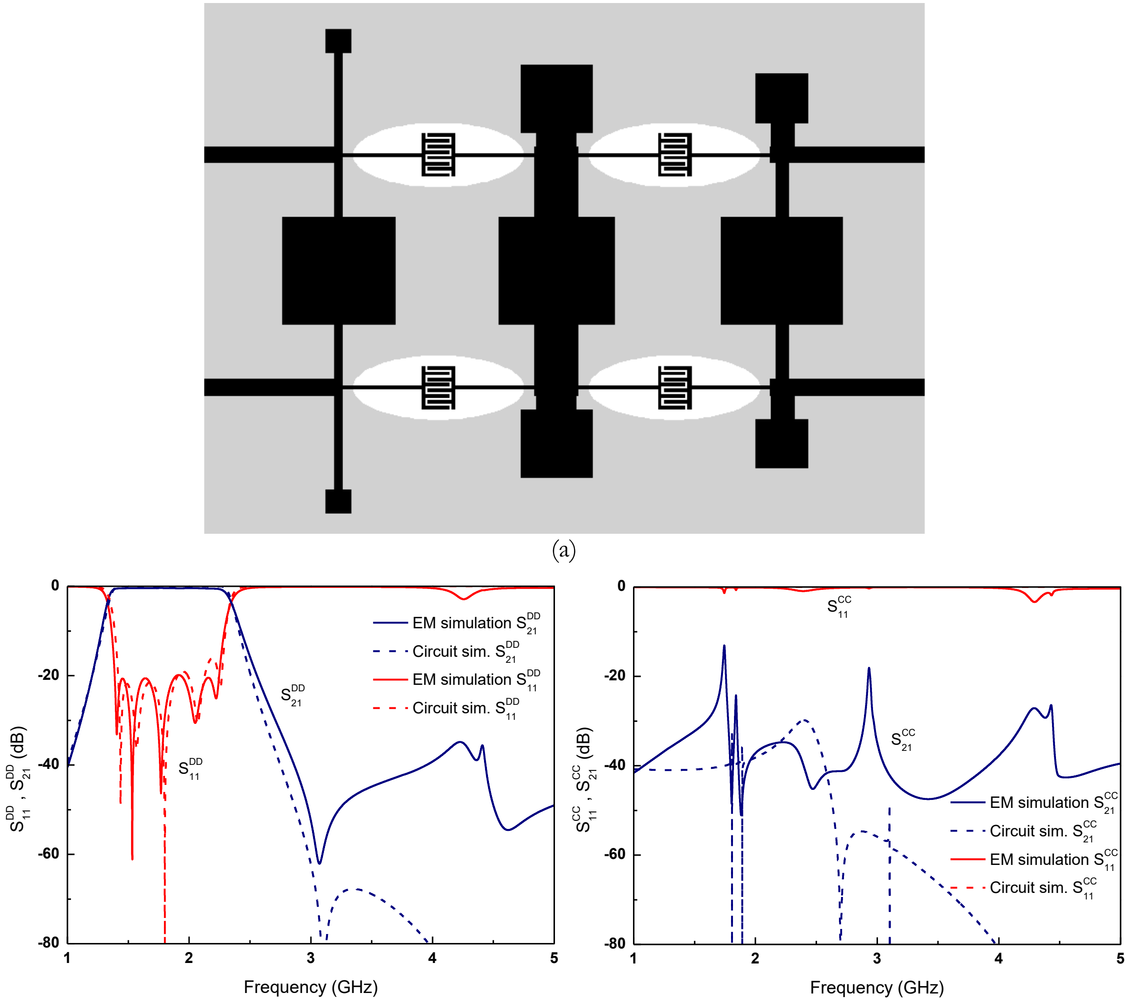

(a)

(b) (c)

Figure 4.25. **TMTT18** 5th order compact balanced wideband bandpass filter layout (a). Differential-mode (b) and common-mode (c) measured responses.

By applying this post-optimization iterative algorithm to the structure resulting from the first complete ASM scheme, we have been able (after three iterations) to obtain a filter layout exhibiting a common-mode rejection level better than -28 dB. Note that L_s, C_s, C_{par} and the geometry of the series resonators is kept unaltered in this post-optimization iterative process, since the readjustment of the transmission zeros does not affect the series branches. Figure 4.26 shows the comparison between the lossy EM simulation and the measurement of the synthesized filter layout responses, obtained after such *Transmission Zeros* post-optimization scheme. The filter is fabricated in a *Rogers RO4003C* substrate with thickness h = 813 µm, dielectric constant ε_r = 3.55 and loss tangent $tan\delta$ = 0.0021.

As can be observed, the agreement between the responses is good, although the measured in-band return loss for the differential-mode is a bit degraded as compared to the electromagnetic simulation. This degradation is due to tolerances in the fabrication process, considering that there is the need of very small gaps and track widths to form the interdigital capacitors, which is critical for the standard PCB technology process. Moreover, perfect symmetry is also difficult to achieve in practice, and there are two pairs of symmetric interdigital capacitors that make this aspect even more critical. Nevertheless, the measured in-band return loss (differential-mode) is better than 11.5 dB and the in-band insertion loss is better than 1dB. The differential-mode stop band exhibits a rejection level better than 22 dB up to at least 6.5 GHz and the common-mode is suppressed with a rejection level better than 28 dB from DC up to at least 6.5 GHz as well. Finally, filter size is as small as 51.5 mm × 48.2 mm, corresponding to $0.51\lambda_g \times 0.48\lambda_g$ in terms of the wavelength at the filter central frequency, f_0, which makes this combination of filter size and performance very competitive.

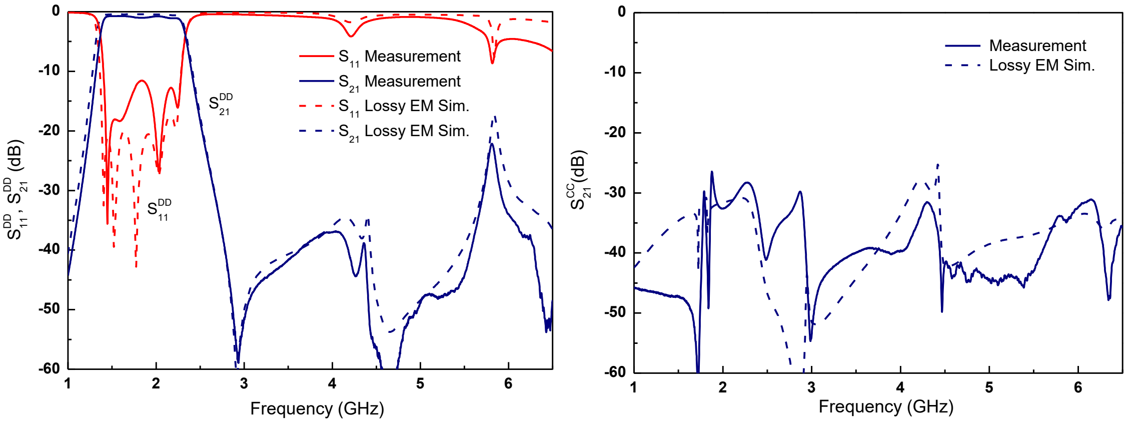

(b) (c)

Figure 4.26. **TMTT18** 5th order compact balanced wideband bandpass filter differential-mode (a) and common-mode (b) measured responses obtained after the post-*Transmission Zeros* optimization scheme.

Therefore, this example proves the automatic filter synthesis method under study, based on three specifically developed algorithms (an ASM-based algorithm preceded and followed by *Transmission Zeros* optimization algorithms), where few iterations suffice to achieve convergence in all three cases.

In Article **NEMO17***, an example of the automatic synthesis of the same filter structure is reported. In this case, the filter layout synthesis is focused on a 3rd order filter and it is developed uniquely by means of the ASM scheme reported in Figure 4.24. Thus, the response obtained for such filter is not fully optimized since the pre- and post- *Transmission Zeros* scheme have not been applied in this case.

Chapter 5

Conclusions and Future Work

The conclusions and future work that can be derived from this research work are discussed in this chapter. The achievements provided along the thesis, concerning the new concepts in microwave filter optimization and synthesized filter topologies, previously proven with valid and consistent results, are summarized. Moreover, an overview of further lines of research that can be initiated from this work are also outlined.

5.1 Conclusions

This thesis provides a significant contribution to the state of the art of the automatic design of microwave filters by means of ASM techniques, including the unattended synthesis of single-ended and balanced filters based on SIRs. The automatic and efficient EM optimization of microwave devices is a topic of growing interest in the microwave community, and more specially in the synthesis of balanced microwave filters since these components are very suitable for modern communications systems, despite their increased complexity as compared with their single-ended counterparts. Moreover, the combination of ASM techniques with the synthesis of balanced microwave filters is treated, to the best of our knowledge, for the first time in this thesis, which places this work in a pioneer position in this research field. The feasibility of the ASM concept applied to the automatic filter optimization has been demonstrated through the development of specific ASM algorithms driven by the filter topologies proposed in **Chapter 3** and **Chapter 4**. The validity of the algorithms developed has been proved by appropriate examples, and novel theoretical contributions to the ASM formulation have been introduced for such purpose. In addition, novel complex balanced filter structures, based on SIRs and interdigital capacitors, have been presented in order to overcome the narrowband limitations of the filters based on SIRs coupled through quarter-wavelength transmission lines.

In order to place the reader into context and provide the appropriate conceptual basis for the two main topics developed throughout this work, in **Chapter 2** an extensive state of the art revision concerning the ASM technique applied to microwave filter design has been provided, and the main novel aspects introduced by this research work have been highlighted. In addition, the fundamentals of the SM concept as well as the balanced and single-ended filter's theory have been thoroughly presented.

In **Chapter 3**, the validity of the ASM optimization scheme has been proved first in the automatic synthesis of a high order (and hence highly selective) single-ended wideband bandpass filter based on SIRs coupled through quarter-wavelength admittance inverters. It has been demonstrated that the developed ASM algorithm is able to synthesize such filter topology very efficiently and following a completely unattended scheme. Initially, the response degradation mainly derived from the bandwidth limitations of such admittance inverters has been compensated in this case by over dimensioning the filter design specifications in advance (mainly the filter's bandwidth, although the center frequency and the passband ripple have been slightly tuned as well). In order to overcome such inverters narrowband phenomena, a novel *Two-Step ASM* algorithm has been formulated for the first time. This strategy is based in a two-stage ASM scheme, where the first ASM is meant to obtain the optimum filter schematic that compensates such inverters bandwidth degradation, and the second ASM is meant to provide the optimum layout from the obtained optimum schematic, in such a way that the design filter specifications are satisfied automatically with no further manual interaction. The validity of the *Two-Step ASM* scheme has been demonstrated with several filter designs, including the automatic synthesis of a 9th order filter.

Due to the increased interest in the design of balanced microwave filters in recent years, **Chapter 4** is devoted to the automatic synthesis of balanced wideband bandpass filters based on SIRs. In this chapter the successful outcome of combining the ASM concept with the synthesis of balanced filters is presented for the first time. To the best of our knowledge, the application of automatic EM optimization techniques to the synthesis of balanced filters was not reported so far (at least in filters based on SIRs), placing this thesis as a pioneer in this field. Several balanced filter topologies have been used to prove the validity of the concept, all of them providing the differential-mode pass band response subjected to specifications while efficiently suppressing the common-mode at the same time, at least in the differential-mode passband frequency range. Two different filter topologies, both based on SIRs coupled through admittance inverters, have been automatically synthesized from specifications under the *Two-Step ASM* scheme proposed in **Chapter 3**. Successful results have been presented for both topologies, proving the validity and robustness of the *Two-Step ASM* concept also in balanced filters. Moreover, a novel balanced filter topology based on SIRs and interdigital capacitors has been presented. The main advantage of such topology is that the admittance inverters implemented through quarter-wave transmission lines are no longer used in this new filter structure. Thus, the narrowband effects inherent to these transmission line based admittance inverters are eliminated, so that there is no need to compensate for such inverter undesired effects by means of the *Two-Step ASM* scheme. Therefore, although the filter complexity is slightly increased due to the replacement of the quarter-wavelength transmission line inverters by those interdigital capacitors, the overall optimization process is notably simplified since the optimum filter schematic is directly inferred from the design specifications and only the ASM stage providing the optimum layout needs to be implemented, leading to a more efficient optimization scheme. Moreover, the overall filter size is also reduced because of the reduced size of the interdigital capacitors compared to the quarter-wavelength transmission lines. Nevertheless, due to the sensitivity of the interdigital capacitors (the PCB technology limits are challenged by the implementation of very narrow gaps between the interdigital fingers), a simple but very effective pre- and post- optimization algorithms have been introduced in order to obtain very competitive filter responses for this compact topology, which is able to provide a wideband bandpass differential-mode response with a very broad common- and differential-mode stopbands. The validity of this novel optimization scheme based on one-level ASM and pre- and post-optimization algorithms has been successfully demonstrated through the automatic synthesis of a 5th order filter.

In a nutshell, the initial objectives proposed for this research activity have been achieved. The ASM technique has been successfully applied to the unattended optimization of planar wideband bandpass filters from specifications. Novel contributions to the state of the art have been presented to the ASM formulation and an automatic balanced filters synthesis procedure has been successfully reported for the first time. Last but not least, a novel compact balanced filter topology based on SIRs and interdigital capacitors with very broad common- and differential-mode stopbands has been reported and automatically optimized through the appropriate ASM-based scheme.

5.2 Future Work

Future lines of research can arise from the aforementioned contributions and results provided in the present research work. It has been proven that the ASM concept is a simple and very efficient approach to automatically synthesize microwave filters from design specifications. Thus, a clear research path that can be further explored is the application of such ASM-based optimization scheme to single-ended or balanced filter structures implemented in different technologies, either planar as developed in this thesis or others least explored yet. For instance, further developments could be applied to the synthesis of filters based on metamaterial-inspired, SIW, DGS or coaxial resonators, to mention some of them. Moreover, regardless the technology used, the ASM technique could be applied to the automatic synthesis of filter devices providing more specific responses rather than wideband passband responses as reported in this work. For instance, bandstop, dual-band or UWB filter responses may be used as a target, while implemented in balanced topologies would be a plus. Going a bit further, the ASM technique could even be applied to the automatic synthesis of diplexers or even more complex filtering structures.

Another feasible research line that can be derived from this thesis is the application of the ASM to automatically synthesize other microwave passive structures such as directional couplers, splitters, combiners, matching networks, etc. The publications presented so far indicate that the versatility of the ASM algorithm makes it suitable to be applied to a very broad set of structures, independently of the technology used to implement them. Such research line would widen the application range of the space mapping concept, which for now its validity has been mostly demonstrated through the synthesis of microwave filters.

Last but not least, the whole optimization concept reported in the present thesis could potentially be translated into a design guide tool embedded into most generic CAD software packages, widely used in the microwave engineering community, such as Keysight® ADS or Ansys® HFSS, among others. The design guide might be envisioned as a set of different passive structures contained in a design guide palette, so that such structures can be automatically synthesized in order to fulfill a predefined set of design specifications, set by the user in advance, by means of the corresponding ASM-based optimization algorithm.

References

[1] S. Sun and L. Zhu, "Multimode-resonator-based bandpass filters," *IEEE Microw. Mag.*, vol. 10, no. 2, pp. 88–98, Apr. 2009.

[2] Z. Hao and J.-S. Hong, "Ultrawideband Filter Technologies," *IEEE Microw. Mag.*, vol. 11, no. 4, pp. 56–68, Jun. 2010.

[3] J. E. Rayas-Sanchez, "Power in simplicity with ASM: Tracing the aggressive space mapping algorithm over two decades of development and engineering applications," *IEEE Microw. Mag.*, vol. 17, no. 4, pp. 64–76, 2016.

[4] J. E. Rayas-Sanchez, "A historical account and technical reassessment of the Broyden-based input space mapping optimization algorithm," in *2017 IEEE MTT-S International Microwave Symposium (IMS)*, 2017, pp. 1495–1497.

[5] J. W. Bandler, R. M. Biernacki, S. H. Chen, P. A. Grobelny, and R. H. Hemmers, "Space mapping technique for electromagnetic optimization," *IEEE Trans. Microw. Theory Tech.*, vol. 42, no. 12, pp. 2536–2544, 1994.

[6] J. W. Bandler, Q. S. Cheng, S. A. Dakroury, A. S. Mohamed, M. H. Bakr, and K. Madsen, "Space Mapping: The State of the Art," *IEEE Trans. Microw. Theory Tech.*, vol. 52, no. 1, pp. 337–361, Jan. 2004.

[7] J. W. Bandler, R. M. Biernacki, S. H. Chen, R. H. Hemmers, and K. Madsen, "Electromagnetic optimization exploiting aggressive space mapping," *IEEE Trans. Microw. Theory Tech.*, vol. 43, no. 12, pp. 2874–2882, 1995.

[8] C. G. Broyden, "A Class of Methods for Solving Nonlinear Simultaneous Equations," *Math. Comput.*, vol. 19, pp. 577–593, 1965.

[9] J. Hong and M. J. Lancaster, *Microstrip Filters for RF/Microwave Applications*, 1st ed. John Wiley & Sons, Inc., 2002.

[10] W. Feng, W. Che, and Q. Xue, "The Proper Balance: Overview of Microstrip Wideband Balance Circuits with Wideband Common Mode Suppression," *IEEE Microw. Mag.*, vol. 16, no. 5, pp. 55–68, Jun. 2015.

[11] F. Martín, L. Zhu, J. Hong, and F. Medina, *Balanced Microwave Filters*, 1st ed. John Wiley & Sons, Inc., 2018.

[12] R. Mongia, I. Bahl, and P. Bhartia, *RF and Microwave Coupled Line Circuits*, 1st ed. Artech

House, 1999.

[13] D. E. Bockelman and W. R. Eisenstadt, "Combined differential and common-mode scattering parameters: theory and simulation," *IEEE Trans. Microw. Theory Tech.*, vol. 43, no. 7, pp. 1530–1539, Jul. 1995.

[14] D. M. Pozar, *Microwave Engineering*, 4th ed. John Wiley & Sons, Inc., 2011.

[15] J. W. Bandler, R. M. Biernacki, S. H. Chen, R. H. Hemmers, and K. Madsen, "Aggressive space mapping for electromagnetic design," in *Proceedings of 1995 IEEE MTT-S International Microwave Symposium*, 1995, pp. 1455–1458.

[16] K.-L. Wu, Y.-J. Zhao, J. Wang, and M. K. K. Cheng, "An Effective Dynamic Coarse Model for Optimization Design of LTCC RF Circuits With Aggressive Space Mapping," *IEEE Trans. Microw. Theory Tech.*, vol. 52, no. 1, pp. 393–402, Jan. 2004.

[17] M. A. Ismail, D. Smith, A. Panariello, Y. Wang, and M. Yu, "EM-Based Design of Large-Scale Dielectric-Resonator Filters and Multiplexers by Space Mapping," *IEEE Trans. Microw. Theory Tech.*, vol. 52, no. 1, pp. 386–392, Jan. 2004.

[18] J. Xu, X. Luo, L. zu Cao, and R. shan Chen, "Optimization of coaxial dielectric resonator filter with aggressive space mapping," in *2012 Asia Pacific Microwave Conference Proceedings*, 2012, pp. 229–231.

[19] Hong-Soon Choi, Dong-Hun Kim, Il-Han Park, and Song-Yop Hahn, "A new design technique of magnetic systems using space mapping algorithm," *IEEE Trans. Magn.*, vol. 37, no. 5, pp. 3627–3630, 2001.

[20] G. Crevecoeur, H. Hallez, P. Van Hese, Y. D'Asseler, and R. Van de Walle, "EEG source analysis using space mapping techniques," *J. Comput. Appl. Math.*, vol. 215, no. 2, pp. 339–347, Jun. 2008.

[21] T. Slawig and M. Prieß, "Surrogate-Based Optimization for Marine Ecosystem Models," *Int. J. Math. Model. Numer. Optim.*, vol. 3, 2012.

[22] M. Redhe and L. Nilsson, "Optimization of the new Saab 9-3 exposed to impact load using a space mapping technique," *Struct. Multidiscip. Optim.*, vol. 27, no. 5, pp. 411–420, Jul. 2004.

[23] G. Crevecoeur, L. Dupre, L. Vandenbossche, and R. Van de Walle, "Reconstruction of local magnetic properties of steel sheets by needle probe methods using space mapping techniques," *J. Appl. Phys.*, vol. 99, no. 8, p. 08H905, Apr. 2006.

[24] J. V. Morro, H. Esteban, P. Soto, V. E. Boria, C. Bachiller, and M. Taroncher, "Fast automated design of waveguide filters using aggressive space mapping with a new segmentation strategy and a hybrid optimization algorithm," *IEEE Trans. Microw. Theory Tech.*, vol. 53, no. 4, pp. 1130–1142, Apr. 2005.

[25] M. Brumos, V. E. Boria, M. Guglielmi, and S. Cogollos, "Correction of Manufacturing Deviations in Waveguide Filters and Manifold Multiplexers without Tuning Screws," *Int. J. Microw. Wirel. Technol.*, vol. 7, no. 3, pp. 219–227, 2015.

[26] Z.-C. Hao, W. Ding, and W. Hong, "Developing Low-Cost W-Band SIW Bandpass Filters Using the Commercially Available Printed-Circuit-Board Technology," *IEEE Trans. Microw. Theory Tech.*, vol. 64, no. 6, pp. 1775–1786, Jun. 2016.

[27] J. W. Bandler, R. M. Biernacki, S. H. Chen, and D. Omeragic, "Space mapping optimization of waveguide filters using finite element and mode-matching electromagnetic simulators," in *IEEE MTT-S International Microwave Symposium Digest*, 1997, vol. 2, pp. 635–638.

[28] R. Lehmensiek and P. Meyer, "An Efficient Adaptive Frequency Sampling Algorithm for Model-based Parameter Estimation as applied to Aggressive Space Mapping," *Microw. Opt. Technol. Lett.*, vol. 24, no. 1, pp. 71–78, 1999.

[29] J. V. Morro, H. Esteban, P. Soto, V. E. Boria, C. Bachiller, and S. Cogollos, "Automated design of waveguide filters using Aggressive Space Mapping with a segmentation strategy and hybrid optimization techniques," in *IEEE MTT-S International Microwave Symposium Digest, 2003*, 2003, pp. 1215–1218.

[30] J. V. Morro, H. Esteban, V. E. Boria, C. Bachiller, and A. Coves, "New multimodel aggressive space mapping technique for the efficient design of complex microwave circuits," in *IEEE MTT-S International Microwave Symposium Digest, 2005.*, 2005, pp. 1613–1616.

[31] J. W. Bandler, R. M. Biernacki, Shao Hua Chen, and Ya Fei Huang, "Design optimization of interdigital filters using aggressive space mapping and decomposition," *IEEE Trans. Microw. Theory Tech.*, vol. 45, no. 5, pp. 761–769, May 1997.

[32] Q. S. Cheng, J. W. Bandler, and S. Koziel, "A Simple ADS Schematic for Space Mapping," in *2009 International Microwave Workshop Series on Signal Integrity and High-Speed Interconnects*, 2009, pp. 35–38.

[33] M. H. Bakr, J. W. Bandler, N. Georgieva, and K. Madsen, "A hybrid aggressive space-mapping algorithm for EM optimization," *IEEE Trans. Microw. Theory Tech.*, vol. 47, no. 12, pp. 2440–2449, 1999.

[34] M. H. Bakr, J. W. Bandler, K. Madsen, J. E. Rayas-Sanchez, and J. Sondergaard, "Space-mapping optimization of microwave circuits exploiting surrogate models," *IEEE Trans. Microw. Theory Tech.*, vol. 48, no. 12, pp. 2297–2306, 2000.

[35] M. H. Bakr, J. W. Bandler, R. M. Biernacki, Shao Hua Chen, and K. Madsen, "A trust region aggressive space mapping algorithm for EM optimization," *IEEE Trans. Microw. Theory Tech.*, vol. 46, no. 12, pp. 2412–2425, 1998.

[36] J. W. Bandler, A. S. Mohamed, M. H. Bakr, K. Madsen, and J. Sondergaard, "EM-based optimization exploiting partial space mapping and exact sensitivities," *IEEE Trans. Microw. Theory Tech.*, vol. 50, no. 12, pp. 2741–2750, Dec. 2002.

[37] J. E. Rayas-Sanchez and V. Gutierrez-Ayala, "EM-Based Monte Carlo Analysis and Yield Prediction of Microwave Circuits Using Linear-Input Neural-Output Space Mapping," *IEEE Trans. Microw. Theory Tech.*, vol. 54, no. 12, pp. 4528–4537, Dec. 2006.

[38] H. Wang, A. Zhang, and D. Fang, "The Design of Cross-Coupled Microstrip Filter Exploiting Aggressive Space Mapping Technique," in *Asia-Pacific Microwave Conference Proceedings*, 2005, vol. 5, pp. 1–3.

[39] J. Selga, A. Rodriguez, V. E. Boria, and F. Martin, "Synthesis of Split-Rings-Based Artificial Transmission Lines Through a New Two-Step, Fast Converging, and Robust Aggressive Space Mapping (ASM) Algorithm," *IEEE Trans. Microw. Theory Tech.*, vol. 61, no. 6, pp. 2295–2308, Jun. 2013.

[40] Q. Deng, T. Fan, and S. Lu, "The design of Ka band filter with active space mapping algorithm," in *Proceedings of 2014 3rd Asia-Pacific Conference on Antennas and Propagation*, 2014, pp. 1140–1143.

[41] F. Xiaolin and P. D. Laforge, "Design of a chebyshev microstrip filter using the reflected group delay method and the aggressive space mapping technique," in *2015 IEEE MTT-S International Microwave Symposium*, 2015, pp. 1–4.

[42] A. Rodríguez, V. E. Boria, J. Selga, M. Sans, and F. Martin, "Synthesis of open complementary split ring resonators (OCSRRs) through aggressive space mapping (ASM) and application to bandpass filters," in *European Microwave Week 2014: Connecting the Future, EuMW 2014 - Conference Proceedings; EuMC 2014: 44th European Microwave Conference*, 2014, pp. 323–326.

[43] J. Selga, P. Velez, M. Sans, A. Rodriguez, V. E. Boria, and F. Martin, "Size reduction

and spurious suppression in microstrip coupled line bandpass filters by means of capacitive electromagnetic bandgaps," in *IEEE MTT-S International Microwave Symposium Digest*, 2016, vol. 2016–Augus.

[44] M. Orellana, J. Selga, M. Sans, A. Rodriguez, V. E. Boria, and F. Martin, "Design of Capacitively Loaded Coupled-Line Bandpass Filters with Compact Size and Spurious Suppression," *IEEE Trans. Microw. Theory Tech.*, vol. 65, no. 4, pp. 1235–1248, 2017.

[45] W. Tang, P. Zhou, X. Chen, and Y. L. Chow, "Design and Optimization of Microstrip Passive Circuits by Field-Based Equivalent Circuit Model with Aggressive Space Mapping," in *2007 International Symposium on Microwave, Antenna, Propagation and EMC Technologies for Wireless Communications*, 2007, pp. 909–912.

[46] W. Tang, P. Zhou, X. Chen, and Y. L. Chow, "Design and Optimization of Stripline Passive Components With Trust-region Aggressive Space Mapping," in *2007 Asia-Pacific Microwave Conference*, 2007, pp. 1–4.

[47] J. Wu, Y. Dong, J. He, and J. Deng, "An ameliorated aggressive space mapping based on responses error," in *The 2012 International Workshop on Microwave and Millimeter Wave Circuits and System Technology*, 2012, pp. 1–4.

[48] J. Selga, J. Naqui, M. Durán-Sindreu, F. Martín, A. Rodríguez, and V. E. Boria, "Application of Aggressive Space Mapping (ASM) to the Efficient Synthesis of Stepped Impedance Resonators (SIRs)," 2013.

[49] J. Selga, A. Rodríguez, M. Gil, J. Carbonell, V. E. Boria, and F. Martín, "Synthesis of Planar Microwave Circuits Through Aggressive Space Mapping Using Commercially Available Software Packages," vol. 20, pp. 527–534, 2010.

[50] A. Rodríguez, J. Selga, M. Sans, F. Martín, and V. Boria, "Automated design of bandpass filters based on open complementary split ring resonators (OCSRRs) using aggressive space mapping (ASM) optimization," *Int. J. Numer. Model. Electron. Networks, Devices Fields*, vol. 30, no. 3–4, p. e2121, May 2017.

[51] J. Bonache, I. Gil, J. Garcia, and F. Martín, "Compact microstrip band-pass filters based on semi-lumped resonators," *IET Microw. Ant. Propag.*, vol. 1, pp. 932–936, 2007.

[52] P. Velez, J. Naqui, A. Fernandez-Prieto, M. Duran-Sindreu, F. Medina, and F. Martin, "Differential bandpass filters with common-mode suppression based on stepped impedance resonators (SIRs)," in *2013 IEEE MTT-S International Microwave Symposium Digest (MTT)*, 2013, pp. 1–4.

[53] P. Velez, J. Selga, M. Sans, J. Bonache, and F. Martin, "Design of differential-mode wideband bandpass filters with wide stop band and common-mode suppression by means of multisection mirrored stepped impedance resonators (SIRs)," in *2015 IEEE MTT-S International Microwave Symposium, IMS 2015*, 2015.

[54] C.-H. Wu, C.-H. Wang, and C. H. Chen, "Stopband-Extended Balanced Bandpass Filter Using Coupled Stepped-Impedance Resonators," *IEEE Microw. Wirel. Components Lett.*, vol. 17, no. 7, pp. 507–509, Jul. 2007.

[55] P. Velez, J. Naqui, A. Fernandez-Prieto, J. Mata-Contreras, F. Medina, and F. Martín, "Ultra-Compact (80mm2) Differential-Mode Ultra-Wideband (UWB) Bandpass Filters With Common-Mode Noise Suppression," *IEEE Trans. Microw. Theory Tech.*, vol. 63, no. 4, pp. 1272–1280, Apr. 2015.

[56] P. Velez, J. Naqui, A. Fernandez-Prieto, M. Duran-Sindreu, F. Medina, and F. Martín, "Differential Bandpass Filter With Common-Mode Suppression Based on Open Split Ring Resonators and Open Complementary Split Ring Resonators," *IEEE Microw. Wirel. Components Lett.*, vol. 23, no. 1, pp. 22–24, Jan. 2013.

[57] A. K. Horestani, M. Duran-Sindreu, J. Naqui, C. Fumeaux, and F. Martin, "S-Shaped

Complementary Split Ring Resonators and Their Application to Compact Differential Bandpass Filters With Common-Mode Suppression," *IEEE Microw. Wirel. Components Lett.*, vol. 24, no. 3, pp. 149–151, Mar. 2014.

[58] L. Li, J. Bao, J.-J. Du, and Y.-M. Wang, "Compact Differential Wideband Bandpass Filters With Wide Common-Mode Suppression," *IEEE Microw. Wirel. Components Lett.*, vol. 24, no. 3, pp. 164–166, Mar. 2014.

[59] W. Feng, W. Che, Y. Ma, and Q. Xue, "Compact Wideband Differential Bandpass Filters Using Half-Wavelength Ring Resonator," *IEEE Microw. Wirel. Components Lett.*, vol. 23, no. 2, pp. 81–83, Feb. 2013.

[60] H. Wang, L.-M. Gao, K.-W. Tam, W. Kang, and W. Wu, "A Wideband Differential BPF With Multiple Differential- and Common-Mode Transmission Zeros Using Cross-Shaped Resonator," *IEEE Microw. Wirel. Components Lett.*, vol. 24, no. 12, pp. 854–856, Dec. 2014.

[61] J. G. Zhou, W. Che, and Y.-C. Chiang, "Compact wideband balanced bandpass filter with high common-mode suppression based on cascade parallel coupled lines," *IET Microwaves, Antennas Propag.*, vol. 8, no. 8, pp. 564–570, Jun. 2014.

[62] X.-H. Wu, Q.-X. Chu, and L.-L. Qiu, "Differential Wideband Bandpass Filter With High-Selectivity and Common-Mode Suppression," *IEEE Microw. Wirel. Components Lett.*, vol. 23, no. 12, pp. 644–646, Dec. 2013.

[63] W. Feng and W. Che, "Novel Wideband Differential Bandpass Filters Based on T-Shaped Structure," *IEEE Trans. Microw. Theory Tech.*, vol. 60, no. 6, pp. 1560–1568, Jun. 2012.

[64] W. Che, Q. Xue, W. Feng, and L. Gu, "High-selectivity wideband balanced bandpass filters using symmetrical multi-mode resonators," *IET Microwaves, Antennas Propag.*, vol. 7, no. 12, pp. 1005–1015, Sep. 2013.

[65] L. Li, J. Bao, J.-J. Du, and Y.-M. Wang, "Differential Wideband Bandpass Filters With Enhanced Common-Mode Suppression Using Internal Coupling Technique," *IEEE Microw. Wirel. Components Lett.*, vol. 24, no. 5, pp. 300–302, May 2014.

[66] T. B. Lim and L. Zhu, "A Differential-Mode Wideband Bandpass Filter on Microstrip Line for UWB Applications," *IEEE Microw. Wirel. Components Lett.*, vol. 19, no. 10, pp. 632–634, Oct. 2009.

[67] T. B. Lim and L. Zhu, "Differential-mode ultra-wideband bandpass filter on microstrip line," *Electron. Lett.*, vol. 45, no. 22, p. 1124, 2009.

[68] J. Shi, C. Shao, J.-X. Chen, Q.-Y. Lu, Y. Peng, and Z.-H. Bao, "Compact Low-Loss Wideband Differential Bandpass Filter With High Common-Mode Suppression," *IEEE Microw. Wirel. Components Lett.*, vol. 23, no. 9, pp. 480–482, Sep. 2013.

[69] X. Guo, L. Zhu, K.-W. Tam, and W. Wu, "Wideband Differential Bandpass Filters on Multimode Slotline Resonator With Intrinsic Common-Mode Rejection," *IEEE Trans. Microw. Theory Tech.*, vol. 63, no. 5, pp. 1587–1594, May 2015.

[70] S. Shi, W.-W. Choi, W. Che, K.-W. Tam, and Q. Xue, "Ultra-Wideband Differential Bandpass Filter With Narrow Notched Band and Improved Common-Mode Suppression by DGS," *IEEE Microw. Wirel. Components Lett.*, vol. 22, no. 4, pp. 185–187, Apr. 2012.

[71] J. Naqui, M. Durán-Sindreu, J. Bonache, and F. Martín, "Implementation of shunt-connected series resonators through stepped-impedance shunt stubs: analysis and limitations," *IET Microwaves, Antennas Propag.*, vol. 5, no. 11, p. 1336, 2011.

[72] J. W. Bandler, Q. S. Cheng, D. M. Hailu, and N. K. Nikolova, "A Space-Mapping Design Framework," *IEEE Trans. Microw. Theory Tech.*, vol. 52, no. 11, pp. 2601–2610,

Nov. 2004.

[73] R. Kshetrimayum, “An introduction to UWB communication systems,” *IEEE Potentials*, vol. 28, no. 2, pp. 9–13, Mar. 2009.

PhD Thesis Main Articles

Fundamental Articles

TMTT14: M. Sans, J. Selga, A. Rodríguez, J. Bonache, V. E. Boria, and F. Martín, "Design of planar wideband bandpass filters from specifications using a two-step aggressive space mapping (ASM) Optimization Algorithm" *IEEE Trans. Microw. Theory Tech.*, vol. 62, no. 12, pp. 3341–3350, Dec. 2014.

TMTT15: M. Sans, J. Selga, P. Vélez, A. Rodríguez, J. Bonache, V. E. Boria, and F. Martín, "Automated Design of Common-Mode Suppressed Balanced Wideband Bandpass Filters by Means of Aggressive Space Mapping", *IEEE Trans. Microw. Theory Tech.*, vol. 63, no. 12, pp. 3896–3908, Dec. 2015.

IJMWT16: M. Sans, J. Selga, P. Vélez, A. Rodríguez, J. Bonache, V. E. Boria, and F. Martín, "Automated design of balanced wideband bandpass filters based on mirrored stepped impedance resonators (SIRs) and interdigital capacitors", *Int. J. Microw. Wirel. Technol.*, vol. 8, no. 4–5, pp. 731–740, June 2016.

TMTT18: M. Sans, J. Selga, P. Vélez, A. Rodríguez, J. Bonache, V. E. Boria, and F. Martín, "Compact Wideband Balanced Bandpass Filters with Very Broad Common-Mode and Differential-Mode Stopbands" *IEEE Trans. Microw. Theory Tech.*, vol. 66, pp. 737–750, Feb. 2018.

Non-Fundamental Articles

IMS14[*]: J. Selga, M. Sans, J. Bonache, A. Rodríguez, V. E. Boria, and F. Martín, "Automated synthesis of planar wideband bandpass filters based on stepped impedance resonators (SIRs) and shunt stubs through aggressive space mapping (ASM)", *IEEE MTT-S International Microwave Symposium Digest* (IMS'14), Tampa, FL (USA), June 2014.

EUMC15[*]: M. Sans, J. Selga, P. Vélez, J. Bonache, A. Rodríguez, V. E. Boria, and F. Martín, "Application of aggressive space mapping (ASM) to the automated design of differential-mode wideband bandpass filters with common-mode suppression", *European Microwave Conference Proceedings* (EuMC'15), Paris (France), Sept. 2015.

SPMS16[*]: M. Sans, J. Selga, A. Rodríguez, P. Vélez, V. E. Boria, J. Bonache, and F. Martín, "Unattended design of wideband planar filters using a two-step aggressive space mapping (ASM) optimization algorithm", Koziel S., Leifsson L., Yang XS. (eds) Simulation-Driven Modeling and Optimization. *Springer Proceedings in Mathematics and Statistics*, vol. 153, pp. 135–159, Feb. 2016.

NEMO17[*]: M. Sans, J. Selga, P. Vélez, A. Rodríguez, J. Bonache, V. E. Boria, and F. Martín, "Optimized wideband differential-mode bandpass filters with broad stopband and common-mode suppression based on multi-section stepped impedance resonators and interdigital capacitors", *IEEE MTT-S International Conference on Numerical Electromagnetic and Multiphysics Modeling and Optimization for RF, Microwave, and Terahertz Applications* (NEMO'17), Seville (Spain), May 2017.

---

[*] Conference articles and book chapter are included in this thesis for completeness but are not considered as a fundamental part of the thesis articles compendium.

IMS14*

J. Selga, M. Sans, J. Bonache, A. Rodríguez, V. E. Boria, and F. Martín

"Automated Synthesis of Planar Wideband Bandpass Filters based on Stepped Impedance Resonators (SIRs) and Shunt Stubs through Aggressive Space Mapping (ASM)"

Automated Synthesis of Planar Wideband Bandpass Filters based on Stepped Impedance Resonators (SIRs) and Shunt Stubs through Aggressive Space Mapping (ASM)

Jordi Selga[1], Marc Sans[1], Jordi Bonache[1], Ana Rodriguez[2], Vicente E. Boria[2], and Ferran Martín[1]

[1]GEMMA/CIMITEC, Departament d'Enginyeria Electrònica, Universitat Autònoma de Barcelona, Bellaterra, 08193, Spain.

[2] Departamento de Comunicaciones-iTEAM, Universidad. Politécnica de Valencia, 46022, Spain.

Abstract — This paper is focused on the automated synthesis of wideband bandpass filters by means of aggressive space mapping (ASM). The considered filters are microstrip filters implemented through a combination of shunt connected stepped impedance resonators (SIRs) and grounded stubs coupled through impedance inverters. By virtue of the transmission zeros introduced by the shunt connected SIRs, the filters exhibit a wide rejection band with strong attenuation. The main contribution and originality of the paper is the fact that the layout of the whole filter is automatically generated from the circuit schematic without human intervention in the process. In a first step, the ASM algorithm is applied to the SIR/stub resonators and inverters. After that, each filter cell is automatically generated, and no further optimization is required. As an example, the synthesis of an order-7 bandpass filter is reported. The agreement between the electromagnetic response of the synthesized filter and the target response is very good, pointing out the validity of the proposed synthesis approach.

Index Terms — Space Mapping, bandpass filters, stepped impedance resonators, microstrip technology.

I. INTRODUCTION

Space mapping is a technique extensively used for the synthesis of microwave devices [1]-[3]. Such technique makes use of two simulation spaces: in the optimization space, $\mathbf{X}_c$, the variables are linked to a coarse model, which is simple and computationally efficient, although not accurate; in the validation space, $\mathbf{X}_f$, the variables are linked to a fine model, typically more complex and CPU intensive, but significantly more precise. In each space, a vector containing the different model parameters is defined. These vectors are designated as $\mathbf{x}_\mathbf{f}$ and $\mathbf{x}_c$ for the fine and coarse model parameters, respectively, and their responses are denoted as $\mathbf{R}_f(\mathbf{x}_f)$ and $\mathbf{R}_c(\mathbf{x}_c)$. In planar microwave circuits, the vectors $\mathbf{x}_f$ and $\mathbf{x}_c$ typically contain a set of geometric and circuit parameters, respectively, whereas the model responses are related to the evaluation of the device behaviour, e.g., a scattering parameter, such as S_{11} or S_{21}, computed in a certain frequency range.

In this work, the objective is to apply the so-called Aggressive Space Mapping (ASM) [2] to the automated synthesis of microstrip bandpass filters implemented by a combination of stepped impedance resonators (SIRs), shunt stubs, and impedance inverters. Using these filters, formerly reported in [4], wideband responses with significant attenuation in the stop band can be achieved. The proposed ASM algorithm is a two-step process, where the layouts of the different filter elements constituting each cell (resonator and inverter) are first generated; after that, the ASM technique is applied to the automated generation of the different filter cells. The key aspect of the present approach is that after this second step the different filter stages are cascaded and no further optimization is required to achieve the target response.

II. TOPOLOGY OF THE PROPOSED FILTERS AND CIRCUIT SCHEMATIC

The filters considered in this work are implemented through a combination of semi-lumped and distributed elements (see Fig. 1) [4]. The semi-lumped elements are shunt-connected SIRs and grounded stubs. The SIRs are described by means of shunt-connected series resonators (with capacitance C_r and inductance L_r) to a very good approximation [5], whereas the shunt stubs (grounded through vias) are modeled by a shunt inductance L_p. The distributed elements are quarter wavelength transmission lines acting as impedance inverters at the central filter frequency. It is noteworthy that the SIRs introduce transmission zeros above the filter pass band, useful to improve the frequency selectivity and rejection in the stop band. Moreover, with such filter topology, wideband bandpass responses are possible since the required susceptance slopes are easily achievable thanks to the flexibility offered by the stub/SIR combination as a three-element shunt resonator.

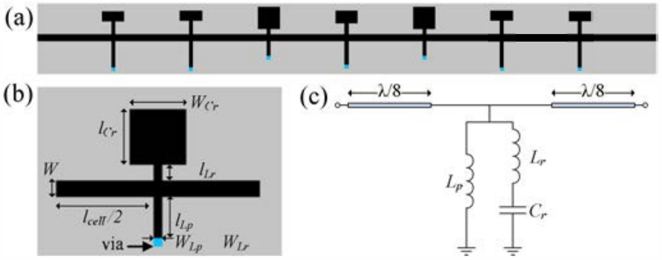

Fig. 1. Typical topology (order-7) of the considered wideband microstrip filters (a), topology of the filter cell and relevant dimensions (b), and circuit schematic of a filter cell (c).

III. AUTOMATIC LAYOUT SYNTHESIS THROUGH ASM

The design process of the considered filters has two stages. In the first stage, the circuit schematic that provides the target response (optimization space) must be determined. Once the filter elements are known, the second stage consists on the synthesis of the layout giving the target response in the validation space, inferred through electromagnetic simulation with commercial solvers (*Agilent Momentum* was used). This work is focused on this second aspect, i.e., the automatic determination of the filter layout from the elements of the circuit schematic by using specific ASM algorithms.

A. Filter schematic

Let us consider the synthesis of an order-7 bandpass filter with the following specifications: central frequency, $f_0 = 3.87$ GHz, 3dB fractional bandwidth, $FBW = 52\%$ (i.e., 3GHz-5GHz), in-band return loss better than 10 dB, and, finally, the transmission zero frequency located at $f_z = 8$GHz (this provides good stop band selectivity and spurious suppression). To determine the schematic of the filter providing such specifications, we have used an iterative process. The elements at each iteration step are inferred from the susceptance slope and central frequency corresponding to a Chebyshev response, where the nominal fractional bandwidth is iteratively updated (the transmission zero frequency allows us to univocally determine the three circuit elements of each filter cell). The initial fractional bandwidth is over dimensioned due to the narrowing effects caused by the limited functionality of the inverters (the inverters are simply quarter wavelength transmission lines at f_0 with normalized impedance $K = 1$, i.e., $Z_0 = 50\ \Omega$). The nominal fractional bandwidth is iteratively updated by comparing the resulting fractional bandwidth of the previous iteration (inferred from circuit simulation) with the target value. The process ends once the target filter bandwidth is achieved.

By applying the previous procedure (the details of the iteration process are out of the scope of this paper), the circuit elements of the 7-order filter were inferred (see table I). The circuit simulation inferred by cascading ideal 50 Ω quarter wavelength transmission lines between the resonator stages is depicted in Fig. 2, where it can be appreciated that the above specifications are satisfied.

TABLE I. FILTER ELEMENT VALUES

	Filter stage			
	1 , 7	**2 , 6**	**3 , 5**	**4**
L_r (nH)	0.5155	0.5132	0.3108	0.4715
C_r (pF)	0.7678	0.7711	1.2733	0.8394
L_p (nH)	1.5464	1.5397	0.9325	1.4146

B. Automated layout synthesis

The next step, and main contribution of this work, is the determination of the layout of each filter stage, composed by the shunt connected SIR/stub resonator inserted between a pair of λ/8 lines.

In the first step, the SIR/stub resonator and line topologies are determined through specific ASM algorithms developed in MATLAB®. ASM [2] is an advanced space mapping optimization technique that uses a quasi-Newton type iteration to find the target solution. The goal in ASM is to solve the following set of non-linear equations

$$\mathbf{f}(\mathbf{x}_f) = \mathbf{P}(\mathbf{x}_f) - \mathbf{x}_c^* = 0 \tag{1}$$

where $\mathbf{x}_c^*$ is the vector that contains the target circuit elements, and $\mathbf{P}(\mathbf{x}_f)$ is a function that gives the circuit parameters extracted from the electromagnetic response of the layout.

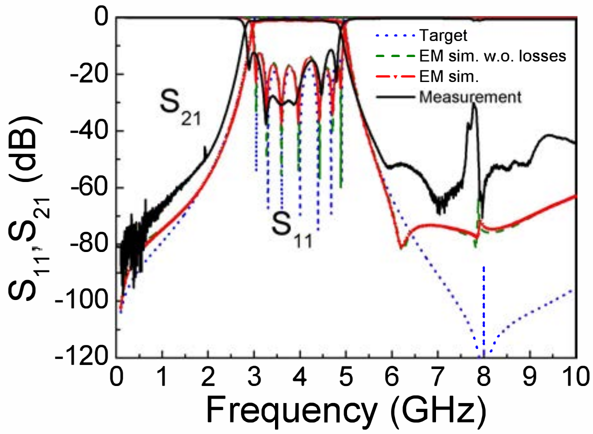

Fig. 2. Frequency response of the synthesized order-7 filter, including circuit simulation, electromagnetic simulation with and without losses, and measurement. The layout of the fabricated filter is the one depicted in Fig. 1(a).

For the SIR/stub resonator, $\mathbf{x}_f$ is a vector that contains the lengths l_{Cr} and l_{Lr} of the low- and high-impedance transmission line sections, respectively, of the SIR, and l_{Lp}, the length of the shunt stub. The widths are set to certain values (i.e., $W_{Cr} = 2$ mm and $W_{Lr} = W_{Lp} = 0.3$ mm) to reduce the number of free parameters [see Fig. 1 (b)]. Assuming that $\mathbf{x}_f^{(j)}$ is the j-th approximation to the solution of (1), and $\mathbf{f}^{(j)}$ the error function corresponding to $\mathbf{f}(\mathbf{x}_f^{(j)})$. The next vector of the iterative process $\mathbf{x}_f^{(j+1)}$ is found by a quasi-Newton iteration, i.e.,

$$\mathbf{x}_f^{(j+1)} = \mathbf{x}_f^{(j)} + \mathbf{h}^{(j)} \tag{2}$$

where $\mathbf{h}^{(j)}$ is given by:

$$\mathbf{B}^{(j)}\mathbf{h}^{(j)} = -\mathbf{f}^{(j)} \tag{3}$$

and $\mathbf{B}^{(j)}$ is an approach to the Broyden matrix [2]:

$$\mathbf{B}^{(j+1)} = \mathbf{B}^{(j)} + \frac{\mathbf{f}^{(j+1)}\mathbf{h}^{(j)T}}{\mathbf{h}^{(j)T}\mathbf{h}^{(j)}} \tag{4}$$

which is also updated at each iterative step. In (4), $\mathbf{f}^{(j+1)}$ is obtained by evaluating (1) using a certain parameter extraction method providing the circuit elements from the layout. Specifically, the circuit parameters of the SIR/stub resonator

978-1-4799-3869-8/14/$31.00 ©2014 IEEE

are extracted from the transmission zero frequency, susceptance slope and resonance frequency, given by

$$f_z = \frac{1}{2\pi\sqrt{L_r C_r}} \tag{5}$$

$$b = \omega_0 \frac{C_r (L_r + L_p)^2}{L_p^2} \tag{6}$$

$$f_0 = \frac{1}{2\pi\sqrt{(L_r + L_p) C_r}} \tag{7}$$

respectively, and easily inferred from electromagnetic simulation.

To initiate the algorithm it is necessary to obtain an initial layout for the SIR/stub resonator. This is obtained from formulas published in [4-6] that give the lengths l_{Cr} and l_{Lr} and l_{Lp}. Once the initial layout is known, the Broyden matrix is obtained by slightly perturbing the above lengths and obtaining L_r, C_r and L_p from parameter extraction [7]. Hence the algorithm can start iterating using (2), where the first error function in (3) is calculated from the extracted parameters of the first layout.

The synthesis of the quarter wavelength (at f_0) transmission line is much simpler, since it involves only the line width, W, that must be determined from the target characteristic impedance (Z_0 = 50Ω). The initial width is estimated from formulas provided in several microwave textbooks (for instance [6]). Once the initial width is determined, the ASM algorithm is applied, following a similar procedure to that corresponding to the SIR/stub resonator. The initial Broyden matrix (actually just composed of one element) is inferred by perturbing the line width and obtaining the characteristic impedance through electromagnetic simulation. It is important to mention that the line length is not subjected to optimization at this stage since the presence of the resonator is expected to cause some phase shift. Therefore the line length is optimized in the second stage (filter cell synthesis).

The remaining geometrical parameter to determine each filter cell is simply its length, l_{cell}, that is, the length of the pair of $\lambda/8$ lines. To this end, a single parameter ASM optimization is applied to the whole filter cell (filter cell synthesis), where the initial filter cell length is inferred from the well-known formula [6] that gives the line length as a function of the required phase (90^o) and frequency (f_o). At this stage, the ASM optimization consists of varying the length of the lines cascaded to the resonator until the required phase (90^o) per filter cell is achieved (the other geometrical parameters of the cell are kept unaltered). The phase is directly inferred from the frequency response of the cell obtained from electromagnetic simulation at each iteration step.

Once each filter cell has been synthesized, the cells are simply cascaded to generate the final filter layout. By considering the *Rogers RO3010* substrate with dielectric constant ε_r = 10.2, and thickness h = 635 μm, the resulting layout is the one depicted in Fig. 1 (dimensions summarized in table II, except the line width, which does not depend on the filter stage, i.e., W = 0.58 mm). The electromagnetic simulation (with and without losses) of the filter is also included in Fig. 2. The agreement between the lossless electromagnetic simulation and the response of the filter schematic is very good, pointing out the validity of the synthesis method. The filter has been fabricated by means of a *LPKF H100* drilling machine (see the inset of Fig. 2), and the measured frequency response (also included in Fig. 2) has been obtained by means of an *Agilent N5221A* vector network analyzer. The measured response is in good agreement with the lossy electromagnetic simulation, and reveals that filter specifications are satisfied.

TABLE II. GEOMETRY PARAMETERS OF THE FILTER

	Filter stage			
	1 , 7	**2 , 6**	**3 , 5**	**4**
l_{Lr} (mm)	1.2259	1.2783	0.5317	1.0537
l_{Cr} (mm)	0.9016	0.8646	1.9906	1.0963
l_{Lp} (mm)	2.4965	2.4991	1.4639	2.2787
l_{cell} (mm)	6.8966	6.9178	6.9245	6.9016

IV. CONCLUSION

In conclusion, we have proposed an ASM-based software tool for the automated layout synthesis of wideband microstrip bandpass filters based on SIR/stub resonators and quarter wavelength transmission lines. The synthesis is a two-step process where the topologies of resonators and lines are first determined, considering them as isolated elements. After that, each filter stage (i.e., the synthesized resonators inserted between λ/8 lines) is optimized, also using ASM. The main concluding aspect is that by cascading the optimized filter stages, the target (schematic) filter response is achieved. The agreement between the response of the schematic (circuit level) and the electromagnetic simulation (excluding losses) is very good. The synthesized 7-order filter has also been fabricated and measured for further validation of the synthesis method.

ACKNOWLEDGEMENT

This work was supported in part by MICIIN-Spain under Projects TEC2010-17512 METATRANSFER, TEC2010-21520-C04-01, and CONSOLIDER EMET CSD2008-00066, and by Generalitat de Catalunya under Project 2009SGR-421. Ferran Martin is in debt to Institució Catalana de Recerca i Estudis Avançats (ICREA) for being awarded with an ICREA Academia distinction (call 2008).

REFERENCES

[1] J.W. Bandler, R.M. Biernacki, S.H. Chen, P.A. Grobelny and R.H. Hemmers, "Space mapping technique for electromagnetic optimization", *IEEE Trans. Microw. Theory Techn.*, vol. 42, pp. 2536-2544, Dec. 1994.

[2] J.W. Bandler, R.M. Biernacki, S.H. Chen, R.H. Hemmers, and K. Madsen, "Electromagnetic optimization exploiting aggressive space mapping", *IEEE Trans. Microw. Theory Techn.*, vol. 43, pp. 2874-25442882, Dec. 1995.

[3] J. W. Bandler, Q. S. Cheng, S. A. Dakroury, A. S. Mohamed, M. H. Bakr, K. Madsen, and J. Søndergaard, "Space mapping: the state of the art," *IEEE Trans. Microw. Theory Tech*., vol. 52, pp. 337-361, Jan. 2004.

[4] J. Bonache, I. Gil, J. García-García and F. Martín, "Compact microstrip band-pass filters based on semi-lumped resonators", *IET Microw. Ant. Propag.*, vol. 1, pp. 932-936, Aug. 2007.

[5] J. Naqui, M. Durán-Sindreu, J. Bonache and F. Martín, "Implementation of shunt connected series resonators through stepped-impedance shunt stubs: analysis and limitations", *IET Microw. Ant. Propag.*, vol. 5, pp. 1336-1342, Aug. 2011.

[6] D.M. Pozar, *Microwave Engineering*, Addison Wesley, Reading, MA, 1990.

[7] J. Selga, A. Rodríguez, V. E. Boria, F. Martín, " Synthesis of split-rings-based artificial transmission lines through a new two-step, fast converging, and robust aggressive space mapping (ASM) algorithm", *IEEE Trans. Microw. Theory Techn*., vol. 61, no. 6, pp. 2295-2308, June 2013.

TMTT14

M. Sans, J. Selga, A. Rodríguez, J. Bonache, V. E. Boria, and F. Martín

“Design of Planar Wideband Bandpass Filters from Specifications using a Two-Step Aggressive Space Mapping (ASM) Optimization Algorithm”

Design of Planar Wideband Bandpass Filters From Specifications Using a Two-Step Aggressive Space Mapping (ASM) Optimization Algorithm

Marc Sans, Jordi Selga, *Member, IEEE*, Ana Rodríguez, *Student Member, IEEE*, Jordi Bonache, *Member, IEEE*, Vicente E. Boria, *Senior Member, IEEE*, and Ferran Martín, *Fellow, IEEE*

***Abstract*—This paper is focused on the automated and unattended optimization of a type of planar wideband bandpass filters by means of aggressive space mapping (ASM). The considered filters are microstrip filters implemented through a combination of shunt connected stepped impedance resonators (SIRs) and grounded stubs coupled through admittance inverters. The most relevant and novel aspect of this paper is the fact that the filter layout is automatically generated from filter specifications, i.e., central frequency, fractional bandwidth, in-band ripple and order, without the need of any external aid to the design process. To achieve this layout generation, filter optimization has been divided into two independent ASM processes. The first one generates the filter schematic (circuit element values) providing the required specifications. This first iterative process is necessary since, due to the narrow band operation of the admittance inverters, the target specifications are achieved by compensating the effects of such narrow band operation. The purpose of the second ASM algorithm is to automatically generate the layout from the filter schematic resulting from the first ASM process. To validate the new two-step ASM optimization tool, two sets of filter specifications (inputs of the developed tool), are considered. The generated filter layouts exhibit frequency responses that satisfy the specifications, and are in excellent agreement with the responses of the schematics.**

***Index Terms*—Bandpass filters, circuit optimization, microstrip technology, optimization, space mapping (SM), stepped impedance resonators (SIRs).**

I. INTRODUCTION

THE DESIGN of planar microwave components able to satisfy certain specifications has been a subject of interest for microwave engineers during years. Most commercial computer-aided design (CAD) tools and electromagnetic solvers of planar circuits include optimizers. However, depending on the circuit complexity, it may not be so straightforward to find those topologies able to satisfy the design requirements. Namely, convergence to the optimum solution is not always guaranteed (for instance due to limitations related to local minima), unless the seeding layout is already very close to the one providing the target response.

Among the considered techniques for microwave circuit design and optimization, space mapping (SM), first proposed by Bandler *et al.*. in 1994 [1], has revealed to be a powerful and efficient approach. Since that seminal work, several variants of SM have been proposed and applied to the design and optimization of many different microwave components, including not only planar circuits [2]–[4], but also waveguide-based components [5]–[7].

In this paper, the interest is focused on the so-called aggressive space mapping (ASM) [2], an approach that uses quasi-Newton type iteration to find the optimum solution of the considered problem. Particularly, the ASM optimization scheme will be adapted in order to find the layout of a class of bandpass filters (BPFs) that satisfies the design specifications. The considered filters are well suited to achieve wide fractional bandwidths, and can also be designed to exhibit high selectivity and wide stop bands by virtue of the controllable transmission zeros present above the pass band. Such filters consist of a combination of shunt connected stepped impedance resonators (SIRs) and grounded inductive stubs, coupled through admittance inverters [8]. Due to the narrow band operation of the admittance inverters (implemented by means of transmission line sections), ASM optimization will be first applied to the design of the optimum circuit schematic satisfying the specifications. Then, an additional (independent) ASM iterative process will be applied to the automatic generation of the filter layout. Hence, the proposed optimization tool will be able to automatically generate the filter layout from device specifications in a two-step ASM process. The optimum solution giving the target response is thus inferred following a completely unattended scheme.

This paper is organized as follows. The general formulation of ASM is briefly reviewed in Section II for completeness. Section III is focused on the first ASM algorithm, where the details to find the optimum filter schematic (the one that satisfies design requirements) are presented and discussed. This

---

Manuscript received June 25, 2014; revised September 11, 2014; accepted October 15, 2014. Date of publication November 12, 2014; date of current version December 02, 2014. This work was supported by MINECO-Spain (projects TEC2010-17512 METATRANSFER, TEC2010-21520-C04-01 and TEC2013-47037-C5-1-R, CONSOLIDER EMET CSD2008-00066, TEC2013-40600-R and TEC2013-49221-EXP), Generalitat de Catalunya (project 2014SGR-157), and Institució Catalana de Recerca i Estudis Avançats (who has awarded F. Martín). This paper was presented in part at the IEEE MTT-S International Microwave Symposium, Tampa Bay, FL, USA, June 1–6, 2014.

M. Sans, J. Selga, J. Bonache, and F. Martín are with GEMMA/CIMITEC, Departament d'Enginyeria Electrònica, Universitat Autònoma de Barcelona, 08193 Bellaterra, Spain (e-mail: Ferran.Martin@uab.es).

A. Rodríguez and V. E. Boria are with Departamento de Comunicaciones-iTEAM, Universitat Politècnica de València, 46022 Valencia, Spain (e-mail: vboria@dcom.upv.es).

Color versions of one or more of the figures in this paper are available online at http://ieeexplore.ieee.org.

Digital Object Identifier 10.1109/TMTT.2014.2365477

first ASM optimization algorithm constitutes the main contribution and originality of this paper. It provides the schematics of the considered filters satisfying the design specifications. Moreover, the proposed ASM algorithm can be easily modified in order to synthesize many other types of planar filters. Once the filter schematic is determined, a second ASM algorithm is used to derive the filter layout. The details and specificities of this algorithm, similar to the one reported in [9], are provided in Section IV. For further clarification, Sections III and IV are supported by the design of an order-5 filter (the electromagnetic response of the filter is compared to measurements at the end of Section IV). Nevertheless, to demonstrate the potential of the proposed optimization technique, Section V is focused on the design of an additional order-9 filter (also fabricated and measured). Finally, the main conclusions are highlighted in Section VI.

II. General Formulation of ASM

SM is a technique extensively used for the design and optimization of microwave components. It uses two simulation spaces [1], [2], [10]: 1) the optimization space, $\mathbf{X_c}$, where the variables are linked to a coarse model, which is simple and computationally efficient, although not accurate and 2) the validation space, $\mathbf{X_f}$, where the variables are linked to a fine model, typically more complex and CPU intensive, but significantly more precise. In each space, a vector containing the different model parameters can be defined. Let us call such vectors $\mathbf{x_f}$ and $\mathbf{x_c}$ for the fine and coarse model spaces, respectively, and let us designate by $\mathbf{R_f}(\mathbf{x_f})$ and $\mathbf{R_c}(\mathbf{x_c})$ their corresponding responses. The key idea behind any SM optimization process is to generate an appropriate parameter transformation

$$\mathbf{x_c} = \mathbf{P}(\mathbf{x_f}) \tag{1}$$

mapping the fine model parameter space to the coarse model parameter space such that

$$\left\|\mathbf{R_f}(\mathbf{x_f}) - \mathbf{R_c}(\mathbf{x_c})\right\| \leq \eta \tag{2}$$

in some predefined region, $\|\cdot\|$ being a certain suitable norm and η a small positive number close to zero. If $\mathbf{P}$ is invertible, then the inverse transformation

$$\mathbf{x_f} = \mathbf{P}^{-1}(\mathbf{x_c^*}) \tag{3}$$

is used to find the fine model solution, which is the image of the coarse model solution, $\mathbf{x_c^*}$, that gives the target response, $\mathbf{R_c}\ (\mathbf{x_c^*})$.

The determination of $\mathbf{P}$ according to the procedure reported in [1] follows an iterative process that is rather inefficient. The efficiency of the method was improved by introducing quasi-Newton type iteration [2], resulting in a faster convergence, and giving rise to the so-called ASM [2]. The goal in ASM is to minimize the following error function:

$$\mathbf{f}(\mathbf{x_f}) = \mathbf{P}(\mathbf{x_f}) - \mathbf{x_c^*}. \tag{4}$$

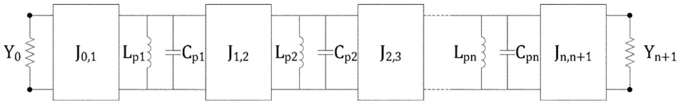

Fig. 1. Generalized bandpass filter network based on shunt resonators coupled through admittance inverters.

Let us assume that $\mathbf{x_f}^{(j)}$ is the jth approximation to the solution in the validation space, and $\mathbf{f}^{(j)}$ the error function corresponding to $\mathbf{f}(\mathbf{x_f}^{(j)})$. The next vector of the iterative process $\mathbf{x_f}^{(j+1)}$ is obtained by a quasi-Newton iteration according to

$$\mathbf{x_f}^{(j+1)} = \mathbf{x_f}^{(j)} + \mathbf{h}^{(j)} \tag{5}$$

where $\mathbf{h}^{(j)}$ is given by

$$\mathbf{h}^{(j)} = -\left(\mathbf{B}^{(j)}\right)^{-1}\mathbf{f}^{(j)} \tag{6}$$

and $\mathbf{B}^{(j)}$ is an approach to the Jacobian matrix, which is updated according to the Broyden formula [2]

$$\mathbf{B}^{(j+1)} = \mathbf{B}^{(j)} + \frac{\mathbf{f}^{(j+1)}\mathbf{h}^{(j)T}}{\mathbf{h}^{(j)T}\mathbf{h}^{(j)}}. \tag{7}$$

In (7), $\mathbf{f}^{(j+1)}$ is obtained by evaluating (4), using a certain parameter extraction method providing the coarse model parameters from the fine model parameters, and the super-index T stands for transpose.

The implementation of the ASM algorithm is well reported in [2]. In the next two sections, the details of the two ASM algorithms involved in the automated design of the filters considered in this work are discussed in detail.

III. First ASM Algorithm: Determination of the Optimum Filter Schematic

In this section we first present the considered wideband bandpass filters, including their schematic and topology, and then we describe the proposed ASM algorithm for the determination of the filter schematic that satisfies the design specifications.

A. Schematic and Topology of the Considered Wideband Bandpass Filters

The filters to be synthesized in this work are based on shunt resonators coupled through admittance inverters (see Fig. 1), according to the well-known network of a bandpass filter reported in many textbooks [11]. In order to achieve wide fractional bandwidth, high selectivity at the upper transition band and spurious free responses over broad frequency bands, the shunt resonators are implemented through a combination of stepped impedance resonators (SIRs) and grounded stubs. The SIRs provide transmission zeros (at frequencies designated as f_z) above the central filter frequency, f_0, which are useful for spurious suppression and for achieving a pronounced fall-off above the upper band edge. Moreover, with the parallel combination of SIRs and inductive stubs, the susceptance slopes at the filter central frequency can be made small, as required to achieve broad fractional bandwidths [8].

The typical topology and circuit schematic of the filter are depicted in Fig. 2, where the SIRs are described by the resonators

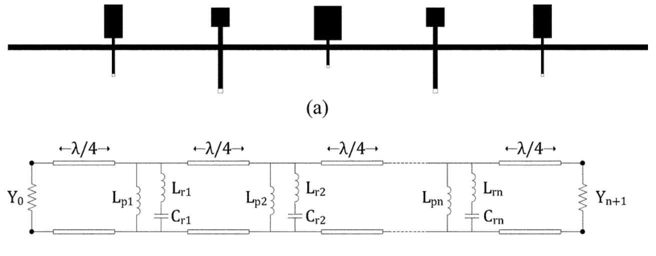

(a)

(b)

Fig. 2. (a) Typical topology and (b) circuit schematic of the considered wideband bandpass filters. The topology corresponds to an order-5 filter.

TABLE I
ELEMENT VALUES OF THE SHUNT RESONATORS

Stage	***L_p*** (nH)	***L_r*** (nH)	***C_r*** (pF)
1,5	1.3202	0.4401	2.4983
2,4	1.3226	0.4409	2.4937
3	0.8164	0.2721	4.0400

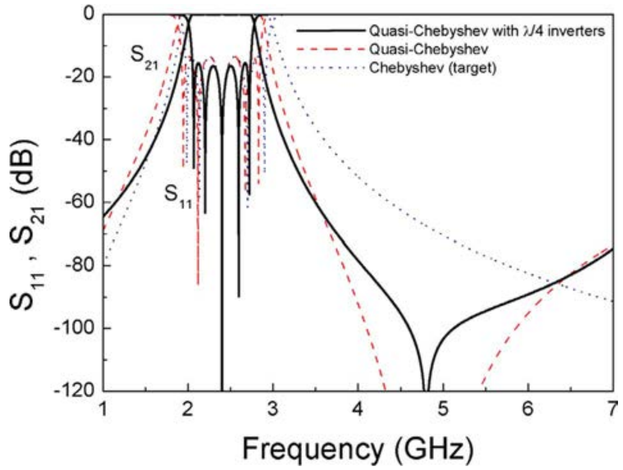

Fig. 3. Quasi-Chebyshev response of the filter that results by using the element values of Table I and ideal admittance inverters (red dashed line), compared to the filter response that results by replacing the ideal inverters with quarter wavelength transmission lines (black solid line), and with the ideal Chebyshev (target) response.

$L_{\mathrm{ri}}-C_{\mathrm{ri}}$, and L_{pi} accounts for the grounded stubs (i denotes the filter stage). The admittance inverters of the network of Fig. 1 are usually implemented by means of quarter wavelength (at f_0) transmission line sections. If the filter is narrowband, the target response (i.e., the one provided by the schematic considering ideal admittance inverters) can be achieved to a good approximation by means of quarter wavelength transmission lines. However, in wideband filters the narrowband functionality of these lines as admittance inverters degrades (decreases) the fractional bandwidth, and modifies the central frequency and the in-band return loss level. To solve this problem, it is necessary to tailor the parameters of the circuit schematic of Fig. 2(b), that is, the reactive parameters (L_{ri}, C_{ri}, and L_{pi}) and the electrical lengths of the transmission line sections. In the next subsection, we will present an ASM-based algorithm that automatically recalculates these parameters in order to satisfy the filter specifications. The generated schematic after this iterative ASM process will be designated as the optimum filter schematic.

B. Implementation of the ASM Algorithm

Let us consider that the filter order n is set to a certain value that suffices to achieve the required filter selectivity. The filter specifications are the central frequency f_0, the fractional bandwidth FBW, and the in-band ripple level L_{Ar} (or minimum return loss level). The transmission zero frequencies provided by the SIRs are all set to $f_z = 2f_0$, since this has been demonstrated to be a convenient approach to achieve spurious suppression, and to improve filter selectivity above the upper band edge [8], [9]. From the well-known impedance and frequency transformations from the low pass filter prototype [11], and assuming a Chebyshev response, the reactive elements of the shunt resonators of the network of Fig. 2 (L_{ri}, C_{ri}, and L_{pi}) can be easily inferred (the admittance of the inverters is set to $J = 0.02$ S). The three conditions to unequivocally determine L_r, C_r, and L_p are: 1) the filter central frequency, given by

$$f_0 = \frac{1}{2\pi\sqrt{(L_{ri}+L_{pi})C_{ri}}}; \tag{8}$$

2) the transmission zero frequency

$$f_z = \frac{1}{2\pi\sqrt{L_{ri}C_{ri}}}; \tag{9}$$

and 3) the susceptance slope at f_0 (dependent on the filter stage)

$$b_i = 2\pi f_0 \frac{C_{ri}(L_{ri}+L_{pi})^2}{L_{pi}^2}. \tag{10}$$

Considering that the target is an order-5 ($n = 5$) Chebyshev response with $f_0 =$ 2.4 GHz, $\mathrm{FBW} = 40\%$ (corresponding to a 43.96% -3-dB fractional bandwidth) and $L_{Ar} =$ 0.2 dB, the element values of the shunt resonators are found to be those indicated in Table I. It is important to mention that for Chebyshev bandpass filters the fractional bandwidth is given by the ripple level and is hence smaller than the -3-dB fractional bandwidth. However, in this paper we will deal with the -3-dB fractional bandwidth since the ripple level is not constant in the optimization process (to be described). From now on, this -3-dB fractional bandwidth is designated as FBW, rather than $\mathrm{FBW}_{-3\mathrm{dB}}$ (as usual), for simplicity, and to avoid an excess of subscripts in the formulation.

The quasi-Chebyshev filter response (i.e., the one inferred from the schematic of Fig. 2(b), but with ideal admittance inverters), depicted in Fig. 3, is similar to the ideal (target) Chebyshev response in the pass band region, and it progressively deviates from it as frequency approaches f_z, as expected. The discrepancies are due to the fact that the shunt resonator is actually a combination of a grounded series resonator (providing the transmission zero) and a grounded inductor. The quasi-Chebyshev response satisfies the specifications to a rough approximation. Hence the target is considered to be the ideal Chebyshev response, except for the transmission zero frequency. In Fig. 3, the responses have been obtained by implementing a specific code, implemented in MATLAB [12], that calculates the transfer $(ABCD)$ matrix of the filter from the individual matrices of the different filter sections.

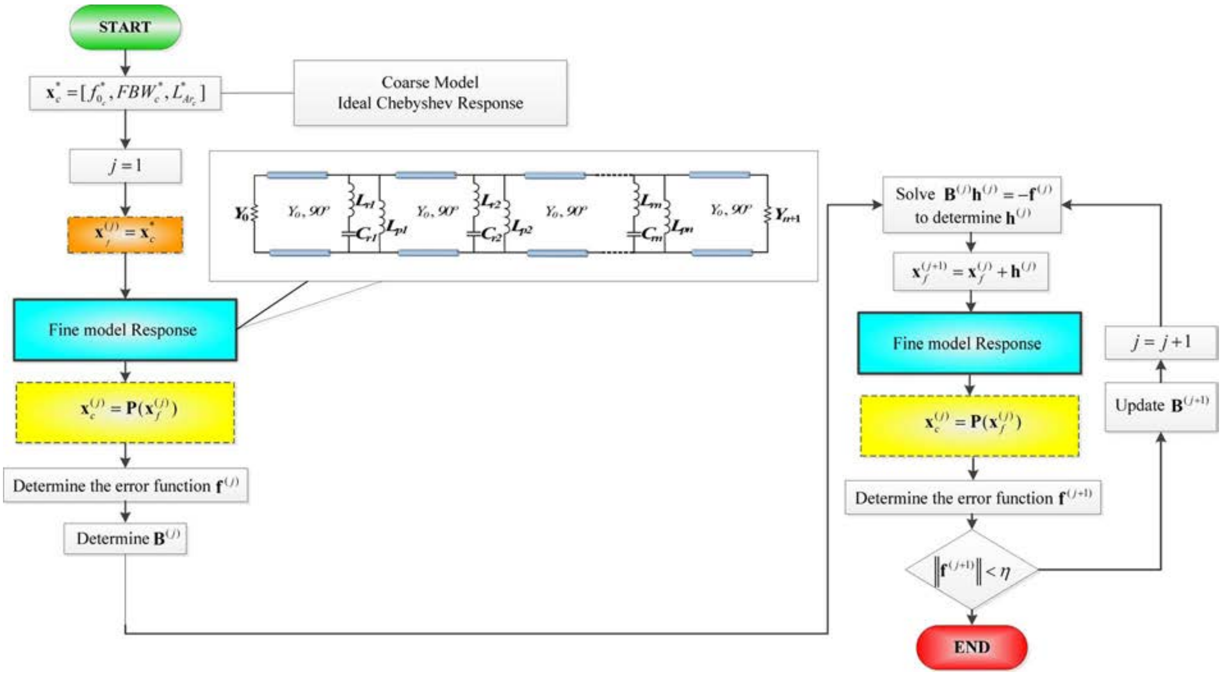

Fig. 4. Flow diagram of the first ASM algorithm.

If we now replace the ideal admittance inverters with quarter wavelength transmission lines, the response is further modified, as Fig. 3 illustrates. Thus, our aim is to find the filter schematic [see Fig. 2(b)] able to satisfy the specifications. To this end, a new ASM concept that carries out the optimization at the schematic level is proposed in this work.

The key point in the development of this novel iterative ASM algorithm, is to assume that there is a set of filter specifications, different from the target, that leads to a filter schematic (inferred by substituting the ideal admittance inverters with quarter wavelength transmission lines), whose response satisfies the target specifications. Let us now try to define the optimization (coarse model) space and the validation (fine model) space in the proposed ASM iterative scheme. The first one is constituted by the set of specifications f_0, FBW, $L_{\rm Ar}$, being its response the ideal Chebyshev response-target response-depicted in Fig. 3. The validation space is constituted by the same variables, but their response is inferred from the schematic of Fig. 2(b), with element values calculated as specified above, and quarter wavelength transmission lines at f_0, where f_0 is the considered value of this element in the validation space (not necessarily the target filter central frequency). The variables of each space are differentiated by a subscript. Thus, the corresponding vectors in the coarse and fine models are written as $\mathbf{x_c} = [f_{0\rm c}, {\rm FBW_c}, L_{\rm Arc}]$ and $\mathbf{x_f} = [f_{0\rm f}, {\rm FBW_f}, L_{\rm Arf}]$, respectively. The coarse model solution (target specifications) is expressed as $\mathbf{x_c^*} = [f_{0\rm c}{}^*, {\rm FBW_c^*}, L_{\rm Arc}{}^*]$. Notice that the transmission zero frequency, necessary to unequivocally determine the element values of the shunt resonators, is set to $f_z = 2f_0$, as indicated before. Hence f_z is not a variable in the optimization process.

Following the standard procedure in ASM, the first step before starting the iterative process is to make an estimation of the first vector in the validation space $\mathbf{x_f^{(1)}}$. Since the variables in both spaces are the same, the most canonical (and simplest) procedure is to consider $\mathbf{x_f^{(1)}} = \mathbf{x_c^*}$. From $\mathbf{x_f^{(1)}}$, the response of the fine model space is obtained (using the schematic with quarter wavelength transmission lines), and from it we directly extract the parameters of the coarse model by direct inspection of that response, i.e., $\mathbf{x_c^{(1)}} = \mathbf{P}(\mathbf{x_f^{(1)}})$. Applying (4), we can thus obtain the first error function. To iterate the process [obtaining $\mathbf{x_f^{(2)}}$ from (5), using (6)], we need to initiate the Jacobian matrix. To this end, we have slightly perturbed the parameters of the fine model, $f_{0\rm f}, {\rm FBW_f}, L_{\rm Arf}$, and we have inferred the effects of such perturbations on the coarse model parameters, $f_{0\rm c}, {\rm FBW_c}, L_{\rm Arc}$. Thus, the first Jacobian matrix is given by

$$\mathbf{B} = \begin{pmatrix} \frac{\delta f_{0\rm c}}{\delta f_{0\rm f}} & \frac{\delta f_{0\rm c}}{\delta {\rm FBW_f}} & \frac{\delta f_{0\rm c}}{\delta L_{\rm Arf}} \\ \frac{\delta {\rm FBW_c}}{\delta f_{0\rm f}} & \frac{\delta {\rm FBW_c}}{\delta {\rm FBW_f}} & \frac{\delta {\rm FBW_c}}{\delta L_{\rm Arf}} \\ \frac{\delta L_{\rm Arc}}{\delta f_{0\rm f}} & \frac{\delta L_{\rm Arc}}{\delta {\rm FBW_f}} & \frac{\delta L_{\rm Arc}}{\delta L_{\rm Arf}} \end{pmatrix}. \qquad (11)$$

Once the first Jacobian matrix is obtained, the process can be iterated until convergence is obtained. At each iteration, the elements of the coarse space vector, $\mathbf{x_c^{(j)}}$, are compared to the target (filter specifications), $\mathbf{x_c^*}$, and the error function is obtained according to

$$\|f_{\rm norm}\| = \sqrt{\left(1 - \frac{f_{0\rm c}}{f_{0\rm c}^*}\right)^2 + \left(1 - \frac{\rm FBW_c}{\rm FBW_c^*}\right)^2 + \left(1 - \frac{L_{\rm Arc}}{L_{\rm Arc}^*}\right)^2}. \qquad (12)$$

The scheme of the proposed ASM algorithm is depicted in Fig. 4. The core program has been written in MATLAB [12], and the fine model responses have been obtained, also using MATLAB, by first calculating the *ABCD* matrix and transforming it to the scattering matrix.

Applying the developed ASM algorithm to the considered example ($\mathbf{x_c}^* = [f_{0c}{}^*, \mathrm{FBW_c}{}^*, L_{\mathrm{Arc}}{}^*] = [2.4\ \mathrm{GHz}, 43.96\%, 0.2\ \mathrm{dB}]$), we have found that the error function rapidly decreases, reducing the error to around 11% after iteration $N = 2$, and smaller than 1.2% after $N = 13$ iterations. The evolution of the error function is depicted in Fig. 5. The fine model parameters for $N = 2$ are $\mathbf{x_f}^{(2)} = [f_{0\mathrm{f}}^{(2)}, \mathrm{FBW}_{\mathrm{f}}^{(2)}, L_{\mathrm{Arf}}^{(2)}] = [2.4690\ \mathrm{GHz}, 65.37\%, 0.3902\ \mathrm{dB}]$ and the coarse model parameters are $\mathbf{x_c}^{(2)} = [f_{0c}{}^{(2)}, \mathrm{FBW}_{\mathrm{c}}^{(2)}, L_{\mathrm{Arc}}{}^{(2)}] = [2.3998\ \mathrm{GHz}, 43.75\%, 0.1780\ \mathrm{dB}]$, whereas for the last iteration ($N = 13$) the fine model parameters are $\mathbf{x_f}^{(13)} = [f_{0\mathrm{f}}^{(13)}, \mathrm{FBW}_{\mathrm{f}}^{(13)}, L_{\mathrm{Arf}}{}^{(13)}] = [2.4690\ \mathrm{GHz}, 65.53\%, 0.4413\ \mathrm{dB}]$ and the coarse model parameters are $\mathbf{x_c}{}^{(13)} = [f_{0c}{}^{(13)}, \mathrm{FBW}_{\mathrm{c}}^{(13)}, L_{\mathrm{Arc}}{}^{(13)}] = [2.3999\ \mathrm{GHz}, 43.75\%, 0.1978\ \mathrm{dB}]$. Thus in both iterations, $\mathbf{x_f}$ is appreciably different than $\mathbf{x_c}^*$. The optimum filter schematic is the one given by the last fine model response (which provides an error below a predefined value). The elements of the shunt resonators for this optimum filter schematic are indicated in Table II, whereas the 50-Ω line sections are quarter wavelength transmission lines at $f_{0\mathrm{f}}{}^{(13)} \neq f_0{}^* = 2.4$ GHz. The response of the optimum schematic is compared to the target response in Fig. 6. The agreement in terms of central frequency, bandwidth and in-band ripple is very good, as expected on account of the small error function that has been obtained after 13 iterations. Note, however, that the position of the reflection zero frequencies are different in both responses. The reason is that we have not considered these frequency positions as goals in the optimization process. Unavoidably, it is not possible to perfectly match the Chebyshev (target) response by replacing the ideal admittance inverters with transmission line sections and the LC shunt resonators of Fig. 1 with the resonators of the schematic of Fig. 2(b). Nevertheless the synthesized circuit fulfills the target specifications, and hence it is the optimum filter schematic used as the starting point in the ASM algorithm developed to obtain the filter layout, to be described in the next section.

To end this section, we would like to highlight that the previous procedure to find the optimum filter schematic, based on an iterative ASM algorithm, represents clear progress as compared to the method reported in [9], and it is the main relevant contribution of this paper. In [9], we simply applied an iterative process to find the optimum schematic, involving only one variable: the fractional bandwidth. We iteratively readjusted the nominal fractional bandwidth until the resulting response (at the schematic level) converged to the required bandwidth. However, by means of such procedure we cannot guarantee that the in-band ripple is within the required level. Conversely, through the ASM-based method proposed in this paper it has been demonstrated that the filter specifications (central frequency, fractional bandwidth and in-band ripple) can be fully satisfied by the automatically generated filter schematic. The reason is that the new developed ASM involves the previous set of specifications as variables in the optimization process.

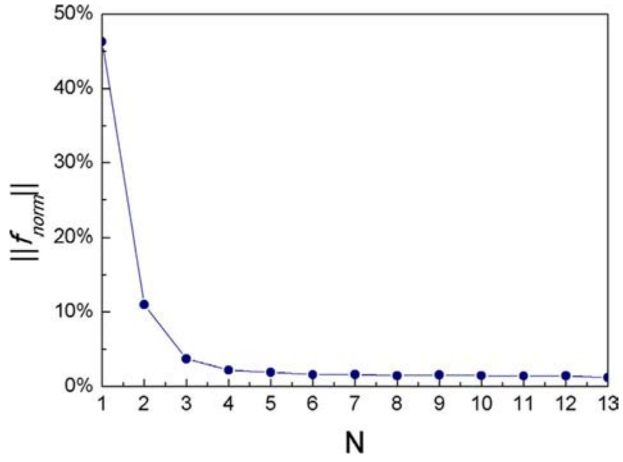

Fig. 5. Evolution of the error function of the first ASM algorithm for the considered example.

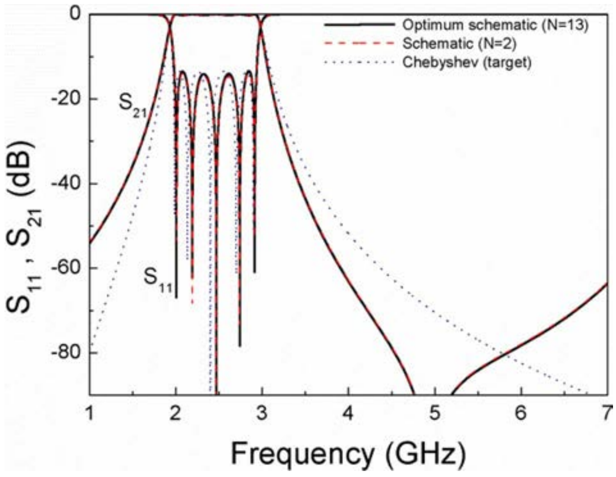

Fig. 6. Response of the optimum filter schematic, derived from the ASM algorithm, compared with the Chebyshev target response. The response at the second iteration ($N = 2$), also included, is very close to the final solution ($N = 13$).

TABLE II
ELEMENT VALUES OF THE SHUNT RESONATORS FOR THE OPTIMUM FILTER SCHEMATIC

Stage	***L_p*** (nH)	***L_r*** (nH)	***C_r*** (pF)
1,5	1.6090	0.5363	1.9368
2,4	2.1196	0.7065	1.4703
3	1.0685	0.3562	2.9168

IV. SECOND ASM ALGORITHM: AUTOMATED LAYOUT GENERATION

Once the optimum filter schematic has been found, the next step is to determine the layout of the filter. To this end, a second ASM algorithm, firstly reported in [9], is considered. We have to synthesize each filter cell from the element values of the shunt resonator and the characteristic impedance of the cascaded $\lambda/8$ (at $f_{0\mathrm{f}}{}^{(13)}$) transmission lines independently. This second ASM process involves three stages: 1) determination of the resonator layout; 2) determination of the line width; and 3) optimization of

TABLE III
GEOMETRY PARAMETERS OF THE SYNTHESIZED ORDER-5 FILTER

Stage	l_{Lr} (mm)	l_{Cr} (mm)	l_{Lp} (mm)	l_{cell} (mm)	W_{Cr} (mm)	W_{Lp} (mm)
1,5	0.7062	3.6710	2.5955	11.4003	2	0.3
2,4	1.9438	2.1037	4.2334	11.2583	2	0.5
3	0.4725	3.7461	1.6629	11.4786	3	0.3

TABLE IV
ELEMENT VALUES OF THE SHUNT RESONATORS FOR THE OPTIMUM FILTER SCHEMATIC OF THE 9^{TH} ORDER FILTER

Stage	L_p (nH)	L_r (nH)	C_r (pF)
1,9	5.2439	1.7480	3.4077
2,8	4.7471	1.5824	3.7643
3,7	3.0439	1.0146	5.8707
4,6	4.2765	1.4255	4.1786
5	2.9547	0.9849	6.0478

TABLE V
GEOMETRY PARAMETERS OF THE SYNTHESIZED ORDER-9 FILTER

Stage	l_{Lr} (mm)	l_{Cr} (mm)	l_{Lp} (mm)	l_{cell} (mm)	W_{Cr} (mm)	W_{Lp} (mm)
1,9	4.6273	4.0264	10.5715	27.5994	3	0.5
2,8	4.0219	3.6428	9.6523	27.5952	4	0.5
3,7	2.1062	5.4739	6.2752	27.5922	5	0.5
4,6	3.3853	4.344	8.7157	27.6578	4	0.5
5	2.0049	5.6627	6.1136	27.5662	5	0.5

the line length. Let us now discuss in detail the implementation of these three specific ASM algorithms.

A. *Optimization of the Resonators*

In order to obtain the layout of the filter resonators, composed by the SIRs parallel connected to the grounded stubs, a specific ASM iterative process has been designed. The variables in the optimization space are the resonator elements, i.e., $\mathbf{x_c} = [L_p, L_r, C_r]$, and the coarse model response is obtained through circuit simulation. The validation space is constituted by a set of variables defining the resonator layout. In order to deal with the same number of variables in both spaces, the widths of the grounded stubs, W_{Lp}, as well as the widths of the low- and high-impedance transmission line sections of the SIRs, W_{Cr} and W_{Lr}, respectively, are set to fixed values. Specifically, we have considered the values of W_{Cr} and $W_{Lr} = W_{Lp}$ indicated in Tables III and V. There is some flexibility to choose these widths, but it is convenient to consider wide capacitive and narrow inductive sections to reduce the length of the SIRs and inductive stubs. We have opted in this work to consider moderate widths of the capacitive sections to avoid transversal resonances in the frequency region of interest (i.e., up to frequencies above f_z). The widths of the inductive sections have been set to values above the tolerance limits (representing a good balance between SIR/stub dimensions and fabrication accuracy). Thus, the variables in the validation space are the remaining dimensions of the shunt resonators, that is, the length of the grounded stub, l_{Lp}, and the lengths l_{Lr} and l_{Cr} of the high- and low-impedance transmission line sections, respectively, of the SIR (i.e., $\mathbf{x_f} = [l_{Lp}, l_{Lr}, l_{Cr}]$). The fine model response is obtained through electromagnetic simulation of the layout, inferred from the fine model variables plus the fixed dimensions (specified above) and substrate parameters. In this work, the *Agilent Momentum* commercial software has been used to obtain the electromagnetic response of the structures, and the considered substrate parameters are those of the *Rogers RO3010* with thickness $h = 635$ μm and dielectric constant $\varepsilon_r = 10.2$.

Following the general scheme of the ASM optimization described in Section II, to initiate the algorithm it is necessary to obtain an initial layout for the SIR and shunt stub. This is obtained from the well-known (and simple) approximate formulas providing the inductance and capacitance of a narrow and wide, respectively, electrically small transmission line section [14]. Isolating the lengths, we obtain

$$l_{Lr} = \frac{L_r v_{ph}}{Z_h} \tag{13a}$$

$$l_{Cr} = C_r v_{pl} Z_l \tag{13b}$$

$$l_{Lp} = \frac{L_p v_{ph}}{Z_h} \tag{13c}$$

where v_{ph} and v_{pl} are the phase velocities of the high- and low-impedance transmission lines sections, respectively, and Z_h and Z_l the corresponding characteristic impedances. Once the initial layout (i.e., $\mathbf{x_f}^{(1)}$) is determined, the circuit elements can be extracted from the electromagnetic response using (8)–(10). This provides $\mathbf{x_c}^{(1)} = \mathbf{P}(\mathbf{x_f}^{(1)})$, and using (4), the first error function can be inferred. To iterate the process using (5), with $\mathbf{h}^{(1)}$ derived from (6), a first approximation of the Jacobian matrix is needed. Following a similar approach to the one explained in Section III-B, we have slightly perturbed the lengths l_{Lp}, l_{Lr}, l_{Cr}, and we have obtained the values of L_p, L_r, and C_r resulting after each perturbation from parameter extraction. The first Jacobian matrix can thus be expressed as

$$\mathbf{B} = \begin{pmatrix} \frac{\delta L_r}{\delta l_{Lr}} & \frac{\delta L_r}{\delta l_{Cr}} & \frac{\delta L_r}{\delta l_{Lp}} \\ \frac{\delta C_r}{\delta l_{Lr}} & \frac{\delta C_r}{\delta l_{Cr}} & \frac{\delta C_r}{\delta l_{Lp}} \\ \frac{\delta L_p}{\delta l_{Lr}} & \frac{\delta L_p}{\delta l_{Cr}} & \frac{\delta L_p}{\delta l_{Lp}} \end{pmatrix}. \tag{14}$$

By applying this procedure to the resonator elements of each filter stage, the corresponding layouts of the SIRs and grounded stubs are determined.

B. *Determination of the Line Width*

The optimization of the quarter wavelength (at $f_{0\mathrm{f}}^{(13)}$) transmission lines is much simpler, since it involves only the line width, W, that must be determined from the target characteristic impedance ($Z_0 = 50\ \Omega$). The line length is not subjected to optimization at this stage, since the presence of the resonator is expected to cause some extra phase shift. Therefore the line length is optimized in the next stage, where the required phase shift is forced in the whole structure, including the pair of lines and the resonator.

The initial line width is estimated from the formulas provided in several microwave textbooks (for instance [15]). Once the initial width is estimated, the specific ASM algorithm developed to determine the line width is applied. In such one-variable ASM scheme, the initial Jacobian matrix (actually just composed of

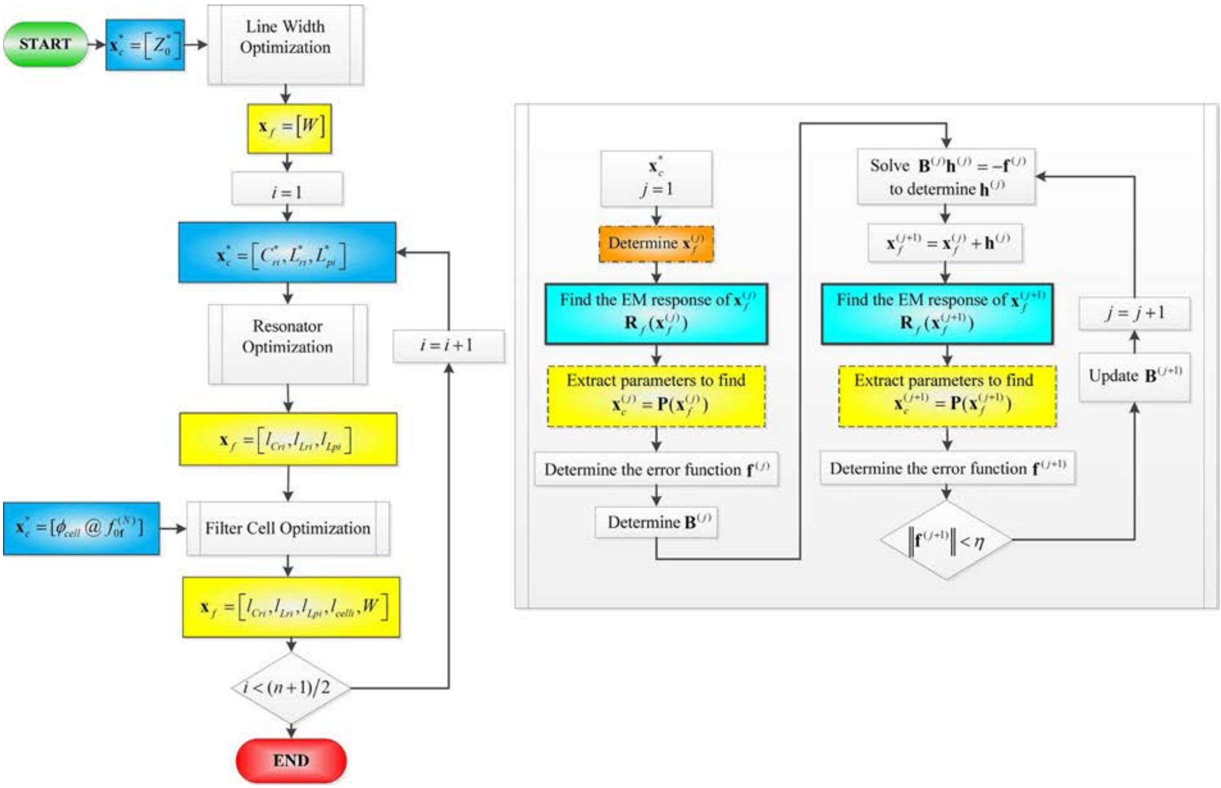

Fig. 7. Flow diagram of the second ASM algorithm. The sub-process depicted at the right of the figure represents a typical ASM algorithm used in each optimization process (particularly the indicated one is for the resonator optimization). Notice that the loop must be executed $(n+1)/2$ times, n being the filter order (which is assumed to be odd), since for odd Chebyshev response the cells i and $n+1-i$ are identical. However, this does not affect line width optimization since line width is identical for all filter stages.

one element) is inferred by perturbing the line width and obtaining the characteristic impedance through electromagnetic simulation (i.e., the fine model variable is the line width, W, whereas the variable of the coarse model is the characteristic impedance).

C. Optimization of the Line Length (Filter Cell Optimization)

As mentioned before, the length of the lines cascaded to the resonant elements is optimized by considering the whole filter cell. Let us define l_{cell} as the length of the cell excluding the width of the grounded stubs, W_{Lp}, (roughly corresponding to $\lambda/4$ at $f_{0\text{f}}^{(13)}$). To determine l_{cell}, a single parameter ASM optimization is applied to the filter cell (filter cell optimization), where the initial value of l_{cell} is inferred from the well-known formula [14] that gives the line length as a function of the required phase (90°) and frequency $(f_{0\text{f}}^{(13)})$. At this stage, the ASM optimization consists of varying the length of the lines cascaded to the resonator until the required phase at $f_{0\text{f}}^{(13)}$ (i.e., 90°) per filter cell is achieved (the other geometrical parameters of the cell are kept unaltered). The phase is directly inferred from the frequency response of the cell obtained from electromagnetic simulation at each iteration step.

Once each filter cell has been synthesized, the cells are simply cascaded to generate the final filter layout (coupling between adjacent resonators is not taken into account since the results reveal that this effect is not significant). The scheme of the complete ASM process able to automatically provide the layout from the optimum filter schematic, and consisting of three independent quasi-Newton iterative algorithms, is depicted in Fig. 7. Using the element values of Table II, corresponding to the optimum filter schematic of the example reported in Section III, where the lines present between adjacent resonators exhibit a characteristic impedance of $Z_o = 50\ \Omega$ and an electrical length of 90° at ${f_{0\text{f}}}^{(13)} = 2.4690$ GHz, we have applied the developed ASM algorithm to automatically generate the filter layout (which is actually the one depicted in Fig. 2). The dimensions are summarized in Table III, except the line width, which does not depend on the filter stage, i.e., $W = 0.6055$ mm. Notice that the cell length slightly varies from cell to cell. This variation is due to the phase effects produced by the different resonators, and justifies the need to optimize the length of the lines by considering the complete filter cell (as described in the preceding paragraph).

The electromagnetic simulation (excluding losses) of the synthesized filter is compared to the response of the optimum filter schematic and to the target (ideal Chebyshev) response in Fig. 8. The agreement between the lossless electromagnetic simulation and the response of the optimum filter schematic (where losses are excluded) is very good, pointing out the validity of the second ASM optimization method. The filter has been fabricated by means of an *LPKF H100* drilling machine [see Fig. 9(a)], and the measured frequency response [see Fig. 9(b)] has been obtained by means of an *Agilent N5221A* vector network analyzer. The measured response is in reasonable agreement with the lossy electromagnetic simulation, and reveals that filter specifications are satisfied to a good approximation. Slight discrepancies between the measured response and the lossy electromagnetic simulation can be mainly

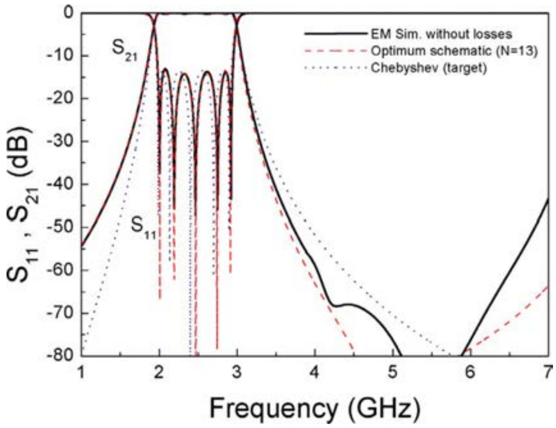

Fig. 8. Lossless electromagnetic simulation of the synthesized order-5 filter, compared to the response of the optimum filter schematic and target response.

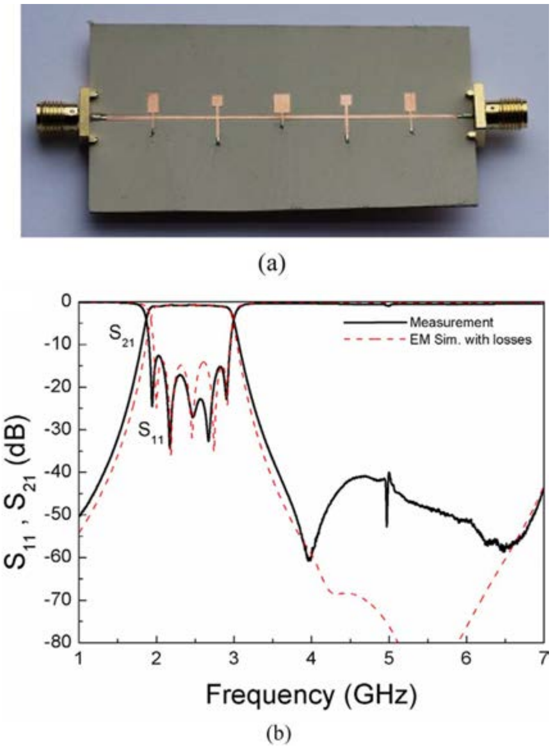

Fig. 9. (a) Photograph of the fabricated order-5 filter and (b) measured response compared to the lossy electromagnetic simulation. The layout of the fabricated filter is the one depicted in Fig. 2.

attributed to inaccuracies in the dielectric constant provided by the substrate supplier, although they can be also influenced by fabrication related tolerances, substrate anisotropy and foil roughness. Nevertheless, these effects are not considered in the optimization process, because the aim was to automatically obtain the filter layout providing a lossless electromagnetic simulation able to satisfy the specifications. Hence, the results of Fig. 8 reveal that this objective has been fully achieved. Note also that the effects of placing the filter in a shielding box are not taken into account in this work (filter response might be affected by box resonances if they are present in the region of interest).

It is also worth highlighting that layout generation with the proposed two-step ASM procedure (design and optimization of the filter schematic and of the filter layout) is obtained following a completely unattended scheme. External action is only required in the first step, to provide the filter specifications, which are the input variables of the proposed two-step ASM algorithm.

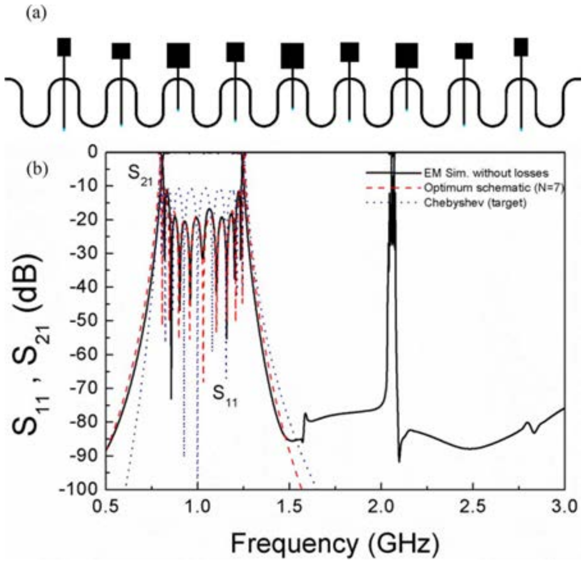

Fig. 10. (a) Layout of the synthesized order-9 filter and (b) lossless electromagnetic simulation compared to the response of the optimum filter schematic and target response.

At this point it is worth mentioning that the scheme of the second ASM is similar to the so-called knowledge embedded space mapping technique reported in [16], in the sense that we make use of analytical formulas to link dimensions (layout geometry) and parameters of equivalent circuit model (inductances and capacitances for the resonators). However, there is a noticeable difference with regard to the cited work, since in our case we avoid the need of using an embedded buffer space, and we have solved the problem of employing a Jacobian matrix B that can directly relate circuit elements with layout geometrical dimensions. Furthermore, the key point of the present paper is the first ASM scheme providing the optimum filter schematic.

On the other hand, for the optimization of filter layout (second ASM), an alternative solution could be port tuning ASM [17]. Nevertheless, it has been found that the proposed procedure, based on a classical ASM approach with three sub-processes, provides convergence in few steps and accurate results. The reason is that for the worst sub-process (resonator optimization), only three variables are involved, the initial layout is very close to the target and no significant inter-resonator coupling arises. Thus, we have opted to apply the proposed ASM scheme for the second ASM (layout generation).

V. DESIGN OF A 9^{TH}-ORDER FILTER

In order to demonstrate the potential of the proposed two-step ASM algorithm for the design and optimization of the considered type of filters, let us now apply the developed tool to the design of a higher order filter. In [9], a 7^{th}-order filter (where the first ASM algorithm was not applied) was synthesized. Therefore, in this section we consider the design of a 9^{th}-order filter. The specifications are: $f_0 = 1$ GHz, FBW $= 45.3\%$ (-3-dB fractional bandwidth) and $L_{Ar} = 0.4$ dB. Application of the

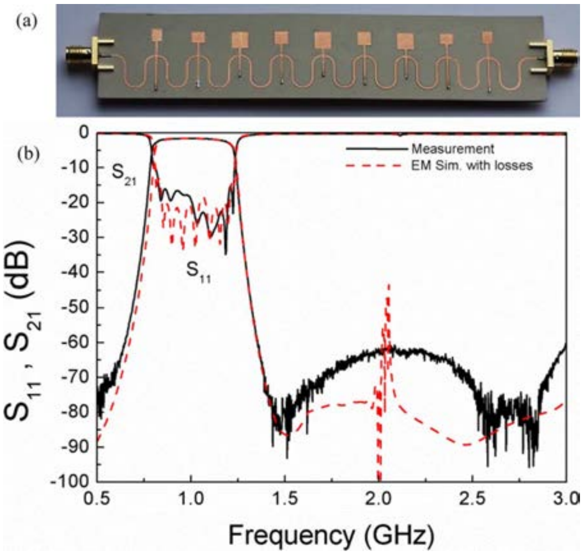

Fig. 11. (a) Photograph of the fabricated order-9 filter and (b) measured response compared to the lossy electromagnetic simulation.

first ASM algorithm gives the schematic with element values indicated in Table IV and 90° (at ${f_{0f}}^{(7)} = 1.0311$ GHz) transmission line sections. Convergence has been achieved after $N = 7$ iterations, when the error function is as small as 0.63%.

Application of the second ASM algorithm, considering the substrate used for the 5^{th}-order filter (*Rogers RO3010* with thickness $h = 635\ \mu$m and dielectric constant $\varepsilon_r = 10.2$), provides the filter geometry indicated in Table V. For this filter, we have meandered the line sections in order to reduce device dimensions.

Fig. 10 shows the layout of the filter and the lossless electromagnetic simulation, compared to the optimum filter schematic and target responses. The fabricated filter is depicted in Fig. 11, together with the measured response and the lossy electromagnetic simulation. Again, very good agreement between the different responses can be appreciated. Moreover, the filter response satisfies the considered specifications. Thus, it has been demonstrated that the proposed and developed two-step ASM tool is able to automatically provide the layout of the considered type of filters for different orders and specifications.

VI. CONCLUSION

In conclusion, we have developed an iterative tool for the automatic optimization of bandpass filters based on a combination of SIRs and shunt inductive stubs coupled through admittance inverters. These filters are useful to simultaneously achieve wide fractional bandwidths, high selectivity and spurious-free responses up to high frequencies (thanks to the inherent transmission zeros provided by the SIRs). The tool is based on a two-step ASM algorithm, where the optimum filter schematic is first determined from the filter specifications. Once the filter schematic is inferred, the element values are the inputs of the second ASM algorithm, which provides the final filter layout, determining the free geometrical parameters of each filter cell independently. The main relevant contribution of this paper is the development of the first ASM algorithm, able to provide a filter schematic (optimum) fully satisfying the specifications. In this optimum schematic the admittance inverters are implemented by means of transmission line sections exhibiting an electrical length of 90° at a frequency provided by the ASM algorithm (this frequency does not necessarily coincide with the filter central frequency). Indeed, in the first ASM algorithm, the set of specifications are considered to be the variables in both the optimization and validation spaces, and the iterative ASM process ends when the variables of the optimization space coincide with the target (specifications). The developed two-step ASM tool has been proven with the design of a 5^{th}-order filter, which has been used as an example to conduct and give the details of the tool, and then it has been successfully applied to the complete design of a 9^{th}-order filter. In both cases, it has been found that the response of the optimum filter schematic (generated by the first ASM) satisfies the specifications, and that the generated layout (second ASM) exhibits a frequency response in very good agreement with that of the schematic. Thus, the developed two-step ASM design technique has been validated by means of two different examples, including a very high order filter. In both examples, the layout of the filters has been inferred in a completely unattended optimization scheme.

REFERENCES

[1] J. W. Bandler, R. M. Biernacki, S. H. Chen, P. A. Grobelny, and R. H. Hemmers, “Space mapping technique for electromagnetic optimization,” *IEEE Trans. Microw. Theory Techn.*, vol. 42, no. 12, pp. 2536–2544, Dec. 1994.

[2] J. W. Bandler, R. M. Biernacki, S. H. Chen, R. H. Hemmers, and K. Madsen, “Electromagnetic optimization exploiting aggressive space mapping,” *IEEE Trans. Microw. Theory Techn.*, vol. 43, no. 12, pp. 2874–2882, Dec. 1995.

[3] M. H. Bakr, J. W. Bandler, K. Madsen, J. E. Rayas-Sánchez, and J. Søndergaard, “Space-mapping optimization of microwave circuits exploiting surrogate models,” *IEEE Trans. Microw. Theory Techn.*, vol. 43, no. 12, pp. 2297–2306, Dec. 2000.

[4] S. Koziel, Q. S. Cheng, and J. W. Bandler, “Space mapping,” *IEEE Microwave Mag.*, vol. 9, pp. 105–122, Dec. 2008.

[5] J. W. Bandler, R. M. Biernacki, S. H. Chen, and D. Omeragic, “Space mapping optimization of waveguide filters using finite element and mode-matching electromagnetic simulators,” presented at the IEEE MTT-S Int. Microwave Symp., Denver, CO, USA, Jun. 1997.

[6] J. W. Bandler, Q. S. Cheng, D. M. Hailu, and N. K. Nikolova, “A space-mapping design framework,” *IEEE Trans. Microw. Theory Techn.*, vol. 53, no. 11, pp. 2601–2610, Nov. 2004.

[7] J. V. Morro, P. Soto, H. Esteban, V. E. Boria, C. Bachiller, M. Taroncher, S. Cogollos, and B. Gimeno, “Fast automated design of waveguide filters using aggressive space mapping with a new segmentation strategy and a hybrid optimization algorithm,” *IEEE Trans. Microw. Theory Techn.*, vol. 53, no. 4, pp. 1130–1142, Apr. 2005.

[8] J. Bonache, I. Gil, J. García-García, and F. Martín, “Compact microstrip band-pass filters based on semi-lumped resonators,” *IET Microwaves Antennas Propag.*, vol. 1, pp. 932–936, Aug. 2007.

[9] J. Selga, M. Sans, A. Rodríguez, J. Bonache, V. Boria, and F. Martín, “Automated synthesis of planar wideband bandpass filters based on stepped impedance resonators (SIRs) and shunt stubs through aggressive space mapping (ASM),” presented at the IEEE MTT-S Int. Microwave Symp., Tampa, FL, USA, Jun. 2014.

[10] J. W. Bandler, Q. S. Cheng, S. A. Dakroury, A. S. Mohamed, M. H. Bakr, K. Madsen, and J. Søndergaard, “Space mapping: the state of the art,” *IEEE Trans. Microw. Theory Techn.*, vol. 52, no. 1, pt. 2, pp. 337–361, Jan. 2004.

[11] J. S. Hong and M. J. Lancaster, *Microstrip Filters for RF/Microwave Applications*. New York, NY, USA: Wiley, 2001.

[12] The MathWorks Inc., Boston, MA, USA, MATLAB ver. 2010a, 2010.

[13] Agilent Technologies, Santa Clara, CA, USA, “Agilent Momentum ver. 8.20.374,” 2008.

[14] D. M. Pozar, *Microwave Engineering*. Boston, MA, USA: Addison Wesley, 1990.

[15] I. Bahl and P. Barthia, *Microwave Solid State Circuit Design*. New York, NY, USA: Wiley, 1998.

[16] K. L. Wu, R. Zhang, M. Ehlert, and D. G. Fang, "An explicit knowledge-embedded space mapping technique and its application to optimization of LTCC RF passive circuits," *IEEE Trans. Compon. Packaging Techn.*, vol. 26, no. 2, pp. 399–406, Jun. 2003.

[17] Q. S. Cheng, J. C. Rautio, J. W. Bandler, and S. Koziel, "Progress in simulator-based tuning-the art of tuning space mapping," *IEEE Microw. Mag.*, vol. 11, no. 4, pp. 96–110, Jun. 2010.

Marc Sans was born in Terrassa, Barcelona, Spain, in 1982. He received the B.S. degree in telecommunications engineering–electronic systems, the M.S. degree in telecommunications engineering, and the M.S. degree in electronics engineering from the Universitat Autònoma de Barcelona (UAB), Barcelona, Spain, in 2006, 2008, and 2013, respectively. He is currently working towards the Ph.D. degree in the synthesis of microwave devices based on EM optimization techniques from CIMITEC-UAB.

In 2008, he started his professional career as an RF Engineer with Sony-FTVE developing the RF stage of TV receivers. In 2010, he moved to Mier Comunicaciones S.A. to carry out the design of passive and active devices for VHF-UHF broadcasting units.

Jordi Selga (S'11–M'14) was born in Barcelona, Spain, in 1982. He received the B.S. degree in telecommunications engineering–electronic systems, the M.S. degree in electronics engineering, and the Ph.D. degree in electronics engineering from the Universitat Autònoma de Barcelona (UAB), Barcelona, Spain, in 2006, 2008, and 2013, respectively.

Since 2008, he has been a member of CIMITEC-UAB, a research centre on Metamaterials supported by TECNIO (Catalan Government). He was holder of a national research fellowship from the *Formación de Profesorado Universitario* Program of the Education and Science Ministry (Reference AP2008–4707). He is currently working in subjects related to metamaterials, CAD design of microwave devices, EM optimization methods, and automated synthesis of planar microwave components at the UAB.

Ana Rodriguez (S'10) was born in Lugo, Spain. She received the Telecommunications Engineering degree from the Universidade de Vigo (UV), Pontevedra, Spain, in 2008, and the "Master en Tecnología, Sistemas y Redes de Comunicaciones" from Universitat Politècnica de València (UPV), València, Spain, in 2010, where she is currently pursuing the Ph.D. degree in electrical engineering.

As a student, she participated in the Erasmus exchange program, developing the Master Thesis at the University of Oulu, Finland. Since the end of 2008, she has joined the Institute of Telecommunications and Multimedia Applications (iTEAM), which is part of the scientific park at the Universitat Politècnica de València (UPV), Spain. Her main research interests include CAD design of microwave devices, EM optimization methods, and metamaterials.

Jordi Bonache (S'05–M'07) was born in 1976 in Barcelona, Spain. He received the Physics and Electronics Engineering degrees and the Ph.D. degree in electronics engineering from the Universitat Autònoma de Barcelona, Barcelona, Spain, in 1999, 2001, and 2007, respectively.

Currently, he is leading the research in RFID and antennas in GEMMA/CIMITEC, Departament d'Enginyeria Electrònica, Universitat Autònoma de Barcelona, Bellaterra, Spain. In 2000, he joined the "High Energy Physics Institute" of Barcelona (IFAE), where he was involved in the design and implementation of the control and monitoring system of the MAGIC telescope. In 2001, he joined the Department of Electronics Engineering of the Universitat Autònoma de Barcelona where he is currently a Lecturer. From 2006 to 2009, he worked as an Executive Manager of CIMITEC. His research interests include active and passive microwave devices, metamaterials, antennas, and RFID.

Vicente E. Boria (S'91–A'99–SM'02) was born in Valencia, Spain, on May 18, 1970. He received the "Ingeniero de Telecomunicación" degree (with first-class honors) and the "Doctor Ingeniero de Telecomunicación" degree from the Universidad Politécnica de Valencia, Valencia, Spain, in 1993 and 1997, respectively.

In 1993, he joined the "Departamento de Comunicaciones", Universidad Politécnica de Valencia, where he has been Full Professor since 2003. In 1995 and 1996, he was holding a Spanish Trainee position with the European Space Research and Technology Centre, European Space Agency (ESTEC-ESA), Noordwijk, The Netherlands, where he was involved in the area of EM analysis and design of passive waveguide devices. He has authored or co-authored 7 chapters in technical textbooks, 75 papers in refereed international technical journals, and over 150 papers in international conference proceedings. His current research interests are focused on the analysis and automated design of passive components, left-handed and periodic structures, as well as on the simulation and measurement of power effects in passive waveguide systems.

Dr. Boria has been a member of the IEEE Microwave Theory and Techniques Society (IEEE MTT-S) and the IEEE Antennas and Propagation Society (IEEE AP-S) since 1992. He is reviewer of the IEEE Transactions on Microwave Theory and Techniques, Proceeding of the IET (Microwaves, Antennas, and Propagation), and IET Electronics Letters. Since 2013, he serves as an Associate Editor of the IEEE Microwave and Wireless Components Letters. He is also a member of the Technical Committees of the IEEE-MTT International Microwave Symposium and of the European Microwave Conference.

Ferran Martín (M'04–SM'08–F'12) was born in Barakaldo (Vizcaya), Spain in 1965. He received the B.S. degree in physics and the Ph.D. degreefrom the Universitat Autònoma de Barcelona (UAB), Barcelona, Spain, in 1988 and 1992, respectively.

From 1994 to 2006, he was an Associate Professor in electronics with the Departament d'Enginyeria Electrònica, Universitat Autònoma de Barcelona, and since 2007, he is Full Professor of electronics. In recent years, he has been involved in different research activities including modelling and simulation of electron devices for high frequency applications, millimeter wave, and THz generation systems, and the application of electromagnetic bandgaps to microwave and millimeter wave circuits. He is now very active in the field of metamaterials and their application to the miniaturization and optimization of microwave circuits and antennas. He is the head of the Microwave Engineering, Metamaterials, and Antennas Group (GEMMA Group), UAB, and director of CIMITEC, a research Center on Metamaterials supported by TECNIO (Generalitat de Catalunya). He has authored and co-authored over 450 technical conference, letter, journal papers and book chapters, he is co-author of the book on Metamaterials entitled *Metamaterials with Negative Parameters: Theory, Design and Microwave Applications* (Wiley, 2008), and he has generated 14 Ph.D.s. He has filed several patents on metamaterials and has headed several Development Contracts.

Prof. Martín is a member of the IEEE Microwave Theory and Techniques Society (IEEE MTT-S). He is reviewer of the IEEE Transactions on Microwave Theory and Techniques and IEEE Microwave and Wireless Components Letters, among many other journals, and he serves as member of the Editorial Board of IET Microwaves, Antennas, and Propagation and International Journal of RF and Microwave Computer-Aided Engineering. He has acted as Guest Editor for three Special Issues on Metamaterials in three International Journals. He has organized several international events related to metamaterials, including Workshops at the IEEE International Microwave Symposium (2005 and 2007) and European Microwave Conference (2009), and the Fifth International Congress on Advanced Electromagnetic Materials in Microwaves and Optics (Metamaterials 2011), where he has acted as chair of the Local Organizing Committee. He is also a member of the Technical Committees of the European Microwave Conference (EuMC) and International Congress on Advanced Electromagnetic Materials in Microwaves and Optics (Metamaterials). Among his distinctions, he was a recipient of the 2006 Duran Farell Prize for Technological Research, he holds the *Parc de Recerca UAB—Santander* Technology Transfer Chair, and he has been the recipient of two ICREA ACADEMIA Awards (calls 2008 and 2013).

EUMC15*

M. Sans, J. Selga, P. Vélez, J. Bonache, A. Rodríguez, V. E. Boria, and F. Martín

“Application of Aggressive Space Mapping (ASM) to the Automated Design of Differential-Mode Wideband Bandpass Filters with Common-Mode Suppression”

Application of Aggressive Space Mapping (ASM) to the Automated Design of Differential-Mode Wideband Bandpass Filters with Common-Mode Suppression

Marc Sans[1], Jordi Selga[*1], Paris Vélez[1], Ana Rodríguez[2], Jordi Bonache[1], Vicente E. Boria[2] and Ferran Martín[1]

[1]GEMMA/CIMITEC, Departament d'Enginyeria Electrònica, Universitat Autònoma de Barcelona, 08193 Bellaterra, Spain

[2]Departamento de Comunicaciones-iTEAM, Universitat Politècnica de València, 46022 Valencia, Spain

*E-mail: Jordi.Selga@uab.cat Phone: +34935813524

Abstract— **This paper is focused on the automated design of microstrip differential-mode (balanced) wideband bandpass filters based on mirrored stepped impedance resonators (SIRs) coupled through admittance inverters. The central metallic patches of the mirrored SIRs introduce common-mode transmission zeros, useful for the suppression of that mode in the differential filter pass band. The main relevant and novel aspect of this paper is the implementation of an unattended filter design algorithm, able to automatically provide the filter layout of these differential filters satisfying predefined specifications. The optimization algorithm is based on a two-step aggressive space mapping (ASM) scheme. The first ASM algorithm provides the optimum filter schematic; namely, it recalculates the lumped elements of the resonators and the electrical lengths of the transmission line sections (impedance inverters), in order to compensate the bandwidth reduction related to the limited functionality of the inverters. Once the filter schematic providing the required specifications (optimum schematic) is determined, the second ASM automatically generates the filter layout. The two-step ASM algorithm is validated through the design of an order-5 common-mode suppressed balanced Chebyshev bandpass filter with 40% fractional bandwidth (corresponding to 43.96% -3dB fractional bandwidth) centered at f_0 = 2.4 GHz. Filter design is achieved following a completely unattended scheme, and the response satisfies the specifications to a very good approximation.**

Keywords— Space Mapping, balanced bandpass filters, stepped impedance resonators, microstrip technology.

I. INTRODUCTION

The design of differential-mode wideband bandpass filters with common-mode noise suppression has been object of growing interest in recent years [1-4]. These filters are key elements in balanced circuits and systems (e.g., high-speed digital circuits), of increasing demand for their inherent high immunity to noise, electromagnetic interference (EMI) and crosstalk. The typical requirements of these filters are: (i) small size, (ii) good differential-mode characteristics (including a wide stop band), and (iii) common-mode rejection in the region of interest (differential filter pass band).

The wideband balanced filters reported in [4], based on mirrored stepped impedance resonators (SIRs) coupled through admittance inverters (implemented by means of quarter-wavelength transmission lines), satisfy these requirements. Such filters are adequately described by the schematic proposed in [4], which combines lumped elements (describing the mirrored SIRs) and transmission line sections (to account for the inverters). However, the classical design approach [5] is not valid for wideband filter design, due to the limited (i.e., narrowband) functionality of the inverters, resulting in degraded (narrower) bandwidths, as compared to the nominal values.

Bandwidth reduction can be compensated by over dimensioning the filter bandwidth in the design process. This solution typically involves an iterative process which is rather inefficient. In this work, we propose a systematic approach, based on aggressive space mapping (ASM), to automatically determine the schematic (lumped element values and electrical length and characteristic impedance of the transmission lines) providing the required specifications. After this first ASM, a second ASM algorithm is used to generate the filter layout. This is the first time that a two-step ASM algorithm is applied to the automated and unattended design of a balanced wideband bandpass filter.

II. TOPOLOGY OF THE PROPOSED FILTERS AND CIRCUIT SCHEMATIC

The differential filters considered in this work are implemented through a combination of semi-lumped and distributed elements [Fig.1(a)] [4]. The semi-lumped elements are mirrored SIRs, described by means of a combination of capacitances and inductances, as indicated in Fig. 1(b). The distributed elements are quarter wavelength transmission lines acting as admittance inverters. The circuit schematic of these filters is depicted in Fig. 1(b). Note that the symmetry plane is an electric wall for the differential-mode, and hence the capacitances C_{zi} do not play an active role for that mode (since they are grounded). Thus, the equivalent circuit schematic for the differential-mode is the canonical circuit of a bandpass filter [Fig. 1(c)] [5]. Conversely, the symmetry plane for the common-mode is a magnetic wall (open circuit) and the equivalent circuit schematic is the one depicted in Fig. 1(d). The resonators L_{pi}-C_{zi} provide transmission zeros that are useful for the suppression of the common-mode in the region of interest (differential filter pass band). According to the schematics of Figs. 1(c)-(d), the position of the transmission zeros does not affect the differential-mode response.

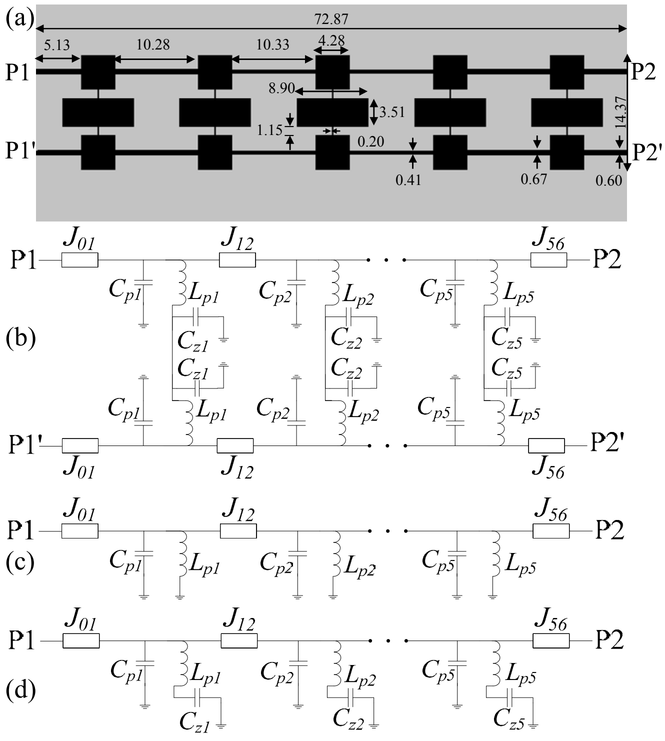

Fig. 1. Typical topology (order-5) of the considered balanced wideband bandpass filters (a), circuit schematic (b), and circuit schematic for the differential (c) and common (d) modes. Dimensions, in millimeters, correspond to the designed prototype.

III. SYNTHESIS OF THE OPTIMUM FILTER SCHEMATIC (FIRST ASM)

The first step of the design process is the determination of the optimum filter schematic for the differential-mode, namely the one that satisfies the specifications. Although this method is similar to the one reported in [6] for single-ended filters, it is described for the case under study for completeness. Let us consider that the filter order, n, is set to a certain value that suffices to achieve the required filter selectivity. The filter specifications are the central frequency, f_0, the fractional bandwidth, FBW, and the in-band ripple level L_{Ar} (or minimum return loss level). The schematic of the filter with ideal admittance inverters can be easily obtained from well-known formulas [5], considering the standard Chebyshev approximation (and hence the lowpass filter prototype element values). In this work we will deal with identical resonators (and thus $L_{pi} = L_p$ and $C_{pi} = C_p$ for $i = 1,2,...,n$), but different admittance inverters. The reason is that, from a topological point of view, it is convenient to implement the filter layout with identical mirrored SIRs, since the impedance inverters can thus be implemented by transmission line sections parallel to the line axis.

Let us consider the following differential filter specifications: $n = 5$, $f_0 = 2.4$GHz, $FBW = 40\%$ (corresponding to a 43.96% −3dB fractional bandwidth, considered in the optimization) and $L_{Ar} = 0.2$dB. The ideal Chebyshev response is depicted in Fig. 2. Such response is achieved by considering $L_p = 0.9902$ nH, $C_p = 4.4413$ pF and ideal admittance inverters with $J_{0,1} = J_{5,6} = 0.02$ S, $J_{1,2} = J_{4,5} = 0.02002$ S, $J_{2,3} = J_{3,4} = 0.0157$ S. Obviously, if we replace the admittance inverters with quarter wavelength transmission lines, the response (bandwidth) is degraded, as shown in Fig. 2. Therefore, the purpose is to re-design the schematic in order to satisfy the specifications (optimum schematic). To this end, an ASM algorithm that carries out the optimization at the schematic level is proposed. The key point in the development of this novel iterative ASM algorithm, is to assume that there exists a set of filter specifications, different than the target, that leads to a filter schematic (inferred by substituting the ideal admittance inverters with quarter wavelength transmission lines), whose response satisfies the target specifications.

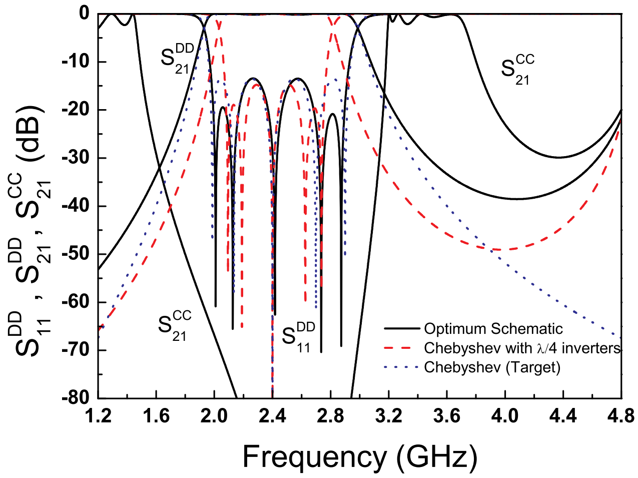

Fig. 2. Ideal Chebyshev response of the differential bandpass filter, response that results by replacing the ideal inverters with quarter wavelength transmission lines, and response of the optimum schematic that results after applying the first ASM algorithm.

Space mapping [7] is a technique that makes use of two simulation spaces: the optimization space, $\mathbf{X_c}$, where the variables are linked to a coarse model, which is simple and computationally efficient, although not accurate; and the validation space, $\mathbf{X_f}$, where the variables are linked to a fine model, typically more complex and CPU intensive, but significantly more precise. In each space, a vector containing the different model parameters is defined. Such vectors are designated as $\mathbf{x_f}$ and $\mathbf{x_c}$ for the fine and coarse model parameters, respectively, and their responses are denoted as $\mathbf{R_f}(\mathbf{x_f})$ and $\mathbf{R_c}(\mathbf{x_c})$. For the determination of the optimum schematic, the so-called aggressive space mapping (ASM) [8] is applied, where a quasi-Newton type iteration is used. The optimization space is constituted by the set of specifications, f_0, FBW, L_{Ar}, being its response the ideal Chebyshev response - target response- depicted in Fig. 2. The validation space is constituted by the same variables, but their response is inferred from the schematic of Fig. 1(c) by replacing the inverters with quarter wavelength transmission lines at f_0, where f_0 is the considered value of this element in the validation space (not necessarily the target filter central frequency). The variables of each space are differentiated by a subscript. Thus, the corresponding vectors in the coarse and fine models are written as $\mathbf{x_c} = [f_{0\mathrm{c}}, FBW_\mathrm{c}, L_{Ar\mathrm{c}}]$ and $\mathbf{x_f} = [f_{0\mathrm{f}}, FBW_\mathrm{f}, L_{Ar\mathrm{f}}]$, respectively. The coarse model solution (target specifications) is expressed as $\mathbf{x_c}^* = [f_{0\mathrm{c}}{}^*, FBW_\mathrm{c}{}^*, L_{Ar\mathrm{c}}{}^*]$.

Following the standard procedure in ASM, the first step before starting the iterative process is to make an estimation of the first vector in the validation space, $\mathbf{x_f}^{(1)}$. Since the variables in both spaces are the same, the most canonical (and simplest) procedure is to consider $\mathbf{x_f}^{(1)} = \mathbf{x_c}^*$. From $\mathbf{x_f}^{(1)}$, the response of the fine model space is obtained (using the schematic with quarter wavelength transmission lines), and from it we directly extract the parameters of the coarse model by direct inspection of that response. This allows us to obtain the first error function (by comparing to the target), i.e.,

$$\mathbf{f}(\mathbf{x_f}) = \mathbf{P}(\mathbf{x_f}) - \mathbf{x_c}^* \tag{1}$$

where $\mathbf{P}(\mathbf{x_f})$ is the vector corresponding to the coarse model parameters extracted from the response of the fine model. To iterate the process following the standard quasi-Newton type ASM approach, the new fine model vector is obtained according to

$$\mathbf{x_f}^{(j+1)} = \mathbf{x_f}^{(j)} + \mathbf{h}^{(j)} \tag{2}$$

where $\mathbf{h}^{(j)}$ is given by:

$$\mathbf{h}^{(j)} = -\left(\mathbf{B}^{(j)}\right)^{-1} \mathbf{f}^{(j)} \tag{3}$$

and $\mathbf{B}^{(j)}$ is an approach to the Jacobian matrix, which is updated according to the Broyden formula:

$$\mathbf{B}^{(j+1)} = \mathbf{B}^{(j)} + \frac{\mathbf{f}^{(j+1)} \mathbf{h}^{(j)T}}{\mathbf{h}^{(j)T} \mathbf{h}^{(j)}} \tag{4}$$

In (4), $\mathbf{f}^{(j+1)}$ is obtained by evaluating (1), and the super-index T stands for transpose. To initiate the Jacobian matrix, we have slightly perturbed the parameters of the fine model, $f_{0\mathrm{f}}$, FBW_f, $L_{Ar\mathrm{f}}$, and we have inferred the effects of such perturbations on the coarse model parameters, $f_{0\mathrm{c}}$, FBW_c, $L_{Ar\mathrm{c}}$). Convergence is achieved once the error function is smaller than a certain predefined value.

The application of this first ASM algorithm to the considered example provides an error function smaller than 0.7% after $N = 3$ iterations. The resulting fine and coarse model parameters are $\mathbf{x_f}^{(3)} = [f_{0\mathrm{f}}{}^{(3),}\ FBW_\mathrm{f}{}^{(3),}\ L_{Ar\mathrm{f}}{}^{(3)}]$ = [2.4166 GHz, 65.33%, 0.278 dB] and $\mathbf{x_c}^{(3)} = [f_{0\mathrm{c}}{}^{(3)}, FBW_\mathrm{c}{}^{(3)}, L_{Ar\mathrm{c}}{}^{(3)}]$ = [2.400 GHz, 44.08%, 0.201 dB], and the resulting response is depicted in Fig. 2. This means that the optimum filter schematic is the result of applying the standard formulas [5] and replacing the ideal inverters with quarter wavelength transmission lines, but considering the specifications given by $\mathbf{x_f}^{(3)}$. The element values of the resonators are $L_p = 1.365$ nH, $C_p = 3.176$ pF, and the admittance of the quarter wavelength (at $f_{0\mathrm{f}}{}^{(3)}$) transmission line sections are $J_{0,1} = J_{5,6} = 0.02$ S, $J_{1,2} = J_{4,5} = 0.0211$ S, $J_{2,3} = J_{3,4} = 0.0168$ S. To complete the schematic of Fig. 1(b), the capacitances C_{zi} must be set to a certain value. In this work, we have opted for setting all the transmission zero frequencies to the same value, i.e., $f_z = 1.1 f_0$. This gives a good common-mode rejection ratio (CMRR) in the whole differential filter pass band. With this value of f_z the value of the central patch capacitances is $C_z = 2.625$ pF.

IV. SYNTHESIS OF THE FILTER LAYOUT (SECOND ASM)

For the synthesis of the layout, we have to obtain each filter cell from the element values of the shunt resonator and the characteristic impedance and the phase of the transmission lines sections. Therefore, this second ASM has three stages. First of all, the line width for each transmission line section is optimized (this is simple since it involves only one parameter in each space, i.e., the width in the validation space, and the characteristic impedance in the optimization space). In the second stage, the layout of the mirrored SIRs is determined, using an ASM algorithm with three variables. The variables in the optimization space are the elements of the shunt resonator from the circuit schematic for the common mode depicted in Fig. 1(d), i.e., $\mathbf{x_c} = [L_{pi}, C_{pi}, C_{zi}]$, and the coarse model response is obtained through circuit simulation. The validation space is constituted by a set of variables defining the resonator layout. In order to deal with the same number of variables in both spaces, the widths of the central patch, W_{Czi}, as well as the widths of the high- and low-impedance transmission line sections of the SIRs, W_{Lpi} and W_{Cpi}, respectively, are set to fixed values. There is some flexibility to choose these widths, but it is convenient to consider wide capacitive and narrow inductive sections to reduce the length of the SIRs. Concerning the width of the central capacitive patch, it is suitable to set it to be smaller than the length of the $\lambda/4$ transmission line sections, in order to avoid overlapping between adjacent patches. Thus, the variables in the validation space are the remaining dimensions of the shunt resonators, that is, the length of the central capacitive patch, l_{Czi}, and the lengths l_{Lpi} and l_{Cpi} of the high- and low-impedance transmission line sections, respectively, of the SIR (i.e., $\mathbf{x_f} = [l_{Lp}, l_{Lr}, l_{Czi}]$). A parameter extraction method is applied in order to extract the coarse model parameters from the electromagnetic simulation of the isolated mirrored SIRs at each iterative step [4]. Specifically, we can obtain L_{pi} and C_{pi} from the differential mode response, and C_{zi} from the common mode response (depicted in Fig. 3). The final solution is obtained after few iterations (N=6) with a reasonable error (<1.7%) and the frequency response is very close to the target solution.

Finally, the length of the lines cascaded to the resonant elements is optimized by considering the whole filter cell. This is necessary since the patch capacitances corresponding to C_{pi} introduce some phase shift. However, this optimization is simple since only the length of the lines cascaded to the resonators must be optimized.

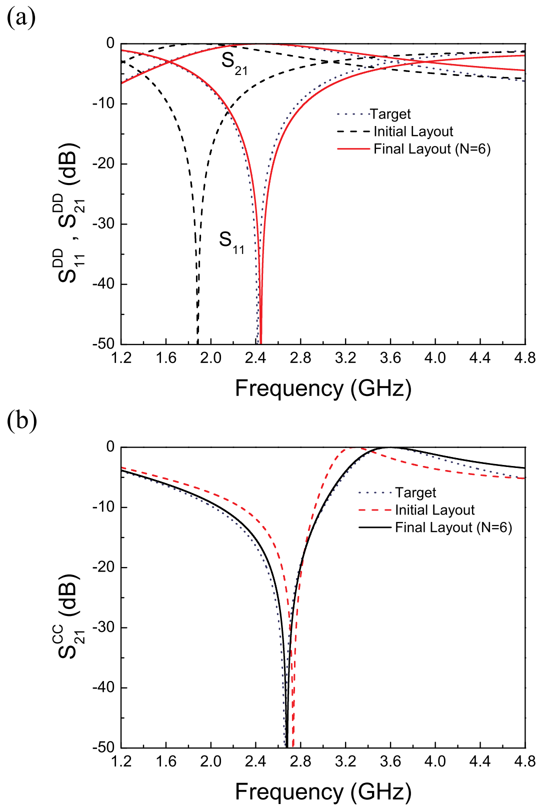

Fig. 3. Frequency response of the optimitzed mirrored SIR. (a) differential mode; (b) and common mode.

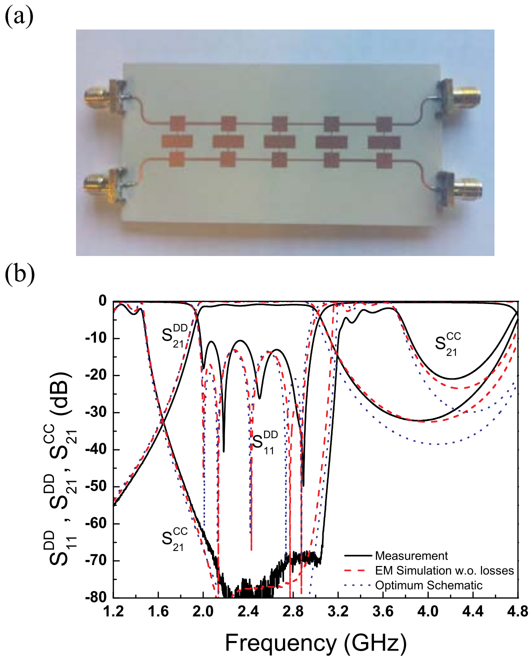

Fig. 4. Photograph of the fabricated prototype of the designed balanced order-5 bandpass filter (a) and frequency response (differential and common-mode) (b). The considered substrate is *Rogers RO3010* with dielectric constant $\varepsilon_r = 10.2$ and thickness $h = 635$ µm.

V. RESULTS

By merely cascading the filter cells, the layout is obtained (see Fig. 1). The lossless electromagnetic response (inferred by *Agilent Momentum*) is very close to the target response [Fig. 4]. It is noteworthy to say that no further optimization has been carried out. The fabricated device [depicted in Fig. 4(a)] exhibits a frequency response in very good agreement to the target (with the exception of the loss level). The filter layout has been determined from the specifications without the need of any further action during the optimization process.

VI. CONCLUSION

In conclusion, we have developed a two-step ASM algorithm useful for the automated and unattended optimization of common-mode suppressed balanced filters based on mirrored SIRs coupled through admittance inverters. Conveniently adapted, this two-step ASM iterative algorithm can be applied to the automated design of many other balanced and single-ended filters.

ACKNOWLEDGMENT

This work has been supported by MINECO-Spain (projects TEC2010-17512 METATRANSFER, TEC2010-21520-C04-01, TEC2013-47037-C5-1-R, CONSOLIDER EMET CSD2008-00066, TEC2013-40600-R and TEC2013-49221-EXP), Generalitat de Catalunya (project 2014SGR-157), and Institució Catalana de Recerca i Estudis Avançats (who has awarded Ferran Martín).

REFERENCES

[1] T.B. Lim, and L. Zhu, “A differential-mode wideband bandpass filter on microstrip line for UWB applications,” *IEEE Microw. Wireless Compon. Lett.*, vol. 19, pp. 632-634, Oct. 2009.

[2] A.M. Abbosh, “Ultrawideband balanced bandpass filter”, *IEEE Microw. Wireless Compon. Lett.*, vol. 21, pp. 480-482, Sep. 2011.

[3] X-H. Wu, Q-X. Chu, “Compact differential ultra-wideband bandpass filter with common-mode suppression”, *IEEE Microw. Wireless Compon. Lett.*, vol. 22, pp. 456-458, Sep. 2012.

[4] P. Vélez, M. Durán-Sindreu, J.Bonache, A. Fernández-Prieto, J. Martel, F. Medina and F. Martín, “Differential bandpass filters with common-mode suppression based on stepped impedance resonators (SIRs)”, *IEEE MTT-S Int. Microwave Symp.*, June 2013, Seattle (USA).

[5] J.S. Hong and M.J. Lancaster, *Microstrip Filters for RF/Microwave Applications*, John Wiley, 2001.

[6] M. Sans, J. Selga, A. Rodríguez, J. Bonache, V.E. Boria, and F. Martín, “Design of planar wideband bandpass filters from specifications using a two-step aggressive space mapping (ASM) optimization algorithm”, *IEEE Trans. Microw. Theory Techn.*, vol. 62, pp. 3341-3350, Dec. 2014.

[7] J.W. Bandler, R.M. Biernacki, S.H. Chen, P.A. Grobelny and R.H. Hemmers, “Space mapping technique for electromagnetic optimization”, *IEEE Trans. Microw. Theory Techn.*, vol. 42, pp. 2536–2544, Dec. 1994.

[8] J.W. Bandler, R.M. Biernacki, S.H. Chen, R.H. Hemmers, and K. Madsen, “Electromagnetic optimization exploiting aggressive space mapping”, *IEEE Trans. Microw. Theory Techn.*, vol. 43, pp. 2874–2882, Dec. 1995.

TMTT15

M. Sans, J. Selga, P. Vélez, A. Rodríguez, J. Bonache, V. E. Boria, and F. Martín

"Automated Design of Common-Mode Suppressed Balanced Wideband Bandpass Filters by Means of Aggressive Space Mapping"

Automated Design of Common-Mode Suppressed Balanced Wideband Bandpass Filters by Means of Aggressive Space Mapping

Marc Sans, *Student Member, IEEE*, Jordi Selga, *Member, IEEE*, Paris Vélez, *Member, IEEE*,
Ana Rodríguez, *Member, IEEE*, Jordi Bonache, *Member, IEEE*, Vicente E. Boria, *Senior Member, IEEE*, and
Ferran Martín, *Fellow, IEEE*

***Abstract*—The automated and unattended design of balanced microstrip wideband bandpass filters by means of aggressive space mapping (ASM) optimization is reported in this paper. The proposed filters are based on multisection mirrored stepped impedance resonators (SIRs) coupled through quarter-wavelength transmission lines, acting as admittance inverters. Such resonant elements provide transmission zeros useful for the suppression of the common mode in the region of interest (differential filter pass band) and for the improvement of the differential-mode stopband (rejection level and selectivity). Due to the limited functionality of the inverters, related to the wide fractional bandwidths, the automated filter design requires a two-step process. With the first ASM, the filter schematic satisfying the required specifications (optimum filter schematic) is determined. Then, the layout is synthesized by means of a second ASM algorithm. Both algorithms are explained in detail and are applied to the synthesis of two filters, as illustrative (and representative) examples. With this paper, it is demonstrated that the two-step ASM optimization scheme (first providing the optimum schematic and then the layout), previously applied by the authors to wideband single-ended filters, can be extended (conveniently modified) to common-mode suppressed differential-mode bandpass filters. Thus, the value of this two-step ASM approach is enhanced by demonstrating its potential for the unattended design of complex filters, as those considered in this paper.**

***Index Terms*—Balanced filters, bandpass filters, circuit synthesis, microstrip technology, optimization, space mapping (SM), stepped impedance resonators (SIRs).**

I. INTRODUCTION

IN recent years, many efforts have been dedicated to the design of compact common-mode suppressed balanced wideband and ultrawideband (UWB) bandpass filters [1]–[16]. This interest is justified by the increasing demand of balanced circuits and systems (e.g., high-speed digital circuits), related to their inherent high immunity to noise, electromagnetic interference (EMI), and crosstalk. In some reported balanced filters, efficient common-mode suppression in the region of interest (differential-mode pass band) is achieved at the expense of filter size, by cascading additional stages specifically designed to reject the common mode [17], [18]. To reduce the device size, filter topologies able to intrinsically reject the common mode, and simultaneously providing the filtering functionality for the differential mode, are needed. This is indeed the case of most of the reported wideband and UWB balanced filters. However, frequency selectivity and stopband rejection level and bandwidth for the differential mode are typically limited in such filters. Exceptions are the filters reported in [10], [13], and [16], where good stopband behavior for the differential mode above the passband of interest, mainly due to the presence of transmission zeros for that mode, is demonstrated. Nevertheless, the filters reported in [13] are implemented by means of three metal layers (i.e., increasing fabrication complexity), whereas the design and synthesis of the filters presented in [10] is not straightforward, since open split-ring resonators (OSRRs) in microstrip technology cannot be described by a simple circuit model.

This paper is focused on the balanced filters first reported in [16]. These filters exhibit good performance (i.e., wide differential-mode bandwidth, good stopband rejection level, bandwidth and selectivity, and intrinsic common-mode suppression), small size, and simple fabrication process (two metal levels and via free), and they can be accurately described through a circuit schematic that combines lumped and distributed elements (important for design purposes). Specifically, the considered filters are inspired by the highly selective single-ended filters reported in [19]. By mirroring such single-ended filters and by adding central capacitive patches in the bisecting symmetry plane, a highly selective wideband bandpass response for the differential-mode and common-mode suppression over a wide band are simultaneously achieved [16]. As compared with [16], in this paper, we provide a systematic design procedure of these filters, able to provide the filter layout following a completely unattended scheme. Moreover, we report two design examples, a comparison to many other wideband balanced filters, and a discussion on bandwidth limitations for the differential mode.

Manuscript received May 29, 2015; revised August 30, 2015; accepted October 05, 2015. Date of publication November 05, 2015; date of current version December 02, 2015. This work was supported by MINECO-Spain (projects TEC2013-47037-C5-1-R, TEC2013-40600-R, TEC2013-49221-EXP), *Generalitat de Catalunya* (project 2014SGR-157), *Institució Catalana de Recerca i Estudis Avançats* (who awarded Ferran Martín), and by FEDER funds.

M. Sans, J. Selga, P. Vélez, J. Bonache, and F. Martín are with GEMMA/CIMITEC, Departament d'Enginyeria Electrònica, Universitat Autònoma de Barcelona, 08193 Bellaterra, Spain (e-mail: Ferran.Martin@uab.es).

A. Rodríguez and V. E. Boria are with Departamento de Comunicaciones-iTEAM, Universitat Politècnica de València, 46022 Valencia, Spain (e-mail: vboria@dcom.upv.es).

Color versions of one or more of the figures in this paper are available online at http://ieeexplore.ieee.org.

Digital Object Identifier 10.1109/TMTT.2015.2495180

The resulting filters are thus composed of transverse multisection stepped impedance resonators (SIRs) [20] coupled through admittance inverters (implemented by means of quarter wavelength transmission lines). As it is well known, these lines are not able to provide the inverter functionality over wide bands. Thus, to compensate for the bandwidth degradation associated to the limited functionality of the inverters, a design method based on aggressive space mapping (ASM) optimization [21]–[24] is reported here. Several efficient methods have been developed since ASM, such as response correction techniques [25], manifold mapping [26] feature-based optimization [27], or faster techniques based on SM [28]. However, the ASM optimization technique has been chosen to develop the design method presented due to the good results obtained in previous works [29]–[31]. This method provides the filter schematic (optimum schematic) able to satisfy the specifications for the differential-mode and common-mode responses. Then, once the schematic is determined, a second ASM algorithm is applied to the determination of the filter layout. Hence, the proposed unattended design tool follows a two-step ASM process, similar to the one reported in [32] for the design of the single-ended counterparts. However, the balanced (symmetric) topologies considered force us to substantially modify the two-step ASM algorithm reported in [32]. The details of such algorithm are the essential part of this paper.

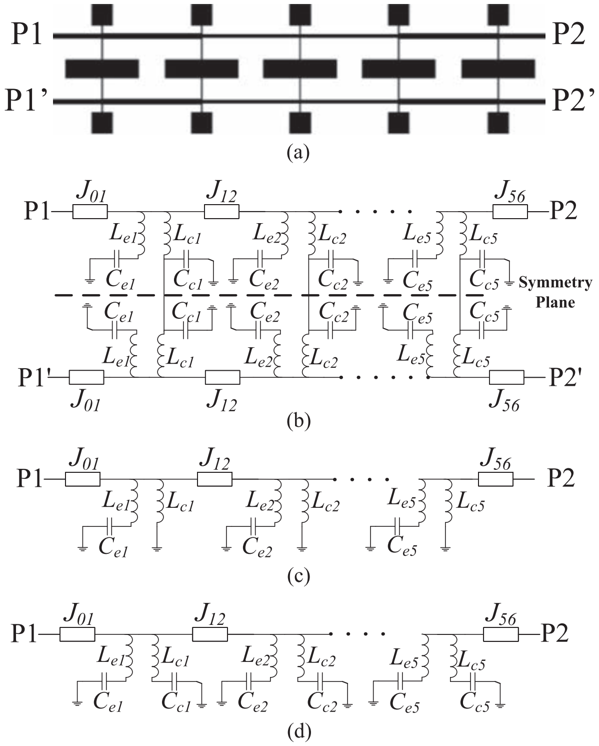

Fig. 1. Topology (order-5) of the considered (a) balanced wideband bandpass filters, (b) circuit schematic, and circuit schematic for the (c) differential and (d) common modes.

The paper is organized as follows. The topology and general circuit schematic of the considered balanced filters, including the schematics for the differential and common modes, are presented in Section II. Section III is devoted to give the details of the first ASM algorithm, providing the optimum filter schematic. A succinct review of the general formulation of ASM, necessary for coherence and completeness, is also included in this section. The next section (Section IV) is focused on the second ASM, where the details to generate the filter layout are provided. Sections III and IV include a conducting case example of an order-5 balanced filter, for better understanding of the proposed two-step ASM algorithm. Nevertheless, an additional synthesis example (an order-7 filter) is reported in Section V, in order to demonstrate the potential and versatility of the approach. A comparative analysis of the proposed filters, in the context of other solutions for balanced filters reported in the literature, is presented in Section VI. Section VII is devoted to discuss the bandwidth limitations of the reported filters. Finally, the main conclusions are highlighted in Section VIII.

II. TOPOLOGY AND CIRCUIT SCHEMATIC

The proposed balanced wideband bandpass filters are implemented by combining semi-lumped and distributed elements [Fig. 1(a)]. The semi-lumped elements are transverse multisection mirrored SIRs, described by means of a combination of capacitances and inductances, as indicated in Fig. 1(b). The distributed elements are quarter-wavelength differential transmission lines acting as admittance inverters.

The circuit schematic of these filters is depicted in Fig. 1(b). The symmetry plane is an electric wall for the differential mode. Hence, the capacitances C_{ci} do not play an active role for that mode since they are grounded. Thus, the equivalent circuit schematic for the differential mode is the one depicted in Fig. 1(c). Conversely, the symmetry plane for the common mode is a magnetic wall (open circuit), and the equivalent circuit schematic is the one depicted in Fig. 1(d). The resonators $L_{ci} - C_{ci}$ provide transmission zeros that are useful for the suppression of the common mode in the region of interest (differential filter passband). According to the schematics of Fig. 1(c) and (d), the position of the common-mode transmission zeros does not affect the differential-mode response. Similarly, the resonators $L_{ei} - C_{ei}$ provide transmission zeros for both the differential and common modes. By allocating these transmission zeros above the differential-mode passband, frequency selectivity and stopband rejection for the differential mode can be enhanced.

III. DETERMINATION OF THE OPTIMUM FILTER SCHEMATIC

As indicated in the introduction, wideband bandpass filters based on resonant elements coupled through admittance inverters (in practice, quarter-wavelength transmission line sections), designed by means of the classical formulas [33] from the lowpass filter prototype, are subjected to a fundamental limitation related to the narrowband functionality of the real inverters: bandwidth reduction (as compared with the nominal value). It is obvious that by overdimensioning the bandwidth, such inherent bandwidth degradation can be compensated. However, the in-band return loss level (or ripple) is also modified as a consequence of the limited functionality of the inverters. Thus, a systematic procedure to guarantee that the required filter specifications (central frequency f_0, fractional bandwidth (FBW), and ripple L_{Ar}) can be satisfied is needed.

Such a procedure was reported in [32], where it was successfully applied to the automated design of wideband single-ended filters. In this paper, the method is adapted for its application to the unattended design of common-mode suppressed balanced wideband bandpass filters of the type depicted in Fig. 1.

The main hypothesis of the method is that there exists a set of filter specifications (f_0, FWB, and L_{Ar}), different than the target, that provide a filter response (after application of the synthesis formulas and replacement of the inverters with quarter wavelength transmission lines) satisfying the target specifications. If these specifications (different than the target) are known, the resulting filter schematic (composed of lumped elements, i.e., the resonators, plus distributed elements, namely, the quarter-wavelength transmission lines) is the one that must be synthesized by the considered layout. Thus, filter design is a two-step process, where first the filter schematic providing the required specifications (optimum filter schematic) is determined, and then the layout is generated. For the two design steps, an ASM algorithm is developed. The first one is detailed in this section, whereas the second one is left for Section IV. Nevertheless, the general formulation of ASM is first reported for completeness and for better comprehension of the reported ASM algorithms.

A. General Formulation of ASM

Space mapping (SM) [21]–[24] uses two simulation spaces: i) the optimization space $\mathbf{X_c}$, where the variables are linked to a coarse model, which is simple and computationally efficient, although not accurate, and ii) the validation space $\mathbf{X_f}$, where the variables are linked to a fine model, typically more complex and CPU intensive, but significantly more precise. In each space, a vector containing the different model parameters can be defined. Such vectors are denoted as $\mathbf{x_f}$ and $\mathbf{x_c}$ for the fine and coarse model spaces, respectively, and their corresponding responses are $\mathbf{R_f}(\mathbf{x_f})$ and $\mathbf{R_c}(\mathbf{x_c})$. In a typical SM optimization algorithm involving a planar microwave circuit described by a lumped element model, the variables of the optimization space are the set of lumped elements, and the response in this space is inferred from the circuit simulation of the lumped element model. The variables of the validation space are the set of dimensions that define the circuit layout (the substrate parameters are usually fixed and hence they are not optimization variables), and the response in this space is obtained from the electromagnetic simulation of the layout.

In this paper, we consider the so-called ASM [22], where the goal is to find a solution of the following system of nonlinear equations $\mathbf{f}(\mathbf{x_f}) = 0$ where

$$\mathbf{f}(\mathbf{x_f}) = \mathbf{P}(\mathbf{x_f}) - \mathbf{x_c^*} \tag{1}$$

and $\mathbf{x_c^*}$ is the coarse model solution that gives the target response, $\mathbf{R_c}(\mathbf{x_c^*})$, and $\mathbf{P}(\mathbf{x_f})$ is a parameter transformation mapping the fine model parameter space to the coarse model parameter space. In reference to the two spaces considered above, $\mathbf{P}(\mathbf{x_f})$ provides the coarse model parameters from the fine model parameters typically by means of a parameter extraction procedure [34], [35].

Let us assume that $\mathbf{x_f}^{(j)}$ is the jth approximation to the solution in the validation space, and $\mathbf{f}^{(j)}$ the error function corresponding to $\mathbf{f}(\mathbf{x_f}^{(j)})$. The next vector of the iterative process $\mathbf{x_f}^{(j+1)}$ is obtained by a quasi-Newton iteration according to

$$\mathbf{x_f}^{(j+1)} = \mathbf{x_f}^{(j)} + \mathbf{h}^{(j)} \tag{2}$$

where $\mathbf{h}^{(j)}$ is given by

$$\mathbf{h}^{(j)} = -\left(\mathbf{B}^{(j)}\right)^{-1} \mathbf{f}^{(j)} \tag{3}$$

and $\mathbf{B}^{(j)}$ is an approach to the Jacobian matrix, which is updated according to the Broyden formula [22]

$$\mathbf{B}^{(j+1)} = \mathbf{B}^{(j)} + \frac{\mathbf{f}^{(j+1)}\mathbf{h}^{(j)T}}{\mathbf{h}^{(j)T}\mathbf{h}^{(j)}}. \tag{4}$$

In (4), $\mathbf{f}^{(j+1)}$ is obtained by evaluating (1), and the super-index T stands for transpose.

B. ASM Applied to the Synthesis of the Optimum Filter Schematic

The differential-mode response of the proposed filters is described by a circuit schematic consisting of shunt resonators coupled through admittance inverters [Fig. 1(c)]. The circuit is identical to the one reported in [32], in reference to the single-ended balanced filters of that work. Thus, a similar ASM approach to the one reported in [32] to determine the optimum filter schematic has been developed. Note that the capacitances C_{ci} [Fig. 1(d)] do not have any influence on the differential-mode response. Indeed, the first ASM applies only to the schematic corresponding to the differential mode. Thus, the capacitances C_{ci} are independently determined in order to set the common-mode transmission zeros to the required values, and thus achieve an efficient common-mode suppression in the region of interest (differential-mode pass band). Nevertheless, the second ASM involves the whole filter cell, hence including the patches corresponding to the capacitances C_{ci}. There is, however, an important difference between the filter schematic (differential-mode) of this work, and the one considered in [32] for the single-ended counterparts. In [32], the admittance of the inverters (quarter wavelength transmission line sections) were forced to be identical (0.02 S), resulting in different resonators from stage to stage. In this paper, we have considered identical resonators and different admittances of the inverters [note that this is the case of the topology shown in Fig. 1(a)]. The reason is that by considering identical resonators, the synthesis of the layout is simpler since it is guaranteed that the distance between the pair of lines is uniform along the whole filter. Otherwise, if we deal with different resonators, the inductances L_{ci} may be different, resulting in different lengths if the widths are considered identical, as is the case (see Section IV-A). Note that these widths are identical in order to reduce the number of geometrical parameters in the second ASM. Hence, different length means that the distance between the bi-section plane and the lines is not uniform unless meanders are used, which is not considered to be the optimum solution.

Considering that the filter order n is set to a certain value that suffices to achieve the required filter selectivity, the filter specifications (differential-mode) are the central frequency

f_0, the fractional bandwidth (FBW), and the in-band ripple level L_{Ar} (or minimum return loss level). The transmission zero frequencies provided by the resonators L_{ei}, C_{ei} are set to $f_z = 2f_0$, since this provides spurious suppression, and good filter selectivity above the upper band edge [32]. From the well-known impedance and frequency transformations from the lowpass filter prototype [33], and assuming a Chebyshev response, the reactive elements of the shunt resonators (L_e, C_e, and L_c), identical for all stages for the explained reasons, can be easily inferred. The three conditions to unequivocally determine L_e, C_e, and L_c are i) the filter central frequency, given by

$$f_0 = \frac{1}{2\pi\sqrt{(L_e + L_c)C_e}} \tag{5}$$

and ii) the transmission zero frequency

$$f_z = \frac{1}{2\pi\sqrt{L_e C_e}} \tag{6}$$

and iii) the susceptance slope at f_0

$$b = 2\pi f_0 \frac{C_e(L_e + L_c)^2}{L_c^2}. \tag{7}$$

Considering that the target is an order-5 ($n = 5$) Chebyshev response with $f_0 = 2.4$ GHz, FBW = 40% (corresponding to a 43.91% −3-dB fractional bandwidth) and $L_{\mathrm{Ar}} = 0.2$ dB, and setting the susceptance slope to $b = 0.067$ S, the element values of the shunt resonators are found to be $L_e = 0.4401$ nH, $C_e = 2.4983$ pF, and $L_c = 1.3202$ nH, and the admittance of the inverters $J_{0,1} = J_{5,6} = 0.0200$ S, $J_{1,2} = J_{4,5} = 0.0200$ S, and $J_{2,3} = J_{3,4} = 0.0157$ S. This susceptance slope value has been chosen in order to obtain an admittance value of 0.02 S for the inverters of the extremes of the device. It is worth to mention that for Chebyshev bandpass filters the fractional bandwidth is given by the ripple level and is hence smaller than the −3-dB fractional bandwidth. However, in this paper we will deal with the −3-dB fractional bandwidth since the ripple level is not constant in the optimization process (to be described). From now on, this −3-dB fractional bandwidth is designated as FBW, rather than $\mathrm{FBW}_{-3\ \mathrm{dB}}$ (as usual), for simplicity, and to avoid an excess of subscripts in the formulation.

The quasi-Chebyshev filter response (i.e., the one inferred from the schematic of Fig. 1(c), but with ideal admittance inverters), depicted in Fig. 2, is similar to the ideal (target) Chebyshev response in the pass band region, and it progressively deviates from it as frequency approaches f_z, as expected. The discrepancies are due to the fact that the shunt resonator is actually a combination of a grounded series resonator (providing the transmission zero) and a grounded inductor. The quasi-Chebyshev response satisfies the specifications to a rough approximation. Hence, the target is considered to be the ideal Chebyshev response (except for the transmission zero frequency), also included in the figure. If the ideal admittance inverters are replaced with quarter wavelength transmission lines, the response is further modified. Thus, our aim is to find the filter schematic for the differential-mode [Fig. 1(c)] able to satisfy the specifications. To this end, an ASM algorithm, similar to the one reported in [32], that carries out the optimization at the schematic level has been developed.

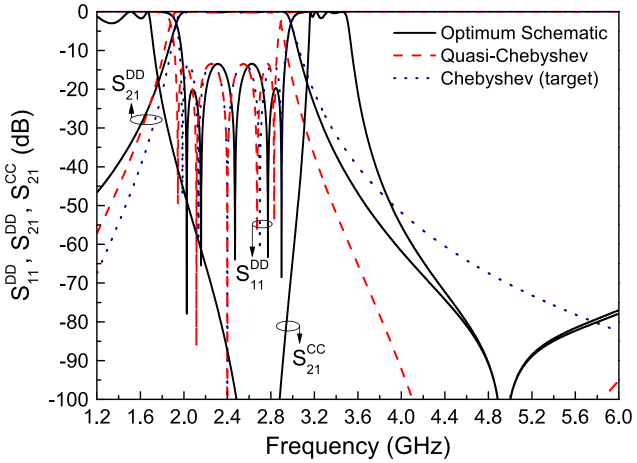

Fig. 2. Differential-mode quasi-Chebyshev response of the filter that results by using the element values indicated in the text and ideal admittance inverters with the indicated admittances, compared with the ideal Chebyshev (target) response and the response of the optimum filter schematic. The response of the optimum filter schematic to the common mode is also included.

As mentioned before, the key point in the development of this first iterative ASM algorithm is to assume that there is a set of filter specifications, different from the target, that leads to a filter schematic (inferred by substituting the ideal admittance inverters with quarter wavelength transmission lines), whose response satisfies the target specifications. In brief, the optimization (coarse model) space is constituted by the set of specifications, f_0, FBW, L_{Ar}, being its response the ideal Chebyshev response(target response) depicted in Fig. 2. The validation space is constituted by the same variables, but their response is inferred from the schematic of Fig. 1(c), with element values calculated as specified above, and quarter-wavelength transmission lines at f_0, where f_0 is the considered value of this element in the validation space (not necessarily the target filter central frequency). The variables of each space are differentiated by a subscript. Thus, the corresponding vectors in the coarse and fine models are written as $\mathbf{x_c} = [f_{0\mathrm{c}}, \mathrm{FBW_c}, L_{\mathrm{Arc}}]$, and $\mathbf{x_f} = [f_{0\mathrm{f}}, \mathrm{FBW_f}, L_{\mathrm{Arf}}]$, respectively. The coarse model solution (target specifications) is expressed as $\mathbf{x_c^*} = [f_{0\mathrm{c}}^*, \mathrm{FBW_c^*}, L_{\mathrm{Arc}}^*]$. The transmission zero frequency, set to $f_z = 2f_0$, as indicated before, is not a variable in the optimization process.

As it was done in [32], the first vector in the validation space is set to $\mathbf{x_f}^{(1)} = \mathbf{x_c^*}$. From $\mathbf{x_f}^{(1)}$, the response of the fine model space is obtained (using the schematic with quarter wavelength transmission lines), and from it, we directly extract the parameters of the coarse model by direct inspection of that response, i.e., $\mathbf{x_c}^{(1)} = \mathbf{P}(\mathbf{x_f}^{(1)})$. Applying (1), we can thus obtain the first error function. The Jacobian matrix is initiated by slightly perturbing the parameters of the fine model, $f_{0\mathrm{f}}$, $\mathrm{FBW_f}$, and L_{Arf}, and inferring the effects of such perturbations on the coarse model parameters, $f_{0\mathrm{c}}$, $\mathrm{FBW_c}$, and L_{Arc}. Thus, the first Jacobian matrix is given by

$$\mathbf{B} = \begin{pmatrix} \frac{\delta f_{0\mathrm{c}}}{\delta f_{0\mathrm{f}}} & \frac{\delta f_{0\mathrm{c}}}{\delta \mathrm{FBW_f}} & \frac{\delta f_{0\mathrm{c}}}{\delta L_{\mathrm{Arf}}} \\ \frac{\delta \mathrm{FBW_c}}{\delta f_{0\mathrm{f}}} & \frac{\delta \mathrm{FBW_c}}{\delta \mathrm{FBW_f}} & \frac{\delta \mathrm{FBW_c}}{\delta L_{\mathrm{Arf}}} \\ \frac{\delta L_{\mathrm{Arc}}}{\delta f_{0\mathrm{f}}} & \frac{\delta L_{\mathrm{Arc}}}{\delta \mathrm{FBW_f}} & \frac{\delta L_{\mathrm{Arc}}}{\delta L_{\mathrm{Arf}}} \end{pmatrix} \tag{8}$$

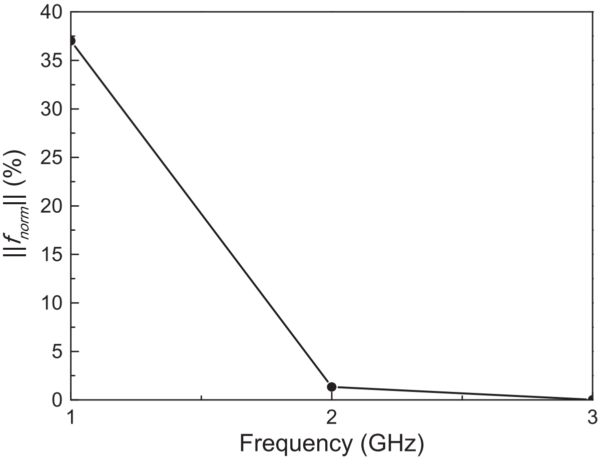

Fig. 3. Evolution of the error function of the first ASM algorithm for the considered example.

Once the first Jacobian matrix is obtained, the process is iterated [obtaining $\mathbf{x_f}^{(2)}$ from (2), using (3), and so on] until convergence is obtained. At each iteration, the elements of the coarse space vector $\mathbf{x_c}^{(j)}$ are compared with the target (filter specifications), $\mathbf{x_c^*}$, and the error function is obtained according to

$$||f_{\mathrm{norm}}||=\sqrt{\left(1-\frac{f_{0\mathrm{c}}}{f_{0\mathrm{c}}^*}\right)^2+\left(1-\frac{\mathrm{FBW_c}}{\mathrm{FBW_c^*}}\right)^2+\left(1-\frac{L_{\mathrm{Arc}}}{L_{\mathrm{Arc}}^*}\right)^2}. \tag{9}$$

The flow diagram of this first ASM algorithm, able to provide the optimum filter schematic, can be found in [32], and, hence, it is not reproduced here. Applying the developed ASM algorithm to the considered example ($\mathbf{x_c^*} = [f_{0\mathrm{c}}^*, \mathrm{FBW_c^*}, L_{\mathrm{Arc}}^*] = [2.4\ \mathrm{GHz}, 43.91\%, 0.2\ \mathrm{dB}]$), we have found that the error function rapidly decreases, with the error being smaller than 0.02% after $N = 3$ iterations. The evolution of the error function is depicted in Fig. 3. The fine model parameters for the last iteration ($N = 3$) are $\mathbf{x_f}^{(3)} = [f_{0\mathrm{f}}^{(3)}, \mathrm{FBW_f}^{(3)}, L_{\mathrm{Arf}}^{(3)}] = [2.4703\ \mathrm{GHz}, 65.3\%, 0.2786\ \mathrm{dB}]$, and the coarse model parameters are $\mathbf{x_c}^{(3)} = [f_{0\mathrm{c}}^{(3)}, \mathrm{FBW_c}^{(3)}, L_{\mathrm{Arc}}^{(3)}] = [2.400\ \mathrm{GHz}, 43.91\%, 0.199987\ \mathrm{dB}]$. Note that $\mathbf{x_f}$ is appreciably different than $\mathbf{x_c^*}$. The optimum filter schematic is the one that gives the last fine model response (which provides an error below a predefined value). The elements of the shunt resonators for this optimum filter schematic are $L_e = 0.5935$ nH, $C_e = 1.7486$ pF, and $L_c = 1.7804$ nH, whereas the admittances of the inverters (quarter-wavelength transmission line sections at $f_{0\mathrm{f}}^{(3)} = 2.4703\ \mathrm{GHz} \neq f_0^*$ are $J_{0,1} = J_{5,6} = 0.02$ S, $J_{1,2} = J_{4,5} = 0.0211$ S, $J_{2,3} = J_{3,4} = 0.0168$ S.

The response of the optimum schematic is compared with the target response in Fig. 2. The agreement in terms of central frequency, bandwidth, and in-band ripple is very good, as expected on account of the small error function that has been obtained after $N = 3$ iterations. However, the position of the reflection zero frequencies are different in both responses, since we have not considered these frequency positions as goals in the optimization process. Nevertheless, the synthesized circuit fulfills the target specifications for the differential mode. To complete the circuit schematic of Fig. 1(b), valid for both modes, the capacitances C_{ci} need to be determined. As mentioned before, such capacitances are determined by the position of the transmission zeros for the common mode according to

$$f_{zi}^{cc} = \frac{1}{2\pi\sqrt{L_c C_{ci}}} \tag{10}$$

where the superindex indicates that these transmission zeros correspond to the common mode, and the subindex i indicates the filter stage. Note that there is no reason, *a priori*, to set the transmission zeros to the same value. Nevertheless, for the considered example, all the transmission zeros have been set to 2.717 GHz (i.e., 1.1 $f_{0\mathrm{f}}^{(3)}$), and, hence, $C_{ci} = 1.9268$ pF (the resulting response for the common mode is also depicted in Fig. 2). Thus, the schematic resulting from this first ASM process, including C_{ci}, is the optimum filter schematic used as the starting point in the ASM algorithm developed to obtain the filter layout, to be described in the next section.

IV. LAYOUT SYNTHESIS

The layout synthesis involves the determination of i) the dimensions of the resonant elements (multi-section mirrored SIRs), ii) the width of the transmission line sections (inverters), and iii) their lengths. Hence, three specific ASM subprocesses are developed for the automated synthesis of the filter layout, following a scheme similar to that reported in [32] for the synthesis of single-ended filters. However, there are important differences, mainly relative to the synthesis of the resonant elements, since these elements are made of multisection SIRs. Nevertheless, the resonant elements are all identical (for the reasons explained before), and, hence, the ASM devoted to the determination of resonator dimensions is applied only once. Let us now discuss in detail these three independent ASM subprocesses.

A. Resonator Synthesis

In the ASM process devoted to the resonator synthesis, the variables in the optimization space are the resonator elements, i.e., $\mathbf{x_c} = [L_e, L_c, C_e, C_c]$, and the coarse model response is obtained through circuit simulation. The validation space is constituted by a set of four geometrical variables. The other geometrical variables necessary to completely define the resonator layout are set to fixed values and are not variables of the optimization process. By this means, we deal with the same number of variables in both spaces, necessary for the inversion of the Jacobian matrix. Specifically, the variables in the validation space are the lengths of the narrow (inductive) and wide (capacitive) sections of the multisection mirrored SIRs, i.e., $\mathbf{x_f} = [l_{Le}, l_{Lc}, l_{Ce}, l_{Cc}]$. The fine model response is obtained through electromagnetic simulation of the layout, inferred from the fine model variables plus the fixed dimensions, namely the widths of the narrow and wide sections of the mirrored SIRs, and substrate parameters. The Agilent Momentum commercial software has been used to obtain the electromagnetic response of the structures, and the considered substrate parameters are those of the Rogers RO3010 with thickness $h = 635 \mu$m and dielectric constant $\varepsilon_r = 10.2$. Concerning the fixed dimensions, the values are set to $W_{Le} = W_{Lc} = 0.2$ mm, and there are two bounded values $W_{Ce} = l_{Ce}$ (i.e., a square shaped geometry for the external patch capacitors is chosen), and $W_{Cc} = 0.75\ \lambda/4$ mm, where λ is the guided wavelength at the central frequency of the optimum filter schematic. The value of 0.2 mm for the narrow inductive strips is slightly above the critical dimensions that are realizable with the available technology (LPKF HF100 milling machine). Concerning the square geometry of the external capacitive patches, with this shape factor the patches are described by a lumped capacitance to a very good approximation. Finally, the width of the central patches W_{Cc} has been chosen with the above criterion in order to avoid overlapping between adjacent patches.

In order to initiate the ASM algorithm it is necessary to obtain an initial layout for the multisection SIR. This is obtained from the following approximate formulas [36], [37]:

$$l_{Le} = \frac{L_e v_{ph}}{Z_h} \tag{11a}$$

$$l_{Ce} = C_e v_{pl} Z_l \tag{11b}$$

$$l_{Lc} = \frac{L_c v_{ph}}{Z_h} \tag{11c}$$

$$l_{Cc} = C_c v_{pl} Z_l \tag{11d}$$

where v_{ph} and v_{pl} are the phase velocities of the high- and low-impedance transmission lines sections, respectively, and Z_h and Z_l the corresponding characteristic impedances.

Once the initial layout (i.e., $\mathbf{x_f}^{(1)}$) is determined, the four circuit elements can be extracted from the electromagnetic response using (5)–(7) and (10). The specific procedure is as follows: the four-port S-parameters (considering 50 Ω ports) of the multisection SIR is obtained by means of the Agilent Momentum electromagnetic solver. From these results, the S-parameters corresponding to the differential and common mode are inferred from well-known formulas [38]. Then, from f_0, f_z, and b [expressions (5)–(7)] of the differential-mode response, the element values L_e, C_e, and L_c are extracted, whereas C_c is determined from the transmission zero (expression 10) corresponding to the common-mode response. This provides $\mathbf{x_c}^{(1)} = \mathbf{P}(\mathbf{x_f}^{(1)})$, and using (1), the first error function can be inferred. To iterate the process using (2), with $\mathbf{h}^{(1)}$ derived from (3), a first approximation of the Jacobian matrix is needed. Following a similar approach to the one explained in Section III-B, we have slightly perturbed the lengths $l_{Le}, l_{Lc}, l_{Ce}, l_{Cc}$, and we have obtained the values of L_e, L_c, C_e, C_c resulting after each perturbation from parameter extraction. This provides the first order-4 Jacobian matrix. By means of this procedure, the layouts of the multisection mirrored SIRs are determined.

B. Determination of the Line Width

The widths of the quarter-wavelength (at $f_{0\mathrm{f}}^{(3)}$) transmission lines are determined through the one-variable ASM procedure explained in [32], where the fine model variable is the linewidth W, whereas the variable of the coarse model is the characteristic impedance (the details of this simple ASM procedure are given in [32]). However, it has to be taken into account that this ASM must be repeated as many times as different admittance inverters are present in the filter. It is also important to bear in mind that the pair of differential lines are widely separated so that the differential- and common-mode impedances take the same value, i.e., identical to that of the isolated line.

C. Optimization of the Line Length (Filter Cell Synthesis)

To determine the length of the inverters, the procedure is to consider the whole filter cell, consisting of the resonator cascaded in between the inverter halves (not necessarily of the same width, or admittance). As it was pointed out in [32], optimization of the whole filter cell is necessary since the resonators may introduce some (although small) phase shift. In [32], the whole filter cell was forced to exhibit a phase shift of 90° at the central frequency of the optimum schematic. However, the fact that the inverters at both sides of the resonator have different admittance means that the phase of S_{21} is no longer 90° at the central frequency of the optimum schematic. Nevertheless, the phase shift of the cell can be easily inferred from circuit simulation, and the resulting value is the goal of this third ASM subprocess. Thus, the ASM optimization consists of varying the length of the lines cascaded to the resonator until the required phase per filter cell is achieved (the other geometrical parameters of the cell are kept unaltered). The phase is directly inferred from the frequency response of the cell obtained from electromagnetic simulation at each iteration step.

Once each filter cell is synthesized, the cells are cascaded, and no further optimization is required. The flow diagram of the complete ASM process able to automatically provide the layout from the optimum filter schematic, consisting of the three independent quasi-Newton iterative algorithms described, is very similar to the one presented in [32], and, hence, it is not reproduced here.

Using the mirrored SIR element values and inverter admittances corresponding to the optimum filter schematic of the example reported in Section III, we have applied the developed ASM algorithm to automatically generate the filter layout (depicted in Fig. 4). Resonator dimensions are $l_{Le} = 0.9075$ mm, $l_{Lc} = 2.4136$ mm, $l_{Ce} = 2.5262$ mm and $l_{Cc} = 1.0986$ mm, and the lengths of the filter cells give admittance inverter lengths of 11.4 mm for all the inverters (the slight variations take place at the third decimal) and the widths are $W_{\mathrm{inv1}} = 0.6015$ mm, $W_{\mathrm{inv2}} = 0.6704$ mm, and $W_{\mathrm{inv3}} = 0.4087$ mm [see Fig. 4(a)] for inverters $J_{0,1} = J_{5,6}$, $J_{1,2} = J_{4,5}$, and $J_{2,3} = J_{3,4}$, respectively.

The electromagnetic simulations (excluding losses) of the differential and common modes of the synthesized filter are compared with the response of the optimum filter schematic (also for the differential and common modes) in Fig. 4(b) and (c). The agreement between the lossless electromagnetic simulations and the responses of the optimum filter schematic (where losses are excluded) is very good, pointing out the validity of the proposed design method. The filter has been fabricated by means of the LPKF H100 drilling machine [see Fig. 5(a)], and the measured frequency responses [Fig. 5(b) and (c)] have been obtained by means of an Agilent N5211A PNA microwave network analyzer. The measured responses are in reasonable agreement with the lossy electromagnetic simulations and reveal that filter specifications are satisfied to a good approximation. Notice that effects such as

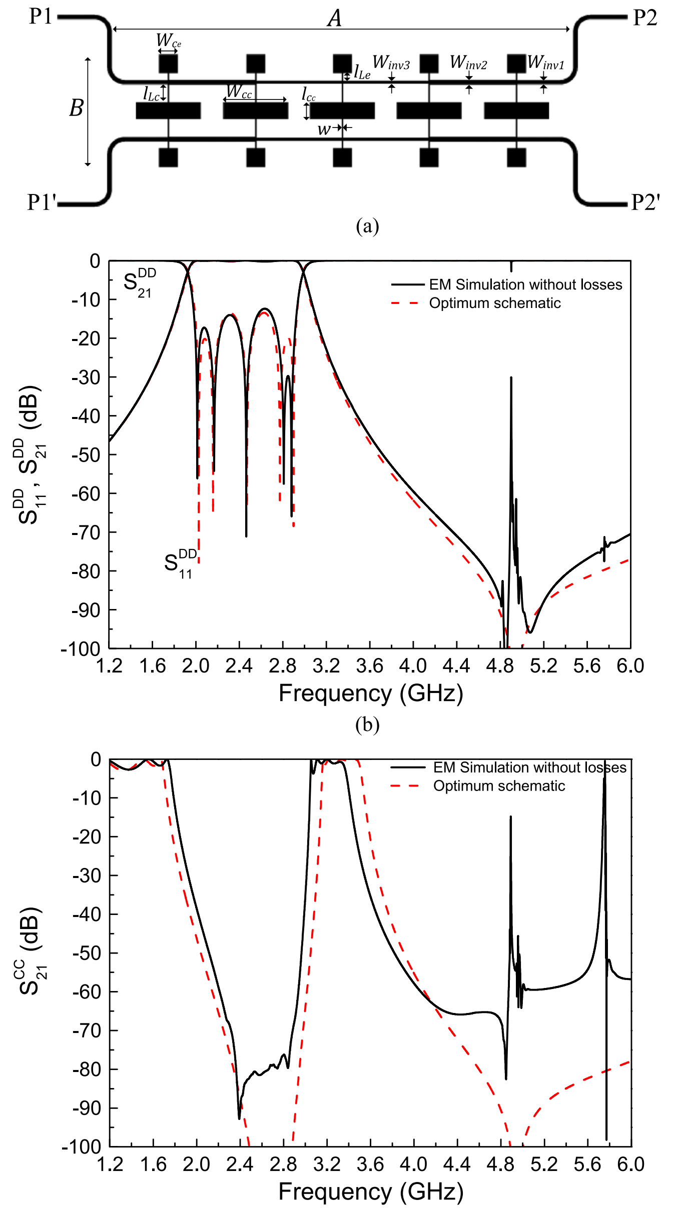

(a)

(b)

(c)

Fig. 4. Layout of the (a) synthesized order-5 filter, (b) differential-mode response, and (c) common-mode response. In (b) and (c), the lossless electromagnetic simulations of the synthesized layout are compared to the circuit simulations of the optimum filter schematic. The relevant dimensions in (a) are $A = 63$ mm and $B = 15$ mm.

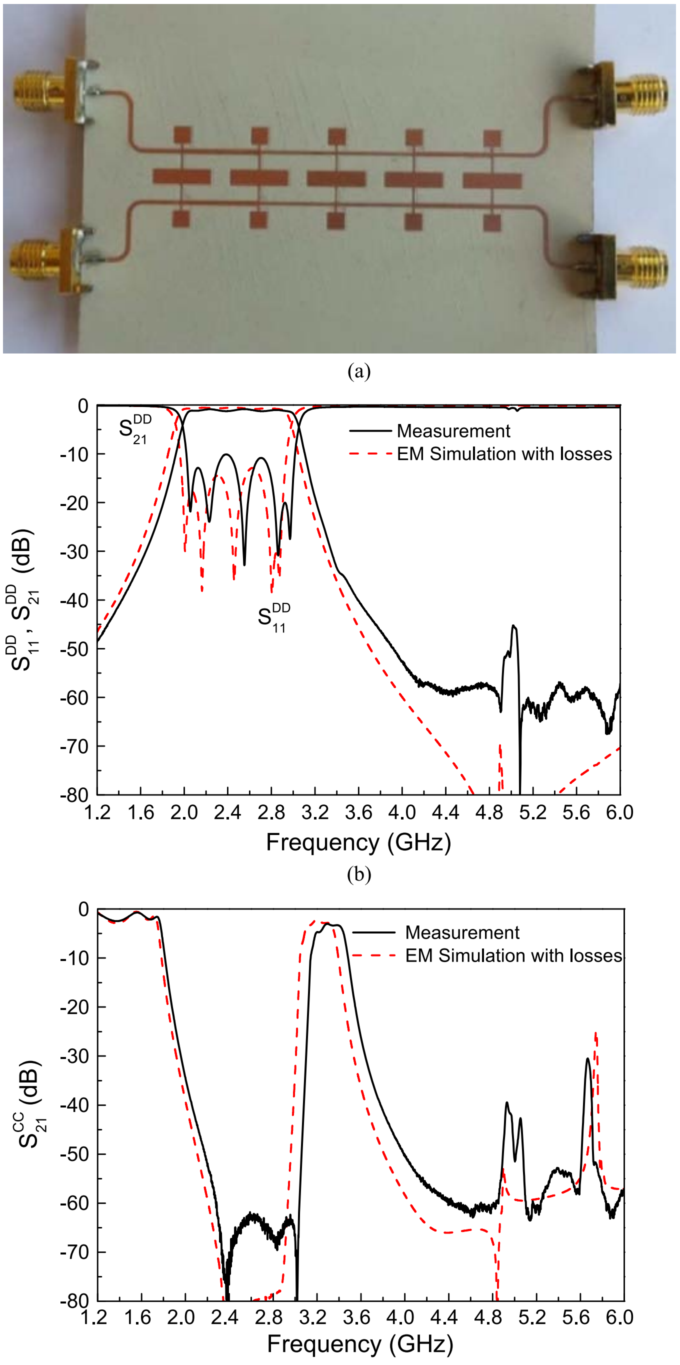

(a)

(b)

(c)

Fig. 5. (a) Photograph of the fabricated order-5 filter, (b) differential-mode response, and (c) common-mode response. In (b) and (c), the measured responses are compared to the lossy electromagnetic simulations of the synthesized layout.

inaccuracies in the dielectric constant provided by the substrate supplier, fabrication related tolerances, substrate anisotropy and foil roughness, among others, may be the cause of the slight discrepancies between the measured responses and the lossy electromagnetic simulations. Nevertheless, the objective of synthesizing the layout of the considered differential-mode bandpass filters subjected to given specifications, following a completely unattended scheme, has been achieved.

V. SYNTHESIS OF A SEVENTH-ORDER FILTER

Let us now consider the synthesis of a seventh-order filter with significantly wider (as compared with the previous case example) differential-mode bandwidth. In this case, the specifications (differential mode) are $f_0 = 3$ GHz, $\mathrm{FBW} = 60\%$ (corresponding to 63.43% -3-dB fractional bandwidth) and $L_{\mathrm{Ar}} = 0.15$ dB. Since the differential-mode bandwidth is wide, a single common-mode transmission zero does not suffice to completely reject this mode over the differential filter passband. Thus, in this case, several transmission zeros for the common mode are generated. Such transmission zeros must be (roughly) uniformly distributed along the differential-mode passband for an efficient common-mode rejection over that band. The fact that several

TABLE I
FREQUENCIES AND CAPACITANCES OF THE COMMON-MODE TRANSMISSION ZEROS OF THE SYNTHESIZED ORDER-7 DIFFERENTIAL FILTER

Stage	1	2	3	4	5	6	7
f_z^{cc} **(GHz)**	2.306	2.596	2.885	3.174	3.572	3.970	4.369
C_c **(pF)**	1.797	1.419	1.148	0.949	0.749	0.606	0.501

common-mode transmission zeros are considered does not affect the first ASM algorithm. However, as many different capacitances C_{ci} as transmission zeros must be calculated by means of expression (10) to completely determine the elements of the optimum filter schematic. Since the capacitances C_{ci} determine the area of the central patches, it follows that the second ASM, for the determination of the layout, must be slightly modified (i.e., the mirrored SIRs are not identical in this case). However, the procedure is very simple (to be described next).

First of all, the layout of the mirrored SIR providing the lower common-mode transmission zero is determined according to the procedure explained in Section IV-A. For the determination of the layout of the other resonant elements, we apply the ASM subprocess described in Section IV-A, but considering as optimization variables of the validation space the widths for the inner sections (the ones between the pair of transmission lines), and the lengths for the outer sections. By this means, the distance between the pair of lines is kept unaltered. Notice that since the element values of the resonators are all identical (except C_{ci}), we do not expect significant variations in the widths from cell to cell, except for the central patch. Indeed, for the optimization of resonator dimensions (layout determination) by applying the ASM, we consider as layout of the first iteration the one corresponding to the synthesis of the first resonator. It has been found that this provides faster convergence. The other two ASM sub-processes (described in Section IV-B and IV-C) are identical.

Application of the first ASM algorithm (optimum filter schematic) has provided the following element and admittance values: $L_e = 0.8836$ nH, $L_c = 2.6507$ nH, $C_e = 0.7114$ pF, and $J_{0,1} = J_{7,8} = 0.02$ S, $J_{1,2} = J_{6,7} = 0.0199$ S, $J_{2,3} = J_{5,6} = 0.0154$ S, $J_{3,4} = J_{4,5} = 0.0148$ S with $f_{0\mathrm{f}}^{(5)} = 3.1739$ GHz. Convergence has been achieved after $N = 5$ iterations, with an error function as small as 0.021%. On the other hand, by considering seven common-mode transmission zeros distributed in order to cover the bandwidth, the corresponding patch capacitances take the values given in Table I.

Application of the second ASM algorithm, considering the substrate used for the seventh-order filter (Rogers RO3010 with thickness $h = 635\mu$m and dielectric constant $\varepsilon_r = 10.2$), provides the filter geometry indicated in Table II (where all dimensions are given in mm). Note that the lengths and widths of the inverters (W_{inv} and l_{inv}) are those corresponding to the inverter to the right of the resonant element (the inverter to the left of the first resonator is identical to the last one). Moreover, the following dimensions in the mirrored SIRs are all identical: $l_{Lc} = 3.58$ mm, $W_{Ce} = 1.2$ mm and $l_{Cc} = 2.92$ mm. On the other hand, $W_{Lei} = W_{Lci}$. Note that the optimization variables are those of Table II.

TABLE II
GEOMETRY PARAMETERS OF THE SYNTHESIZED ORDER-7 DIFFERENTIAL FILTER

Stage	W_{Lc}	W_{Cc}	l_{Le}	l_{Ce}	W_{inv}	l_{inv}
1	0.2	6.77	1.92	1.2	0.59	8.87
2	0.201	5.24	1.94	1.2	0.32	8.87
3	0.205	4.14	2.09	1.19	0.29	8.86
4	0.209	3.3	2.14	1.18	0.29	8.86
5	0.22	2.47	2.2	1.16	0.32	8.85
6	0.233	1.86	2.19	1.12	0.59	8.84
7	0.253	1.4	2.38	1.06	0.59	8.76

Fig. 6 shows the layout of the designed filter and the lossless electromagnetic simulation, compared to the optimum filter schematic and target responses (differential and common-modes). The fabricated differential-mode filter is depicted in Fig. 7, together with the measured response and the lossy electromagnetic simulation. Very good agreement between the different responses can be observed, and it is found that the filter responses satisfy the considered specifications, including an efficient common-mode rejection over the differential filter passband, with a common-mode rejection ratio better than CMRR $=$ 30 dB in the whole the differential filter passband.

Note that the agreement between the lossless electromagnetic simulation and the response of the optimum filter schematic for both the differential and common modes is excellent in this order-7 filter (Fig. 6). For the order-5 filter reported before, there is also very good agreement between these responses for the differential mode, but the agreement is not so good for the common-mode (Fig. 4). The reason is that parameter extraction uses three conditions for the differential mode [expressions (5)–(7)], whereas only one for the common mode (expression (10)). However, for the seventh-order filter, seven different common-mode transmission zeros are set in order to efficiently cover the (wider) differential filter passband, i.e., much more conditions as compared to the fifth-order filter (where only one common-mode transmission zero was considered). The synthesis method guarantees that the common-mode transmission zeros are identical for the lossless electromagnetic simulation and for the response of the optimum schematic, and, hence, one expects a very good agreement if the number of transmission zero is high (as it actually occurs with the order-7 filter). Nevertheless, the aim of the paper is to satisfy the specifications for the differential mode and reject the common mode over the differential filter passband, and this objective has been reached in both examples.

VI. COMPARISON TO OTHER APPROACHES

In order to appreciate the competitiveness, in terms of performance and dimensions, of the proposed filters, a comparison to other wideband differential bandpass filters (with comparable FBW) is summarized in Table III. In this table, the common-mode rejection ratio (CMRR) is the ratio between $|\mathrm{S}_{21}|$ for the common mode and the differential mode at f_0, expressed in decibels, f_{1dd} and f_{2dd} are the lower and upper differential-mode cutoff frequencies, respectively, and f_{1cc} and f_{2cc} are the -3-dB common-mode cutoff frequencies. The filters reported in

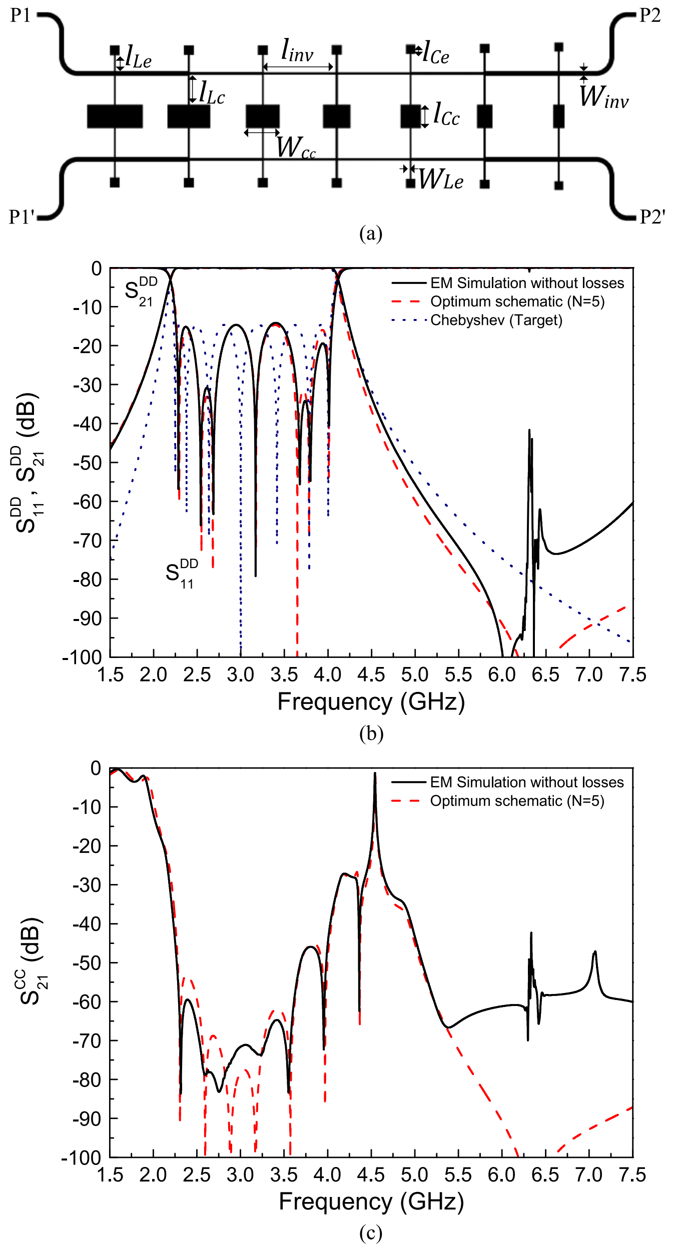

(a)

(b)

(c)

Fig. 6. (a) Layout of the synthesized order-7 balanced filter, and lossless electromagnetic simulation compared to the response of the optimum filter schematic and target response for the (b) differential and (c) common mode.

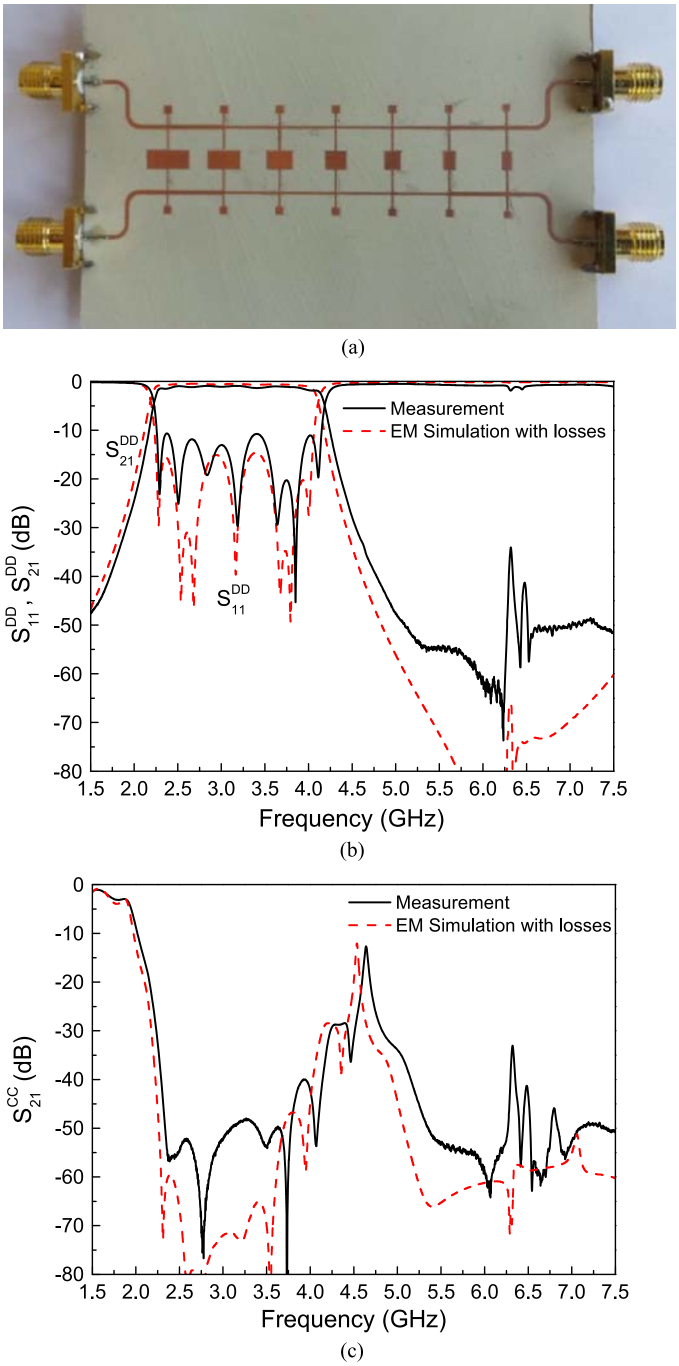

(a)

(b)

(c)

Fig. 7. (a) Photograph of the fabricated order-7 filter and measured response compared to the lossy electromagnetic simulation for the (b) differential and (c) common mode.

this work exhibit a common-mode rejection comparable to that of the filters reported in [4], [10], [12], [16], [40], [42], and [43]. However, the rejection level at $2f_0$ for the differential mode is larger in our filters, with the exception of the filter of [16], which is indeed the same order-5 filter as the one reported here (same specifications) although the layout was not inferred automatically in [16]. Thus, Table III reveals that our filters are competitive in terms of CMRR and out-of-band rejection level (specifically at $2f_0$) for the differential mode. Despite the fact that the CMRR at f_0 is a figure of merit, it is interesting to compare the filters proposed in this work with other filters with regard to the worst CMRR within the differential filter passband. This makes sense if the differential-mode passbands are comparable. Thus, the comparison is made between the filters reported in [10] and [12] and the filter of Fig. 5 (with comparable fractional bandwidth). The worst CMRR in the whole differential filter passband is 18 and 63 dB for the filters of [10] and [12], respectively. In our approach, the measurement shows a CMRR better than 35 dB in the differential filter passband. Moreover, the filter of Fig. 5 has better differential out-of-band rejection (58 dB at $2f_0$), as compared with the filters of references [10] and [12]. The filters reported in [1] and [39], with comparable fractional bandwidth to the filter of Fig. 7, have a CMRR in the whole differential passband better than 22 and 14.5 dB, respectively. In our approach, the measurement shows a CMRR better

TABLE III
COMPARISON OF VARIOUS DIFFERENTIAL WIDEBAND BANDPASS FILTERS

Ref.	***FBW*** **(–3dB)**	***CMRR*** **@f_0 (dB)**	**S_{21dd} ($2f_0$) (dB)**	**f_{1cc}/f_{1dd}**	**f_{2cc}/f_{2dd}**	**Effective area**
[1]	65%	29	46	0.96	1.09	$0.25\lambda_g^2$
[4]	50%	48	23	1.25	0.94	$0.25\lambda_g^2$
[10]	45%	53	35	0	1.04	$0.045\lambda_g^2$
[12]	43%	63	38	0.66	1.11	$0.6\lambda_g^2$
[14]	15%	27	9	0	1.15	$0.022\lambda_g^2$
[15]	70%	18.7	15	0.89	1.01	$0.52\lambda_g^2$
[16]	42%	65	66	0.54	1.09	$0.37\lambda_g^2$
[39]	66.6%	14.5	40	0	2.21	$0.163\lambda_g^2$
[40]	40%	55	22	-	-	$0.25\lambda_g^2$
[41]	53%	13	7	0	>3.37	$0.175\lambda_g^2$
[42]	59.5%	47	54	0.38	1.35	$0.39\lambda_g^2$
[43]	56.7%	40	37	0	>2.2	$0.2\lambda_g^2$
[44]	79%	35	32	0	>3.54	$0.19\lambda_g^2$
This work	**43%**	**65**	**58**	**0.87**	**1.05**	$\mathbf{0.36\lambda_g^2}$
This work	**65%**	**50**	**63**	**0.85**	**1.11**	$\mathbf{0.28\lambda_g^2}$

than 30 dB in the differential filter passband. Moreover, the filter of Fig. 7 has better differential out-of-band rejection (63 dB at $2f_0$) as compared with the filters of references [1] and [39].

Concerning size, the filters reported in references [10], [14], [39], [41], [44] are smaller than our filters, but at the expense of obtaining a lower *CMRR* and rejection level for the differential mode (at $2f_0$). From the fabrication point of view, the filters reported here are very simple since only two metal levels are needed and vias are not present. Additionally, the considered filter topologies, consisting of multi-section mirrored SIRs coupled through quarter wavelength differential lines, are accurately described by a mixed distributed-lumped model (schematic) over a wide frequency band, and this is very important for design purposes, as has been demonstrated in this paper.

VII. DISCUSSION ON BANDWIDTH LIMITATIONS

The synthesis technique presented in Sections III and IV is able to provide the filter layout able to satisfy the specifications, as demonstrated by the guide example (order-5 differential filter) and by the example reported in Section V, corresponding to a seventh-order balanced filter. The bandwidth for the differential mode in this second example is quite wide (i.e., the filter exhibits a −3-dB fractional bandwidth of 63.43%), and an efficient rejection of the common mode over that band has been achieved. Thus, it is clear that wideband balanced filters with common-mode suppression are achievable with this approach, and filter design is simple since the determination of the filter layout does not need any external aid during the whole synthesis process. However, it does not mean that any combination of bandwidth and in-band ripple level (or return loss level) for the differential mode can be achieved. Indeed, it has been found that for a bandwidth as wide as FBW $=$ 120%, ripple level of $L_{\mathrm{Ar}} = 0.45$ dB (corresponding to a very reasonable 10-dB in-band return loss level), central frequency $f_0 = 3$ GHz, and order $n = 7$, the first ASM converges. The response of the optimum filter schematic (differential mode), compared with the target Chebyshev response, is depicted in Fig. 8. Note that the return loss level of the optimum schematic is better than 10 dB, and the central frequency and bandwidth are very close to the target values. Typically, the frequency selectivity of the optimum schematic is somehow better than the one of the Chebyshev response at the upper transition band (due to the transmission zero), but it is worst at the lower transition band (see also Fig. 2). This occurs because the selectivity is not a variable in the optimization process, but, certainly, the discrepancies at the lower band edge increase as bandwidths widens.

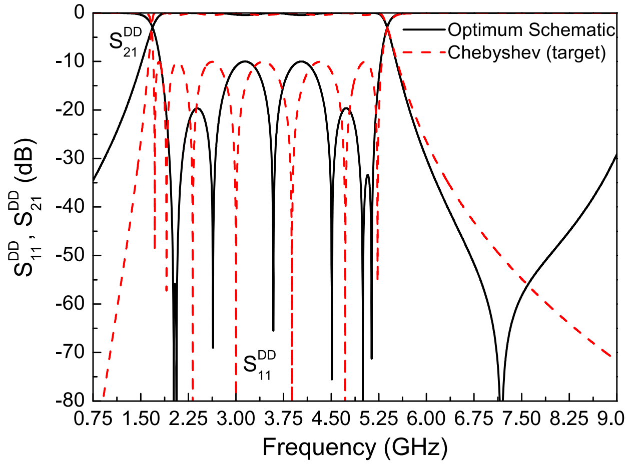

Fig. 8. Comparison between the order-7 Chebyshev response with fractional bandwidth, ripple level, and central frequency indicated in the text, and the response of the resulting optimum schematic, after applying the first ASM algorithm.

It may be accepted that a response like the one of the optimum filter schematic of Fig. 8 is reasonable. However, it has been found that the second ASM algorithm does not converge, at least by considering the same substrate used in the two reported examples. The reason is that the element values of the resonators (capacitances) are so small that the resulting impedance contrast of the mirrored SIRs (by considering square shaped capacitors) is small, and the model is not valid (note that the impedance contrast in the example of Fig. 7 is lower than the one of Fig. 5). Moreover, it should be also taken into account that for wide bandwidths, the lumped element approximation of the patch capacitors and narrow inductive strips is not necessarily valid over the whole differential band, and more complex models are required for an accurate description of the structures [45]. Thus, with the present approach, bandwidth is limited by layout generation, rather than by the schematic. Nevertheless, significant bandwidths have been demonstrated in the reported examples. Work is in progress in order to modify the second ASM algorithm, particularly the square shaped geometry of the external capacitors, and try to design wider differential-mode bandpass filters with common-mode suppression.

VIII. CONCLUSION

In conclusion, a design tool for the unattended synthesis of common-mode suppressed differential-mode bandpass filters based on multisection mirrored SIRs coupled through admittance inverters has been proposed. The tool consists of a two-step ASM algorithm, where the filter schematic satisfying the specifications is first determined, and then the layout of the filter is automatically generated. It has been demonstrated that for moderate differential-mode bandwidths, a single common-mode transmission zero suffices to achieve efficient common-mode suppression over the differential filter pass band. However, for wideband balanced bandpass filters implemented by this approach, several common-mode transmission zeros distributed along the differential-mode pass band are necessary. Two case examples, namely, an order-5 balanced filter with a single common-mode transmission zero, and a seventh-order filter with several common-mode transmission zeros, have been reported. In both cases, the two-step ASM algorithm has provided the filter layouts after few iterative steps, and the synthesized filter layouts provide the filter specifications to a good approximation. The measured responses of the fabricated filters are also in good agreement with the electromagnetic simulations and with the circuit simulations of the optimum schematics, and the measured common-mode rejection ratios at the central filter frequency are as high as 65 and 50 dB for the order-5 and order-7 balanced filters, respectively.

Finally, by comparing the proposed filter with other approaches, it has been found that the combination of size, performance, and easy fabrication (vias are not present and only two metal levels are required) makes the approach very competitive. This fact is worth highlighting since the reported filters can be automatically synthesized by means of a completely unattended ASM process.

REFERENCES

[1] T. B. Lim and L. Zhu, "A differential-mode wideband bandpass filter on microstrip line for UWB applications," *IEEE Microw. Wireless Compon. Lett.*, vol. 19, pp. 632–634, Oct. 2009.

[2] T. B. Lim and L. Zhu, "Differential-mode ultra-wideband bandpass filter on microstrip line," *Electron. Lett.*, vol. 45, no. 22, pp. 1124–1125, Oct. 2009.

[3] X. H. Wang, Q. Xue, and W. W. Choi, "A novel ultra-wideband differential filter based on double-sided parallel-strip line," *IEEE Microw. Wireless Compon. Lett.*, vol. 20, no. 8, pp. 471–473, Aug. 2010.

[4] T. B. Li and L. Zhu, "Highly selective differential-mode wideband bandpass filter for UWB application," *IEEE Microw. Wireless Compon. Lett.*, vol. 21, no. 3, pp. 133–135, Mar. 2011.

[5] A. M. Abbosh, "Ultrawideband balanced bandpass filter," *IEEE Microw. Wireless Compon. Lett.*, vol. 21, pp. 480–482, Sep. 2011.

[6] H. T. Zhu, W. J. Feng, W. Q. Che, and Q. Xue, "Ultra-wideband differential bandpass filter based on transversal signal-interference concept," *Electron. Lett.*, vol. 47, no. 18, pp. 1033–1035, Sep. 2011.

[7] S. Shi, W.-W. Choi, W. Che, K.-W. Tam, and Q. Xue, "Ultra-wideband differential bandpass filter with narrow notched band and improved common-mode suppression by DGS," *IEEE Microw. Wireless Compon. Lett.*, vol. 22, no. 4, pp. 185–187, Apr. 2012.

[8] C.-H. Lee, C.-I. G. Hsu, and C.-J. Chen, "Band-notched balanced UWB BPF with stepped-impedance slotline multi-mode resonator," *IEEE Microw. Wireless Compon. Lett.*, vol. 22, no. 4, pp. 182–184, Apr. 2012.

[9] X.-H. Wu and Q.-X. Chu, "Compact differential ultra-wideband bandpass filter with common-mode suppression," *IEEE Microw. Wireless Compon. Lett.*, vol. 22, pp. 456–458, Sep. 2012.

[10] P. Vélez, J. Naqui, A. Fernández-Prieto, M. Durán-Sindreu, J. Bonache, and J. Martel *et al.*, "Differential bandpass filter with common mode suppression based on open split ring resonators and open complementary split ring resonators," *IEEE Microw. Wireless Compon. Lett.*, vol. 23, no. 1, pp. 22–24, Jan. 2013.

[11] X.-H. Wang, H. Zhang, and B.-Z. Wang, "A novel ultra-wideband differential filter based on microstrip line structures," *IEEE Microw. Wireless Compon. Lett.*, vol. 23, pp. 128–130, March 2013.

[12] P. Vélez, J. Naqui, M. Durán-Sindreu, J. Bonache, A. F. Prieto, and J. Martel *et al.*, "Differential bandpass filters with common-mode suppression based on stepped impedance resonators (SIRs)," presented at the IEEE MTT-S Int. Microw. Symp., Seattle, WA, USA, Jun. 2013.

[13] J. Shi, C. Shao, J.-X. Chen, Q.-Y. Lu, Y. Peng, and Z.-H. Bao, "Compact low-loss wideband differential bandpass filter with high common-mode suppression," *IEEE Microw. Wireless Compon. Lett.*, vol. 23, no. 9, pp. 480–482, Sep. 2013.

[14] A. K. Horestani, M. Durán-Sindreu, J. Naqui, C. Fumeaux, and F. Martín, "S-shaped complementary split ring resonators and application to compact differential bandpass filters with common-mode suppression," *IEEE Microw. Wireless Compon. Lett.*, vol. 24, no. 3, pp. 150–152, Mar. 2014.

[15] X.-H. Wang and H. Zhang, "Novel balanced wideband filters using microstrip coupled lines," *Microw. Opt. Technol. Lett.*, vol. 56, pp. 1139–1141, May 2014.

[16] P. Velez, J. Selga, M. Sans, J. Bonache, and F. Martin, "Design of differential-mode wideband bandpass filters with wide stop band and common-mode suppression by means of multisection mirrored stepped impedance resonators (SIRs)," presented at the IEEE MTT-S Int. Microw. Symp., Phoenix, AZ, USA, May 2015.

[17] J. Naqui, A. Fernández-Prieto, M. Durán-Sindreu, F. Mesa, J. Martel, and F. Medina *et al.*, "Common mode suppression in microstrip differential lines by means of complementary split ring resonators: Theory and applications," *IEEE Trans. Microw. Theory Tech.*, vol. 60, pp. 3023–3034, Oct. 2012.

[18] A. Fernandez-Prieto, J. Martel-Villagrán, F. Medina, F. Mesa, S. Qian, and J.-S. Hong *et al.*, "Dual-band differential filter using broadband common-mode rejection artificial transmission line," *Progr. Electromagn. Res. (PIER)*, vol. 139, pp. 779–797, 2013.

[19] J. Bonache, I. Gil, J. García-García, and F. Martín, "Compact microstrip band-pass filters based on semi-lumped resonators," *IET Microw. Antennas Propag.*, vol. 1, pp. 932–936, Aug. 2007.

[20] M. Makimoto and S. Yamashita, "Compact bandpass filters using stepped impedance resonators," *Proc. IEEE*, vol. 67, no. 1, pp. 16–19, Jan. 1979.

[21] J. W. Bandler, R. M. Biernacki, S. H. Chen, P. A. Grobelny, and R. H. Hemmers, "Space mapping technique for electromagnetic optimization," *IEEE Trans. Microw. Theory Tech.*, vol. 42, pp. 2536–2544, Dec. 1994.

[22] J. W. Bandler, R. M. Biernacki, S. H. Chen, R. H. Hemmers, and K. Madsen, "Electromagnetic optimization exploiting aggressive space mapping," *IEEE Trans. Microw. Theory Tech.*, vol. 43, pp. 2874–2882, Dec. 1995.

[23] S. Koziel, Q. S. Cheng, and J. W. Bandler, "Space mapping," *IEEE Microw. Mag.*, vol. 9, pp. 105–122, Dec. 2008.

[24] S. Koziel, L. Leifsson, and S. Ogurtsov, "Space mapping for electromagnetic-simulation-driven design optimization," in *Surrogate-Based Modeling and Optimization*. New York, NY, USA: Springer, 2013, pp. 1–25.

[25] S. Koziel and L. Leifsson, "Response correction techniques for surrogate-based design optimization of microwave structures," *Int. J. RF Microw. Comput.-Aided Eng.*, vol. 22, no. 2, pp. 211–223, Mar. 2012.

[26] S. Koziel, L. Leifsson, and S. Ogurtsov, "Reliable EM-driven microwave design optimization using manifold mapping and adjoint sensitivity," *Microw. Opt. Technol. Lett.*, vol. 55, no. 4, pp. 809–813, April 2013.

[27] S. Koziel and J. W. Bandler, "Rapid yield estimation and optimization of microwave structures exploiting feature-based statistical analysis," *IEEE Trans. Microw. Theory Tech.*, vol. 63, no. 1, pp. 107–114, Jan. 2015.

[28] A. Khalatpour, R. K. Amineh, Q. S. Cheng, M. H. Bakr, N. K. Nikolova, and J. W. Bandler, "Accelerating input space mapping optimization with adjoint sensitivities," *IEEE Microw. Wireless Compon. Lett.*, vol. 21, no. 6, pp. 280–282, Jun. 2011.

[29] L. J. Rogla, J. E. Rayas-Sanchez, V. E. Boria, and J. Carbonell, "EM-based space mapping optimization of left-handed coplanar waveguide filters with split ring resonators," in *Proc. IEEE MTT-S Int. Microw. Symp.*, Honolulu, HI, USA, Jun. 3–8, 2007, pp. 111, 114.

[30] J. Selga, A. Rodriguez, V. E. Boria, and F. Martin, “Synthesis of split-rings-based artificial transmission lines through a new two-step, fast converging, robust aggressive space mapping (ASM) algorithm,” *IEEE Trans. Microw. Theory Tech.*, vol. 61, no. 6, pp. 2295–2308, Jun. 2013.

[31] A. Rodríguez, V. E. Boria, J. Selga, M. Sans, and F. Martín, “Synthesis of open complementary split ring resonators (OCSRRs) through aggressive space mapping (ASM) and application to bandpass filters,” in *Proc. 44th Eur. Microw. Conf. (EuMC)*, Rome, Italy, Oct. 6–9, 2014, pp. 323–326.

[32] M. Sans, J. Selga, A. Rodríguez, J. Bonache, V. E. Boria, and F. Martín, “Design of planar wideband bandpass filters from specifications using a two-step aggressive space mapping (ASM) optimization algorithm,” *IEEE Trans. Microw. Theory Tech.*, vol. 62, pp. 3341–3350, Dec. 2014.

[33] J. S. Hong and M. J. Lancaster, *Microstrip Filters for RF/Microwave Applications*. New York, NY, USA: Wiley, 2001.

[34] J. Bonache, M. Gil, I. Gil, J. Garcia-García, and F. Martín, “On the electrical characteristics of complementary metamaterial resonators,” *IEEE Microw. Wireless Compon. Lett.*, vol. 16, pp. 543–545, Oct. 2006.

[35] F. Aznar, M. Gil, J. Bonache, J. D. Baena, L. Jelinek, and R. Marqués *et al.*, “Characterization of miniaturized metamaterial resonators coupled to planar transmission lines,” *J. Appl. Phys.*, vol. 104, Dec. 2008, paper 114501-1-8.

[36] D. M. Pozar, *Microwave Engineering*. Reading, MA, USA: Addison-Wesley, 1990.

[37] I. Bahl and P. Barthia, *Microwave Solid State Circuit Design*. New York, NY, USA: Wiley, 1998.

[38] W. R. Eisenstadt, B. Stengel, and B. M. Thompson, *Microwave Differential Circuit Desing Using Mixed Mode S-Parameters*. Norwood, MA, USA: Artech House, 2006.

[39] L. Li, J. Bao, J.-J. Du, and Y.-M. Wang, “Compact differential wideband bandpass filters with wide common-mode suppression,” *IEEE Microw. Wireless Compon. Lett.*, vol. 24, no. 3, pp. 164–166, March 2014.

[40] H. Wang, L.-M. Gao, K.-W. Tam, W. Kang, and W. Wu, “A wideband differential BPF with multiple differential- and common-mode transmission zeros using cross-shaped resonator,” *IEEE Microw. Wireless Compon. Lett.*, vol. 24, no. 12, pp. 854–856, Oct. 2014.

[41] W. Feng, W. Che, and Q. Xue, “High selectivity wideband differential bandpass filter with wideband common mode suppression using marchand balun,” presented at the IEEE Int. Wireless Symp., Xian, China, Mar. 2014.

[42] L. Li, J. Bao, J.-J. Du, and Y.-M. Wang, “Differential wideband bandpass filters with enhanced common-mode suppression using internal coupling technique,” *IEEE Microw. Wireless Compon. Lett.*, vol. 24, no. 5, pp. 300–302, May 2014.

[43] J. G. Zhou, Y.-C. Chiang, and W. Che, “Compact wideband balanced bandpass filter with high common-mode suppression based on cascade parallel coupled lines,” *IET Microw., Antennas, Propag.*, vol. 8, no. 8, pp. 564–570, Jun. 2014.

[44] W. Feng, W. Che, Y. Ma, and Q. Xue, “Compact wideband differential bandpass filters using half-wavelength ring resonator,” *IEEE Microw. Wireless Compon. Lett.*, vol. 23, no. 2, pp. 81–83, Feb. 2013.

[45] P. Vélez, J. Naqui, A. Fernández-Prieto, J. Bonache, J. Mata-Contreras, and J. Martel *et al.*, “Ultra-compact ($80\ \mathrm{mm}^2$) differential-mode ultra-wideband (UWB) bandpass filters with common-mode noise suppression,” *IEEE Trans. Microw. Theory Tech.*, vol. 63, no. 4, pp. 1272–1280, Apr. 2015.

Marc Sans (S’15) was born in Terrassa, Barcelona, Spain, in 1982. He received the B.S. degree in telecommunications engineering—electronic systems, the M.S. degree in telecommunications engineering, and the M.S. degree in electronics engineering, all from the Universitat Autònoma de Barcelona (UAB), in 2006, 2008, and 2013, respectively.

In 2008, he started his professional career as a RF Engineer at Sony-FTVE, developing the RF stage of TV receivers. In 2010, he moved to Mier Comunicaciones S.A. to carry out the design of passive and active devices for VHF–UHF broadcasting units. Since 2014, he has been working towards the Ph.D. degree at CIMITEC-UAB in the synthesis of microwave devices based on EM optimization techniques.

Jordi Selga (S’11–M’14) was born in Barcelona, Spain, in 1982. He received the B.S. degree in telecommunications engineering—electronic systems, the M.S. degree in electronics engineering, and the Ph.D. degree in electronics engineering, all from the Universitat Autònoma de Barcelona (UAB), Barcelona, Spain, in 2006, 2008, and 2013, respectively.

Since 2008, he has been a member of CIMITEC-UAB, a research center on metamaterials supported by TECNIO (Catalan Government). He was holder of a national research fellowship from the Formación de Profesorado Universitario Program of the Education and Science Ministry (Reference AP2008-4707). He is currently working in subjects related to metamaterials, CAD design of microwave devices, EM optimization methods, and automated synthesis of planar microwave components at the UAB.

Paris Vélez (S’10–M’15) was born in Barcelona, Spain, in 1982. He received the Telecommunications Engineering degree, specializing in electronics, and the Electronics Engineering degree from the Universitat Autònoma de Barcelona (UAB), Barcelona, Spain, in 2008 and 2010, respectively, and the Ph.D. degree in electrical engineering from UAB in 2014, with a thesis entitled “Common Mode Suppression Differential Microwave Circuits Based on Metamaterial Concepts and Semilumped Resonators.”

During the Ph.D. studies, he was awarded with a predoctoral teaching and research fellowship by the Spanish Government from 2011 to 2014. Currently, his scientific activity is focused on the miniaturization of passive circuits RF/microwave-based metamaterials at CIMITEC-UAB.

Dr. Vélez is a reviewer of the IEEE TRANSACTIONS ON MICROWAVE THEORY AND TECHNIQUES among other journals.

Ana Rodríguez (S’10–M’15) was born in Lugo, Spain. She received the Telecommunications Engineering degree from the Universidade de Vigo (UV), Spain, in 2008. As a student, she participated in the Erasmus exchange program, developing the Master’s thesis at the University of Oulu, Finland. At the end of 2008, she joined the Institute of Telecommunications and Multimedia Applications (iTEAM), which is part of the scientific park at the Universitat Politècnica de València (UPV), València, Spain. She received the Master en Tecnología, Sistemas y Redes de Comunicaciones and the Ph.D. degree from UPV in 2010 and 2014, respectively.

She currently works at iTEAM-UPV. Her main research interests include CAD design of microwave devices, EM optimization methods, and metamaterials.

Jordi Bonache (S’05–M’07) was born in Barcelona, Spain, in 1976. He received the Physics degree, the Electronics Engineering degree, and Ph.D. degree in electronics engineering, all from the Universitat Autònoma de Barcelona (UAB), Barcelona, Spain, in 1999, 2001, and 2007, respectively.

In 2000, he joined the High Energy Physics Institute of Barcelona (IFAE), Spain, where he was involved in the design and implementation of the control and monitoring system of the MAGIC telescope. In 2001, he joined the Department of Electronics Engineering of the Universitat Autònoma de Barcelona, where he is currently Lecturer. In addition, he worked as Executive Manager of CIMITEC, UAB, from

2006 to 2009 and currently is leading the research in RFID and antennas in CIMITEC. His research interests include active and passive microwave devices, metamaterials, antennas, and RFID.

Vicente E. Boria (S'91–A'99–SM'02) was born in Valencia, Spain, on May 18, 1970. He received the Ingeniero de Telecomunicación degree (First-Class Hons.) and the Doctor Ingeniero de Telecomunicación degree from the Universidad Politécnica de Valencia, Valencia, Spain, in 1993 and 1997, respectively.

In 1993, he joined the Departamento de Comunicaciones, Universidad Politécnica de Valencia, where he has been Full Professor since 2003. In 1995 and 1996, he was holding a Spanish Trainee position with the European Space Research and Technology Centre, European Space Agency (ESTEC-ESA), Noordwijk, The Netherlands, where he was involved in the area of EM analysis and design of passive waveguide devices. He has authored or coauthored ten chapters in technical textbooks, 135 papers in refereed international technical journals, and over 185 papers in international conference proceedings. His current research interests are focused on the analysis and automated design of passive components, left-handed and periodic structures, as well as on the simulation and measurement of power effects in passive waveguide systems.

Dr. Boria has been a member of the IEEE Microwave Theory and Techniques Society (IEEE MTT-S) and the IEEE Antennas and Propagation Society (IEEE AP-S) since 1992. He is reviewer of the IEEE TRANSACTIONS ON MICROWAVE THEORY AND TECHNIQUES, Proceeding of the IET (Microwaves, Antennas and Propagation) and *IET Electronics Letters*. Since 2013, he has served as Associate Editor of the IEEE MICROWAVE AND WIRELESS COMPONENTS LETTERS. He is also a member of the Technical Committees of the IEEE-MTT International Microwave Symposium and of the European Microwave Conference.

Ferran Martín (M'04–SM'08–F'12) was born in Barakaldo, Vizcaya, Spain, in 1965. He received the B.S. Degree in physics and the Ph.D. degree from the Universitat Autònoma de Barcelona (UAB), Barcelona, Spain, in 1988 and 1992, respectively.

From 1994 up to 2006, he was Associate Professor in electronics at the Departament d'Enginyeria Electrònica (Universitat Autònoma de Barcelona), and since 2007, he has been a Full Professor of electronics. In recent years, he has been involved in different research activities, including modeling and simulation of electron devices for high-frequency applications, millimeter wave, and THz generation systems, and the application of electromagnetic bandgaps to microwave and millimeter-wave circuits. He is now very active in the field of metamaterials and their application to the miniaturization and optimization of microwave circuits and antennas. He is the head of the Microwave Engineering, Metamaterials and Antennas Group (GEMMA Group) at UAB, and Director of CIMITEC, a research center on metamaterials supported by TECNIO (Generalitat de Catalunya).He has authored and coauthored more than 450 technical conference, letter, journal papers, and book chapters; he is coauthor of the book on metamaterials titled *Metamaterials With Negative Parameters: Theory, Design and Microwave Applications* (Wiley, 2008); he has generated 15 Ph.D.s; and he has filed several patents on metamaterials and has headed several development contracts

Prof. Martín is a member of the IEEE Microwave Theory and Techniques Society (IEEE MTT-S). He has organized several international events related to metamaterials, including Workshops at the IEEE International Microwave Symposium in 2005 and 2007 and the European Microwave Conference in 2009, and the Fifth International Congress on Advanced Electromagnetic Materials in Microwaves and Optics (Metamaterials 2011), where he acted as Chair of the Local Organizing Committee. He has acted as Guest Editor for three Special Issues on Metamaterials in three international journals. He is reviewer of the IEEE TRANSACTIONS ON MICROWAVE THEORY AND TECHNIQUES and IEEE MICROWAVE AND WIRELESS COMPONENTS LETTERS, among many other journals, and he serves as member of the Editorial Board of the *IET Microwaves, Antennas and Propagation* and the *International Journal of RF and Microwave Computer-Aided Engineering*. He is also a member of the Technical Committees of the European Microwave Conference (EuMC) and International Congress on Advanced Electromagnetic Materials in Microwaves and Optics (Metamaterials). Among his distinctions, he has received the 2006 Duran Farell Prize for Technological Research, he holds the *Parc de Recerca UAB—Santander* Technology Transfer Chair, and he has been the recipient of two ICREA ACADEMIA Awards (calls 2008 and 2013).

SPMS16*

M. Sans, J. Selga, A. Rodríguez, P. Vélez, V. E. Boria, J. Bonache, and F. Martín

"Unattended Design of Wideband Planar Filters using a Two-Step Aggressive Space Mapping (ASM) Optimization Algorithm"

Unattended Design of Wide-Band Planar Filters using a Two-Step Aggressive Space Mapping (ASM) Optimization Algorithm

[1]Marc Sans, [1]Jordi Selga, [2]Ana Rodríguez, [1]Paris Vélez, [2]Vicente E. Boria, [1]Jordi Bonache, and [1]Ferran Martín

[1]GEMMA/CIMITEC, Departament d’Enginyeria Electrònica, Universitat Autònoma de Barcelona,08193 Bellaterra, Spain

[2]Departamento de Comunicaciones, iTEAM, Universitat Politècnica de València, 46022 Valencia, Spain

Abstract This chapter deals with the automated and unattended design of planar wideband bandpass filters by means of aggressive space mapping (ASM) optimization. The approach can be applied to bandpass filters based on semi-lumped element resonators (e.g., stepped impedance resonators, ring resonators, etc.) coupled through admittance inverters (implemented with quarter-wavelength transmission lines). It will be explained how the filter layout is automatically generated from filter specifications, i.e., central frequency, fractional bandwidth, in-band ripple and order, without the need of any external aid to the design process. For this purpose, a novel optimization algorithm based on two independent ASM processes will be fully described. The proposed automatic design procedure will be detailed and validated through its application to generate several filter layouts starting from different sets of practical specifications.

1 Introduction

The synthesis of planar microwave circuits able to satisfy a set of given specifications is a subject of interest for microwave engineers. Despite the fact that most commercially available computer aided design (CAD) tools and electromagnetic solvers include optimizers, obtaining the circuit topologies that satisfy the design requirements is not always straightforward. This design difficulty increases with circuit complexity, and convergence to the optimum solution is not always guaranteed (for instance due to limitations related to local minima), unless the seeding layout is already very close to the one providing the target response.

This chapter is focused on a specific type of planar circuits, of interest in many different microwave applications, whose design requires significant computational effort: high-order (and hence highly selective) wideband bandpass filters. There are many approaches for the design of wideband planar microwave filters [1,2]. The interest in this chapter is the design of wideband bandpass filters based on semi-lumped (i.e., electrically small and planar) resonant elements coupled through admittance inverters [3] (see the generalized bandpass filter network in Fig. 1). In principle, these filters can be designed by forcing the planar resonant elements to exhibit the fundamental resonance at the filter central frequency, f_0, and the impedance slope at the value of the corresponding LC resonant tank of the generalized bandpass filter network. With such network, standard filter responses (e.g., Butterworth, Chebyshev) can ideally be achieved[1]. However, deviations from the ideal responses are caused by the limited functionality of the inverters (implemented by means of quarter-wavelength transmission lines at f_0) and by the distributed effects of the planar resonators at sufficiently high frequencies. These deviations are more pronounced if the filter is broadband, mainly because the required phase shift (90^o) of the inverters is not preserved over the whole filter pass band. Thus, broadband planar filters designed by implementing the inverters with quarter-wavelength transmission line sections typically exhibit a bandwidth narrower than the required one (nominal bandwidth), unless such bandwidth degradation is compensated at the design stage. One possibility to compensate for this narrowing effect is to over-dimension the filter bandwidth [4]. However, this tends to affect the reflection coefficient (ripple level in Chebyshev filters), and hence this is not an optimum solution. In the present chapter, a systematic design procedure, able to provide the filter layout satisfying the required specifications, and first reported in [5], is studied in detail. Moreover, it will be shown that filter layout is generated from the specifications and order following a completely unattended scheme. Filter design is a two-step process. In the first step, the filter schematic satisfying the specifications (optimum schematic) is obtained. This filter schematic consists in the generalized network of Fig. 1 with the admittance inverters replaced with quarter-wavelength transmission lines (not necessarily at f_0) and the lumped LC parallel tanks substituted by a reactive element network describing the semi-lumped resonators. Once the optimum filter schematic is inferred, the second step consists in determining the filter layout described by the optimum schematic.

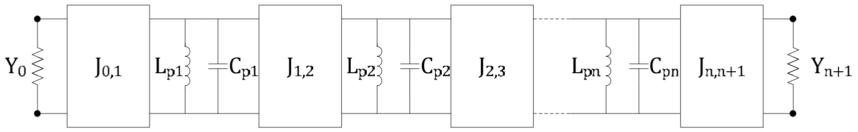

Fig. 1. Generalized bandpass filter network based on shunt LC resonators coupled through admittance inverters. From [5]; reprinted with permission.

---

[1] There are available expressions that provide the element values of the resonators from the filter order, central frequency, bandwidth, and response type (see [3]).

Both design steps (optimum schematic and layout generation) are based on the Aggressive Space Mapping (ASM) methodology [6], a technique that uses quasi-Newton type iteration to obtain the optimum solution. The two-step design process can in principle be applied to the automated synthesis of any type of wideband bandpass filter implemented by means of semi-lumped resonators coupled through admittance inverters. Planar resonant elements such as split rings, stepped impedance resonators (SIRs), and combinations of inductive/capacitive stubs and capacitive patches, among others, can be considered as semi-lumped resonators for filter design based on the approach reported in this chapter.

Chapter organization is as follows. In Section 2, the general formulation of ASM is presented. Section 3 is focused on the first design step, namely on the determination of the optimum filter schematic. Thus, the first ASM iterative algorithm will be presented through a guide example. The second design step (and hence the second ASM), providing the filter layout, will be presented in Section 4. In Section 5, further examples will be reported. Finally, in Section 6, the application of the two-step ASM algorithm will be applied to the design of wideband balanced filters.

2 General formulation of ASM

Among the considered techniques for microwave circuit synthesis and optimization, space mapping (SM), first proposed by Bandler *et al.* in 1994 [7], has revealed to be a powerful and efficient approach. Since this seminal work, several variants of SM have been proposed and applied to the synthesis and optimization of many different microwave components, including not only planar circuits [6], [8,9], but also waveguide-based components [10]-[12]. The interest in this chapter is on the so-called Aggressive Space Mapping (ASM) [6], an approach that uses quasi-Newton type iteration to find the optimum solution of the considered problem, as mentioned before. ASM uses two simulation spaces [6,7], [13]: (i) the optimization space, $\mathbf{X_c}$, where the variables are linked to a coarse model, which is simple and computationally efficient, although not accurate, and (ii) the validation space, $\mathbf{X_f}$, where the variables are linked to a fine model, typically more complex and CPU intensive, but significantly more precise. In each space, a vector containing the different model parameters can be defined. Let us call such vectors $\mathbf{x_f}$ and $\mathbf{x_c}$ for the fine and coarse model spaces, respectively, and let us designate by $\mathbf{R_f}(\mathbf{x_f})$ and $\mathbf{R_c}(\mathbf{x_c})$ their corresponding responses. The goal in ASM is to minimize the following error function:

$$\mathbf{f}(\mathbf{x_f}) = \mathbf{P}(\mathbf{x_f}) - \mathbf{x_c^*} \tag{1}$$

where $\mathbf{x_c}^*$ is a vector containing the target parameters in the coarse model (so that $\mathbf{R_c}(\mathbf{x_c}^*)$ is the target response), and $\mathbf{P}(\mathbf{x_f})$ is a mapping function that gives (via a parameter extraction procedure) the corresponding coarse model parameters that provide the same response of the fine model parameters.

Let us assume that $\mathbf{x_f}^{(j)}$ is the j-th approximation to the solution in the validation space, and $\mathbf{f}^{(j)}$ the corresponding error function to this solution. The next vector of the iterative process $\mathbf{x_f}^{(j+1)}$ is obtained by a quasi-Newton iteration according to

$$\mathbf{x}_\mathbf{f}^{(j+1)} = \mathbf{x}_\mathbf{f}^{(j)} + \mathbf{h}^{(j)} \tag{2}$$

where $\mathbf{h}^{(j)}$ is given by:

$$\mathbf{h}^{(j)} = -\left(\mathbf{B}^{(j)}\right)^{-1}\mathbf{f}^{(j)} \tag{3}$$

and $\mathbf{B}^{(j)}$ is an approach to the Jacobian matrix, which is updated according to the Broyden formula [6]:

$$\mathbf{B}^{(j+1)} = \mathbf{B}^{(j)} + \frac{\mathbf{f}^{(j+1)}\mathbf{h}^{(j)T}}{\mathbf{h}^{(j)T}\mathbf{h}^{(j)}} \tag{4}$$

In (4), $\mathbf{f}^{(j+1)}$ is obtained by evaluating (1), using a certain parameter extraction method providing the coarse model parameters from the fine model parameters, and the super-index T stands for transpose.

A typical scenario in ASM optimization is the determination of the layout of a certain microwave circuit (e.g., a filter) described by a lumped element equivalent circuit model. In this case, the coarse model parameters are constituted by the set of lumped elements describing the equivalent circuit, and the response (optimization space) is, for instance, the set of S-parameters, that can be inferred from the electrical analysis of the circuit model. The fine model parameters are a set of geometrical values defining the layout geometry, and the response in the validation space is also given by the S-parameters, typically inferred from electromagnetic simulation by means of commercial solvers. Note that the substrate parameters, necessary for the electromagnetic simulations, i.e., thickness, dielectric constant, and loss tangent, are not optimization variables. The second step in the ASM based optimization method studied in this chapter is very similar to the example of the present paragraph (despite the fact that the considered filters are described by a combination of lumped and distributed components). Namely, the filter layout is synthesized from the circuit schematic in the second ASM algorithm. However, the main relevant aspect of the two-step ASM iterative process concerns the first ASM stage, where the schematic satisfying the filter requirements is determined from the nominal specifications [5]. In the next two sections, these two

ASM algorithms are carefully and independently analyzed, using for that purpose a guide example for better understanding.

3 First ASM algorithm: determination of the optimum filter schematic

The objective of the first ASM algorithm is the determination of the filter schematic able to satisfy the filter requirements (specifications). It can be applied to any type of bandpass filter described by a set of semi-lumped resonators coupled through admittance inverters, where the replacement of the inverters with quarter-wavelength transmission lines in the schematic, which results from direct application of the design formulas [3], degrades the bandwidth. Thus, the objective is to automatically find the filter schematic providing the target response. Such schematic will be designated as optimum filter schematic from now on. It is important to note that each specific filter requires a particular ASM algorithm, and for that reason, a representative case example is considered throughout this section and the next one[2]. Let us thus first present the considered wideband bandpass filters, including their schematic and topology, and then we will describe the first ASM algorithm for the determination of the optimum filter schematic.

The topology and schematic of the case example filters are depicted in Fig. 2 [14]. The shunt resonators are implemented through a combination of stepped impedance resonators (SIRs) and grounded stubs. The SIRs provide transmission zeros (at frequencies designated as f_z) above the central filter frequency, f_0, which are useful for spurious suppression and for achieving a pronounced fall-off above the upper band edge. Moreover, with the parallel combination of SIRs and inductive stubs, the susceptance slopes at the filter central frequency can be made small, resulting in broad fractional bandwidths [14]. In the filter schematic, the resonators L_{ri}-C_{ri} describe the SIRs, the inductances L_{pi} account for the grounded stubs (i denotes the filter stage), and the quarter-wavelength transmission line sections correspond to the admittance inverters in the canonical prototype network (Fig. 1).

As mentioned before, at the schematic level, deviations from the target response (given by the network of Fig. 1 that results from specifications and transformation from the low-pass filter prototype), are due to the limited functionality of the inverters and to the fact that the considered resonators (Fig. 2b) are not purely parallel resonant LC tanks, but inductors connected to series resonators in shunt configuration. However it does not mean that the intended filter response (or at least a very good approximation in the region of interest) cannot be achieved with a certain schematic (described by the circuit of Fig. 2b). The hypothesis is that there exists a set of specifications, different than the target, that provide a fil-

---

[2] Nevertheless, the reported ASM algorithm can be easily adapted to different type of filters (i.e., considering different semi-lumped resonators).

ter schematic satisfying the target specifications [5]. This schematic is obtained by replacing the ideal admittance inverters of the canonical network with quarter-wavelength (not necessarily at f_0) transmission line sections, and the LC parallel resonators with the resonators L_{ri}-C_{ri} connected in parallel to the inductances L_{pi}, with the reactance values necessary to obtain the reactance slope and central frequency of the given specifications (different from the target)[3]. This means that it is necessary to tailor the parameters of the circuit schematic of Fig. 2(b), that is, the reactive parameters (L_{ri}, C_{ri} and L_{pi}) and the electrical lengths (at f_0) of the transmission line sections. Let us now present an ASM-based algorithm that automatically re-calculates these parameters in order to satisfy the filter specifications, thus providing the optimum filter schematic.

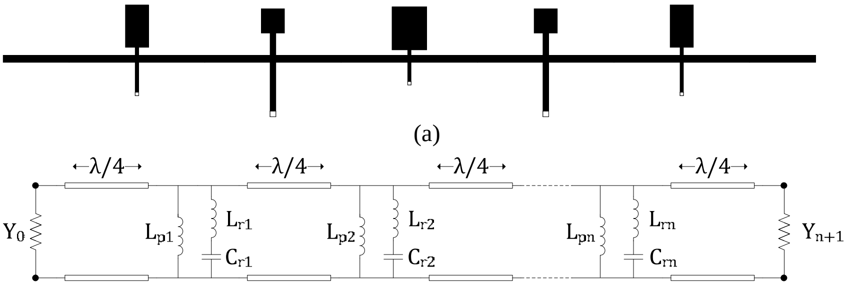

(a)

(b)

Fig.2. Typical topology (a) and circuit schematic (b) of the wideband bandpass filters considered as case example. The topology corresponds to an order-5 filter. From [5]; reprinted with permission.

Let us consider that the filter order, n, is known. The filter order is determined by the required filter selectivity. However, it is important to bear in mind that the responses obtained by the proposed filters are more selective than the Chebyshev responses at the upper transition band (due to the transmission zeros), but somehow less selective at the lower transition band (for the same specifications, i.e., central frequency, fractional bandwidth and ripple). Therefore, although the order can in principle be estimated by considering the standard Chebyshev response, it might be necessary to increase it if the resulting response does not satisfy the selectivity requirements below the pass band. Nevertheless, the ASM algorithm to determine the optimum filter schematic is very fast, and hence a new optimum filter schematic with a higher order (and hence higher selectivity) can be easily inferred.

By considering a quasi-Chebyshev response[4], the filter specifications are the central frequency, f_0, the fractional bandwidth, *FBW*, and the in-band ripple level

---

[3] The additional condition to univocally determine the three element values of the resonators is the transmission zero frequency, set to a fixed value.

[4] As mentioned, the filter responses are similar, but not identical, to the standard Chebyshev responses.

L_{Ar} (or minimum return loss level). On the other hand, as many transmission zeros as SIRs (and hence order) can be forced. However, it is convenient to set all the transmission zeros to $f_z = 2f_0$, since this is an efficient strategy to achieve spurious suppression, and to improve filter selectivity above the upper band edge [4, 14].

From the well-known impedance and frequency transformations from the low pass filter prototype [3], and assuming a Chebyshev response, the reactive elements of the shunt resonators of the network of Fig. 2 (L_{ri}, C_{ri}, and L_{pi}) can be easily inferred. The three conditions to unequivocally determine L_r, C_r, and L_p are:

(i) the filter central frequency, given by

$$f_0 = \frac{1}{2\pi\sqrt{(L_{ri} + L_{pi})C_{ri}}} \tag{5}$$

(ii) the transmission zero frequency

$$f_z = \frac{1}{2\pi\sqrt{L_{ri}C_{ri}}} \tag{6}$$

and (iii) the susceptance slope at f_0 (dependent on the filter stage):

$$b_i = 2\pi f_0 \frac{C_{ri}(L_{ri} + L_{pi})^2}{L_{pi}^2} \tag{7}$$

In (5) and (7), the right hand side terms are the resonance frequency and susceptance slope, respectively, of the LC resonant tanks in the circuit of Fig. 1 corresponding to the required Chebyshev response. Without loss of generality, the admittance of the inverters is set to $J = 0.02$ S [5].

Let us consider for the case example an order-5 ($n = 5$) Chebyshev response with $f_0 = 2.4$ GHz, $FBW = 40\%$ (corresponding to a 43.96% –3-dB fractional bandwidth[6]) and $L_{Ar} = 0.2$ dB [5]. From (5)-(7), the element values of the shunt resonators are found to be those indicated in Table 1.

---

[5] For a given filter response, there is not a unique solution for the network of Fig. 1. However, if the admittance of the inverters is set to a certain value (typically $J = 0.02$ S, as considered in the guide example), then the element values of the resonators are univocally determined. This is a usual procedure, although sometimes the resonator elements are all fixed to the same value, and the resulting admittance of the inverters is univocally determined by the design equations.

[6] Note that for Chebyshev bandpass filters the fractional bandwidth is given by the ripple level and is hence smaller than the –3-dB fractional bandwidth. However, the considered fractional bandwidth in this chapter is the –3-dB fractional bandwidth, since the ripple level is not constant in the optimization process (to be described). Thus, from now on, this –3-dB fractional bandwidth is designated as FBW, rather than FBW_{-3dB} (as usual), for simplicity, and to avoid an excess of subscripts in the formulation.

Table 1 Element Values of the Shunt Resonators [5].

Stage	L_p (nH)	L_r (nH)	C_r (pF)
1,5	1.3202	0.4401	2.4983
2,4	1.3226	0.4409	2.4937
3	0.8164	0.2721	4.0400

The quasi-Chebyshev filter response (i.e., the one inferred from the schematic of Fig. 2(b), but with ideal admittance inverters), depicted in Fig. 3, is similar to the ideal Chebyshev response in the pass band region, and it progressively deviates from it as frequency approaches f_z, as expected. The discrepancies are due to the fact that the shunt resonator is actually a combination of a grounded series resonator (providing the transmission zero) and a grounded inductor. The quasi-Chebyshev response satisfies the specifications to a rough approximation. Hence the target is considered to be the ideal Chebyshev response, except for the transmission zero frequency.

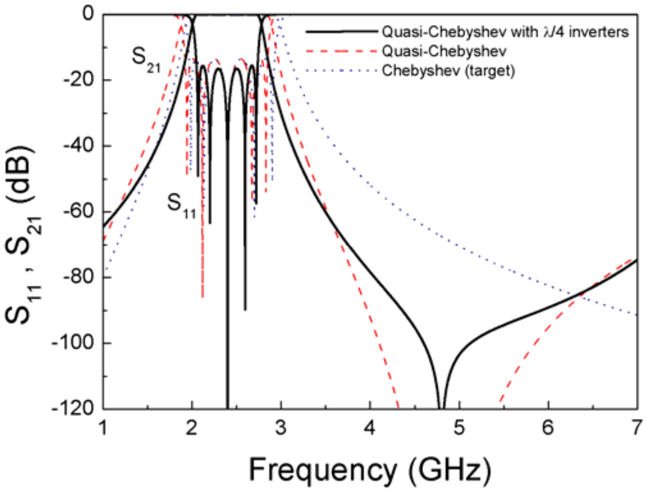

Fig. 3. Quasi-Chebyshev response of the filter that results by using the element values of Table 1 and ideal admittance inverters (dashed line), compared to the filter response that results by replacing the ideal inverters with quarter wavelength transmission lines (black solid line), and with the ideal Chebyshev (target) response. From [5]; reprinted with permission.

Let us now replace the ideal admittance inverters with quarter wavelength transmission lines. The resulting response is further modified, as revealed by the significant bandwidth reduction (see Fig. 3). These results reveal that the three-element resonators and the limited functionality of the quarter-wavelength transmission lines (acting as admittance inverters) degrade the filter bandwidth, as anticipated before, and point out the need to recalculate the element values and electrical lengths of the line sections of the filter schematic of Fig. 2(b), in order to satisfy the specifications. To this end, a new ASM concept that carries out the optimization at the schematic level has been proposed [5], and it is detailed in the following paragraphs.

The main hypothesis in the development of the iterative ASM algorithm able to provide the optimum filter schematic is to assume that there is a set of filter specifications, different than the target, that leads to a filter schematic (inferred by substituting the ideal admittance inverters with quarter wavelength transmission lines), whose response satisfies the target specifications. Let us now try to define the optimization (coarse model) space and the validation (fine model) space in the proposed ASM iterative scheme. The first one is constituted by the set of specifications, f_0, FBW, L_{Ar}, being its response the ideal Chebyshev response -target response- depicted in Fig. 3. The validation space is constituted by the same variables, but their response is inferred from the schematic of Fig. 2(b), with element values calculated as specified above, and quarter wavelength transmission lines at f_0, where f_0 is the considered value of this element in the validation space (not necessarily the target filter central frequency). The variables of each space are differentiated by a subscript. Thus, the corresponding vectors in the coarse and fine models are written as $\mathbf{x_c} = [f_{0\mathrm{c}}, FBW_\mathrm{c}, L_{Ar\mathrm{c}}]$ and $\mathbf{x_f} = [f_{0\mathrm{f}}, FBW_\mathrm{f}, L_{Ar\mathrm{f}}]$, respectively. The optimum coarse model solution (target specifications) is expressed as $\mathbf{x_c}^* = [f_{0\mathrm{c}}^*, FBW_\mathrm{c}^*, L_{Ar\mathrm{c}}^*]$. Notice that the transmission zero frequency, necessary to unequivocally determine the element values of the shunt resonators, is set to $f_z = 2f_0$, as indicated before. Hence f_z is not a variable in the optimization process.

Following the standard procedure in ASM, the first step before starting the iterative process is to make an estimation of the initial vector in the validation space, $\mathbf{x_f}^{(1)}$. Since the variables in both spaces are the same ones, the most canonical (and simplest) procedure is to consider $\mathbf{x_f}^{(1)} = \mathbf{x_c}^*$. From $\mathbf{x_f}^{(1)}$, the response of the fine model space is obtained (using the schematic with quarter wavelength transmission lines), and from it, the parameters of the coarse model can directly be extracted by direct inspection of that response, i.e., $\mathbf{x_c}^{(1)} = \mathbf{P}(\mathbf{x_f}^{(1)})$. Applying (1), the first error function can be obtained. To iterate the process (obtaining $\mathbf{x_f}^{(2)}$ from (2), using (3)), the Jacobian matrix must be initiated. To this end, the parameters of the fine model, $f_{0\mathrm{f}}$, FBW_f, $L_{Ar\mathrm{f}}$, are slightly perturbed, and the effects of such perturbations on the coarse model parameters, $f_{0\mathrm{c}}$, FBW_c, $L_{Ar\mathrm{c}}$, are inferred. Thus, the first Jacobian matrix is given by:

$$\mathbf{B} = \begin{pmatrix} \dfrac{\delta f_{0\mathrm{c}}}{\delta f_{0\mathrm{f}}} & \dfrac{\delta f_{0\mathrm{c}}}{\delta FBW_\mathrm{f}} & \dfrac{\delta f_{0\mathrm{c}}}{\delta L_{Ar\mathrm{f}}} \\ \dfrac{\delta FBW_\mathrm{c}}{\delta f_{0\mathrm{f}}} & \dfrac{\delta FBW_\mathrm{c}}{\delta FBW_\mathrm{f}} & \dfrac{\delta FBW_\mathrm{c}}{\delta L_{Ar\mathrm{f}}} \\ \dfrac{\delta L_{Ar\mathrm{c}}}{\delta f_{0\mathrm{f}}} & \dfrac{\delta L_{Ar\mathrm{c}}}{\delta FBW_\mathrm{f}} & \dfrac{\delta L_{Ar\mathrm{c}}}{\delta L_{Ar\mathrm{f}}} \end{pmatrix} \tag{8}$$

Once the first Jacobian matrix is obtained, the process can be iterated until convergence is obtained. At each iteration, the elements of the coarse space vector, $\mathbf{x_c}^{(j)}$, are compared to the target (filter specifications), $\mathbf{x_c}^*$, and the error function is calculated according to:

$$\| f_{norm} \| = \sqrt{\left(1 - \frac{f_{0\mathrm{c}}}{f_{0\mathrm{c}}^*}\right)^2 + \left(1 - \frac{FBW_\mathrm{c}}{FBW_\mathrm{c}^*}\right)^2 + \left(1 - \frac{L_{Arc}}{L_{Arc}^*}\right)^2} \tag{9}$$

The scheme of the proposed ASM algorithm is depicted in Fig. 4.

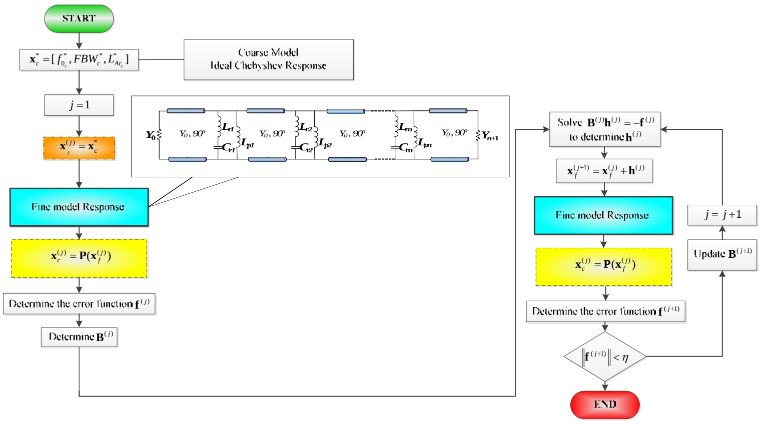

Fig. 4. Flow diagram of the first ASM algorithm. From [5]; reprinted with permission.

Applying the first ASM algorithm to the considered example ($\mathbf{x_c}^* = [f_{0c}^*, FBW_\mathrm{c}^*, L_{Arc}^*] = [2.4$ GHz, 43.96%, 0.2 dB]), the error function rapidly decreases, being the error smaller than 1.2% after $N = 13$ iterations. The evolution of the error function is depicted in Fig. 5. The fine model parameters for $N = 13$ are $\mathbf{x_f}^{(13)} = [f_{0\mathrm{f}}^{(13)}, FBW_\mathrm{f}^{(13)}, L_{Ar\mathrm{f}}^{(13)}] = [2.4690$ GHz, 65.53%, 0.4413 dB], and the coarse model parameters are $\mathbf{x_c}^{(13)} = [f_{0c}^{(13)}, FBW_\mathrm{c}^{(13)}, L_{Arc}^{(13)}] = [2.3999$ GHz, 43.75%, 0.1978 dB]. Note that $\mathbf{x_f}^{(13)}$ is appreciably different than $\mathbf{x_c}^*$. The optimum filter schematic is the one given by the last fine model response (which provides an error below a predefined value). The elements of the shunt resonators for this optimum filter schematic are indicated in Table 2, whereas the 50-Ω line sections are quarter-wavelength transmission lines at $f_{0\mathrm{f}}^{(13)} \neq f_0^* = 2.4$ GHz.

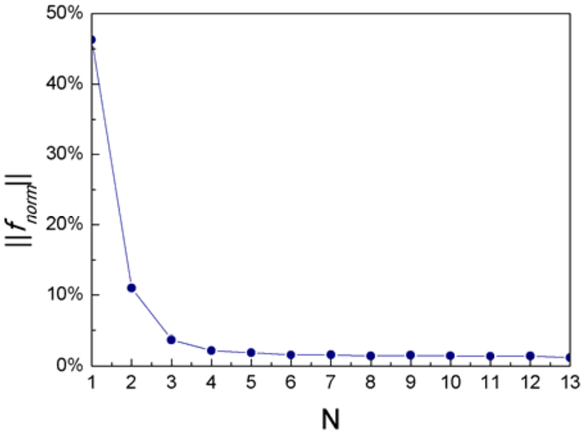

Fig. 5. Evolution of the error function of the first ASM algorithm for the considered example. From [5]; reprinted with permission.

Table 2. Element Values of the Shunt Resonators for the Optimum Filter Schematic [5].

Stage	L_p (nH)	L_r (nH)	C_r (pF)
1,5	1.6090	0.5363	1.9368
2,4	2.1196	0.7065	1.4703
3	1.0685	0.3562	2.9168

The response of the optimum schematic is compared to the target response in Fig. 6. The agreement in terms of central frequency, bandwidth and in-band ripple is very good, as expected on account of the small error function that results after 13 iterations. Note, however, that the position of the reflection zero frequencies are different in both responses. The reason is that these frequency positions are not goals in the optimization process. Unavoidably, it is not possible to perfectly match the Chebyshev (target) response by replacing the ideal admittance inverters with transmission line sections, and the LC shunt resonators of Fig. 1 with the resonators of the schematic of Fig. 2(b). Nevertheless the synthesized circuit fulfills the target specifications, and hence it is the optimum filter schematic. This schematic is used as the starting point in the ASM algorithm developed to obtain the filter layout, to be described in the next section.

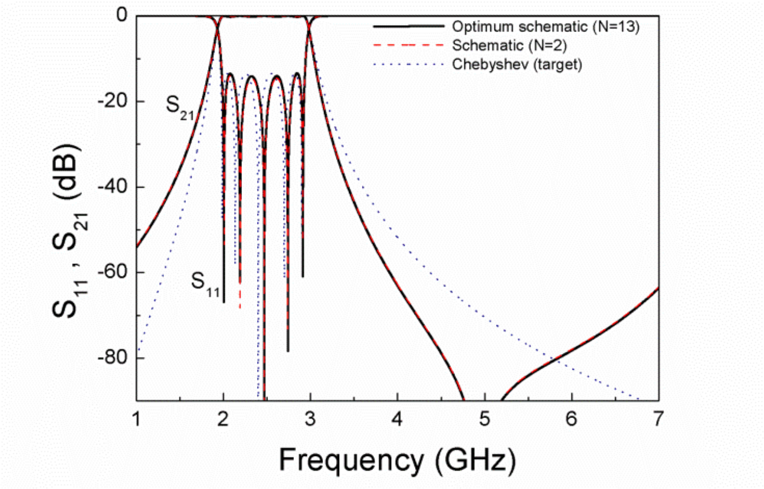

Fig. 6. Response of the optimum filter schematic, derived from the ASM algorithm, compared with the Chebyshev target response. The response at the second iteration (N = 2), also included, is very close to the final solution (N = 13). From [5]; reprinted with permission.

4 Second ASM algorithm: determination of the layout

To determine the filter layout from the optimum filter schematic, a second ASM algorithm is considered. Each filter cell is synthesized from the element values of the shunt resonator and the characteristic impedance of the cascaded $\lambda/4$ (at $f_{0f}^{(13)}$) transmission lines independently. This second ASM process involves three stages: (i) determination of the resonator layout, (ii) determination of the line width, and (iii) optimization of the line length. Let us now discuss in detail the implementation of these three specific ASM algorithms.

4.1 Synthesis of the Resonators

In order to obtain the layout of the filter resonators, composed by the SIRs connected in parallel to the grounded stubs, a specific ASM iterative process is applied. The variables in the optimization space are the resonator elements, i.e., $\mathbf{x}_c = [L_p, L_r, C_r]$, and the coarse model response is obtained through circuit simulation. The validation space is constituted by a set of variables defining the resonator layout. In order to deal with the same number of variables in both spaces, the widths of the grounded stubs, W_{Lp}, as well as the widths of the low- and high-impedance transmission line sections of the SIRs, W_{Cr} and W_{Lr}, respectively, are set to fixed values. Specifically, the values of W_{Cr} and $W_{Lr} = W_{Lp}$ indicated in Tables 3 and 5 have been considered. There is some flexibility to choose these widths, but it is convenient to consider wide capacitive and narrow inductive sections in order to reduce the length of the SIRs and inductive stubs. Nevertheless, extreme widths of the capacitive sections are not convenient, in order to avoid transversal resonances in the frequency region of interest (i.e., up to frequencies above f_z) [15]. The widths of the inductive sections must be set to values above the tolerance limits (representing a good balance between SIR/stub dimensions and fabrication accuracy). Thus, the variables in the validation space are the remaining dimensions of the shunt resonators, that is, the length of the grounded stub, l_{Lp}, and the lengths l_{Lr} and l_{Cr} of the high- and low-impedance transmission line sections, respectively, of the SIR (i.e., $\mathbf{x_f} = [l_{Lp}, l_{Lr}, l_{Cr}]$). The fine model response is obtained through electromagnetic simulation of the layout, inferred from the fine model variables plus the fixed dimensions (specified above) and substrate parameters. Let us consider in the present guide example the substrate parameters of the *Rogers RO3010* with thickness h = 635 μm and dielectric constant $\varepsilon_r = 10.2$.

Following the general scheme of the ASM optimization described in Section II, to initiate the algorithm it is necessary to obtain an initial layout for the SIR and shunt stub. This is obtained from the well-known (and simple) approximate formulas providing the inductance and capacitance of a narrow and wide, respectively, electrically small transmission line section [16]. Isolating the lengths, the following results are obtained:

$$l_{Lr} = \frac{L_r v_{ph}}{Z_h} \tag{10a}$$

$$l_{Cr} = C_r v_{pl} Z_l \tag{10b}$$

$$l_{Lp} = \frac{L_p v_{ph}}{Z_h} \tag{10c}$$

where v_{ph} and v_{pl} are the phase velocities of the high- and low-impedance transmission lines sections, respectively, and Z_h and Z_l the corresponding characteristic impedances. Once the initial layout (i.e., $\mathbf{x}_f^{(1)}$) is determined, the circuit elements can be extracted from the electromagnetic response using (5)-(7). This provides $\mathbf{x}_c^{(1)} = \mathrm{P}(\mathbf{x}_f^{(1)})$, and using (1), the first error function can be inferred. To iterate the process using (2), with $\mathbf{h}^{(1)}$ derived from (3), a first approximation of the Jacobian matrix is needed. Following a similar approach to the one explained in Section 3, the lengths l_{Lp}, l_{Lr}, l_{Cr} are slightly perturbed, and the values of L_p, L_r and C_r resulting after each perturbation are obtained from parameter extraction. The first Jacobian matrix can thus be expressed as:

$$\mathbf{B} = \begin{pmatrix} \frac{\delta L_r}{\delta l_{Lr}} & \frac{\delta L_r}{\delta l_{Cr}} & \frac{\delta L_r}{\delta l_{Lp}} \\ \frac{\delta C_r}{\delta l_{Lr}} & \frac{\delta C_r}{\delta l_{Cr}} & \frac{\delta C_r}{\delta l_{Lp}} \\ \frac{\delta L_p}{\delta l_{Lr}} & \frac{\delta L_p}{\delta l_{Cr}} & \frac{\delta L_p}{\delta l_{Lp}} \end{pmatrix} \tag{11}$$

By applying this procedure to the resonator elements of each filter stage, the corresponding layouts of the SIRs and grounded stubs are determined.

4.2 Determination of the Line Width

The initial line width is estimated from the formulas provided in several microwave textbooks (for instance [17]). Once the initial width is estimated, the specific ASM algorithm developed to determine the line width is applied. In such one-variable ASM scheme, the initial Jacobian matrix (actually just composed of one element) is inferred by perturbing the line width and obtaining the characteristic impedance through electromagnetic simulation (i.e., the fine model variable is the line width, W, whereas the variable of the coarse model is the characteristic impedance).

4.3 Optimization of the Line Length (Filter Cell Synthesis)

As previously mentioned, the length of the lines cascaded to the resonant elements is optimized by considering the whole filter cell. Let us define l_{cell} as the length of the cell excluding the width of the grounded stubs, W_{Lp}, (roughly corresponding to $\lambda/4$ at $f_{0\mathrm{f}}^{(13)}$). To determine l_{cell}, a single parameter ASM optimization is applied to the filter cell (filter cell synthesis), where the initial value of l_{cell} is inferred from the well-known formula [15] that gives the line length as a function of the required phase (90°) and frequency ($f_{0\mathrm{f}}^{(13)}$). At this stage, the ASM optimization consists of varying the length of the lines cascaded to the resonator until the required phase at $f_{0\mathrm{f}}^{(13)}$ (i.e., 90°) per filter cell is achieved (the other geometrical parameters of the cell are kept unaltered). The phase is directly inferred from the frequency response of the cell obtained from electromagnetic simulation at each iteration step.

Once each filter cell has been synthesized, the cells are simply cascaded to generate the final filter layout (coupling between adjacent resonators is not taken into account since the results reveal that this effect is not significant). The scheme of the complete ASM process able to automatically provide the layout from the optimum filter schematic, and consisting of three independent quasi-Newton iterative algorithms, is depicted in Fig. 7. Using the element values of Table 2, corresponding to the optimum filter schematic of the example reported in section III, where the lines present between adjacent resonators exhibit a characteristic impedance of Z_o= 50 Ω and an electrical length of 90° at $f_{0f}^{(13)}$ = 2.4690 GHz, the second ASM algorithm was applied to automatically generate the filter layout (which is actually the one depicted in Fig. 2). The dimensions are summarized in Table 3, except the line width, which does not depend on the filter stage, i.e., W = 0.6055 mm. Notice that the cell length slightly varies from cell to cell. This variation is due to the phase effects produced by the different resonators, and justifies the need to optimize the length of the lines by considering the complete filter cell (as described in the preceding paragraph).

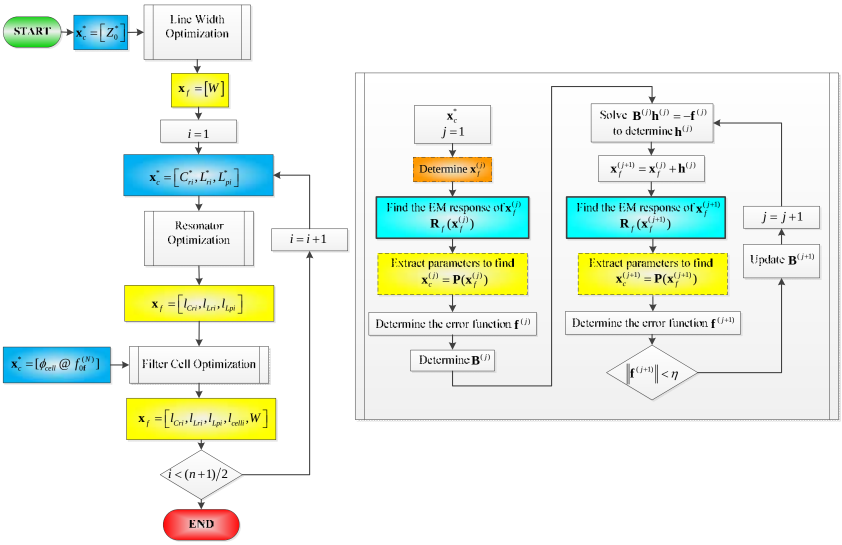

Fig.7. Flow diagram of the second ASM algorithm. The sub-process depicted at the right of the figure represents a typical ASM algorithm used in each optimization process (particularly the indicated one is for the resonator optimization). Notice that the loop must be executed (n+1)/2 times, n being the filter order (which is assumed to be odd), since for odd Chebyshev response the cells i and n+1–i are identical. However, this does not affect line width optimization since line width is identical for all filter stages. From [5]; reprinted with permission.

Table 3. Geometry Parameters of the Synthesized Order-5 Filter [5].

Stage	l_{Lr} (mm)	l_{Cr} (mm)	l_{Lp} (mm)	l_{cell} (mm)	W_{Cr} (mm)	W_{Lp} (mm)
1,5	0.7062	3.6710	2.5955	11.4003	2	0.3
2,4	1.9438	2.1037	4.2334	11.2583	2	0.5
3	0.4725	3.7461	1.6629	11.4786	3	0.3

The electromagnetic simulation (excluding losses) of the synthesized filter is compared to the response of the optimum filter schematic and to the target (ideal Chebyshev) response in Fig. 8. The agreement between the lossless electromagnetic simulation and the response of the optimum filter schematic (where losses are excluded) is very good, pointing out the validity of the second ASM synthesis method. The fabricated filter and the measured frequency response are depicted in Fig. 9. The measured response is in reasonable agreement with the lossy electromagnetic simulation, and reveals that filter specifications are satisfied to a good approximation. Slight discrepancies between the measured response and the lossy electromagnetic simulation can be mainly attributed to inaccuracies in the dielectric constant provided by the substrate supplier, although they can be also influenced by fabrication related tolerances, substrate anisotropy and foil roughness. Nevertheless, these effects are not considered in the optimization process, because the aim is to automatically obtain the filter layout providing a lossless electromagnetic simulation able to satisfy the specifications.

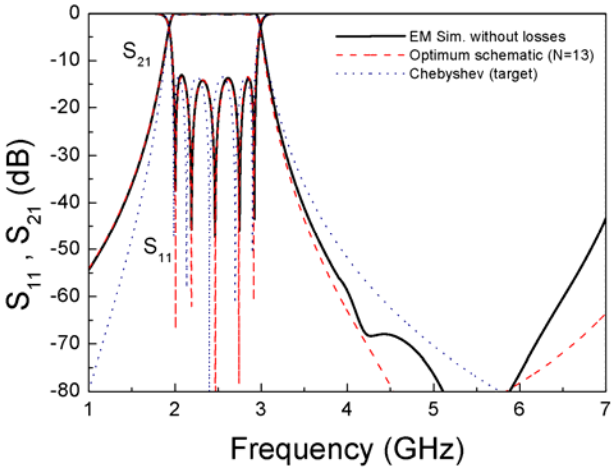

Fig.8. Lossless electromagnetic simulation of the synthesized order-5 filter, compared to the response of the optimum filter schematic and target response. From [5]; reprinted with permission.

It is worth highlighting that layout generation with the reported two-step ASM procedure (synthesis of the filter schematic and synthesis of the filter layout) is obtained following a completely unattended scheme. External action is only required in the first step, to provide the filter specifications, which are the input variables of the proposed two-step ASM algorithm.

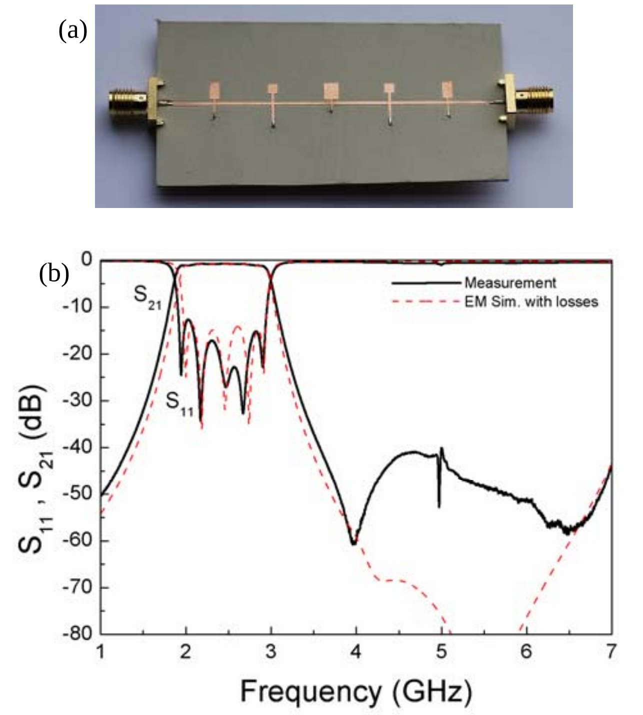

Fig. 9. Photograph of the fabricated order-5 filter (a) and measured response compared to the lossy electromagnetic simulation (b). The layout of the fabricated filter is the one depicted in Fig. 2. From [5]; reprinted with permission.

5 Further examples of filter synthesis

In order to demonstrate the potential of the two-step ASM algorithm for the synthesis of filters based on SIRs and shunt inductive stubs, let us now apply the developed tool to the synthesis of a higher order filter with the following specifications: order $n = 7$, central frequency $f_0 = 3.0$ GHz, fractional bandwidth $FBW = 37.2$ % (–3-dB fractional bandwidth) and ripple level $L_{Ar} = 0.12$ dB. Application of the first ASM algorithm gives the schematic with element values indicated in Table 4 and 90° (at $f_{0f}^{(8)} = 3.0638$ GHz) transmission line sections. Convergence has been achieved after $N = 8$ iterations, when the error function is as small as 0.1%.

Application of the second ASM algorithm, considering the substrate used for the filter of the previous section (*Rogers RO3010* with thickness $h = 635$ μm and dielectric constant $\varepsilon_r = 10.2$), provides the filter geometry indicated in Table 5. Figure 10 shows the layout of the filter and the lossless electromagnetic simulation, compared to the optimum filter schematic and target responses. The fabricated filter is depicted in Fig. 11, together with the measured response and the lossy electromagnetic simulation. Again, very good agreement between the different responses can be appreciated, and the filter response satisfies the considered specifications.

Table 4. Element Values of the Shunt Resonators for the Optimum Filter Schematic of the 7th Order Filter

Stage	L_p (nH)	L_r (nH)	C_r (pF)
1,7	1.6280	0.5427	1.2431
2,6	1.1377	0.3792	1.7788
3,5	0.8442	0.2814	2.3974
4	1.0073	0.3358	2.0092

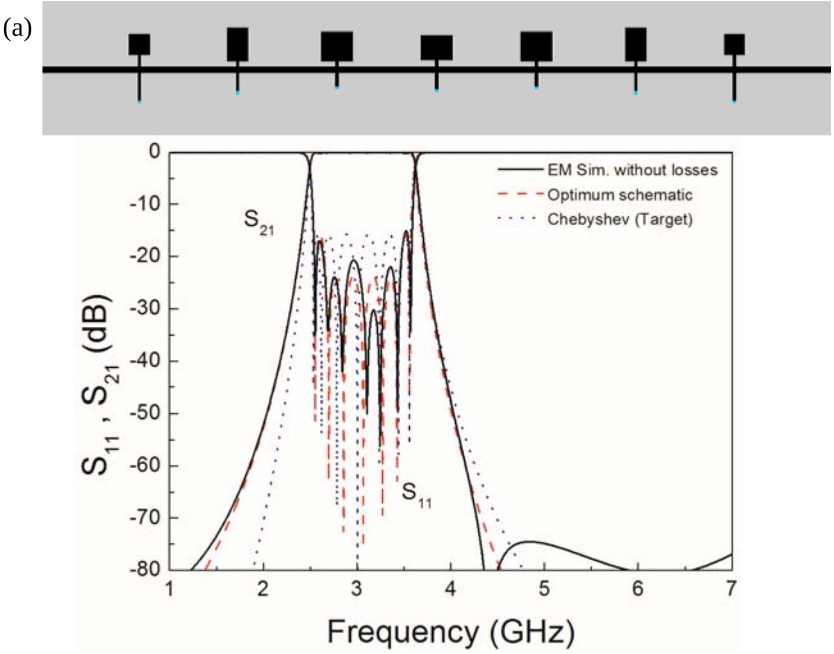

Fig.10. Layout of the synthesized order-7 filter (a), and lossless electromagnetic simulation compared to the response of the optimum filter schematic and target response (b).

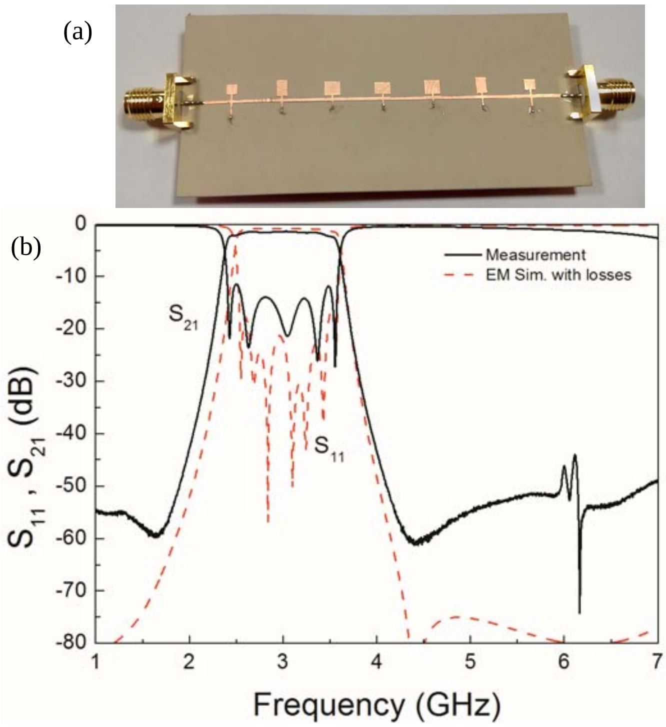

Fig. 11. Photograph of the fabricated order-7 filter (a) and measured response compared to the lossy electromagnetic simulation (b).

Table 5. Geometry Parameters of the Synthesized Order-7 Filter

Stage	l_{Lr} (mm)	l_{Cr} (mm)	l_{Lp} (mm)	l_{cell} (mm)	W_{Cr} (mm)	W_{Lp}(mm)
1,7	1.0493	1.9982	2.6430	9.0701	2.0	0.3
2,6	0.4612	3.2080	1.7949	9.1020	2.0	0.3
3,5	0.4407	2.7972	1.2780	9.2243	3.0	0.3
4	0.5882	2.3437	1.5738	9.1482	3.0	0.3

This additional example of an order-7 filter with different specifications (as compared to the 5th order filter reported before), and other synthesized higher order filters reported in [5], demonstrate that the two-step ASM algorithm discussed in this chapter is a powerful tool to automatically provide the layout of the considered type of filters. In principle, the reported two-step ASM tool can be applied to any type of filter consisting on semi-lumped resonators coupled through admittance inverters. For instance application to wideband bandpass filters based on open complementary split ring resonators (OCSSRs) coupled through admittance inverters, first reported in [18], can be envisaged. It is also possible to apply the reported two-step ASM technique to the synthesis of wideband balanced bandpass filters. Indeed, this is the subject of the next section.

6 Synthesis of wideband balanced bandpass filters

The design of differential-mode wideband bandpass filters with common-mode noise suppression has been an object of growing interest in recent years [19-27]. These filters are key elements in balanced circuits and systems (e.g., high-speed digital circuits), of increasing demand for their inherent high immunity to noise, electromagnetic interference (EMI) and crosstalk. The design of balanced filters by means of resonant elements coupled through differential-mode quarter-wavelength admittance inverters suffers from the same limitations than the single-ended counterparts, i.e., bandwidth degradation [24]. Hence the application of the two-step ASM scheme presented before is fully justified for the automated design of these differential-mode bandpass filters. As an illustrative example, the filter type considered in this section is based on mirrored SIRs coupled through admittance inverters [24]. The typical layout is depicted in Fig. 12(a). The central metallic patches of the mirrored SIRs introduce common-mode transmission zeros, useful for the suppression of that mode in the differential filter pass band.

The mirrored SIRs are described by means of a combination of capacitances and inductances, as indicated in the schematic of Fig. 12(b). Note that the symmetry plane is an electric wall for the differential-mode, and hence the capacitances C_{zi} do not play an active role for that mode (they are grounded). Thus, the equivalent circuit schematic for the differential-mode is the canonical circuit of a bandpass filter (Fig. 12c) [5]. Conversely, the symmetry plane for the common-mode is a magnetic wall (open circuit) and the equivalent circuit schematic is the one depicted in Fig. 12(d). The resonators L_{pi}-C_{zi} provide transmission zeros that are useful for the suppression of the common-mode in the region of interest (differential filter pass band). According to the schematics of Figs. 12(c)-(d), the position of the transmission zeros does not affect the differential-mode response.

For the synthesis of the filter, the two-step process described above, conveniently modified, can be applied. Notice that for the determination of the circuit schematic for the differential mode, the capacitances C_{zi} do not play a role. Moreover, for the differential mode, the shunt resonators only depend on two elements, and hence they are determined from the filter central frequency and reactance slope. An important difference, as compared to the first ASM algorithm reported in Section 3, is that in this case the resonators are considered to be identical, (and thus $L_{pi} = L_p$ and $C_{pi} = C_p$ for $i = 1,2,...,n$), whereas the admittance of the inverters depends on the device stage. The reason is that, from a topological point of view, it is convenient to implement the filter layout with identical mirrored SIRs, since the admittance inverters can thus be implemented by transmission line sections parallel to the line axis.

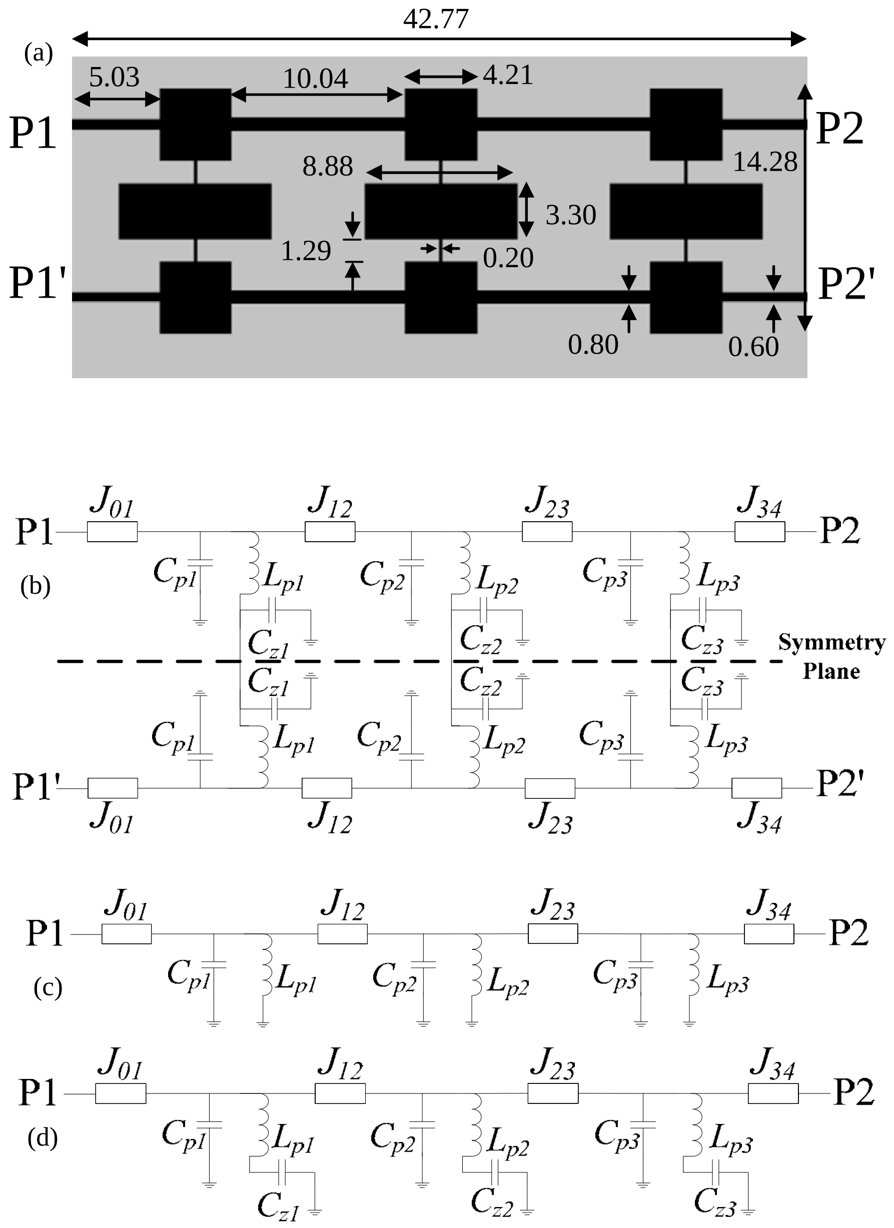

Fig. 12. Typical topology (order-3) of the considered balanced wideband bandpass filters (a), circuit schematic (b), and circuit schematic for the differential (c) and common (d) modes. Dimensions, in millimeters, correspond to the designed prototype.

Let us consider the following differential filter specifications: $n = 3$, $f_0 = 2.4$ GHz, $FBW = 40\%$ (corresponding to a 52.98% –3dB fractional bandwidth, considered in the optimization) and $L_{Ar} = 0.15$ dB. The ideal Chebyshev response is depicted in Fig. 13. Such response is achieved by considering $L_p = 1.1637$ nH, $C_p = 3.7779$ pF and ideal admittance inverters with $J_{0,1} = J_{3,4} = 0.02$ S, $J_{1,2} = J_{2,3} = 0.0199$ S. The application of the first ASM algorithm to the considered example provides an error function smaller than 3.2% after $N = 4$ iterations. The resulting fine and coarse model parameters are $\mathbf{x_f}^{(4)} = [f_{0f}^{(4),}\ FBW_f^{(4),}\ L_{Arf}^{(4)}] =$ [2.423 GHz, 65.78%, 0.332 dB] and $\mathbf{x_c}^{(4)} = [f_{0c}^{(4)}, FBW_c^{(4)}, L_{Arc}^{(4)}] =$ [2.3999 GHz, 0.5344%, 0.1546 dB], and the resulting response is depicted in Fig. 13. The element values of the resonators are $L_p = 2.8195$ nH, $C_p = 1.5302$ pF, and the admittance of the quarter wavelength (at $f_{0f}^{(4)}$) transmission line sections are $J_{0,1} = J_{3,4} = 0.02$ S, $J_{1,2} = J_{2,3} = 0.0223$ S. To complete the schematic of Fig. 12(b), the capacitances C_{zi} must be set to a certain value. In this example, all the transmission zero frequencies have been set to the same value, i.e., $f_z = 1.1 f_0$. This gives a good common-mode rejection ratio (CMRR) in the whole differential filter pass band. With this value of f_z the value of the central patch capacitances is $C_z = 2.3302$ pF.

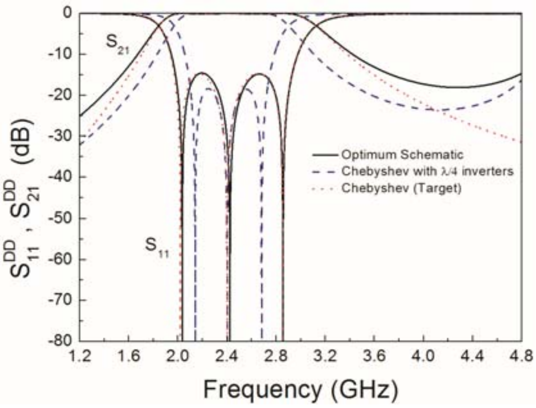

Fig.13. Ideal Chebyshev response of the differential bandpass filter, response that results by replacing the ideal inverters with quarter wavelength transmission lines, and response of the optimum schematic that results after applying the first ASM algorithm.

The second ASM algorithm, necessary to determine the filter layout, is similar to the one reported in Section 4. The resulting layout is the one depicted in Fig. 12. The lossless electromagnetic response is very close to the response of the schematic and hence to the target response (see Fig. 14). The fabricated device (depicted in Fig. 15) exhibits a frequency response in very good agreement to the lossy electromagnetic simulation (see Fig. 15b). As for the single-ended filter synthesis reported before, the layout of the balanced filter has been determined from the specifications without the need of any further action during the optimization process. The results of this section demonstrate that the two-step ASM scheme analyzed in this chapter is also useful for the synthesis of common-mode suppressed balanced filters based on resonators coupled through admittance inverters.

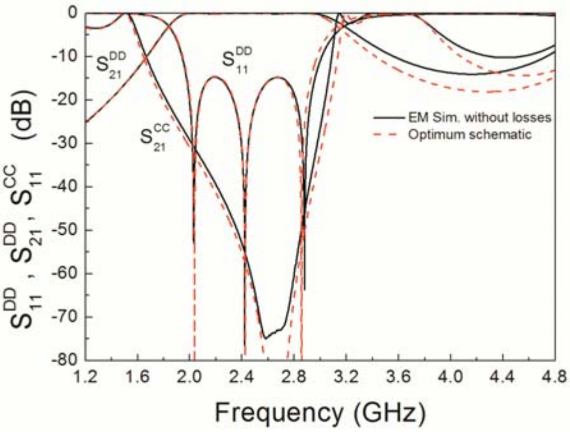

Fig. 14. Lossless electromagnetic simulation of the synthesized order-3 balanced filter, compared to the response of the optimum filter schematic.

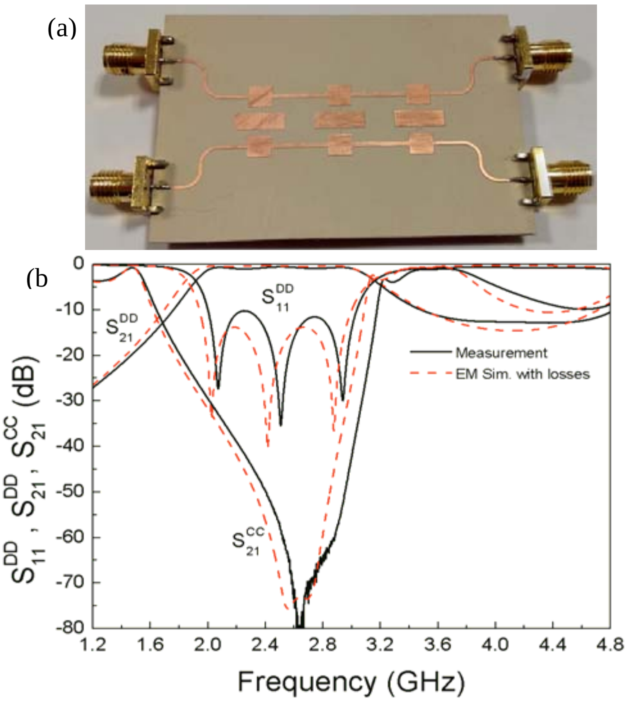

Fig.15. Photograph of the fabricated order-3 balanced filter (a) and measured response compared to the lossy electromagnetic simulation (b). The layout of the fabricated filter is the one depicted in Fig. 12.

7 Conclusions

In summary, a method for the automated and unattended design of single-ended and balanced wideband bandpass filters based on shunt resonators coupled through admittance inverters has been reviewed. It is based on aggressive space mapping (ASM) optimization and is divided in two steps: a first ASM algorithm, devoted to determine the filter schematic able to satisfy the specifications, and a second ASM algorithm, that automatically determines the filter layout. With this approach, the bandwidth degradation typical of wideband filters based on resonators coupled through admittance inverters is solved, and the filter design does not require any external action in the whole process. Several examples of filter design have been reported to demonstrate the viability and flexibility of the method.

Acknowledgements

The results presented in this chapter have been generated thanks to the support of several projects by MINECO-Spain (projects TEC2013-47037-C5-1-R, TEC2013-40600-R, TEC2013-49221-EXP) and *Generalitat de Catalunya* (project 2014SGR-157). This work has also been supported by FEDER funds. Ferran Martín is in debt to *Institució Catalana de Recerca i Estudis Avançats*, who awarded him with an ICREA Academia Prize.

References

[1] S. Sun and L. Zhu, “Multimode resonator-based bandpass filters”, *Microwave Magazine*, vol. 10(2), pp. 88-98, Apr. 2009.

[2] Z.-C. Hao and J-S. Hong, “Ultrawideband filter technologies, *Microwave Magazine*, vol. 11(4), pp. 56-68, Jun. 2010.

[3] J. S. Hong and M. J. Lancaster, *Microstrip Filters for RF/Microwave Applications*, New York, NY, USA: Wiley, 2001.

[4] J. Selga, M. Sans, A. Rodríguez, J. Bonache, V. Boria, F. Martín, “Automated synthesis of planar wideband bandpass filters based on stepped impedance resonators (SIRs) and shunt stubs through aggressive space mapping (ASM)”, *IEEE MTT-S Int. Microwave Symp*., June 2014, Tampa, FL (USA).

[5] M. Sans, J. Selga, A. Rodríguez, J. Bonache, V.E. Boria, and F. Martín, “Design of planar wideband bandpass filters from specifications using a two-step ag-

gressive space mapping (ASM) optimization algorithm”, *IEEE Trans. Microw. Theory Techn.*, vol. 62, pp. 3341-3350, Dec. 2014.

[6] J.W. Bandler, R.M. Biernacki, S.H. Chen, R.H. Hemmers, and K. Madsen, “Electromagnetic optimization exploiting aggressive space mapping”, *IEEE Trans. Microw. Theory Techn*., vol. 43, pp. 2874–2882, Dec. 1995.

[7] J.W. Bandler, R.M. Biernacki, S.H. Chen, P.A. Grobelny and R.H. Hemmers, “Space mapping technique for electromagnetic optimization”, *IEEE Trans. Microw. Theory Techn*., vol. 42, pp. 2536-2544, Dec. 1994.

[8] M.H. Bakr, J.W. Bandler, K. Madsen, J.E. Rayas-Sánche and J. Søndergaard, “Space-mapping optimization of microwave circuits exploiting surrogate models”, IEEE Transactions on Microwave Theory and Techniques, vol. 43, pp. 2297-2306, Dec. 2000.

[9] S. Koziel, Q.S. Cheng, and J.W. Bandler, “Space mapping”, IEEE Microwave Magazine, vol. 9, pp. 105-122, Dec. 2008.

[10] J.W. Bandler, R.M. Biernacki, S.H. Chen, and D. Omeragic, “Space mapping optimization of waveguide filters using finite element and mode-matching electromagnetic simulators”, *IEEE MTT-S Int. Microwave Symp*., June 1997, Denver, CO (USA).

[11] J.W. Bandler, Q.S. Cheng, D.M. Hailu, and N.K. Nikolova, “A space-mapping design framework”, *IEEE Trans. Microw. Theory Techn.*, vol. 53, pp. 2601-2610, Nov. 2004.

[12] J.V. Morro, P. Soto, H. Esteban, V.E. Boria, C. Bachiller, M. Taroncher, S. Cogollos and B. Gimeno, “Electromagnetic optimization exploiting aggressive space mapping”, *IEEE Trans. Microw. Theory Techn.*, vol. 53, pp. 1130-1142, April 2005.

[13] J. W. Bandler, Q. S. Cheng, S. A. Dakroury, A. S. Mohamed, M. H. Bakr, K. Madsen, and J. Søndergaard, “Space mapping: the state of the art,” *IEEE Trans. Microw. Theory Techn*., vol. 52, pp. 337-361, 2004.

[14] J. Bonache, I. Gil, J. García-García and F. Martín, “Compact microstrip band-pass filters based on semi-lumped resonators”, *IET Microw. Antennas Propag.*, vol. 1, pp. 932-936, August 2007.

[15] J. Naqui, M. Durán-Sindreu, J. Bonache and F. Martín, “Implementation of shunt connected series resonators through stepped-impedance shunt stubs: analysis and limitations”, *IET Microw. Antennas Propag.*, vol. 5, pp. 1336-1342, Aug. 2011.

[16] D.M. Pozar, *Microwave Engineering*, Addison Wesley, 1990.

[17] I. Bahl and P. Barthia, *Microwave Solid State Circuit Design*, John Wiley, 1998.

[18] P. Vélez, J. Naqui, M. Durán-Sindreu, J. Bonache, and F. Martín, "Broadband Microstrip Bandpass Filter Based on Open Complementary Split Ring Resonators (OCSRRs)", *Int. Journal of Antennas and Propagation*, vol. 2012, Article ID 174023, 6 pages, doi:10.1155/2012/174023, 2012.

[19] T. B. Lim, and L. Zhu, "A differential-mode wideband bandpass filter on microstrip line for UWB applications," *IEEE Microw. Wireless Compon. Lett.*, vol. 19, pp. 632-634, Oct. 2009.

[20] A. M. Abbosh, "Ultrawideband balanced bandpass filter", *IEEE Microw. Wireless Compon. Lett.*, vol. 21, pp. 480-482, Sep. 2011.

[21] H. T. Zhu, W. J. Feng, W. Q. Che and Q. Xue, "Ultra-wideband differential bandpass filter based on transversal signal-interference concept", *Electronic Letters*, vol.47, Sep. 2011.

[22] X-H. Wu, Q-X. Chu, "Compact differential ultra-wideband bandpass filter with common-mode suppression", *IEEE Microw. Wireless Compon. Lett.*, vol. 22, pp. 456-458, Sep. 2012.

[23] P. Vélez, J. Naqui, A. Fernández-Prieto, M. Durán-Sindreu, J. Bonache, J. Martel, F. Medina, and F. Martín, "Differential bandpass filter with common mode suppression based on open split ring resonators and open complementary split ring resonators", *IEEE Microw. Wireless Compon. Lett.*, vol. 23, pp. 22-24, Jan. 2013.

[24] P. Vélez, M. Durán-Sindreu, J.Bonache, A. Fernández-Prieto, J. Martel, F. Medina and F. Martín, "Differential bandpass filters with common-mode suppression based on stepped impedance resonators (SIRs)", *IEEE MTT-S Int. Microwave Symp.*, June 2013, Seattle (USA).

[25] X.-H. Wang, H. Zhang and B.-Z. Wang, "A novel ultra-wideband differential filter based on microstrip line structures", *IEEE Microw. Wireless Compon. Lett.*, vol. 23, pp. 128-130, March. 2013.

[26] J. Shi, C. Shao, J-X. Chen, Q-Y. Lu, Y. Peng, and Z-H. Bao, "Compact low-loss wideband differential bandpass filter with high common-mode suppression", IEEE Microw. Wireless Compon. Lett., vol. 23, no. 9, pp. 480-482, Sep. 2013.

[27] P. Vélez, J. Naqui, A. Fernández-Prieto, J. Bonache, J. Mata-Contreras, J. Martel, F. Medina, and F. Martín "Ultra-compact (80mm^2) differential-mode ultra-wideband (UWB) bandpass filters with common-mode noise suppression", *IEEE Trans. Microw. Theory Techn.*, to be published.

IJMWT16

M. Sans, J. Selga, P. Vélez, A. Rodríguez, J. Bonache, V. E. Boria, and F. Martín

"Automated Design of Balanced Wideband Bandpass Filters based on Mirrored Stepped Impedance Resonators (SIRs) and Interdigital Capacitors"

International Journal of Microwave and Wireless Technologies, 2016, 8(4/5), 731–740. © Cambridge University Press and the European Microwave Association, 2016
doi:10.1017/S1759078716000672

RESEARCH PAPER

Automated design of balanced wideband bandpass filters based on mirrored stepped impedance resonators (SIRs) and interdigital capacitors

MARC SANS[1], JORDI SELGA[1], PARIS VÉLEZ[1], ANA RODRÍGUEZ[2], JORDI BONACHE[1],
VICENTE E. BORIA[2] AND FERRAN MARTÍN[1]

This paper presents small balanced bandpass filters exhibiting wide differential-mode pass bands and high common-mode suppression. The filters are implemented in microstrip technology and their topology consists of multisection mirrored stepped impedance resonators (SIRs) alternating with mirrored interdigital capacitors. The mirrored SIRs provide the required common-mode transmission zeros to achieve effective rejection of that mode in the region of interest, i.e. the differential-mode pass band. An automated design method for such filters, based on aggressive space mapping, is reported. The method uses the equivalent circuit model of both the mirrored SIRs and the interdigital capacitors, and filter synthesis is based on a quasi-Newton iterative algorithm where parameter extraction is the key aspect. The automated design approach is illustrated through an order-3 filter, where it is demonstrated that the filter topology is generated from the specifications. As compared with previous balanced filters based on mirrored SIRs coupled through admittance inverters, the proposed filters of this work are smaller and the design method is simplified, since bandwidth compensation due to the narrowband functionality of the inverters is avoided.

Keywords: Balanced filters, Bandpass filters, Stepped impedance resonators (SIRs), Space mapping (SM)

Received 22 October 2015; Revised 22 April 2016; Accepted 4 May 2016; first published online 6 June 2016

I. INTRODUCTION

The design of differential-mode (or balanced) wideband bandpass filters with common-mode noise suppression is a very active research topic today [1–18]. These filters are fundamental elements in balanced circuits and systems (e.g. high-speed digital circuits), of increasing demand for their inherent high immunity to noise, electromagnetic interference, and crosstalk. Filter size and performance, i.e. good differential-mode characteristics (including a wide stop band) and significant common-mode suppression in the region of interest (differential filter pass band), are the warhorses of the researchers working on this topic. In this regard, we have recently proposed a type of balanced filters, based on mirrored stepped impedance resonators (SIRs), which fulfill these requirements [10]. However, these filters are based on admittance inverters implemented through quarter-wavelength transmission lines, and hence size is not fully optimized (the filters in [10] can be considered to consist of a combination of semi-lumped and distributed elements). Moreover, the limited (narrowband) functionality of the admittance inverters means that a method for bandwidth compensation is necessary if filter specifications must be satisfied to a good approximation. In [19], such method was presented, and it was demonstrated that the reported wideband balanced filters accurately reproduce the desired response (typically a Chebyshev response) in the region of interest. However, this method complicates significantly the design of the filters, since the aggressive space mapping (ASM)-based tool used for this purpose must include an algorithm able to determine the schematic satisfying the specifications. This filter schematic is different than the one directly inferred from the required filter response, provided the quarter wavelength transmission lines acting as admittance inverters have a bandwidth limited functionality. The result is that the unattended design method reported in [19], inspired by the one reported in [20] for single-ended filters, is actually based on a two-step ASM algorithm, where first the optimum schematic is found, and then the filter layout is generated. Nevertheless, by replacing the inverters with interdigital capacitors, modeled as a series resonant tank with parasitic capacitances (as it will be later detailed), the structure can be roughly described by the canonical circuit of a bandpass filter, filter size is reduced, and the first

[1]Departament d'Enginyeria Electrònica, Universitat Autònoma de Barcelona, CIMITEC, 08193 Bellaterra, Spain. Phone: +34 93 581 35 24
[2]Departamento de Comunicaciones-iTEAM, Universitat Politècnica de València, 46022 Valencia, Spain
Corresponding author:
J. Selga
Email: jordi.selga@uab.cat

ASM algorithm is avoided since the resulting filter is composed of semi-lumped elements accurately described by their corresponding circuit models over wide frequency ranges.

According to the previous paragraph, this paper presents novel wideband balanced filters inspired by those reported in [10, 19], but representing a clear improvement in terms of size and design complexity. The paper is organized as follows. In Section II, the filter topology and the lumped element equivalent circuit model of the different filter stages (mirrored SIRs and interdigital capacitors) are presented and validated. The ASM method, used to automatically determine the filter layout once the elements of the equivalent circuit of the filter are known (directly inferred from the specifications), is presented in Section III. Section IV presents an illustrative example, in order to demonstrate the potentiality of the method as a tool for the automated design of these filters. Finally, the main conclusions are highlighted in Section V.

II. FILTER TOPOLOGY AND CIRCUIT MODEL

The differential-mode microstrip bandpass filters proposed in this paper are implemented by combining shunt connected mirrored SIRs and series connected interdigital capacitors. The typical topology is depicted in Fig. 1(a). Figures 1(b) and 1(c) show the lumped element equivalent circuit model of the mirrored SIRs and the interdigital capacitors. The mirrored SIRs are described by a combination of capacitances (C_{pi}, C_{zi}) and inductances (L_{pi}, L_{par}). The parasitic inductance L_{par} was neglected in previous works [10, 11], but it is necessary to be included for an accurate description of the mirrored SIR. The interdigital capacitors are modeled by a π-model with series resonators L_{si}, C_{si}, and shunt parasitic capacitors, C_{par}. Note that in previous works, where the inductance L_{par} is ignored, the capacitance C_{par} is connected in parallel with the capacitance C_{pi} (differential mode), simplifying the circuit model for the differential mode to the one of the canonical circuit of a band pass filter, but this assumption is not made here.

The symmetry plane of the filter is an electric wall for the differential mode, and hence the capacitances C_{zi} do not play an active role for that mode (since they are grounded). Thus, the equivalent circuit model for the differential mode is roughly the canonical circuit of a bandpass filter, as depicted in Fig. 1(d) [21] (note that the parasitic inductances L_{par} prevent from that canonicity, but since L_{par} is small, the resulting responses are similar to those inferred from the canonical circuit, as will be shown later). Conversely, the symmetry plane for the common mode is a magnetic wall (open circuit) and the equivalent circuit model is the one depicted in Fig. 1(e). The resonators L_{pi}–C_{zi} provide transmission zeros that are useful for the suppression of the common-mode in the region of interest (differential filter pass band). It is also worth-mentioning that the position of these common-mode transmission zeros does not affect the differential-mode response. To validate the filter model, we have separately considered the mirrored SIRs and the interdigital capacitors. The simulated (using *Keysight Momentum*) response (differential- and common-modes) of the mirrored SIR of Fig. 2(a) is depicted in Fig. 2(b). We have extracted the circuit elements by analyzing the series and shunt impedances of the T-model. The shunt elements are derived from the differential-mode resonance frequency of the shunt branch (where $Y_p = 0$) and the susceptance slope at this frequency. On the other hand, since the series impedance is purely inductive, the value of L_{par} can be directly extracted at any arbitrary point from the differential-mode response. Concerning the capacitance C_{zi}, it is inferred from the common-mode transmission zero. The resulting element values, indicated in the caption of Fig. 2, provide the circuit response also depicted in the figure, where excellent

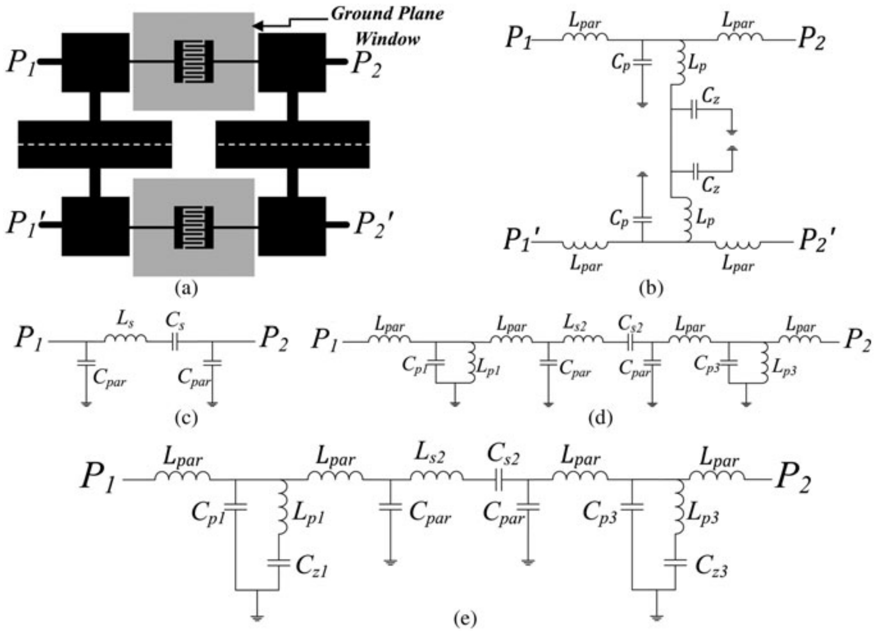

Fig. 1. Typical topology of the proposed differential bandpass filters (a), lumped element equivalent circuit model for the mirrored SIR (b), circuit model of the interdigital capacitors (c), circuit model for the differential-mode (d), and circuit model for the common mode (e).

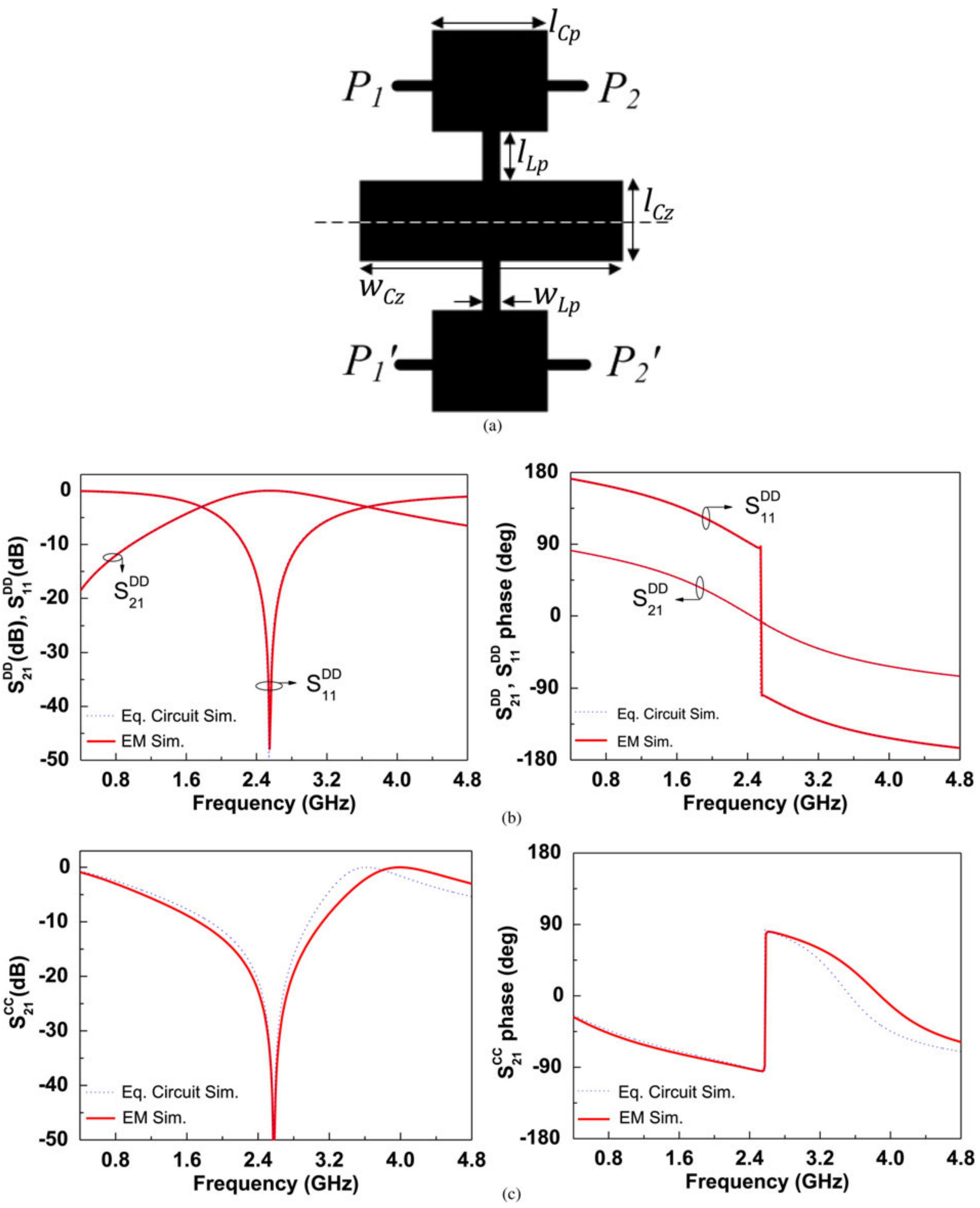

(a)

(b)

(c)

Fig. 2. Topology of the mirrored SIR used for model validation (a) and simulated frequency response for both modes – differential (b) and common (c). The considered substrate is the *Rogers RO3010* with thickness $h = 254$ μm and dielectric constant $\varepsilon_r = 10.2$. Dimensions are (in mm): $l_{Cp} = 2.414$, $l_{Lp} = 5.767$, $l_{Cz} = 1.763$, $W_{Ls} = 1.200$, and $W_{Cz} = 5.927$. The element values are: $L_p = 1.1639$ nH, $C_p = 3.5075$ pF, $L_{par} = 0.1819$ nH, and $C_z = 3.1225$ pF.

agreement with the electromagnetic simulation can be appreciated. For the pairs of interdigital capacitors the separation is so large that the differential- and common-mode models are identical. Let us consider the interdigital capacitor depicted in Fig. 3(a), with frequency response inferred from electromagnetic simulation depicted in Fig. 3(b). Notice, that, in this case, the window in the ground plane, necessary to enhance the inductance L_s and decrease the capacitance C_{par}, is circularly shaped in order to minimize the interaction between both resonators. Parameter extraction provides the element values indicated in the caption of Fig. 3. In this case, the element values are inferred be means of resonance

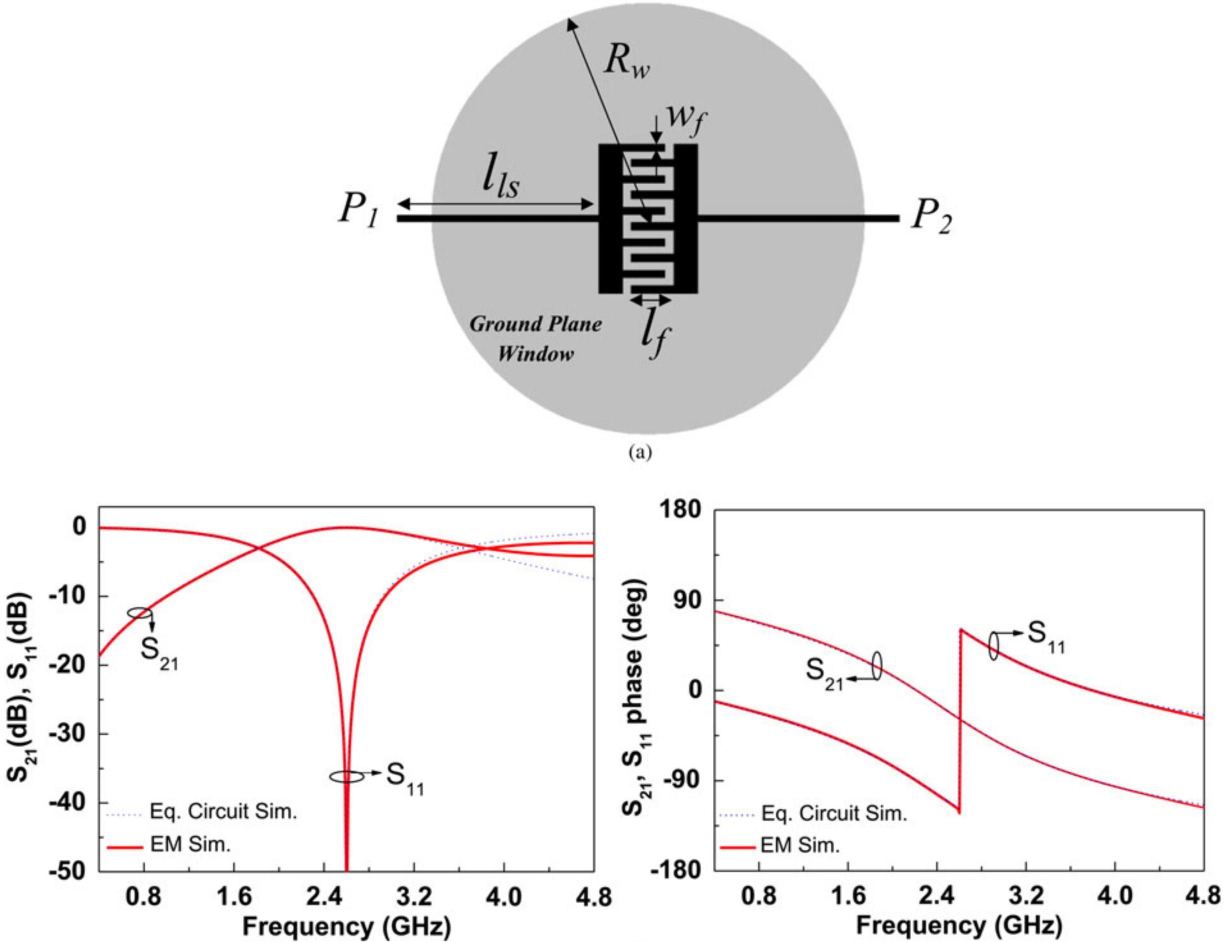

(a)

(b)

Fig. 3. Topology of the interdigital capacitor used for model validation (a) and simulated frequency response (b). The considered substrate is the *Rogers RO3010* with thickness $h = 254$ μm and dielectric constant $\varepsilon_r = 10.2$. Dimensions are (in mm): $R_w = 4.382$, $w_f = 0.160$, $l_{Ls} = 4.015$, and $l_f = 0.7143$. The element values are: $L_s = 9.5496$ nH, $C_s = 0.4586$ pF, and $C_{par} = 0.2728$ pF.

of the series branch (where $Z_s = 0$), the reactance slope at this frequency, and the parasitic capacitance C_{par} is obtained by means of the shunt admittance. By obtaining the circuit response of the corresponding model, it is found that the agreement with the electromagnetic simulation is good as well.

III. FILTER DESIGN BY MEANS OF ASM

Space mapping [22] is a technique that makes use of two simulation spaces: the optimization space, $\mathbf{X_c}$, where the variables are linked to a coarse model, which is simple and computationally efficient, although not accurate; and the validation space, $\mathbf{X_f}$, where the variables are linked to a fine model, typically more complex and CPU intensive, but significantly more precise. In each space, a vector containing the different model parameters is defined. Such vectors are designated as $\mathbf{x_f}$ and $\mathbf{x_c}$ for the fine and coarse model parameters, respectively, and their responses are denoted as $\mathbf{R_f}(\mathbf{x_f})$ and $\mathbf{R_c}(\mathbf{x_c})$. In this paper, an improved version of space mapping, i.e. ASM [23], which uses quasi-Newton-type iteration, is used. The objective is to automatically determine the filter layout from the specifications, without external aid in the process. In this paper, a Chebyshev response for the differential mode is considered. However, the equivalent circuit model for that mode is not exactly the canonical model of a bandpass filter, in which the elements can be determined from well-known transformations [21] from the low-pass filter prototype. Nevertheless, such transformations and filter specifications provide the elements of the series (L_{si}, C_{si}) and shunt (C_{pi}, L_{pi}) resonators. The parasitic elements are not design variables, but they can be extracted and taken into account in the synthesis procedure. Finally, the capacitances C_{zi}, are dictated by the position of the transmission zeros for the common mode. The key aspect is to find the elements of the equivalent circuit of the differential mode, including the parasitics, which provide a response as close as possible to the target. Once the elements of the equivalent circuit model of the filter are known, the next step is the generation of the layout.

The two considered simulation spaces are constituted by the filter layout (validation space) and by the equivalent circuit (optimization space). It is worth to mention that, in both spaces the conductor and substrate losses are not taken into account for simplicity and to reduce the computation cost. The variables in the validation space are formed by a set of geometrical parameters of the filter, and the corresponding response is obtained through electromagnetic simulation (in this paper using the *Keysight Momentum* commercial software); the variables in the optimization space are the elements of the equivalent circuit, and the response is given by the circuit simulation, which can be easily inferred, e.g. by means of *Keysight ADS*. Nevertheless, in this paper, rather than obtaining the filter layout in a single process, we have determined the layout of each filter stage independently and finally all the isolated resonators are concatenated. However, before detailing the ASM processes applied to determine the layout of the mirrored SIRs and interdigital capacitors separately, let us briefly summarize the general formulation of ASM for completeness.

A) General formulation of ASM

The first step before starting the iterative process is to make an estimation of the first vector in the validation space, $\mathbf{x_f}^{(1)}$. From $\mathbf{x_f}^{(1)}$, the response of the fine model space is obtained, and from it we extract the parameters of the coarse model. This allows us to obtain the first error function (by comparing to the target, $\mathbf{x_c^*}$), i.e.

$$\mathbf{f}(\mathbf{x_f}) = \mathbf{P}(\mathbf{x_f}) - \mathbf{x_c^*}, \tag{1}$$

where $\mathbf{P}(\mathbf{x_f})$ is the vector corresponding to the coarse model parameters extracted from the response of the fine model. To iterate the process following the standard quasi-Newton-type ASM approach, the new fine model vector is obtained according to

$$\mathbf{x_f}^{(j+1)} = \mathbf{x_f}^{(j)} + \mathbf{h}^{(j)}, \tag{2}$$

where $\mathbf{h}^{(j)}$ is given by:

$$\mathbf{h}^{(j)} = -(\mathbf{B}^{(j)})^{-1}\mathbf{f}^{(j)} \tag{3}$$

and $\mathbf{B}^{(j)}$ is an approach to the Jacobian matrix, which is updated according to the Broyden formula:

$$\mathbf{B}^{(j+1)} = \mathbf{B}^{(j)} + \frac{\mathbf{f}^{(j+1)}\mathbf{h}^{(j)T}}{\mathbf{h}^{(j)T}\mathbf{h}^{(j)}}. \tag{4}$$

In (4), $\mathbf{f}^{(j+1)}$ is obtained by evaluating (1), and the super-index T stands for transpose. To initiate the Jacobian matrix, the elements of the fine model are slightly perturbed, being the effects on the extracted parameters inferred, and expressed as derivatives in matrix form. This process is iterated until convergence is achieved (once the error function is smaller than a certain predefined value).

B) ASM applied to the interdigital capacitors

Once the elements of the series resonator of the interdigital capacitors are known, a specific ASM process for the determination of the layout giving such elements is necessary. In this ASM algorithm, the variables in the optimization space are $x_c = (L_{si}, C_{si})$, whereas the variables in the validation space are the length of the inductive line, l_{Ls}, and the length of the fingers, l_f, i.e. $\mathbf{x_f} = (l_{Ls}, l_f)$. The other geometrical parameters are set to 0.16 mm. The first vector of the validation space, $x_f^{(1)}$, is estimated from approximate formulas providing the inductance of a narrow inductive strip and the capacitance of an interdigital capacitor [24]. Parameter extraction is carried out as indicated in Section II. Finally, the first approach to the Broyden matrix, necessary to iterate the process as indicated above, is given by:

$$\mathbf{B} = \begin{pmatrix} \frac{\delta L_s}{\delta l_{Ls}} & \frac{\delta L_s}{\delta l_f} \\ \frac{\delta C_s}{\delta l_{Ls}} & \frac{\delta C_s}{\delta l_f} \end{pmatrix}. \tag{5}$$

With this ASM scheme, the layout providing the target elements of the series branch is determined, and from this layout, the parasitic capacitance C_{par} is also inferred. The value of C_{par} is relevant since it must be subtracted to the capacitance C_{pi} of the mirrored SIRs, as it will be justified later.

3) ASM applied to the mirrored SIRs

The layout of the mirrored SIRs is determined using an ASM algorithm with three variables. The variables in the optimization space are the elements of the shunt resonator from the circuit schematic for the common mode depicted in Fig. 1(d), i.e. $\mathbf{x_c} = (L_{pi}, C_{pi}, C_{zi})$. The validation space is constituted by a set of variables defining the resonator layout. In order to deal with the same number of variables in both spaces, the widths of the central patch, W_{Czi}, as well as the widths of the high- and low-impedance transmission line sections of the SIRs, W_{Lpi}, and W_{Cpi}, respectively, are set to fixed values. Thus, the variables in the validation space are the remaining dimensions of the shunt resonators, that is, the length of the central capacitive patch, l_{Czi}, and the lengths l_{Lpi} and l_{Cpi} of the high- and low-impedance transmission line sections, respectively, of the SIR (i.e. $\mathbf{x_f} = (l_{Lpi}, l_{Cpi}, l_{Czi})$). The specific procedure to determine the layout is similar to the one detailed in [20]. The first vector of the validation space, $\mathbf{x_f}^{(1)}$, is estimated from the well-known (and simple) approximate formulas providing the inductance and capacitance of a narrow and wide, respectively, electrically small transmission line section [24]. Isolating the lengths, we obtain:

$$l_{Lp} = \frac{L_p v_h}{Z_h}, \tag{6a}$$

$$l_{Cp} = C_p v_{lp} Z_{lp}, \tag{6b}$$

$$l_{Cz} = C_z v_{lz} Z_{lz}, \tag{6c}$$

where v_h and $v_{lp,z}$ are the phase velocities of the high- and low-impedance transmission lines sections, respectively, and Z_h and $Z_{lp,z}$ the corresponding characteristic impedances (note that the sub-indices p, z in the phase velocity, and characteristic impedance of the low-impedance transmission line sections are used to differentiate the central, C_z, and external, C_p, patches). Parameter extraction is carried out as specified in Section II. Finally, the first approach to the Broyden matrix, necessary to iterate the process, is given by:

$$\mathbf{B} = \begin{pmatrix} \frac{\delta L_p}{\delta l_{Lp}} & \frac{\delta L_p}{\delta l_{Cp}} & \frac{\delta L_p}{\delta l_{Cz}} \\ \frac{\delta C_p}{\delta l_{Lp}} & \frac{\delta C_p}{\delta l_{Cp}} & \frac{\delta C_p}{\delta l_{Cz}} \\ \frac{\delta C_z}{\delta l_{Lp}} & \frac{\delta C_z}{\delta l_{Cp}} & \frac{\delta C_z}{\delta l_{Cz}} \end{pmatrix}. \tag{7}$$

With this ASM scheme, the layout providing the target elements of the shunt branch is determined, and from this layout, the parasitic capacitance L_{par} is also inferred.

D) Strategy to determine the circuit schematic satisfying specifications

With the previous ASM algorithms, the layouts of the filter stages corresponding to the interdigital capacitors and mirrored SIRs can be determined. However, the presence of the parasitic elements forces us to recalculate the circuit schematic taking into account such parasitics. The hypothesis in the design process is to assume that once the parasitics are inferred, following the processes indicated above, the values do not significantly depend on the specific geometry. Hence, the next step is to set the element values of the parasitics to the inferred values, and consider the remaining elements as variables that must be tuned at the circuit level in order to satisfy the filter specifications. However, as long as the inductance L_{par} is small, as it has been verified, one expects that by subtracting the parasitic capacitance C_{par} to the capacitance of the mirrored SIR, C_p, the variables in the optimization process do not need to be modified so much. Indeed, it has been verified that it is enough to tune L_s to satisfy the filter specifications. Thus, by tuning this element, the final circuit schematic, including the parasitics, is determined. Therefore, the layout of the interdigital capacitors must be recalculated following the previous ASM algorithms. Then the resulting layouts are cascaded, and filter topology is thus constructed.

IV. ILLUSTRATIVE EXAMPLE

As an example, let us consider the synthesis of an order-3 Chebyshev filter with fractional bandwidth $FBW = 40\%$, ripple $L_{Ar} = 0.15$ dB, and central frequency $f_o = 2.4$ GHz. The element values of the canonic circuit are: $L_s = 9.57087$ nH, $C_s = 0.495948$ pF, $L_p = 1.1637$ nH, and $C_p = 3.77899$ pF. The application of ASM to the interdigital capacitors provides the layout depicted in Fig. 3, and the element values are also depicted in the caption of Fig. 3 result. The error of this ASM process after convergence is 0.3%. For the shunt branch, we have reduced the value of the capacitance C_{par} from C_p, for the reasons explained before. The resulting layout by applying the explained ASM procedure is the one depicted in Fig. 2, and the element values are indicated in the caption. Less than 0.05% error has resulted in this case. Once the element values are inferred, we have tuned L_s at the circuit level in order to recalculate the schematic, including parasitic that satisfies the specifications. The value of L_s has been found to be: $L_s = 9.06$ nH. Figure 4 shows a comparison between the ideal Chebyshev response, and the one of the optimized circuit schematic. As can be seen, the responses are very similar, thus validating the approach based on the tuning of L_s only. Once the new value of L_s is found, it is necessary to recalculate the new layout of the interdigital capacitor by applying the ASM algorithm explained before. This layout is depicted in Fig. 5 (dimensions are indicated in the caption), together with the frequency response. The resulting element values are $L_s = 9.0644$ nH, $C_s = 0.4599$ pF, $C_{par} = 0.2706$ pF, and the error is smaller than 0.1%. Note that the parasitic capacitance C_{par} has changed only slightly, as anticipated.

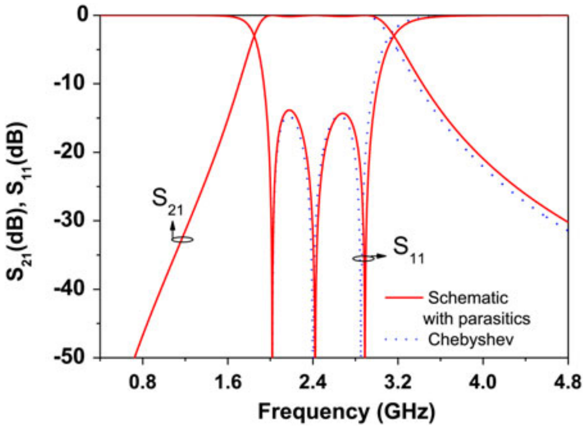

Fig. 4. Comparison between the ideal Chebyshev response and the frequency response of the filter schematic including parasitic elements.

The layout of the final filter has been obtained by cascading the three stages. It is depicted in Fig. 6(a), whereas the photograph of the fabricated prototype is depicted in Fig. 6(b). The *LPKF H-100* drilling machine has been used for the fabrication of the prototype. The frequency response of the filter, including the simulation of the optimum schematic, electromagnetic simulation, and measurement is depicted in Fig. 7. The agreement between the electromagnetic simulation and circuit simulation is reasonable, and discrepancies with the measurement can be attributed to fabrication-related tolerances. The maximum measured insertion loss for the differential mode is 0.8 dB between 1.90 and 2.85 GHz ($FBW = 40\%$), whereas the return loss is higher than 14 dB within the same frequency range. The common-mode response is reasonably predicted by the circuit model, as depicted in Fig. 7(b). Common-mode rejection is better than 17 dB in the whole differential filter pass band with a maximum rejection of 58 dB at 2.5 GHz. Concerning dimensions, these are as small as 24.0 × 17.5 mm^2, that is $0.48 \times 0.35\lambda^2$ (excluding the tapered access lines), λ being the guided wavelength at the central filter frequency.

For comparison purposes, we include a table (Table 1) where the size (effective area, expressed in terms of the square wavelength at the filter central frequency, f_o), and filter performance, including the -3 dB fractional bandwidth, common-mode rejection ratio at f_o, and differential-mode insertion loss at $2f_o$, are provided. According to this table, where filters with fractional bandwidth of the same order are considered, the proposed filter exhibits a good balance between size and performance. However, the main relevant aspect of this paper is the fact that the filter has been designed following an unattended procedure.

V. CONCLUSIONS

In conclusion, novel wideband differential-mode microstrip bandpass filters with common-mode suppression, plus an automated synthesis method for such filters, based on ASM, have been presented in this paper. The filter has been described by means of lumped elements, and it has been demonstrated that the circuit model provides a good description of the filter response for both the differential- and common-modes. As compared with previous wideband

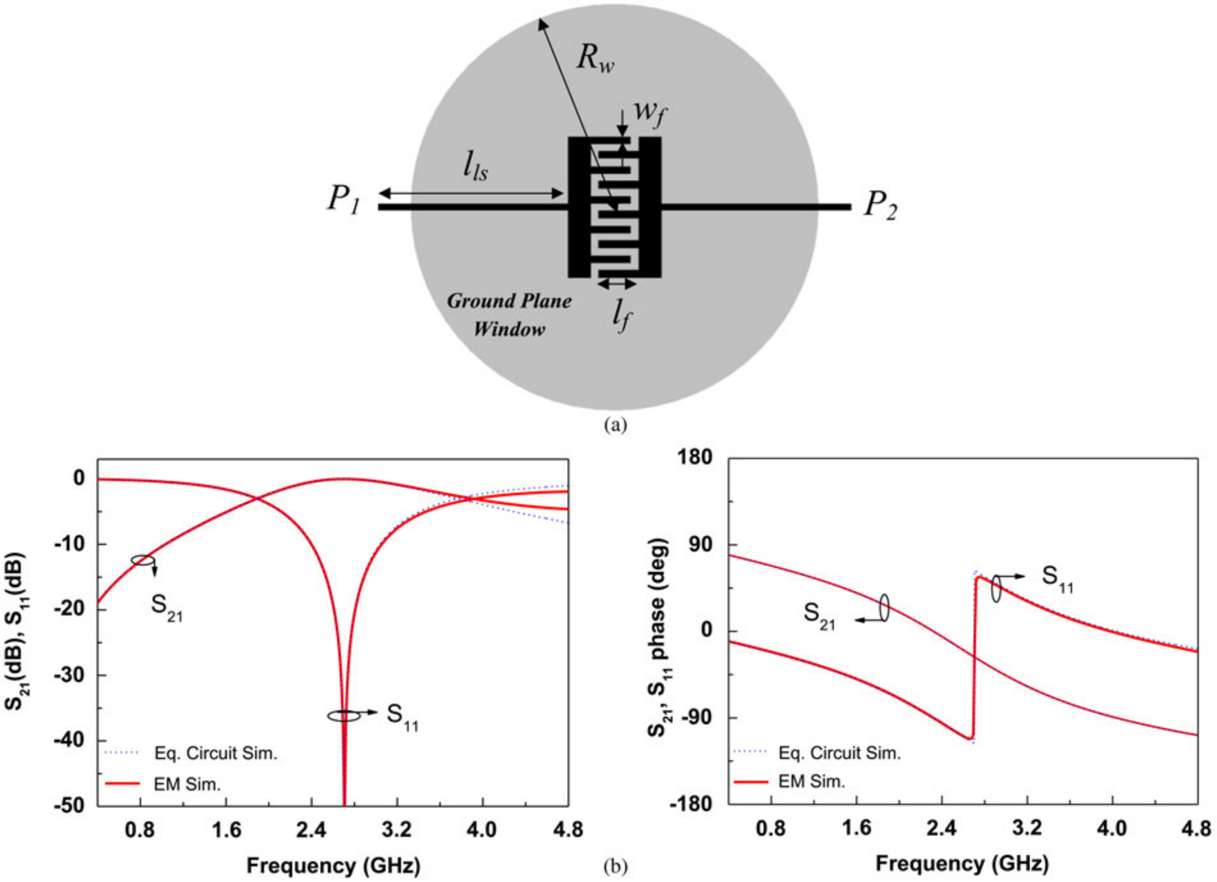

Fig. 5. Final layout of the interdigital capacitors (a) and frequency response (b). Dimensions are (in mm): $R_w = 4.189$, $w_f = 0.160$, $l_{Ls} = 3.820$, and $l_f = 0.718$. The element values are: $L_s = 9.0644$ nH, $C_s = 0.4599$ pF, and $C_{par} = 0.2706$ pF.

balanced bandpass filters based on SIRs coupled through admittance inverters (in practice implemented by means of quarter-wavelength transmission line sections), the proposed filters are described (differential mode) by an equivalent circuit similar to the canonical model of a bandpass filter, where the circuit schematic is composed by reactive elements (inductances and capacitances). However, the circuit model includes parasitic elements, and the design process takes into account these elements. By replacing the inverters of previous implementations (e.g. [19]) with interdigital capacitors, a clear improvement in terms of filter size is achieved. But also in terms of circuit design, since the ASM-based synthesis method of these filters utilizes only one iterative step (rather than two) for the determination of the filter layout from the circuit schematic. It is remarkable that filter design follows an unattended scheme, where the layout is generated from the required Chebyshev (differential-mode) response. The specific ASM synthesis tool has been explained in detail

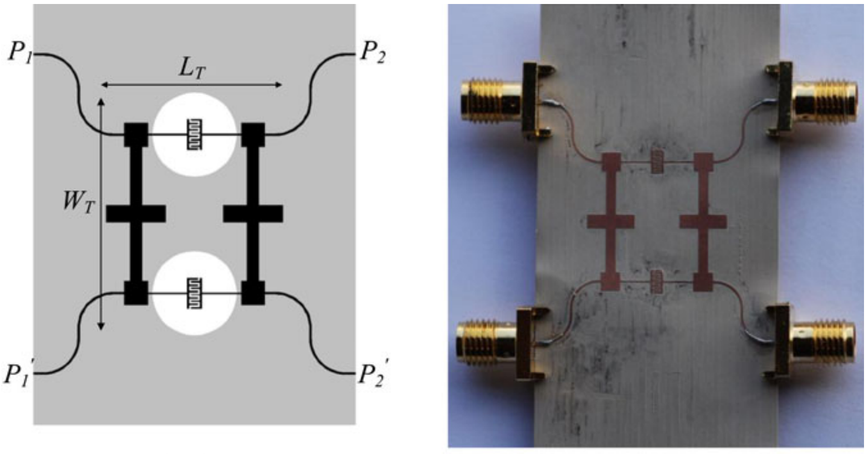

(a) (b)

Fig. 6. Final layout of the filter (a) and photograph of the fabricated prototype (b). The dimensions are (in mm): $W_T = 24$ and $L_T = 17.5$.

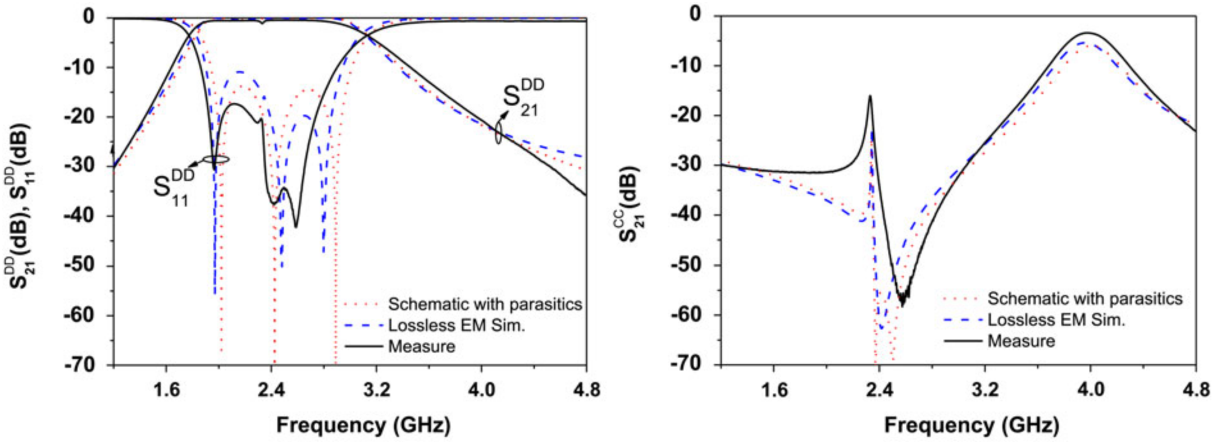

(a) (b)

Fig. 7. Frequency response of the filter. Differential mode (a) and common mode (b). The measured unloaded quality factor is $Q_u(\omega_o) = 79.84$ [21].

Table 1. Comparison of various differential filters.

Ref.	**FBW (−3 dB) (%)**	**CMRR @ f_o (dB)**	**S_{21dd} ($2f_o$) (dB)**	**Effective area (λ^2)**
[1]	65	29	46	0.25
[3]	50	48	23	0.25
[7]	70	15	35	0.28
[8]	79	35	32	0.19
[9]	66	10	20	0.023
[10]	43	63	38	0.60
[11]	45	53	35	0.045
[16]	59.5	47	54	0.39
This work	56	40	35	0.17

and then it has been applied to the synthesis of an order-3 balanced bandpass filter with common-mode suppression. The obtained results have pointed out the efficiency of the iterative algorithm (3 and 11 iterations are necessary to generate the layout of the SIR and interdigital capacitor stages, respectively) and the small size of the resulting prototype (achieved by virtue of the use of interdigital capacitors for the series branches). This iterative process means a CPU effort of approximately 35 min (using a Intel®Core™ with 8 GB of RAM and a 2.86 GHz clock processor). Moreover, the characterization results indicate that these filters provide significant common-mode suppression in the differential filter pass band.

ACKNOWLEDGEMENTS

This work was supported by *MINECO-Spain* (projects no. TEC2013-47037-C5-1-R, TEC2013-40600-R, and TEC2013-49221-EXP), *Generalitat de Catalunya* (project no. 2014SGR-157), and *Institució Catalana de Recerca i Estudis Avançats* (who has awarded Ferran Martín).

REFERENCES

[1] Lim, T.B.; Zhu, L.: A differential-mode wideband bandpass filter on microstrip line for UWB applications. IEEE Microw. Wireless Compon. Lett., **19** (2009), 632–634.

[2] Lim, T.B.; Zhu, L.: Differential-mode ultra-wideband bandpass filter on microstrip line. Electron. Lett., **45** (2009), 1124–1125.

[3] Lim, T.B.; Zhu, L.: Highly selective differential-mode wideband bandpass filter for UWB application. IEEE Microw. Wireless Compon. Lett., **21** (2011), 133–135.

[4] Abbosh, A.M.: Ultrawideband balanced bandpass filter. IEEE Microw. Wireless Compon. Lett., **21** (2011), 480–482.

[5] Zhu, H.T.; Feng, W.J.; Che, W.Q.; Xue, Q.: Ultra-wideband differential bandpass filter based on transversal signal-interference concept. Electron. Lett., **47** (2011), 1033–1035.

[6] Wu, X-H.; Chu, Q-X.: Compact differential ultra-wideband bandpass filter with common-mode suppression. IEEE Microw. Wireless Compon. Lett., **22** (2012), 456–458.

[7] Feng, W.; Che, W.: Novel wideband differential bandpass filters based on T-shaped structure. IEEE Trans. Microw. Theory. Tech., **60** (2012), 1560–1568.

[8] Feng, W.; Che, W.; Ma, Y.; Xue, Q.: Compact wideband differential bandpass filters using half-wavelength ring resonator. IEEE Microw. Wireless Compon. Lett., **23** (2013), 81–83.

[9] Wu, X.-H.; Chu, Q.-X.; Qiu, L.-L.: Differential wideband bandpass filter with high-selectivity and common-mode suppression. IEEE Microw. Wireless Compon. Lett., **23** (2013), 644–646.

[10] Vélez, P. et al.: Differential bandpass filters with common-mode suppression based on stepped impedance resonators (SIRs). *IEEE MTT-S Int. Microwave Symp.*, 2013, Seattle (USA).

[11] Vélez, P. et al.: Differential bandpass filter with common mode suppression based on open split ring resonators and open complementary split ring resonators. IEEE Microw. Wireless Compon. Lett., **23** (2013), 22–24.

[12] Horestani, A.K.; Durán-Sindreu, M.; Naqui, J.; Fumeaux, C.; Martín, F.: S-shaped complementary split ring resonators and their application to compact differential bandpass filters with common-mode suppression. IEEE Microw. Wireless Compon. Lett., **24** (2014), 150–152.

[13] Wang, X.-H., Zhang, H.; Wang, B.-Z.: A novel ultra-wideband differential filter based on microstrip line structures. IEEE Microw. Wireless Compon. Lett., **23** (2013), 128–130.

[14] Shi, J.; Shao, C.; Chen, J.-X.; Lu, Q.-Y.; Peng, Y.; Bao, Z.-H: Compact low-loss wideband differential bandpass filter with high common-mode suppression. IEEE Microw. Wireless Compon. Lett., **23** (2013), 480–482.

[15] Vélez, P.; Durán-Sindreu, M.; Naqui, J.; Bonache, J.; Martín, F.: Common-mode suppressed differential bandpass filter based on open complementary split ring resonators (OCSRRs) fabricated in microstrip technology without ground plane etching. Microw. Opt. Technol. Lett., **56** (2014), 910–916.

[16] Li, L.; Bao, J.; Du, J.-J.; Wang, Y.-M.: Differential wideband bandpass filters with enhanced common-mode suppression using internal coupling technique. IEEE Microw. Wireless Compon. Lett., **24** (2014), 300–302.

[17] Vélez, P. et al.: Ultra-compact (80 mm^2) differential-mode ultra-wideband (UWB) bandpass filters with common-mode noise suppression. IEEE Trans. Microw. Theory Tech., **63** (2015), 1272–1280.

[18] Guo, X.; Zhu, L.; Tam, K.-W.; Wu, W.: Wideband differential bandpass filters on multimode slotline resonator with intrinsic common-mode rejection. IEEE Trans. Microw. Theory Tech., **63** (2015), 1587–1594.

[19] Sans, M.; Selga, J.; Vélez, P.; Rodríguez, A.; Boria, V.E.; Martín, F.: Application of aggressive space mapping (ASM) to the automated design of differential-mode wideband bandpass filters with common-mode suppression. *European Microwave Conf.*, Paris, France, 6–11 September 2015.

[20] Sans, M.; Selga, J.; Rodríguez, A.; Bonache, J.; Boria, V.E.; Martín, F.: Design of planar wideband bandpass filters from specifications using a two-step aggressive space mapping (ASM) optimization algorithm. IEEE Trans. Microw. Theory Tech., **62** (2014), 3341–3350.

[21] Hong, J.S.; Lancaster, M.J.: Microstrip Filters for RF/Microwave Applications, Wiley, New York, NY, USA, 2001.

[22] Bandler, J.W.; Biernacki, R.M.; Chen, S.H.; Grobelny, P.A.; Hemmers, R.H.: Space mapping technique for electromagnetic optimization. IEEE Trans. Microw. Theory Tech., **42** (1994), 2536–2544.

[23] Bandler, J.W.; Biernacki, R.M.; Chen, S.H.; Hemmers, R.H.; Madsen, K.: Electromagnetic optimization exploiting aggressive space mapping. IEEE Trans. Microw. Theory Tech., **43** (1995), 2874–2882.

[24] Pozar, D.M.: Microwave Engineering, Addison-Wesley, Boston, MA, USA, 1990.

Marc Sans was born in Terrassa (Barcelona), Spain, in 1982. He received the B.S. degree in Telecommunications Engineering – Electronic Systems in 2006, the M.S. degree in Telecommunications Engineering in 2008, and the M.S. degree in Electronics Engineering in 2013 from the Universitat Autònoma de Barcelona (UAB). In 2008, he started his professional career as a RF Engineer at Sony-FTVE developing the RF stage of TV receivers. In 2010, he moved to Mier Comunicaciones S.A. to carry out the design of passive and active devices for VHF-UHF broadcasting units. Since 2014, he is working toward the Ph.D. degree at CIMITEC-UAB in the synthesis of microwave devices based on EM optimization techniques.

Jordi Selga was born in Barcelona, Spain, in 1982. He received the B.S. degree in Telecommunications Engineering – Electronic Systems in 2006, the M.S. degree in Electronics Engineering in 2008, and the Ph.D. degree in Electronics Engineering in 2013 from the Universitat Autònoma de Barcelona (UAB), Barcelona, Spain. Since 2008 he is a member of CIMITEC-UAB, a research center on Metamaterials supported by TECNIO (Catalan Government). He was holder of a national research fellowship from the *Formación de Profesorado Universitario* Program of the Education and Science Ministry (Reference no. AP2008-4707). He is currently working in subjects related to metamaterials, CAD design of microwave devices, EM optimization methods, and automated synthesis of planar microwave components at the UAB.

Paris Vélez was born in Barcelona (Spain) in 1982. He received the degree in Telecommunications Engineering, specializing in Electronics in 2008 and the Electronics Engineering degree in 2010 from the Universitat Autònoma de Barcelona (UAB). In 2014, he received his Ph.D. in Electrical Engineering from the UAB with a thesis entitled "Common mode suppression differential microwave circuits based on Metamaterial concepts and semilumped resonators". During the Ph.D. he was awarded with a predoctoral teaching and research fellowship by the Spanish Government from 2011 to 2014. Dr. Vélez is a reviewer of the IEEE T-MTT and of other journals. Actually, his scientific activity is focused on the miniaturization of passive circuits RF/microwave based Metamaterials.

Ana Rodriguez was born in Lugo, Spain. She received the Telecommunications Engineering degree from the Universidade de Vigo (UV), Spain, in 2008. As a student, she participated in the Erasmus exchange program, developing the Master Thesis at the University of Oulu, Finland. Since the end of 2008, she has joined the Institute of Telecommunications and Multimedia Applications (iTEAM), which is part of the scientific park at the Universitat Politècnica de València (UPV), Spain. She obtained "Master en Tecnología, Sistemas y Redes de Comunicaciones" in 2010 from UPV, and the Ph.D. degree in 2014. Her main research interests include CAD design of microwave devices, EM optimization methods, and metamaterials.

Jordi Bonache was born in 1976 in Barcelona (Spain). He received the Physics and Electronics Engineering degrees from the Universitat Autònoma de Barcelona (UAB) in 1999 and 2001, respectively and the Ph.D. degree in Electronics Engineering from the same university in 2007. In 2000, he joined the "High Energy Physics Institute" of Barcelona (IFAE), where he was involved in the design and implementation of the control and monitoring system of the MAGIC telescope. In 2001, he joined the Department of Electronics Engineering of the UAB where he is currently a Lecturer. From 2006 to 2009 he worked as an executive manager of CIMITEC. Currently is leading the research in RFID and antennas in CIMITEC. His research interests include active and passive microwave devices, metamaterials, antennas, and RFID.

Vicente E. Boria was born in Valencia, Spain, on May 18, 1970. He received his "Ingeniero de Telecomunicación" degree (with first-class honors) and the "Doctor Ingeniero de Telecomunicación" degree from the Universidad Politécnica de Valencia, Valencia, Spain, in 1993 and 1997, respectively. In 1993, he joined the "Departamento de Comunicaciones", Universidad Politécnica de Valencia, where he has been Full Professor since 2003. In 1995 and 1996, he was holding a Spanish Trainee position with the European Space Research and Technology Centre, European Space Agency (ESTEC-ESA), Noordwijk, The Netherlands, where he was involved in the area of EM analysis and design of passive waveguide devices. He has authored or co-authored ten chapters in technical textbooks, 135 papers in refereed international technical journals, and over 180 papers in international conference proceedings. His current research interests are focused on the analysis and automated design of passive components, left-handed and periodic structures, as well as on the simulation and measurement of power effects in passive waveguide systems.

Dr. Boria has been a member of the IEEE Microwave Theory and Techniques Society (IEEE MTT-S) and the IEEE Antennas and Propagation Society (IEEE AP-S) since 1992. He is reviewer of the IEEE Transactions on Microwave Theory and Techniques, Proceeding of the IET (Microwaves, Antennas and Propagation) and IET Electronics Letters. Since 2013, he serves as an Associate Editor of IEEE Microwave and Wireless Components Letters. He is also a member of the Technical Committees of the IEEE-MTT International Microwave Symposium and of the European Microwave Conference.

Ferran Martín received the B.S. degree in Physics from the Universitat Autònoma de Barcelona (UAB) in 1988 and the Ph.D. degree in 1992. From 1994 up to 2006, he was an Associate Professor in Electronics at the Departament d'Enginyeria Electrònica (Universitat Autònoma de Barcelona), and since 2007 he is a Full Professor of Electronics. In recent years, he has been involved in different research activities, including modeling and simulation of electron devices for high-frequency applications, millimeter wave and THz generation systems, and the application of electromagnetic bandgaps to microwave and millimeter wave circuits. He is now very active in the field of metamaterials and their application to the miniaturization and optimization of microwave circuits and antennas. He is the head of the Microwave Engineering, Metamaterials and Antennas Group (GEMMA Group) at UAB, and director of CIMITEC, a research Center on Metamaterials supported by TECNIO (Generalitat de Catalunya). He has organized several international events related to metamaterials, including Workshops at the IEEE International Microwave Symposium (years 2005 and 2007) and European Microwave Conference (2009), and the Fifth International Congress on Advanced Electromagnetic Materials in Microwaves and Optics (Metamaterials 2011), where he has acted as chair of the Local Organizing Committee. He has acted as Guest Editor for three Special Issues on Metamaterials in three International Journals. He has authored and co-authored over 450 technical conference, letter, journal papers, and book chapters; he is co-author of the book on Metamaterials entitled *Metamaterials with Negative Parameters: Theory, Design and Microwave Applications* (John Wiley & Sons Inc. 2008), author of the book *Artificial Transmission Lines for RF and Microwave Applications* (John Wiley & Sons Inc. 2015), and he has generated 15 Ph.D.s. Ferran Martín has filed several patents on metamaterials and has headed several Development Contracts.

Prof. Martín is a member of the IEEE Microwave Theory and Techniques Society (IEEE MTT-S). He is a reviewer of the IEEE Transactions on Microwave Theory and Techniques and IEEE Microwave and Wireless Components Letters, among many other journals, and he serves as a member of the Editorial Board of IET Microwaves, Antennas and Propagation and International Journal of RF and Microwave Computer-Aided Engineering. He is also a member of the Technical Committees of the European Microwave Conference (EuMC) and International Congress on Advanced Electromagnetic Materials in Microwaves and Optics (Metamaterials). Among his distinctions, Ferran Martín has received the 2006 Duran Farell Prize for Technological Research, he holds the *Parc de Recerca UAB – Santander* Technology Transfer Chair, and he has been the recipient of two ICREA ACADEMIA Awards (calls 2008 and 2013). He is an IEEE Fellow since 2012.

NEMO17*

M. Sans, J. Selga, P. Vélez, A. Rodríguez, J. Bonache, V. E. Boria, and F. Martín

"Optimized Wideband Differential-Mode Bandpass Filters with Broad Stopband and Common-Mode Suppression based on Multi-Section Stepped Impedance Resonators and Interdigital Capacitors"

2017 IEEE MTT-S International Conference on Numerical Electromagnetic and Multiphysics Modeling and Optimization for RF, Microwave, and Terahertz Applications (NEMO)

Optimized Wideband Differential-Mode Bandpass Filters with Broad Stopband and Common-Mode Suppression based on Multi-Section Stepped Impedance Resonators and Interdigital Capacitors

Marc Sans, Jordi Selga, Paris Vélez, Jordi Bonache,
Ferran Martín
GEMMA/CIMITEC, Departament d'Enginyeria Electrònica
Universitat Autònoma de Barcelona
08193 Bellaterra, Spain
Ferran.Martin@uab

Ana Rodríguez, Vicente E. Boria
Departamento de Comunicaciones-iTEAM
Universitat Politècnica de València
46022 Valencia, Spain
vboria@dcom.upv.es

***Abstract*— This paper presents optimized balanced microstrip filters, in terms of size and design simplicity, by combining multi-section mirrored stepped impedance resonators (SIRs) and interdigital capacitors. The mirrored SIRs provide the necessary transmission zeros (for both the differential- and common-mode responses) to simultaneously achieve a broad stopband for the differential mode and efficient common mode suppression in the region of interest (differential-mode pass band) and beyond. The interdigital structures actually act as series resonators and allow for the design of filters with smaller size (as compared to other implementations based on quarter wavelength admittance inverters) and, most important, reduce the complexity of the automated (and unattended) design algorithm, based on aggressive space mapping (ASM). The design of an order-3 balanced quasi-Chebyshev filter with central frequency f0 = 1.5 GHz, fractional bandwidth FBW = 43% and 0.15 dB ripple, is reported as an illustrative example.**

Keywords— Balanced filters; stepped impedance resonators; interdigital capacitors; aggressive space mapping.

I. INTRODUCTION

In recent years, the design of balanced lines, circuits and filters at microwave frequencies has experienced a significant growth due to the high immunity to noise, electromagnetic interference (EMI) and crosstalk of differential signals [1]. Since bandpass filters are essential components in any microwave system, the design of balanced microwave filters has been a particular topic of increasing interest. The main objectives in the design of these filters are to reduce the size as much as possible, to achieve a good filter performance for the mode of interest (differential mode), particularly spurious cancellation, and to efficiently suppress the common mode over the broadest possible band.

Efficient common mode suppression can be achieved by cascading common mode filters to the designed differential filters [2]. However, this strategy adds extra size to the final filter. Therefore, the design of balanced filters based on topologies able to inherently suppress the common-mode is, in general, the preferred approach. Narrow (or moderate) band [3], dual-band [4], wideband [5]-[7] and ultrawide band [8] common-mode suppressed balanced bandpass filters have been recently reported. In this paper, the interest is focused on wideband balanced filters. Of particular interest to this work are the filters reported in [7] and [9], based on mirrored SIRs. In [7], very competitive filters in terms of performance were reported, but size was not optimized, as compared to other filters with similar performance, and filter design was based on a relatively complex (although unattended) two-step process. According to this two-step method, the optimum filter schematic (different than the one resulting from filter specifications) is first determined (this is necessary due to the limited functionality of the considered admittance inverters), and then the layout is automatically generated. In [9], the balanced filters were implemented by combining mirrored SIRs and interdigital capacitors (thus avoiding the use of admittance inverters). By this means, filter size can be reduced and the design process is more agile since the first step (determination of the optimum schematic) is not necessary. However, in the filters reported in [9] the parasitic capacitance of the interdigital capacitors cannot be absorbed by the considered mirrored SIRs (different than those of [7]), and this introduces some difficulty to the determination of the layout.

In the present paper, we combine the mirrored SIRs of [7], with the interdigital capacitors of [9] for the first time, and we provide a systematic procedure, based on aggressive space mapping (ASM), for the unattended design of compact common-mode suppressed wideband balanced bandpass filters. First of all, the parameters of the circuit model are determined from filter specifications and from the position of the differential and common mode transmission zeros (decided by the designer in order to simultaneously achieve broad differential-mode stopband and common-mode suppression). Then the layout is determined following a completely unattended scheme. The reported example is demonstrative of the potential of the approach in terms of filter performance and size for the design of wideband balanced filters.

II. FILTER TOPOLOGY, CIRCUIT MODEL AND ANALYSIS

The typical topology of the proposed filters is depicted in Fig. 1(a). It consists of a cascade of 7-section mirrored SIRs and pairs of symmetric interdigital capacitors alternating. The filter can be described by means of the equivalent circuit depicted in Fig. 1(b). The interdigital capacitors and the narrow strips adjacent to them are accounted for by π-circuits with series resonators $C_{s,i}$-$L_{s,i}$ and parallel (parasitic) capacitances $C_{par,i}$ (the subindex i is used to differentiate the filter stages). The mirrored SIRs are described by the inductances $L_{e,i}$ (narrow strips of the external sections) and $L_{c,i}$ (narrow strips of the central sections), and by the capacitances $C_{e,i}$ (external patches) and $2C_{c,i}$ (central patches). The symmetry plane is an electric wall for the differential mode and a magnetic wall for the common mode. Therefore, the circuit models for these modes are inferred from the model of Fig. 1(a) by bisecting it and by grounding (differential mode) or opening (common mode) the nodes intersecting the symmetry plane [see Figs. 1(c) and (d)].

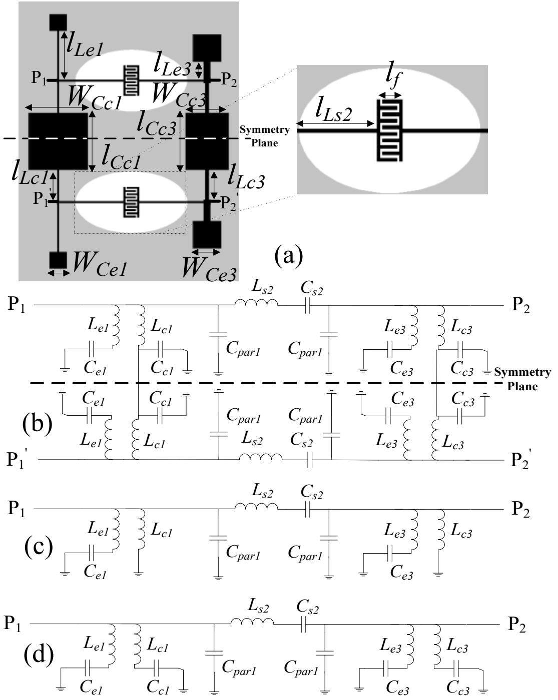

Fig. 1. Topology of the proposed filters (order 3) (a), lumped element equivalent circuit (b), and equivalent circuits for the differential (c) and common (d) modes.

For the differential mode, the capacitances $C_{c,i}$ are short circuited and do not play an active role. Conversely, such capacitances and the inductances $L_{c,i}$ act as shunt connected series resonators for the common mode, providing transmission zeros at the resonance frequencies. The strategy to efficiently suppress the common mode is to distribute these common-mode transmission zeros along the differential mode pass band by varying the dimensions of the central patches (and hence the values of $C_{c,i}$). The external resonators ($L_{e,i}$-$C_{e,i}$) provide transmission zeros for both modes, but their interest is the generation of differential-mode transmission zeros above the pass band of interest, in order to broaden the stop band for that mode and efficiently reject out-of-band differential signals.

Let us assume that the capacitance $C_{par,i}$ is known (it is inferred from the synthesis of the interdigital capacitors, to be described later). The reactance of the shunt branches for the differential mode is given by

$$\chi_{s,diff} = \frac{(\omega^2 L_e C_e - 1)L_c}{\omega^3 C_{par} L_e C_e L_c - \omega(C_e L_c + C_e L_e + C_{par} L_c)} \quad (1)$$

and it depends on three unknowns $L_{e,i}$, $C_{e,i}$ and $L_{c,i}$ [in (1) we have omitted the subindex i for simplicity]. Such parameters are determined by the following three conditions (not given since two of them are cumbersome): (i) the position of the differential mode transmission zero, (ii) the central filter frequency (where the shunt branch opens), and (iii) the susceptance slope (inferred from filter specifications). Note that once $L_{c,i}$ for each stage is known (from the previous conditions), the capacitance of the central patches is determined from the required positions of the common mode transmission zeros. The element values of the series elements describing the interdigital capacitors ($L_{s,i}$,$C_{s,i}$) are easily determined from filter specifications according to standard filter design. Therefore, the element values of the equivalent circuit of the filter are completely determined.

III. LAYOUT DETERMINATION THROUGH ASM

The filter layout can be automatically inferred from the circuit elements by means of a developed software tool based on ASM (see [10] for a general formulation of ASM and [7],[9] for the synthesis of mirrored SIRs and resonators based on interdigital capacitors). Since the parasitic capacitance $C_{par,i}$ is not given by filter specifications, but by the resulting topology of the series resonators, it is first necessary to infer the layout of such resonators. The variables in the optimization space are $L_{s,i}$ and $C_{s,i}$ whereas the variables in the validation space are the length of the inductive line, l_{Ls}, and the length of the fingers, l_f. The other geometrical parameters are set to 0.2 mm. The initial layout is obtained from approximate formulas providing the inductance of a narrow inductive strip and the capacitance of an interdigital capacitor. Then parameter extraction is carried out, and the first approach to the Broyden matrix, necessary to iterate the ASM process, is generated. With this ASM scheme, the layout providing the target elements of the series branch is determined, and from this layout, the parasitic capacitance $C_{par,i}$ is also inferred. However, as long as C_{par} influences the impedance of the shunt branch, optimization of this capacitance at the circuit level in order to achieve a satisfactory in-band response (minimum reflection loss level) has been necessary.

The layout of the mirrored SIRs is obtained following the scheme reported in [7]. The variables in the optimization space are L_e, L_c, C_e, and C_c. For the first SIR, the variables in the validation space are the lengths of the narrow (inductive) and wide (capacitive) sections of the multi-section mirrored SIRs, i.e., l_{Le}, l_{Lc}, l_{Ce}, and l_{Cc}. Concerning the fixed dimensions, the values are set to $W_{Le} = W_{Lc} = 0.2$ mm, and there are two bounded values, $W_{Ce} = l_{Ce}$ and $W_{Cc} = l_{Cc}$ (i.e., a square shaped geometry for the patch capacitors is chosen).

For the second SIR, the variables in the validation space are l_{Le}, l_{Ce}, W_{Cc} and W_{Lc} (the lengths l_{Cc} and l_{Lc} are those of the first SIR, $W_{Ce} = l_{Ce}$ and $W_{Le} = 0.8$ mm).

Once the layout of each filter stage (either mirrored SIR or interdigital resonators) is determined, such stages are simply cascaded and no further optimization is applied to the layout.

IV. ILLUSTRATIVE EXAMPLE

As an illustrative example, we report in this paper the automated design of an order-3 quasi-Chebyshev balanced filter with 43% fractional bandwidth, 1.5 GHz central frequency and 0.15 dB in-band ripple. The transmission zeros for the differential mode are set to 2.45 GHz and 3.45 GHz, whereas for the common mode the transmission zeros are located at 1.58 GHz and 2.10 GHz (the latter slightly above the differential mode pass band to achieve broad common mode suppression). With these specifications, transmission zeros and the resulting parasitic capacitance ($C_{par} = 0.92$ pF), the element values are found to be those indicated as follows: $L_{e1} = 2.74$ nH, $L_{c1} = 3.06$ nH, $C_{e1} = 1.67$ pF, $C_{c1} = 3.83$ pF, $C_{s2} = 0.79$ pF, $L_{s2} = 14.25$ nH, $L_{e3} = 0.68$ nH, $L_{c3} = 2.38$ nH, $C_{e3} = 3.13$ pF, and $C_{c3} = 2.88$ pF.

The application of the ASM tool has provided the layout depicted in Fig. 1 (the considered substrate is the *Rogers RO3010* with dielectric constant $\varepsilon_r = 10.2$ and thickness $h = 0.635$ mm). The response of the filter inferred from lossless electromagnetic simulation (using *Keysight Momentum*) is compared to the circuit simulation in Fig. 2, where good agreement can be appreciated. The filter has been fabricated by means of a *LPKF HF100* drilling machine (see Fig. 3, inset), and the measured response has been obtained by means of the *Agilent PNA N5221A* vector network analyzer. It is depicted in Fig. 3, where it is compared to the electromagnetically simulated response by including losses. Filter dimensions are given in the caption of Fig. 3. Overall filter dimensions (in terms of the wavelength at f_0) are $0.309\lambda \times 0.409\lambda$, which are significantly small for an order-3 filter. Note that only two mirrored SIR stages are required, whereas in the filters reported in [7], as many SIR stages as filter order are necessary. As compared to the filters reported in [9], the filters reported in this work exhibit much better filter response for the differential mode, with a wide stop band. The common mode is significantly rejected over the differential filter pass band and beyond, with common mode rejection ratio (CMRR) better than 20 dB between 0.75 GHz and 3.75 GHz.

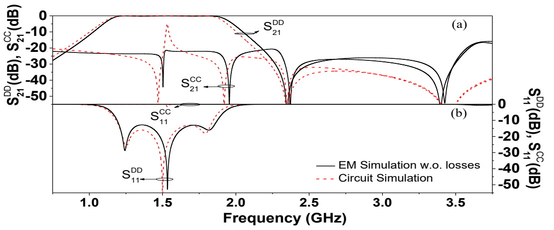

Fig. 2. Electromagnetic (without losses) and circuit simulation of the designed filter for the differential and common modes. (a) Insertion loss; (b) Return loss.

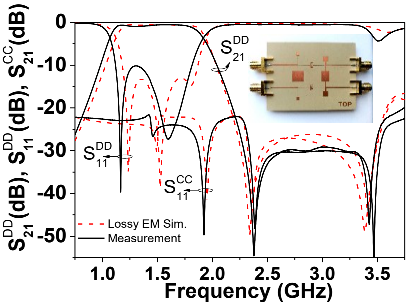

Fig. 3. Measured response compared to the lossy electromagnetic simulation photograph of the fabricated filter depicted as an inset. filter dimensions (in mm), in reference to Fig. 1 are $W_{Ce1} = 2.05$, $l_{Le1} = 5.98$, $l_{Lc1} = 3.78$, $W_{Cc1} = l_{Cc1} = 7.12$, $l_{ls2} = 7.80$, $l_f = 1.11$, $W_{Ce3} = 3.42$, $l_{Le3} = 2.07$, $l_{Lc3} = 3.78$, W_{Cc1} =5.19, $l_{Cc1} = 7.12$.

V. CONCLUSION

The design of common-mode suppressed wideband differential filters based on multi-section mirrored SIRs and interdigital capacitors has been reported. These filters represent a further step as compared to other filters based on mirrored SIRs or mirrored SIRs combined with interdigital capacitors since they exhibit a combination of dimensions, performance and design simplicity not found so far.

REFERENCES

[1] W. Feng, W. Che, and Q. Xue "The proper balance: overview of microstrip wideband balance circuits with wideband common mode suppression", *IEEE Microw. Mag.*, vol. 16, pp. 55-68, Jun. 2015.

[2] J. Naqui, et al., "Common mode suppression in microstrip differential lines by means of complementary split ring resonators: theory and applications", *IEEE Trans. Microw. Theory Techn.*, vol. 60, pp. 3023-3034, Oct. 2012.

[3] A. Fernández-Prieto, A. Lujambio, J. Martel, F. Medina, F. Mesa, and R. R. Boix, "Simple and compact balanced bandpass filters based on magnetically coupled resonators", *IEEE Trans. Microw. Theory Techn.*, vol. 63, pp. 1843-1853, Jun. 2015.

[4] Y.-H. Cho, and S.-W. Yun, "Design of balanced dual-band bandpass filters using asymmetrical coupled lines", *IEEE Trans. Microw. Theory Techn.*, vol. 61, pp. 2814-2820, Aug. 2013.

[5] T. B. Lim, and L. Zhu, "A differential-mode wideband bandpass filter on microstrip line for UWB applications," *IEEE Microw. Wireless Compon. Lett.*, vol. 19, pp. 632-634, Oct. 2009.

[6] L. Li, J. Bao, J-J. Du, and Y-M. Wang, "Differential wideband bandpass filters with enhanced common-mode suppression using internal coupling technique", *IEEE Microw. Wireless Compon. Lett.*, vol. 24, no.5, pp. 300-302, Feb. 2014.

[7] M. Sans, et al., "Automated design of common-mode suppressed balanced wideband bandpass filters by means of agressive space mapping (ASM)", *IEEE Trans. Microw. Theory Techn.*, vol. 63, no. 12, pp. 3896-3908, Dec. 2015.

[8] T. B. Lim and L. Zhu, "Differential-mode ultra-wideband bandpass filter on microstrip line," *Electron. Lett.*, vol.45, no.22, pp. 1124–1125, Oct. 2009.

[9] M. Sans, et al., "Automated design of balanced wideband bandpass filters based on mirrored stepped impedance resonators (SIRs) and interdigital capacitors", *Int. J. Microw. Wireless Technol.*, vol. 8, pp. 731-740, 2016.

[10] J.W. Bandler, et al. , "Electromagnetic optimization exploiting aggressive space mapping", *IEEE Trans. Microw. Theory Techn.*, vol. 43, pp. 2874-2882, Dec. 1995.

TMTT18

M. Sans, J. Selga, P. Vélez, A. Rodríguez, J. Bonache, V. E. Boria, and F. Martín

"Compact Wideband Balanced Bandpass Filters with Very Broad Common-Mode and Differential-Mode Stopbands"

Compact Wideband Balanced Bandpass Filters With Very Broad Common-Mode and Differential-Mode Stopbands

Marc Sans, Jordi Selga, *Member, IEEE*, Paris Vélez, *Member, IEEE*, Jordi Bonache, *Member, IEEE*,
Ana Rodríguez, *Member, IEEE*, Vicente E. Boria, *Senior Member, IEEE*, and Ferran Martín, *Fellow, IEEE*

***Abstract*— Compact balanced bandpass filters based on a combination of multisection mirrored stepped-impedance resonators and interdigital capacitors are presented in this paper. The considered filter topology is useful to achieve wide bandwidths for the differential mode, with broad stop bands for that mode, as well as very efficient common-mode suppression. By conveniently adjusting the transmission zeros for both operation modes, the differential- and common-mode stopbands can be extended up to significantly high frequencies. Filter size and this differential- and common-mode stopband performance are the main relevant characteristics of the proposed balanced filters. The potential of the approach is illustrated by the design of a prototype order-5 balanced bandpass filter, with central frequency $f_0 = 1.8$ GHz, 48% fractional bandwidth (corresponding to 55.4% −3-dB bandwidth), and 0.04-dB ripple level. The filter is automatically synthesized by means of an aggressive space-mapping software tool, specifically developed, and two (pre- and post-) optimization algorithms, necessary to determine the transmission-zero frequencies. The designed filter is as small as $0.48\lambda_g \times 0.51\lambda_g$, where λ_g is the guided wavelength at the central filter frequency, and the differential-mode stopband extends up to at least 6.5 GHz with more than 22-dB rejection. The common-mode suppression is better than 28 dB from dc up to at least 6.5 GHz.**

***Index Terms*— Balanced bandpass filters, common-mode noise suppression, interdigital capacitors, microstrip technology, space mapping, stepped-impedance resonators (SIRs).**

I. INTRODUCTION

BALANCED (or differential mode) microwave filters have attracted the interest of the microwave community in recent years. The reason is the increasing demand of differential circuits and systems, due to the high immunity to noise, electromagnetic interference, and crosstalk of differential signals [1], [2]. Ideally, balanced filters should be able to efficiently suppress the (parasitic) common mode over the widest possible band, and simultaneously exhibit good performance for the mode of interest (differential mode), including low insertion loss and high return loss in the passband, high filter selectivity, and a broad stopband (spurious cancellation). Filter size, design simplicity, and cost are also important aspects.

Solutions to suppress the common mode based on cascaded common-mode filters have been reported [3]–[5]. However, this strategy is not the optimum solution in terms of filter size. For this reason, common-mode suppressed balanced filters are mostly implemented through approaches that inherently reject the common mode. Following these approaches, narrowband [6]–[11], dual-band [4], [12]–[20], wideband [21]–[38], and ultrawideband [39]–[47] balanced bandpass filters have recently reported.

This paper is focused on the design and synthesis of differential-mode bandpass filters, first reported in [36], based on a combination of multisection mirrored stepped-impendence resonators (SIRs) and interdigital capacitors. The proposed topology is useful for the implementation of wideband responses for the differential mode. Due to the presence of multiple (controllable) transmission zeros for the differential and common modes and to the blocking effect of the series connected interdigital capacitors at low frequencies, the common mode is efficiently suppressed from dc up to high frequencies (covering the differential-mode passband and beyond). Good performance in the passband and broad stopband for the differential mode is also achieved with the proposed topology. Moreover, filter size is reduced as compared to other similar filters based on quarter wavelength admittance inverters [34], since these filters are implemented only with semilumped (i.e., electrically small) components. The proposed filters are fully planar, can be fabricated in commercially available microwave substrates, use only two metallic levels, and do not use metallic vias. Hence, they represent a low-cost solution for wideband balanced filters. Finally, the layout of the filters is obtained following an automated scheme, by means of a developed software tool that implements an aggressive space-mapping (ASM) optimization and synthesis algorithm.

Manuscript received July 28, 2017; revised October 4, 2017; accepted November 11, 2017. Date of publication January 11, 2018; date of current version February 5, 2018. This work was supported in part by MINECO-Spain under Project TEC2013-40600-R, Project TEC2016-75650-R, and Project TEC2016-75934-C4-1-R, in part by the Generalitat de Catalunya under Project 2014SGR-157, in part by the Institució Catalana de Recerca i Estudis Avançats (who awarded F. Martín), and in part by by FEDER funds. This paper is an expanded version from the IEEE MTT-S International Conference on Numerical Electromagnetic Modeling and Optimization for RF, Microwave, and Terahertz Applications, Seville, Spain, May 17–19, 2017. *(Corresponding author: Jordi Selga.)*

M. Sans, J. Selga, P. Vélez, J. Bonache, and F. Martín are with the GEMMA/CIMITEC, Departament d'Enginyeria Electrònica, Universitat Autònoma de Barcelona, 08193 Bellaterra, Spain (e-mail: jordi.selga@uab.cat; Ferran.Martin@uab.es).

A. Rodríguez and V. E. Boria are with the Departamento de Comunicaciones-iTEAM, Universitat Politècnica de València, 46022 Valencia, Spain (e-mail: vboria@dcom.upv.es).

Color versions of one or more of the figures in this paper are available online at http://ieeexplore.ieee.org.

Digital Object Identifier 10.1109/TMTT.2017.2785246

As compared to the work presented in [36], in this paper, we provide a detailed analysis of the circuit model, including the equations that provide the reactive element values from filter specifications. We discuss in detail the developed ASM algorithm, necessary to automatically generate the filter layout, as well as the pre- and postoptimization algorithms necessary to determine the positions of the transmission-zero frequencies. Finally, we report an order-5 common-mode suppressed balanced filter, and we dedicate a section to compare the size and performance of such filter with other balanced filters (exhibiting comparable differential-mode bandwidth) available in the literature.

This paper is organized as follows. The filter topology and the equivalent circuit model are presented in Section II. Such section includes the analysis of the circuit model, necessary to achieve the required differential-mode filter response. The determination of the transmission-zero frequencies (for both the differential and common modes), necessary to achieve broadband common-mode suppression, and efficient rejection of the differential mode in the differential-mode stopband, is discussed in Section III. Section IV is devoted to the design and synthesis tool, based on ASM (as mentioned before), able to provide the filter layout following an unattended scheme. An illustrative design example is reported in Section V, specifically a fifth-order wideband balanced filter. In Section VI, a comparative analysis with other wideband balanced filters is carried out. Finally, the main conclusions are highlighted in Section VII.

II. FILTER TOPOLOGY, LUMPED ELEMENT EQUIVALENT CIRCUIT, AND ANALYSIS

The typical topology of the wideband balanced bandpass filters under consideration is depicted in Fig. 1 [36]. Such topology corresponds to a fifth-order filter, but it can be generalized to an arbitrary order by simply adding or removing filter stages. All filter elements can be described by means of simple reactive elements in the frequency region of interest. This means that the filter is electrically small by nature, since it is composed by semilumped elements, rather than by distributed components.

The first-, third-, and fifth-filter stages are transverse mirrored SIRs made of seven alternating sections with high/low characteristic impedance. The second- and fourth-filter stages are made of differential pairs of interdigital capacitors cascaded between inductive (narrow) strips. The elliptical windows etched in the ground plane have the purpose of reducing the parasitic capacitances of the interdigital capacitors and increasing the per unit length inductance of the inductive strips. With this topology, wide bandwidths for the differential mode can be achieved, since it is possible to obtain low reactance slope for the series resonators (interdigital capacitors in series with the inductive strips), and low susceptance slope for the shunt resonators (made by a combination of mirrored SIR elements, as will be later shown). It is interesting to mention that the presence of series connected interdigital capacitors blocks signal transmission at low frequencies for both the differential and common modes. This is particularly useful for the suppression of the common mode at low frequencies.

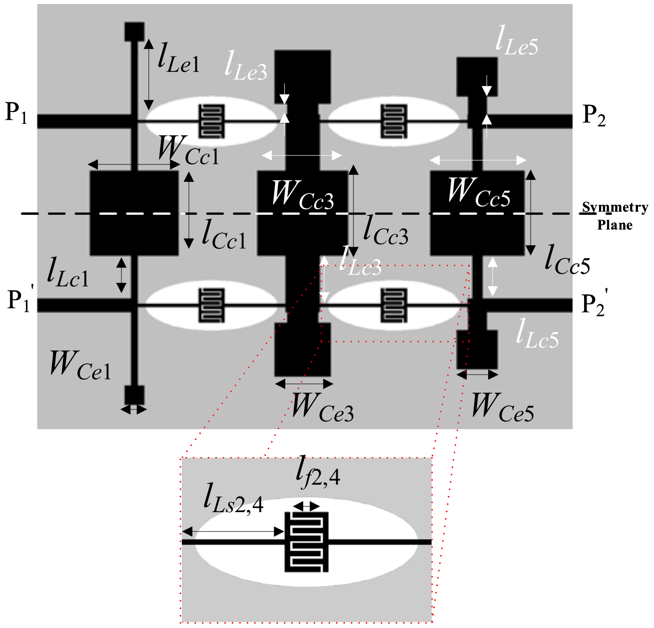

Fig. 1. Topology of the proposed balanced bandpass filters. The upper metal level and ground plane are depicted in black and gray, respectively. Relevant dimensions are indicated.

The lumped element equivalent circuit of the filter is shown in Fig. 2(a). The inductances and capacitances designated as $L_{e,i}$ and $C_{e,i}$ account for the external inductive strips (with length $l_{Le,i}$) and capacitive patches (with width $W_{Ce,i}$), respectively, of the mirrored SIRs, whereas $L_{c,i}$ and $C_{c,i}$ describe the central inductive strips (with length $l_{Lc,i}$) and central patches (with width $W_{Cc,i}$), respectively. The interdigital capacitances are called $C_{s,i}$, whereas $L_{s,i}$ corresponds to the inductive strips cascaded to the interdigital capacitors. The capacitance C_{par} is a parasitic capacitance, necessary to adequately describe the interdigital capacitors and narrow inductive strips adjacent to them. Note, however, that C_{par} is part of the shunt resonators of the preceding and following filter stages, and are, therefore, relevant for the determination of the reactive elements of such stages, as will be later discussed. The subindex i added to the reactive elements of the circuit model indicates the corresponding filter stage.

The circuit models for the differential and common modes are depicted in Fig. 2(b) and (c), respectively. Note that the unique difference between the differential- and common-mode circuits is the absence of the capacitance $C_{c,i}$ in the former circuit. The central patch capacitances are grounded for the differential mode and do not play any role for that mode. However, such capacitances, in combination with the inductances of the central strips, $L_{c,i}$, provide transmission zeros for the common mode, useful for the suppression of this mode. It is interesting to mention that the external resonators, $L_{e,i}$–$C_{e,i}$, provide transmission zeros for both the differential and common modes. Such transmission zeros are useful to further enhance the common-mode stopband bandwidth, to improve the filter selectivity for the differential mode, and to obtain a broad stopband for this mode above the differential-mode passband.

In the design of the filter, the first step is the determination of the elements of the circuit model from filter specifications,

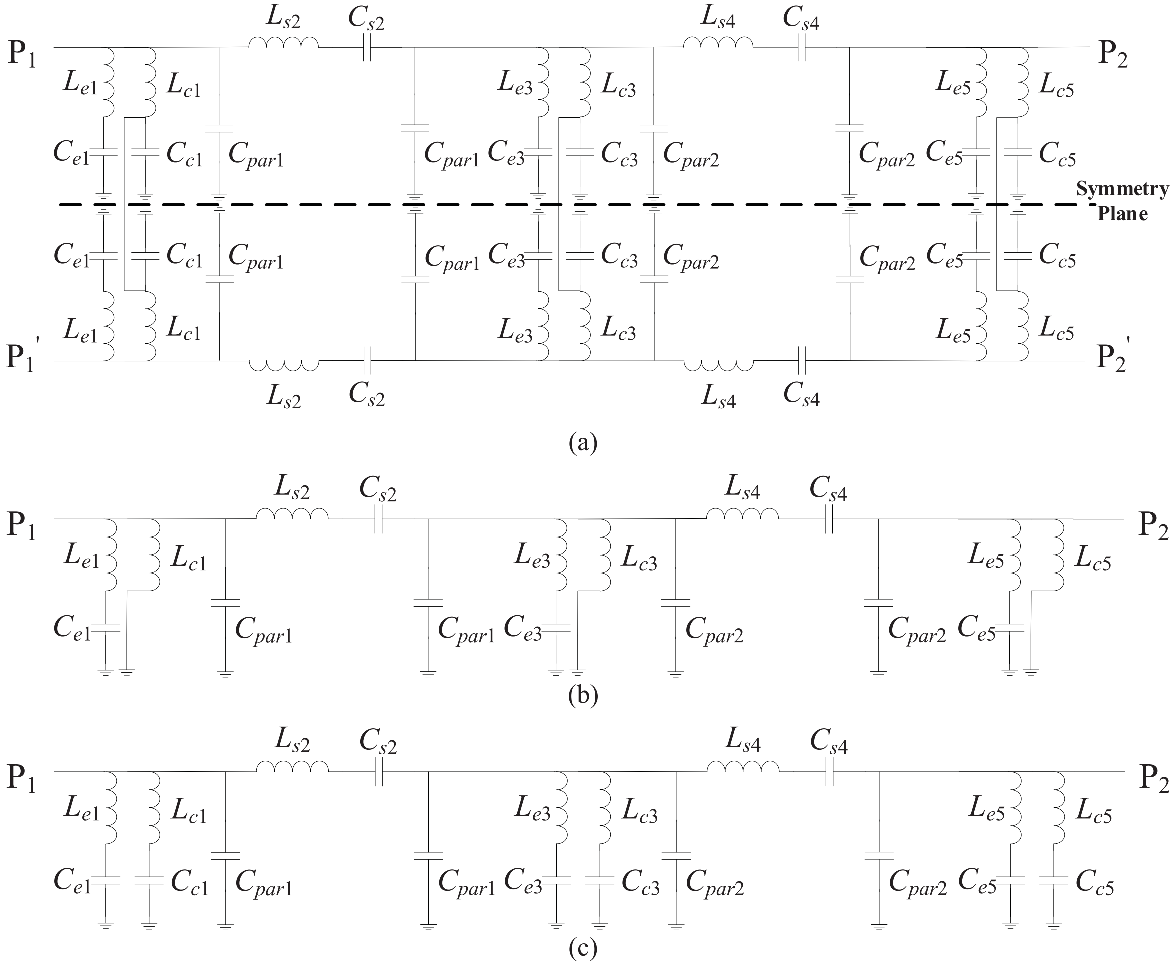

Fig. 2. (a) Lumped element equivalent circuit model of the filter of Fig. 1(a), and equivalent circuits for the (b) differential and (c) common modes.

and by the position of the differential- and common-mode transmission zeros. Once such elements are known, the second step is the determination of the filter layout, to be discussed in Section IV. In the circuit model, the capacitances C_{par} are the single parasitic elements. Such capacitances are due to the series stages (interdigital capacitors and narrow inductive strips), but, as mentioned before, they are part of the shunt stages. The capacitances C_{par} are not easily controllable parameters, but they can be easily inferred once the layouts of the series stages are known. Therefore, in the design flowchart, it is first necessary to determine the series elements, $L_{s,i}$ and $C_{s,i}$, and then synthesize the layouts of the interdigital capacitors and inductive strips. From such layouts, the values of capacitances C_{par} can be derived. The element values $L_{s,i}$ and $C_{s,i}$ can be easily determined from filter specifications (central frequency, bandwidth, filter order, and ripple level), according to standard filter design techniques [48], [49]. Let us assume that the capacitances C_{par} have been inferred from the layouts of the series stages (to be discussed in next section). The other reactive elements of the shunt branches are determined as follows. For the differential mode, the reactance of the shunt branches is given by

$$\chi_{s,\mathrm{diff}} = \frac{(\omega^2 L_e C_e - 1) L_c}{\omega^3 C_{\mathrm{par}} L_e C_e L_c - \omega(C_e L_c + C_e L_e + C_{\mathrm{par}} L_c)} \tag{1}$$

where the subindex i has been omitted for simplicity. The three unknowns that appear in (1), L_c, L_e, and C_e, are given by the position of the transmission zeros for the differential mode

$$f_{z,dd} = \frac{1}{2\pi\sqrt{L_e C_e}} \tag{2}$$

by the filter central frequency, where the shunt reactance for the differential mode, $\chi_{s,\mathrm{diff}}$, opens

$$f_0 = \frac{1}{2\pi}\sqrt{\frac{C_e L_c + C_e L_e + C_{\mathrm{par}} L_c}{C_{\mathrm{par}} L_e C_e L_c}} \tag{3}$$

and by the susceptance slope

$$b = \frac{\omega_0}{2}\left.\frac{dB}{d\omega}\right|_{\omega_0} = \frac{\omega_0 C_{\mathrm{par}}}{2} + \frac{1}{2L_c\omega_0} + \frac{C_e\omega_0\left(1 + L_e C_e \omega_0^2\right)}{2\left(1 - L_e C_e \omega_0^2\right)^2} \tag{4}$$

where $\omega_0 = 2\pi f_0$ is the central angular frequency. The capacitances of the central patches, $C_{c,i}$, are determined from the positions of the common-mode transmission zeros, i.e.,

$$f_{z,cc} = \frac{1}{2\pi\sqrt{L_c C_c}}. \tag{5}$$

Thus, from the solution of (2)–(5), the reactive element values of the shunt branches of the filter are inferred.

Concerning the transmission zeros, it should be noted that there are as many differential-mode transmission zeros as shunt branches, or $(N+1)/2$, where N is the filter order (it is considered that the filter order is odd). The differential-mode transmission zeros are also common-mode transmission zeros. This helps to broaden the common-mode rejection (CMR) bandwidth. However, $(N+1)/2$ additional common-mode transmission zeros, due to the central patch capacitors, are available to suppress the common mode in the frequency region corresponding to the differential-mode passband.

III. OPTIMIZATION OF THE TRANSMISSION-ZERO FREQUENCIES

In this paper, rather than a single (degenerated) common-mode transmission zero, the zeros for that operation mode are distributed in order to achieve good CMR within the differential-mode passband and beyond. With these transmission zeros, and those for the differential mode, necessarily set above the passband of interest (but also active for the common mode), the common mode can be significantly rejected beyond the differential-mode passband, as will be shown later.

The first (lower) differential-mode transmission zero must be positioned not very far from the upper differential-mode cutoff frequency. By this means, filter selectivity at the upper transition band is substantially improved. However, we should avoid locating the first differential-mode transmission zero too close to the upper cutoff frequency, in order to prevent the degradation of the differential-mode return loss in the upper part of the passband. According to the previous comments, a tradeoff is necessary.

In practice, it is difficult to *a priori* predict the positions of the transmission zeros (for the differential and common modes) necessary to optimize the differential and CMR bands. The reason is that filter design is focused on achieving a certain differential-mode response (dictated by specifications). However, the common-mode response (not subjected to specifications) typically exhibits transmission peaks. The position of such peaks depends on the transmission-zero frequencies, but not straightforwardly. Therefore, an iterative algorithm for the optimization of the transmission-zero frequencies (for both the differential and common modes) has been developed (pre-optimization algorithm). To illustrate how this algorithm works, let us consider a specific (conducting) filter example, corresponding to the following specifications: order $N = 5$, quasi-Chebyshev bandpass response with central frequency $f_0 = 1.8$ GHz, fractional bandwidth FBW = 48% (or 55.4% −3-dB fractional bandwidth), and ripple level $L_{\mathrm{ar}} = 0.04$ dB. (These specifications correspond to the filter to be designed later on.)

In a first step, the location of all the transmission zeros (differential and common modes) is set to an arbitrary single frequency, significantly above the upper cutoff frequency of the differential-mode passband, e.g., 2.5 f_0. From filter specifications, we can infer the value of L_s and C_s, corresponding to the second and fourth stages, using well-known formulas [49]. Since the elements of the shunt branches depend on C_{par} [see expression (1)], it is necessary to first synthesize the layout of the series branches, according to the ASM algorithm to be specified later, and, from it, determine the value of C_{par}. Once this parasitic capacitance is known ($C_{\mathrm{par}} = 0.445$ pF, as indicated later), (2)–(5) can be used to determine L_e, L_c, C_e, and C_c for the first-, third-, and fifth-filter stages, and the response of the circuit (differential and common modes) at the schematic level can be inferred [Fig. 3(a)]. From this response, we can identify the common-mode transmission maxima at frequencies 1.942 and 2.047 GHz. (Note that these frequencies can be automatically obtained by means of a simple algorithm able to detect transmission maxima.)

In the second step, we reallocate two of the common-mode transmission zeros in the transmission peak frequencies (for that mode) and set the additional common-mode transmission zero to 1.5 f_0 (2.7 GHz). The differential-mode transmission zeros are kept unaltered in this second step. Thus, the transmission zeros are: $f_{z,cc} = 1.942$ GHz, 1.5 f_0, 2.047 GHz and $f_{z,dd} = 2.5\ f_0$, 2.5 f_0, 2.5 f_0. The new response is the one depicted in Fig. 3(b), where the common-mode transmission peaks are found to be at 1.829, 1.915, and 3.103 GHz.

According to the previous common-mode transmission peaks, in a new (third) iteration, the transmission zeros are set to $f_{z,cc} = 1.829$ GHz,1.5 f_0, 1.915 GHz and $f_{z,dd} =$ 3.103 GHz, 2.5 f_0, 2.5 f_0. Note that the third-common-mode transmission peak (at 3.103 GHz) is canceled by means of the first-differential-mode transmission zero. The new filter response is found to be the one depicted in Fig. 3(c), where it can be appreciated that the common-mode transmission peaks are significantly attenuated. Nevertheless, in this iterative algorithm, the objective is to obtain common-mode transmission peaks within the differential-mode passband with a level below −25 dB. The common-mode transmission peaks are found to be located at 1.811 and 1.895 GHz. Hence, the new set of transmission zeros in the fourth iteration is set to $f_{z,cc} = 1.811$ GHz, 1.5 f_0, 1.895 GHz and $f_{z,dd} =$ 3.103 GHz, 2.5 f_0, 2.5 f_0. The new response is depicted in Fig. 3(d), where there are still two peaks above −25 dB at frequencies 1.808 and 1.892 GHz. Hence, the novel set of transmission zeros is $f_{z,cc} = 1.808$ GHz, $1.5 f_0$, 1.892 GHz and $f_{z,dd} = 3.103$ GHz, $2.5 f_0$, $2.5 f_0$. With these transmission zeros, the filter response [Fig. 3(e)] exhibits CMR above 25 dB up to at least $2.5 f_0$. Therefore, the algorithm stops at this fifth iteration, and the common-mode and differential-mode transmission zeros are located at $f_{z,cc} = 1.808$ GHz, 2.7 GHz, 1.892 GHz and $f_{z,dd} = 3.103$ GHz, 4.5 GHz, 4.5 GHz, respectively.

The comparison between the obtained differential-mode response (circuit level) and the theoretical (ideal) Chebyshev response is depicted in Fig. 4 (the circuit elements of the final circuit are indicated). Although somehow degraded, the return loss in the passband is acceptable on account of the improved filter selectivity beyond the upper cutoff frequency (upper transition band).

IV. FILTER SYNTHESIS THROUGH ASM

Layout generation from the lumped element values is carried out following an ASM scheme [50]–[52]. Specific ASM algorithms for the series resonators (interdigital capacitors

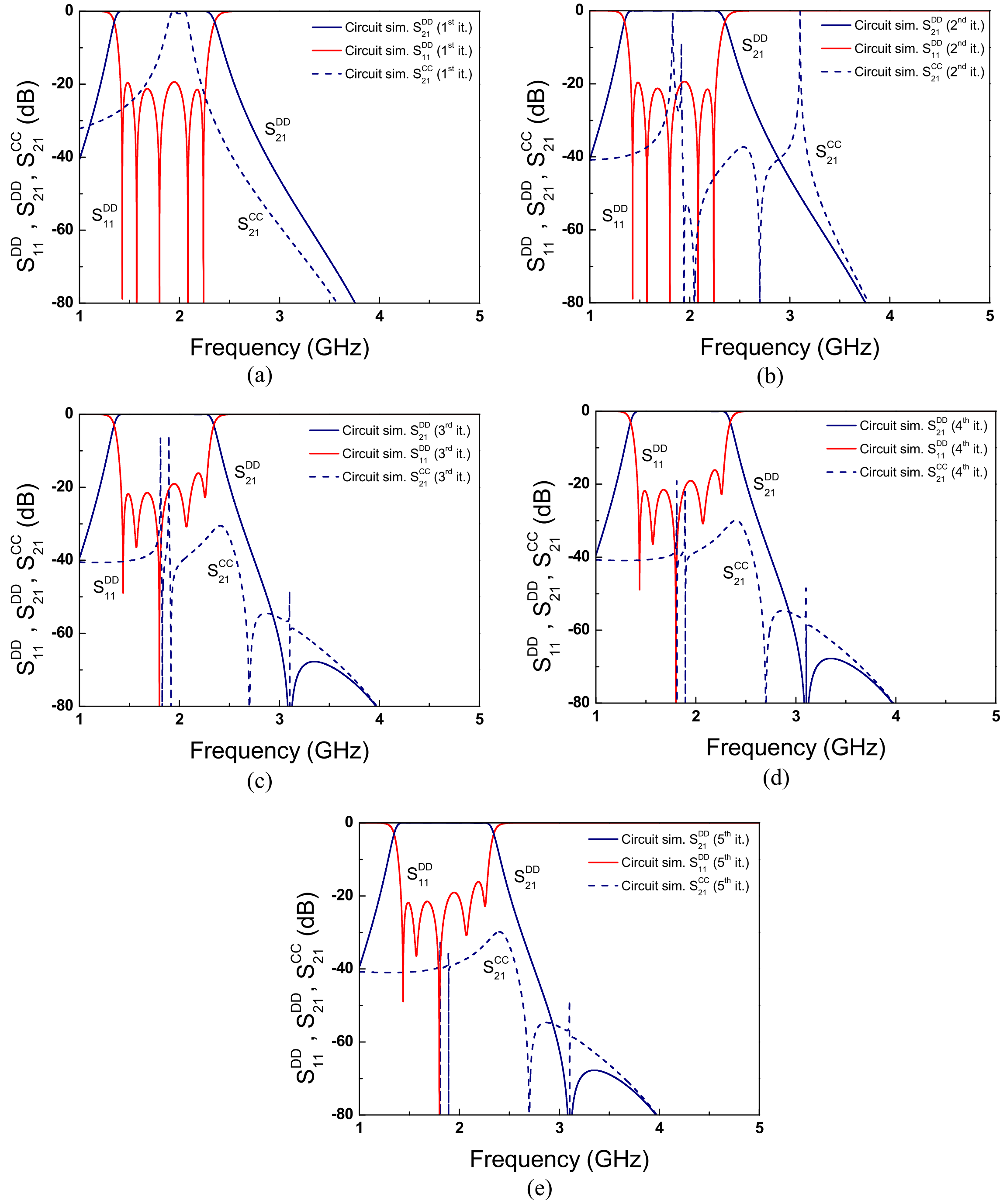

(a) (b) (c) (d) (e)

Fig. 3. Evolution of the differential- and common-mode responses (circuit level) obtained by means of the iterative algorithm used for the optimization of the transmission-zero positions. (For the common mode, only the insertion loss is depicted.) (a) First, (b) second, (c) third, (d) fourth, and (e) fifth iterations.

cascaded between narrow inductive strips) and for the mirrored SIRs have been developed.

A. Synthesis of the Series Resonators

For the series resonators, the variables in the optimization space are $L_{s,i}$ and $C_{s,i}$, whereas the variables in the validation space are the length of the inductive strip, l_{Ls}, and the length of the fingers, l_f. The separation between fingers is set to 0.2 mm. The width of the fingers and inductive strips is set to 0.4 mm. To initiate the ASM algorithm, seeding values for l_{Ls} and l_f are required. These values are inferred from well-known expressions providing the inductance of a narrow strip and the capacitance of an interdigital capacitor [48]. Then, the element values $L_{s,i}$ and $C_{s,i}$ are obtained through parameter extraction, and the first estimation of the Jacobian matrix $\mathbf{B}$ is obtained using a finite difference scheme [51]. Specifically, l_{Ls} and l_f are perturbed, and the effects of these perturbations on the variation of $L_{s,i}$ and $C_{s,i}$ are expressed as derivatives in matrix form. From the extracted values of $L_{s,i}$ and $C_{s,i}$, the first error function is obtained

$$\mathbf{f}(\mathbf{x_f}) = \mathbf{P}(\mathbf{x_f}) - \ \mathbf{x_c^*} \tag{6}$$

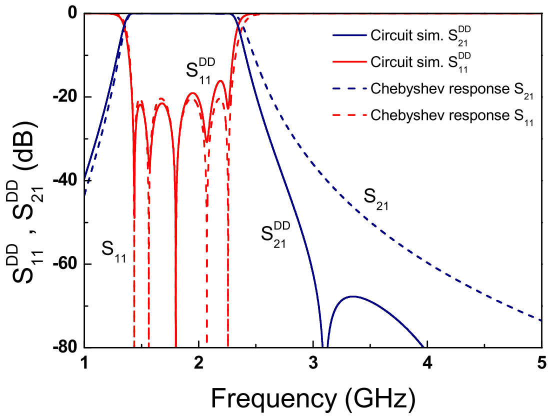

Fig. 4. Comparison between the ideal Chebyshev response subjected to the filter specifications and the differential-mode response of the filter (circuit level) resulting from the iterative algorithm used to determine the location of the transmission zeros. For stages second and fourth, $L_s = 12.622$ nH and $C_s = 0.619$ pF and $C_{\mathrm{par}} = 0.445$ pF. For the shunt branches, the circuit elements are $L_{e,1} = 1.938$ nH, $L_{c,1} = 3.139$ nH, $C_{e,1} = 1.358$ pF, and $C_{c,1} = 2.468$ pF (first stage), $L_{e,3} = 0.311$ nH, $L_{c,3} = 1.378$ nH, $C_{e,3} = 4.020$ pF, and $C_{c,3} = 2.522$ pF (third stage), and $L_{e,5} = 0.575$ nH, $L_{c,5} = 2.576$ nH, $C_{e,5} = 2.176$ pF, and $C_{c,5} = 2.747$ pF (fifth stage).

where $\mathbf{x}_\mathbf{c}^*$ is the vector in the optimization space containing the objective (target) values, $\mathbf{x}_\mathbf{f}$ is the vector in the validation space, with the seeding values for l_{Ls} and l_f in the first iteration, and $\mathbf{P}(\mathbf{x}_\mathbf{f})$ is the vector in the optimization space resulting from parameter extraction from $\mathbf{x}_\mathbf{f}$. If we call $\mathbf{x}_\mathbf{f}^{(j)}$, the jth approximation to the solution in the validation space, and $\mathbf{f}^{(j)}$ the corresponding error function, the next vector of the validation space is obtained according to

$$\mathbf{x}_\mathbf{f}^{(j+1)} = \mathbf{x}_\mathbf{f}^{(j)} + \mathbf{h}^{(j)} \tag{7}$$

where $\mathbf{h}^{(j)}$ is given by

$$\mathbf{h}^{(j)} = -(\mathbf{B}^{(j)})^{-1}\mathbf{f}^{(j)} \tag{8}$$

and $\mathbf{B}^{(j)}$ is an approach to the Jacobian matrix, updated according to the Broyden formula [51]

$$\mathbf{B}^{(j+1)} = \mathbf{B}^{(j)} + \frac{\mathbf{f}^{(j+1)}\mathbf{h}^{(j)T}}{\mathbf{h}^{(j)T}\mathbf{h}^{(j)}}. \tag{9}$$

Convergence is considered to be achieved once the norm of the error function, defined as follows:

$$\|f_{\mathrm{norm}}\| = \sqrt{\left(1 - \frac{L_s}{L_s^*}\right)^2 + \left(1 - \frac{C_s}{C_s^*}\right)^2} \tag{10}$$

is smaller than a certain predefined value. Using this ASM scheme, the layouts of the series resonators are inferred. Once these layouts are known, the values of C_{par} for each series stage are easily obtained.

As an illustrative example, let us consider the synthesis of series resonators with $\mathbf{x}_\mathbf{c}^* = L_s^*, C_s^* = 12.622$ nH, 0.619 pF, corresponding to stages second and fourth of the filter with specifications indicated in Section III (which are also the specifications of the order-5 balanced filter to be synthesized in next section as an example). The seeding values of the variables in the validation space are found to be $\mathbf{x}_\mathbf{f}^{(1)} = l_{Ls}$, $l_f = 9.399$ mm, 4.112 mm, and the reactive element values inferred through parameter extraction are found to be $\mathbf{x}_\mathbf{c}^{(1)} = \mathbf{P}(\mathbf{x}_\mathbf{f}^{(1)}) = 15.547$ nH, 1.026 pF. The considered substrate is Rogers RO4003C with dielectric constant $\varepsilon_r = 3.55$, thickness $h = 0.813$ mm, and loss tangent $\tan\delta = 0.0021$. The specific parameter extraction is as simple as obtaining the series and shunt reactance of the equivalent π-circuit from the electromagnetic simulation of the layout (the Keysight momentum is used). The series elements, L_s and C_s, are obtained from the resonance frequency and from the reactance slope. The shunt reactance provides the capacitance C_{par} (it can be merely obtained from the slope of the susceptance). However, note that C_{par} is not used during the iteration process. As discussed in Section III, this capacitance is necessary to determine the elements of the shunt branches (mirrored SIRs), and it is fundamental in the optimization of the transmission-zero positions.

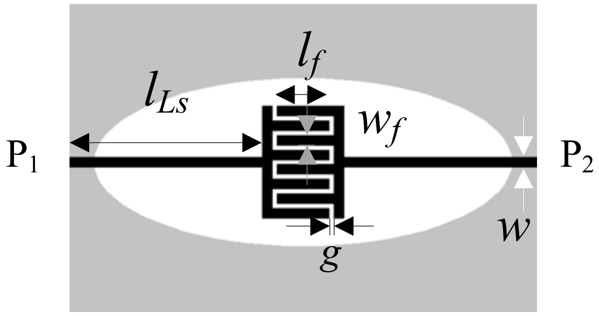

Fig. 5. Generated layout of the series resonator for the designed filter. Dimensions are (in millimeter): $w = 0.4$, $l_{Ls} = 7.868$, $g = 0.2$, $l_f = 2.176$, and $w_f = 0.4$.

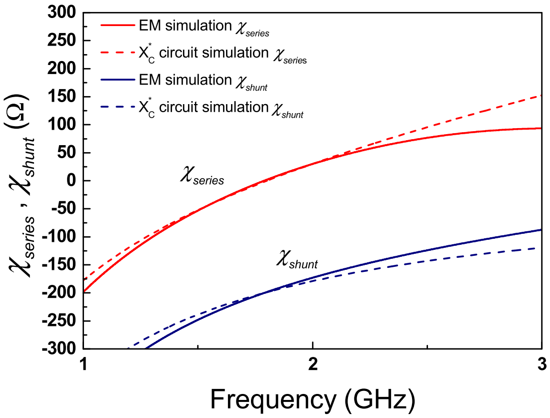

Fig. 6. Series and shunt reactance for the structure depicted in Fig. 5.

Using the ASM scheme explained before, convergence, with an error smaller than 1.7%, is achieved after just 1 iteration. The final vectors in the optimization and validation spaces are $\mathbf{x}_\mathbf{c}^{(2)} = 12.587$ nH, 0.629 pF, and $\mathbf{x}_\mathbf{f}^{(2)} = 7.868$ mm, 2.176 mm, respectively. The resulting parasitic capacitance is found to be $C_{\mathrm{par}} = 0.445$ pF. Fig. 5 depicts the synthesized layout, whereas the series and shunt reactances (inferred from electromagnetic simulation) are shown in Fig. 6. For comparison purposes, the target reactance (series reactance corresponding to $\mathbf{x}_\mathbf{c}^*$) and the reactance of C_{par} are also shown in Fig. 6. As can be seen, the agreement is good in the

TABLE I
WIDTHS OF THE INDUCTIVE STRIPS OF THE MIRRORED SIRs

L_e, L_c (nH)	W_{Le}, W_{Lc} (mm)
>1.6	0.8
[1, 1.6)	1.6
[0.5, 1)	2.4
[0.35, 0.5)	3.2
< 0.35	4

region of interest, pointing out the validity of the employed ASM method.

B. Synthesis of the Mirrored SIRs

For the mirrored SIRs, the procedure is similar to the one reported in [34], but with significant differences. Such differences are due to the fact that in the filters reported in [34], based on mirrored SIRs coupled through admittance inverters, the SIRs were all identical, except the central patch (in order to achieve multiple transmission zeros for the common mode). The filter response in [34] was controlled by the impedance of the inverters, different in each stage. Therefore, the width of the pair of transmission-line sections (inverters) was a variable in the optimization process. However, the transverse distance between these lines was kept constant in [34] thanks to the identical admittance of the shunt (SIR) resonators for the differential mode. Keeping this distance invariable is convenient for design purposes. In this paper, the shunt resonators are not identical since the reactive elements of the SIRs are determined by the admittance slope and transmission zeros (besides the filter central frequency). Hence, the variables in the validation space (geometrical variables) will be different for the various SIRs in order to keep unaltered the transverse distance between the pair of lines along the filter. Conversely, the variables in the optimization space are in all cases L_e, L_c, C_e, and C_c.

Let us now explain in detail, the ASM algorithm applied to the synthesis of the mirrored SIRs. The first one (first stage) is optimized as follows: the widths of the inductive strips W_{Lc} and W_{Le} are set to different values depending on the inductance value. Specifically, these widths are determined according to Table I.

Once these widths are fixed, the variables in the validation space are chosen to be the lengths of these inductances, l_{Lc} and l_{Le}, and the lengths of the capacitive patches, l_{Cc} and l_{Ce} (the widths of such patches are chosen to be identical to the lengths, i.e., $W_{Cc} = l_{Cc}$ and $W_{Ce} = l_{Ce}$, corresponding to a square geometry). Once the four geometrical variables that must be optimized have been decided, we proceed similar to the synthesis of the series resonant elements. From well-known formulas that provide the inductance of a narrow strip and the capacitance of a patch, the seeding value of the geometrical variable is determined. After that, the reactive element parameters, L_e, L_c, C_e, and C_c, are extracted. The first Jacobian (4×4) matrix is obtained by perturbing the geometrical variables, and the first error function is obtained according to (6), where $\mathbf{x}_\mathbf{c}^*$ and $\mathbf{x}_\mathbf{f}$ are the ASM variables of the first mirrored SIR. The iterative process is then carried out using (7)–(9) until convergence is achieved.

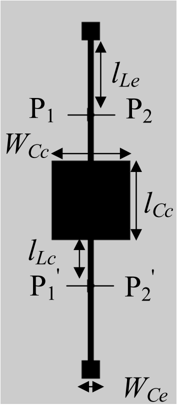

Fig. 7. Dimensions are (in millimeters): $W_{Ce} = 3.543$, $l_{Le} = 6.404$, $W_{Cc} = l_{Cc} = 10.785$, and $l_{Lc} = 5.668$.

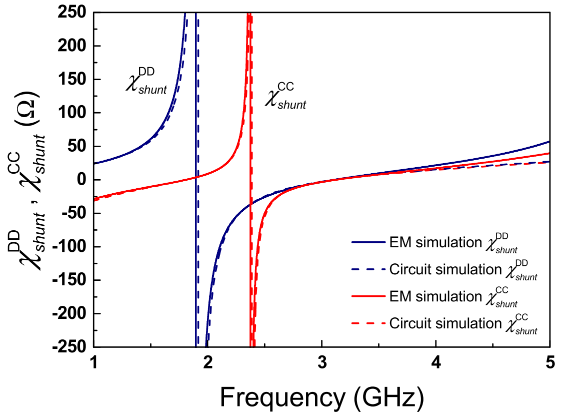

Fig. 8. Differential- and common-mode reactances for the mirrored SIR of Fig. 7.

As an illustrative example, let us consider the synthesis of a mirrored SIR with the following reactive element values (corresponding to the first SIR of the order-5 filter to be presented in next section): $L_e = 1.938$ nH, $L_c = 3.139$ nH, $C_e = 1.358$ pF, and $C_c = 2.468$ pF. The final vectors in the optimization and validation spaces (obtained after six iterations with an error smaller than 0.94%) are found to be $\mathbf{x}_\mathbf{c}^{(6)} = L_e, L_c, C_e, C_c = 1.935$ nH, 3.157 nH, 1.354 pF, 2.452 pF, and $\mathbf{x}_\mathbf{f}^{(6)} = l_{Le}, l_{Lc}, l_{Ce}, l_{Cc} = 6.404$ mm, 5.668 mm, 3.543 mm, 10.785 mm. The corresponding layout is depicted in Fig. 7, whereas the reactances for the differential and common modes inferred from electromagnetic simulations are depicted in Fig. 8. Such reactances are compared to those of the circuit model, and the agreement is very good, as can be appreciated in Fig. 8.

For the other mirrored SIRs, the lengths of the central patch and central inductive strip are set to the corresponding values of the first mirrored SIR, i.e., $l_{Cc,i} = l_{Cc,1}$ and $l_{Lc,i} = l_{Lc,1}$. By this means, the distance between terminals in the differential ports of the mirrored SIRs is identical in all the stages. Thus, the optimization variables in the validation space for such SIRs (with $i > 1$) are: $l_{Le,i}$ (the width of this inductance set using Table I), $W_{Lc,i}$, $W_{Cc,i}$, and $l_{Ce,i}$ (considering $W_{Ce,i} = l_{Ce,i}$ in order to obtain a square geometry for the external patches).

TABLE II
GEOMETRIC PARAMETERS OF THE MIRRORED SIRs

i	l_{Lc}	l_{Cc}	l_{Le}	l_{Ce}	W_{Lc}	W_{Cc}	W_{Le}	W_{Ce}
1	5.668	10.785	6.404	3.543	0.8	10.785	0.8	3.543
3	5.668	10.785	1.471	7.247	4.203	12.007	4	7.247
5	5.668	10.785	2.457	5.270	1.215	11.858	2.4	5.270

All dimensions in mm

One important difference between the synthesis of these filters and those reported in [34] concerns the fact that in [34], the ASM algorithm was actually a two-step process. That is, due to the limited functionality (bandwidth) of the admittance inverters implemented by means of quarter wavelength transmission lines, it was first necessary that an ASM algorithm be able to provide the schematic necessary to compensate for the narrowing effects of the admittance inverters on the filter response (optimum schematic). This first ASM is not necessary for the design of the proposed wideband balanced filters since distributed components are not used. Therefore, by considering the filter topology reported here, a clear benefit in terms of design simplicity and quickness is obtained (nevertheless, an iterative, but very fast, algorithm for the optimization of the transmission-zero frequencies has been necessary, as discussed in Section III).

V. PROTOTYPE DEVICE EXAMPLE

To illustrate the potential of the proposed ASM approach, the filter with specifications indicated in Section III and with the transmission zeros (differential and common modes) allocated at the indicated positions is reported in this section. With such specifications, the series elements L_s and C_s (identical for stages $i = 2$ and $i = 4$), inferred from the low-pass filter prototype Chebyshev tables corresponding to the cited order and ripple, and from well-known impedance and response transformations [48], are those indicated in Section III. The value of C_{par} and the element values of the mirrored SIRs (found from the optimization of the transmission-zero frequencies) are also indicated in Section III (see Fig. 4).

Once these element values are known, layout generation for the series resonators and for each mirrored SIR is obtained by means of the ASM scheme explained in previous section (illustrated in detail for the series resonators and for the mirrored SIR of the first filter stage). The geometric values of the series resonators (interdigital capacitors and inductive strips) are given in Section IV-A, and those corresponding to the different mirrored SIRs are indicated in Table II.

The filter layout is obtained by cascading the synthesized mirrored SIRs and series resonators. The electromagnetic simulation (using Keysight Momentum), including losses, of the filter response for the differential and common modes is depicted in Fig. 9. Despite the fact that the circuit model of the proposed filters provides a reasonable response in the region of interest, it can be appreciated in Fig. 9 that the common mode resulting from lossy electromagnetic simulation (the response of interest) exhibits transmission peaks above −20 dB. The reason is that such peaks are very sensitive to the position of the transmission zeros (as seen in Section III), which may experience some shift in the lossy electromagnetic simulation, as compared to the circuit response.

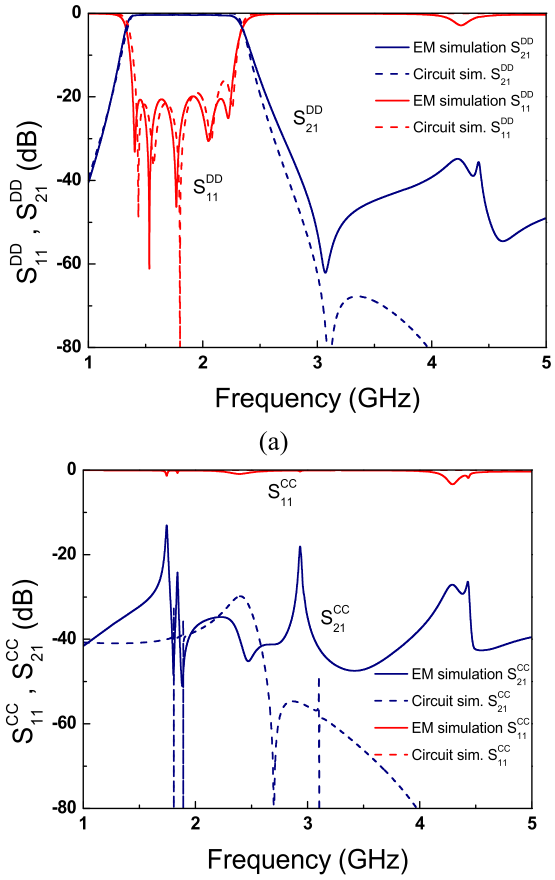

(a)

(b)

Fig. 9. Lossy electromagnetic and lossless circuit simulation of the designed balanced filter. (a) Differential-mode response. (b) Common-mode response.

Since CMR is not satisfactory enough, readjustment of the transmission-zero positions is needed. So, we have developed a second (postoptimization) iterative algorithm similar to the one reported in Section III, but this time the responses are not the circuit simulations of the resulting equivalent circuits, but the electromagnetic simulations (including losses) of the filter after application of the ASM synthesis algorithm. Obviously, this is time consuming, but convergence is obtained after few iterations, provided the initial response (the one inferred from the first ASM—Fig. 9) already exhibits a CMR level better than the target (25 dB), except at certain frequencies. By applying this postoptimization iterative algorithm to the structure resulting from the first ASM, we have been able (after three iterations) to obtain a filter layout exhibiting a CMR level better than −28 dB. The reactive elements of the final filter circuit and the geometrical elements of the optimized layout are indicated in Tables III and IV, respectively. Note that L_s, C_s, C_{par}, and the geometry of the series resonators is kept unaltered in this postoptimization iterative process, since the readjustment of the transmission zeros does not affect the series branches. The final layout of the filter is the one depicted in Fig. 1, and the photograph is shown in Fig. 10 (the filter has been fabricated by means of photo mask etching).

TABLE III

REACTIVE ELEMENT VALUES OF THE OPTIMIZED FILTER

i	L_c (nH)	C_c (pF)	L_e (nH)	C_e (pF)	L_s (nH)	C_s (pF)
1	3.303	2.639	2.456	1.199	---	---
2, 4	---	---	---	---	12.622	0.619
3	1.378	2.522	0.311	4.020	---	---
5	2.576	2.934	0.575	2.176	---	---

TABLE IV

GEOMETRIC PARAMETERS OF THE MIRRORED SIRs FOR THE OPTIMIZED FILTER

i	l_{Lc}	l_{Cc}	l_{Le}	l_{Ce}	W_{Lc}	W_{Cc}	W_{Le}	W_{Ce}
1	5.754	11.401	9.9	2.587	0.8	11.401	0.8	2.587
3	5.754	11.401	1.462	7.209	4.415	11.668	4	7.209
5	5.754	11.401	2.462	5.259	1.272	12.148	2.4	5.259

All dimensions in mm

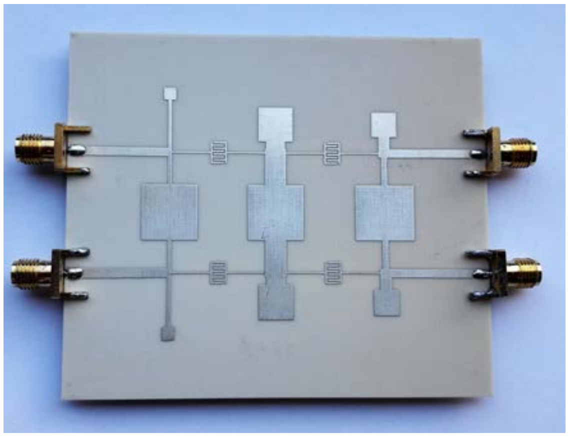

Fig. 10. Photograph of the fabricated balanced filter.

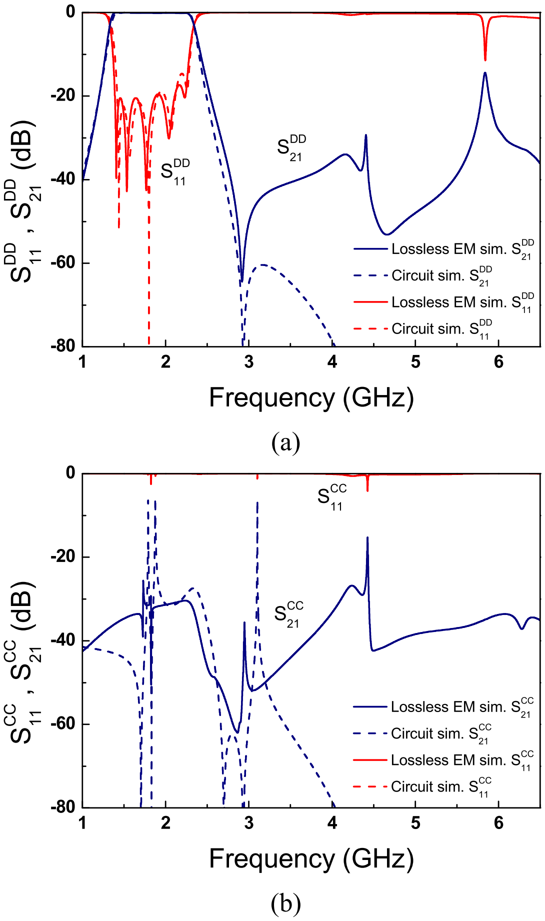

Fig. 11. Lossless electromagnetic and circuit simulation of the designed (optimized) balanced filter. (a) Differential mode. (b) Common mode.

Figs. 11 and 12 depict the lossless and lossy, respectively, electromagnetic simulation of the final filter, including the differential- and common-mode responses. The circuit simulation is also included in Fig. 11. The very good agreement between the circuit and lossless electromagnetic simulation for the differential mode indicates the validity of the proposed filter model (discrepancies above 3 GHz are due to the fact that the filter elements cannot be described by simple reactive elements). Obviously, such agreement is not so good for the common mode, due to the high sensitivity of this mode to the position of the transmission zeros (which has forced us to implement a postoptimization iterative algorithm). Nevertheless, an acceptable coincidence up to approximately 3 GHz, except by the level of the common-mode transmission peaks, can be observed as well. Note that, as we have mentioned before, the postoptimization algorithm is based on forcing the lossy electromagnetic response of the common mode to be below a certain value (-25 dB). Thus, the fact that in Fig. 11(b) such threshold level is not satisfied does not mean that the final filter layout is not optimized. Indeed, in view of Fig. 12(b), the common-mode response inferred from lossy electromagnetic simulation exhibits a rejection level better than -28 dB. Therefore, the target common-mode response is clearly satisfied with the synthesized filter layout.

The measured filter responses for the differential and common modes have been obtained by means of the Agilent PNA N5221A vector network analyzer. Such responses are included in Fig. 12 for a proper comparison with the lossy electromagnetic simulation. The agreement is good, although the measured in-band return loss for the differential mode is somehow degraded, as compared to the electromagnetic simulation. This is due to tolerances in the fabrication process. Note that interdigital capacitors have very small gap ($g = 0.2$ mm), and this is a critical parameter. The sensitivity analysis of Fig. 13, showing the effects of slight variations in g on the frequency response, confirms this point. Also, perfect symmetry is also difficult to achieve in practice, and there are two pairs of symmetric interdigital capacitors that make this aspect more critical. Nevertheless, the measured in-band return loss (differential mode) is better than 11.5 dB. To obtain this measured value, we have forced an in-band ripple at design level (controllable form the element vales of the low-pass filter prototype) small enough (0.04 dB), having in mind the unavoidable degradation of the corresponding return loss due to losses, tolerances, and, in our case, due to the presence of differential-mode transmission zeros close the band of interest. Concerning the in-band insertion loss, it is better than 1 dB. The differential-mode stopband exhibits a rejection level better than 35 dB up to 5.6 GHz (i.e., slightly above $3f_0$), but such

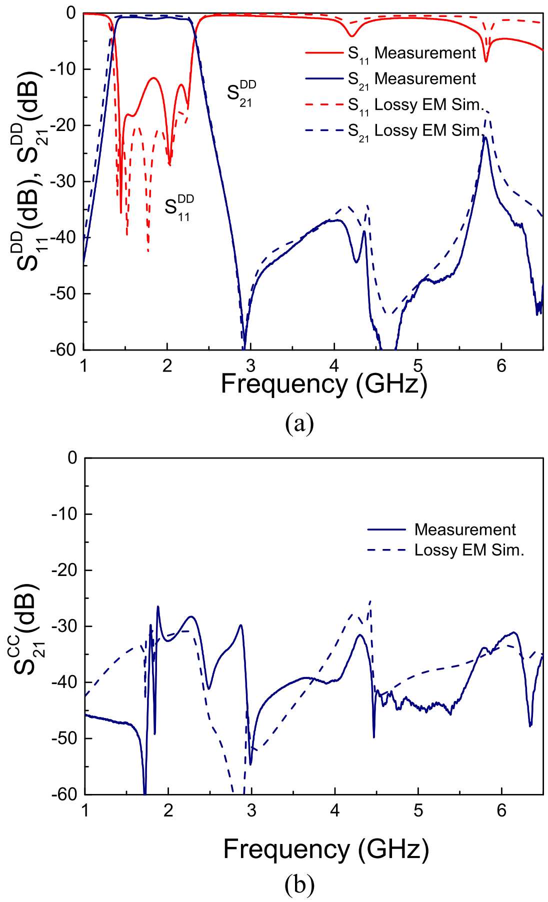

Fig. 12. Lossy electromagnetic simulation and measured response of the designed (optimized) and fabricated balanced filter. (a) Differential mode. (b) Common mode.

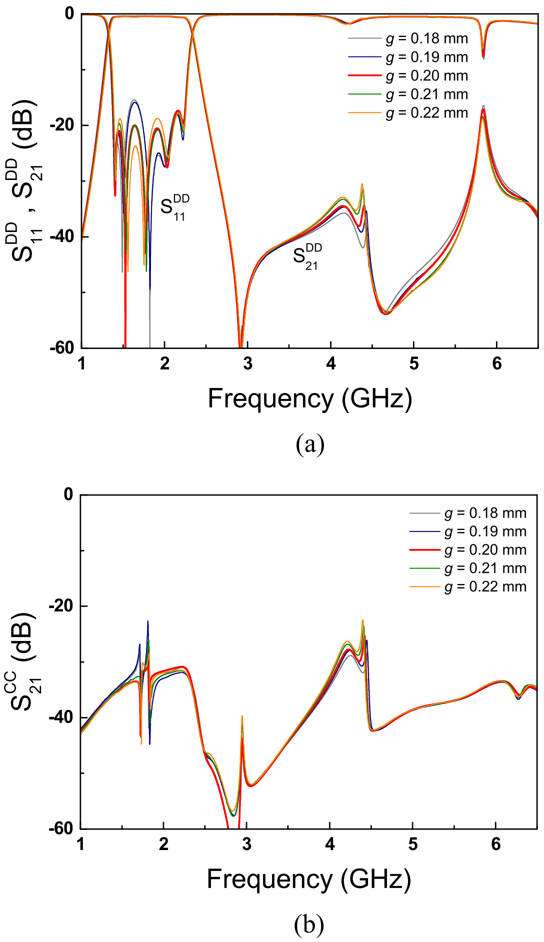

Fig. 13. Frequency responses of the proposed filter obtained through lossy electromagnetic simulation by varying the gap distance g of the interdigital capacitors. (a) Differential mode. (b) Common mode. Variations are between 0.18 and 0.22 mm in steps of 0.01 mm.

band extends up to at least 6.5 GHz with rejection level better than 22 dB. The common mode is suppressed with a rejection level better than 28 dB from dc up to at least 6.5 GHz. Finally, filter size is as small as 51.5 mm × 48.2 mm, corresponding to $0.51\lambda_g \times 0.48\lambda_g$ in terms of the wavelength at the filter central frequency f_0. This combination of size and filter performance is competitive, as will be discussed in the next section.

VI. COMPARISON TO OTHER WIDEBAND BALANCED FILTERS

The reported filter is compared to other wideband balanced bandpass filters in Table V. Such table includes the differential-mode fractional bandwidth (DM-FBW), the central frequency (f_0), the CMR level, including the frequency interval, the differential-mode upper stopband (DM-USB), indicating the stopband rejection level and frequency span, and the effective area, expressed in terms of the square wavelength (with wavelength calculated at f_0). Concerning the CMR, if it is below -28 dB (the value achieved in the proposed filter), we have opted to indicate the frequency interval corresponding to this value for proper comparison. The exception is the filter in [29], where the reported common-mode insertion loss is limited to a narrow band and we cannot determine the frequency span corresponding to a CMR better than -28 dB.

In view of Table V, the filter of Fig. 10 exhibits very good CMR bandwidth. None of the filters reported in the references appearing in Table V exhibits a bandwidth extending from dc up to at least 3.6 f_0 with such CMR ($|S_{21,cc}| < -28$ dB). Indeed, in the filters with lower CMR, the CMR bandwidth is also narrower, as compared to our filter. Nevertheless, the filter of [32] is quite competitive in terms of common-mode suppression performance, since the CMR is better than -27 dB from dc up to 2.8 f_0. In some of the filters, e.g., those of [34], the maximum CMR at f_0 is very high (i.e., $|S_{21,cc}| = -65$ dB and $|S_{21,cc}| = -50$ dB for filters designated as $[34]^a$ and $[34]^b$ in Table V). However, in those filters, such huge rejection level is limited to a narrow bandwidth, as seen in Table V.

Concerning the differential-mode response, specifically the upper stopband (DM-USB), the most competitive filters are those of [23], [33], and [34] and the filter of Fig. 10. Specifically, the filter in [33] exhibits a very good combination of stopband bandwidth and rejection level (-53 dB), but the CMR bandwidth is very limited in this filter. It is worth mentioning that in the filter reported in this paper, there is a transmission zero located very close to the upper cutoff frequency (differential mode). The consequence is high filter selectivity in the upper transition band, with a roll off of roughly -80 dB/GHz. Such high selectivity provides

TABLE V
COMPARISON OF VARIOUS DIFFERENTIAL WIDEBAND BANDPASS FILTERS

Ref.	DM-FBW (–3dB)	f_0 (GHz)	CMR $\lvert S_{21,cc}\rvert$ (dB)	DM-USB $\lvert S_{21,dd}\rvert$ (dB)	Effective area (λ_g^2) / order
[21]	65%	4.0	< -20 $[0.6f_0, 1.4f_0]$	---	0.25 / 3
[22]	50%	4.1	< -16 $[0.3f_0, 1.7f_0]$	< -18 $(> 2.2f_0)$	0.25 / 3
[23]	45%	1.0	< -25 $[0, 1.2f_0]$	< -40 $(2.7f_0)$	0.045 / 3
[25]	43%	2.4	< -28 $[0.6f_0, 1.5f_0]$	< -36 $(2.1f_0)$	0.60 / 5
[26]	15%	1.0	< -25 $[0, 1.15f_0]$	< -20 $(1.8f_0)$	0.022 / 3
[27]	70%	3.0	< -20 $[0.8f_0, 1.7f_0]$	---	0.52 / --
[33]	42%	2.4	< -28 $[0.8f_0, 1.4f_0]$	< -53 $(2.5f_0)$	0.37 / 5
[28]	66.6%	1.62	< -14.5 $[0, 3.0f_0]$	< -30 $(2.5f_0)$	0.163 / 3
[29]	40%	3.5	< -40 $[0.8f_0, 1.2f_0]$	< -20 $(2.3f_0)$	0.25 / 3
[30]	53%	3.0	< -13 $[0, 3.0f_0]$	< -10 $(2.8f_0)$	0.175 / --
[31]	59.5%	1.85	< -28 $[0.4f_0, 1.6f_0]$	< -35 $(2.2f_0)$	0.39 / 3
[32]	56.7%	3.0	< -27 $[0, > 2.8f_0]$	< -31 $(> 2.2f_0)$	0.20 / 3
[24]	79%	3.0	< -13 $[0, 2.7f_0]$	< -25 $(2.6f_0)$	0.192 / 5
[34][a]	43%	2.4	< -28 $[0.8f_0, 1.3f_0]$	< -44 $(> 2.5f_0)$	0.36 / 5
[34][b]	65%	3.0	< -28 $[0.7f_0, 1.5f_0]$	< -34 $(> 2.5\ f_0)$	0.28 / 7
[35]	56%	2.4	< -15 $[0, 1.5f_0]$	---	0.17 / 3
[36]	43%	1.5	< -22 $[0, 2.5f_0]$	< -30 $(> 1.2\ f_0)$	0.13 / 3
[37]	70%	6.85	(< -14.5) $[0, > 2.8f_0]$	< -30 $(> 2.63\ f_0)$	0.28 / 5
[38]	66	3.5	< -6 $[0.5f_0, 1.4f_0]$	< -15 $(> 2.3f_0)$	0.20 / --
This work	**55.4%**	**1.8**	$\mathbf{< -28}$ $\mathbf{[0, > 3.6f_0]}$	$\mathbf{< -22}$ $\mathbf{(> 3.6\ f_0)}$	**0.245 / 5**

a differential-mode rejection level better than -55 dB at 2.9 GHz (1.61 f_0), and better than -38 dB up to 5.6 GHz (3.11 f_0), and is a relevant aspect in the reported filter. Note that the filter of Fig. 10 exhibits the widest differential-mode stopband of all the filters included in Table V.

Concerning filter size, the filters of [23] and [26] are very competitive, but in both cases the CMR bandwidth is very limited, as compared to the filter reported in this paper. Note that these filters [23], [26] are order-3 filters, whereas the filter of Fig. 10 is a fifth-order filter. The third-order filters of [35] and [36] are also very small, but in terms of rejection bandwidth for both the differential and common modes, our filter is by far superior, as can be appreciated in the table. Note that, as mentioned in the introduction, the proposed filter (Fig. 10) is based on the topology of the order-3 filter of [36], from which it follows that the order-5 filter reported here should be electrically larger.

Finally, let us highlight the differences and advantages of the filter proposed in this paper as compared to recently reported similar differential filters proposed by Sans *et al.* [34], [35]. Indeed, the filter proposed in this paper combines the relevant advantageous aspects of the filters of [34] and [35] in the same structure, and at the same time overcomes the limiting aspects, resulting in the proposed new topology of Fig. 10. The result is a filter exhibiting a very good combination of filter size and performance, as compared to [34] and [35] (see Table V). The filters in [34] exhibit relatively good differential-mode stopband, but the common-mode stopband is limited since it does not start at dc. Moreover, these filters use distributed components (quarter-wavelength inverters), and this means that a first ASM to provide the optimum schematic (in order to compensate for the narrowing effect of the—nonideal—transmission-line inverters) is required, as reported in [34]. In this paper, these limitations have been addressed with the proposed topology, thanks to the replacement of the transmission-line inverters with interdigital resonators. By these means, the common mode is rejected over a wide band starting at dc (due to the blocking effect of the series connected interdigital capacitances), and the first ASM used to obtain the optimum schematic is not necessary. Therefore, the introduction of interdigital capacitances represents a significant improvement as compared to the filters of [34], and eases filter design. Moreover, the proposed filter is also more compact, although the filter order is also different.

The main difference as compared to the filter reported in [35] concerns the mirrored SIRs. In the filters reported here, the mirrored SIRs extend out of the DM transmission lines (through the inductive strips with inductance $L_{e,i}$, not present in the filter of [35]). This provides transmission zeros for the differential mode (and also for the common mode), not present in [35], and by this means we achieve a good differential-mode upper stopband. The result is a differential filter with much superior performance.

An additional important and novel aspect proposed (and discussed) in this paper, with direct impact on filter design, is the pre- and postoptimization iterative algorithms considered for the optimization of the transmission-zero positions. Through these algorithms, not applied in [34] and [35], it has been possible to achieve a wide common-mode stopband with significant CMR (a crucial aspect in common-mode suppressed differential filters).

To summarize this section, the proposed filter exhibits a very good combination of size and differential- and common-mode stopband bandwidths. Moreover, filter synthesis has been carried out following an automated scheme. The approach combines an ASM algorithm (that provides filter layout from the elements of the circuit model) with pre- and postoptimization algorithms, necessary to optimize the position of the transmission zeros. (A fundamental aspect to achieve the reported differential- and common-mode stop bands.)

VII. CONCLUSION

In conclusion, a wideband balanced bandpass filter with wide stopband for the differential mode, and common-mode suppression from dc up to frequencies well beyond the differential-mode passband, has been designed and fabricated. The filter has been implemented by cascading multisection mirrored SIRs and interdigital capacitors. The mirrored SIRs provide transmission zeros for the differential and common modes, useful to achieve very broad stopbands for both modes, keeping roughly unaltered the differential-mode passband. The interdigital capacitors are key elements to block the common-mode signals at low frequencies. Moreover, such capacitors, combined with narrow inductive strips, constitute the series resonators of the filter, resulting in a balanced filter fully implemented by means of semilumped (electrically small) elements.

Filter design has been carried out following an ASM optimization algorithm, where the geometry of the different mirrored (shunt connected) SIRs and series resonators has been inferred from the lumped elements of the equivalent circuit model. These elements, in turn, have been obtained from filter specifications and from the transmission-zero frequencies for both modes. Such transmission-zero positions have been determined by means of an iterative pre-optimization algorithm (at circuit level) that guarantees a minimum (specified) level of CMR within the differential-mode passband and beyond. Nevertheless, due to the high sensitivity of common-mode suppression to the transmission-zero frequencies, a postoptimization algorithm (at electromagnetic simulation level) to fine-tune the transmission-zero frequencies has been also developed.

As an illustrative example, the design and synthesis of a fifth-order balanced bandpass filter has been reported. The filter is small on account of the semilumped elements considered in its implementation, and filter performance for the differential mode is good, with insertion loss better than 1 dB in the passband and return loss higher than 11.5 dB in that band. The differential-mode stopband extends up to at least 6.5 GHz ($3.6f_0$), with more than 22-dB rejection (and the rejection level is better than 38 dB up to 5.6 GHz, or $3.11f_0$). Finally, the common mode is rejected with more than 28 dB from dc up to at least 6.5 GHz ($3.6f_0$). This combination of filter size and performance is very competitive. Although filter synthesis uses three specifically developed algorithms (an ASM-based algorithm preceded and followed by transmission-zero optimization algorithms), few iterations suffice to achieve convergence in all cases. This avoids excessive computing times, despite the fact that the latter transmission-zero optimization scheme uses the ASM algorithm at each iteration.

REFERENCES

[1] F. Martín, L. Zhu, F. Medina, and J. S. Hong, *Balanced Microwave Filters*. Hoboken, NJ, USA: Wiley, 2018.

[2] W. Feng, W. Che, and Q. Xue, "The proper balance: Overview of microstrip wideband balance circuits with wideband common mode suppression," *IEEE Microw. Mag.*, vol. 16, no. 5, pp. 55–68, Jun. 2015.

[3] J. Naqui *et al.*, "Common-mode suppression in microstrip differential lines by means of complementary split ring resonators: Theory and applications," *IEEE Trans. Microw. Theory Techn.*, vol. 60, no. 10, pp. 3023–3034, Oct. 2012.

[4] A. Fernandez-Prieto *et al.*, "Dual-band differential filter using broadband common-mode rejection artificial transmission line," *Prog. Electromagn. Res.*, vol. 139, pp. 779–797, Apr. 2013.

[5] A. Fernández-Prieto *et al.*, "Common-mode suppression for balanced bandpass filters in multilayer liquid crystal polymer technology," *IET Microw., Antennas Propag.*, vol. 9, no. 12, pp. 1249–1253, Sep. 2015.

[6] C. H. Wu, C. H. Wang, and C. H. Chen, "Balanced coupled-resonator bandpass filters using multisection resonators for common-mode suppression and stopband extension," *IEEE Trans. Microw. Theory Techn.*, vol. 55, no. 8, pp. 1756–1763, Aug. 2007.

[7] C. H. Wu, C. H. Wang, and C. H. Chen, "Stopband-extended balanced bandpass filter using coupled stepped-impedance resonators," *IEEE Microw. Wireless Compon. Lett.*, vol. 17, no. 7, pp. 507–509, Jul. 2007.

[8] Y. Zhou, H.-W. Deng, and Y. Zhao, "Compact balanced-to-balanced microstrip diplexer with high isolation and common-mode suppression," *IEEE Microw. Wireless Compon. Lett.*, vol. 24, no. 3, pp. 143–144, Mar. 2014.

[9] A. Fernández-Prieto, A. Lujambio, J. Martel, F. Medina, F. Mesa, and R. R. Boix, "Simple and compact balanced bandpass filters based on magnetically coupled resonators," *IEEE Trans. Microw. Theory Techn.*, vol. 63, no. 6, pp. 1843–1853, Jun. 2015.

[10] A. Fernández-Prieto, J. Martel, F. Medina, F. Mesa, and R. R. Boix, "Compact balanced FSIR bandpass filter modified for enhancing common-mode suppression," *IEEE Microw. Wireless Compon. Lett.*, vol. 25, no. 3, pp. 154–156, Mar. 2015.

[11] A. Fernández-Prieto, J. Bhatker, A. Lujambio, J. Martel, F. Medina, and R. R. Boix, "Balanced bandpass filter based on magnetically coupled coplanar waveguide folded-stepped impedance resonators," *Electron. Lett.*, vol. 52, no. 14, pp. 1229–1231, Jul. 2016.

[12] C.-H. Lee, C.-I. G. Hsu, and C.-C. Hsu, "Balanced dual-band BPF with stub-loaded SIRs for common-mode suppression," *IEEE Microw. Wireless Compon. Lett.*, vol. 20, no. 2, pp. 70–72, Feb. 2010.

[13] J. Shi and Q. Xue, "Balanced bandpass filters using center-loaded half-wavelength resonators," *IEEE Trans. Microw. Theory Techn.*, vol. 58, no. 4, pp. 970–977, Apr. 2010.

[14] J. Shi and Q. Xue, "Dual-band and wide-stopband single-band balanced bandpass filters with high selectivity and common-mode suppression," *IEEE Trans. Microw. Theory Techn.*, vol. 58, no. 8, pp. 2204–2212, Aug. 2010.

[15] J. Shi and Q. Xue, "Novel balanced dual-band bandpass filter using coupled stepped-impedance resonators," *IEEE Microw. Wireless Compon. Lett.*, vol. 20, no. 1, pp. 19–21, Jan. 2010.

[16] Y.-H. Cho and S.-W. Yun, "Design of balanced dual-band bandpass filters using asymmetrical coupled lines," *IEEE Trans. Microw. Theory Techn.*, vol. 61, no. 8, pp. 2814–2820, Aug. 2013.

[17] X. Xu, J. Wang, G. Zhang, and J. Chen, "Design of balanced dual-band bandpass filter based on substrate integrated waveguide," *Electron. Lett.*, vol. 49, no. 20, pp. 1278–1280, Sep. 2013.

[18] F. Wei, Y. J. Guo, P. Y. Qin, and X. W. Shi, "Compact balanced dual- and tri-band bandpass filters based on stub loaded resonators," *IEEE Microw. Wireless Compon. Lett.*, vol. 25, no. 2, pp. 76–78, Feb. 2015.

[19] Y. Shen, H. Wang, W. Kang, and W. Wu, "Dual-band SIW differential bandpass filter with improved common-mode suppression," *IEEE Microw. Wireless Compon. Lett.*, vol. 25, no. 2, pp. 100–102, Feb. 2015.

[20] F. Bagci, A. Fernández-Prieto, A. Lujambio, J. Martel, J. Bernal, and F. Medina, "Compact balanced dual-band bandpass filter based on modified coupled-embedded resonators," *IEEE Microw. Wireless Compon. Lett.*, vol. 27, no. 1, pp. 31–33, Jan. 2017.

[21] T. B. Lim and L. Zhu, "A differential-mode wideband bandpass filter on microstrip line for UWB application," *IEEE Microw. Wireless Compon. Lett.*, vol. 19, no. 10, pp. 632–634, Oct. 2009.

[22] T. B. Lim and L. Zhu, "Highly selective differential-mode wideband bandpass filter for UWB application," *IEEE Microw. Wireless Compon. Lett.*, vol. 21, no. 3, pp. 133–135, Mar. 2011.

[23] P. Vélez *et al.*, "Differential bandpass filter with common-mode suppression based on open split ring resonators and open complementary split ring resonators," *IEEE Microw. Wireless Compon. Lett.*, vol. 23, no. 1, pp. 22–24, Jan. 2013.

[24] W. Feng, W. Che, Y. Ma, and Q. Xue, "Compact wideband differential bandpass filters using half-wavelength ring resonator," *IEEE Microw. Wireless Compon. Lett.*, vol. 23, no. 2, pp. 81–83, Feb. 2013.

[25] P. Vélez *et al.*, "Differential bandpass filters with common-mode suppression based on stepped impedance resonators (SIRs)," in *IEEE MTT-S Int. Microw. Symp. Dig.*, Seattle, WA, USA, Jun. 2013, pp. 1–4.

[26] A. K. Horestani, M. Durá-Sindreu, J. Naqui, C. Fumeaux, and F. Martín, "S-shaped complementary split ring resonators and their application to compact differential bandpass filters with common-mode suppression," *IEEE Microw. Wireless Compon. Lett.*, vol. 24, no. 3, pp. 149–151, Mar. 2014.

[27] X.-H. Wang and H. Zhang, "Novel balanced wideband filters using microstrip coupled lines," *Microw. Opt. Technol. Lett.*, vol. 56, no. 5, pp. 1139–1141, 2014.

[28] L. Li, J. Bao, J.-J. Du, and Y.-M. Wang, "Compact differential wideband bandpass filters with wide common-mode suppression," *IEEE Microw. Wireless Compon. Lett.*, vol. 24, no. 3, pp. 164–166, Mar. 2014.

[29] H. Wang, L. M. Gao, K. W. Tam, W. Kang, and W. Wu, "A wideband differential BPF with multiple differential- and common-mode transmission zeros using cross-shaped resonator," *IEEE Microw. Wireless Compon. Lett.*, vol. 24, no. 12, pp. 854–856, Dec. 2014.

[30] W. Feng, W. Che, and Q. Xue, "High selectivity wideband differential bandpass filter with wideband common mode suppression using marchand balun," in *Proc. IEEE Int. Wireless Symp.*, Xian, China, Mar. 2014, pp. 1–4.

[31] L. Li, J. Bao, J.-J. Du, and Y.-M. Wang, "Differential wideband bandpass filters with enhanced common-mode suppression using internal coupling technique," *IEEE Microw. Wireless Compon. Lett.*, vol. 24, no. 5, pp. 300–302, May 2014.

[32] J. G. Zhou, Y.-C. Chiang, and W. Che, "Compact wideband balanced bandpass filter with high common-mode suppression based on cascade parallel coupled lines," *IET Microw., Antennas Propag.*, vol. 8, no. 8, pp. 564–570, Jun. 2014.

[33] P. Vélez, J. Selga, M. Sans, J. Bonache, and F. Martin, "Design of differential-mode wideband bandpass filters with wide stop band and common-mode suppression by means of multisection mirrored stepped impedance resonators (SIRs)," in *IEEE MTT-S Int. Microw. Symp. Dig.*, Phoenix, AZ, USA, May 2015, pp. 1–4.

[34] M. Sans *et al.*, "Automated design of common-mode suppressed balanced wideband bandpass filters by means of aggressive space mapping," *IEEE Trans. Microw. Theory Techn.*, vol. 63, no. 12, pp. 3896–3908, Dec. 2015.

[35] M. Sans *et al.*, "Automated design of balanced wideband bandpass filters based on mirrored stepped impedance resonators (SIRs) and interdigital capacitors," *Int. J. Microw. Wireless Technol.*, vol. 8, nos. 4–5, pp. 731–740, 2016.

[36] M. Sans *et al.*, "Optimized wideband differential-mode bandpass filters with broad stopband and common-mode suppression based on multisection stepped impedance resonators and interdigital capacitors," in *IEEE MTT-S Int. Microw. Symp. Dig.*, Seville, Spain, May 2017, pp. 10–12.

[37] W. Feng and W. Che, "Novel wideband differential bandpass filters based on T-shaped structure," *IEEE Trans. Microw. Theory Techn.*, vol. 60, no. 6, pp. 1560–1568, Jun. 2012.

[38] X.-H. Wu, Q.-X. Chu, and L.-L. Qiu, "Differential wideband bandpass filter with high-selectivity and common-mode suppression," *IEEE Microw. Wireless Compon. Lett.*, vol. 2, no. 12, pp. 644–646, Dec. 2013.

[39] T. B. Lim and L. Zhu, "Differential-mode ultra-wideband bandpass filter on microstrip line," *Electron. Lett.*, vol. 45, no. 22, pp. 1124–1125, 2009.

[40] X.-H. Wu and Q.-X. Chu, "Compact differential ultra-wideband bandpass filter with common-mode suppression," *IEEE Microw. Wireless Compon. Lett.*, vol. 22, no. 9, pp. 456–458, Sep. 2012.

[41] A. M. Abbosh, "Ultrawideband balanced bandpass filter," *IEEE Microw. Wireless Compon. Lett.*, vol. 21, no. 9, pp. 480–482, Sep. 2011.

[42] H. T. Zhu, W. J. Feng, W. Q. Che, and Q. Xue, "Ultra-wideband differential bandpass filter based on transversal signal-interference concept," *Electron. Lett.*, vol. 47, no. 18, pp. 1033–1035, Sep. 2011.

[43] X.-H. Wang, H. Zhang, and B.-Z. Wang, "A novel ultra-wideband differential filter based on microstrip line structures," *IEEE Microw. Wireless Compon. Lett.*, vol. 23, no. 3, pp. 128–130, Mar. 2013.

[44] S. Shi, W.-W. Choi, W. Che, K.-W. Tam, and Q. Xue, "Ultra-wideband differential bandpass filter with narrow notched band and improved common-mode suppression by DGS," *IEEE Microw. Wireless Compon. Lett.*, vol. 22, no. 4, pp. 185–187, Apr. 2012.

[45] C.-H. Lee, C.-I. G. Hsu, and C.-J. Chen, "Band-notched balanced UWB BPF with stepped-impedance slotline multi-mode resonator," *IEEE Microw. Wireless Compon. Lett.*, vol. 22, no. 4, pp. 182–184, Apr. 2012.

[46] J. Shi, C. Shao, J.-X. Chen, Q.-Y. Lu, Y. Peng, and Z.-H. Bao, "Compact low-loss wideband differential bandpass filter with high common-mode suppression," *IEEE Microw. Wireless Compon. Lett.*, vol. 23, no. 9, pp. 480–482, Sep. 2013.

[47] P. Vélez *et al.*, "Ultra-compact (80 mm^2) differential-mode ultra-wideband (UWB) bandpass filters with common-mode noise suppression," *IEEE Trans. Microw. Theory Techn.*, vol. 63, no. 4, pp. 1272–1280, Apr. 2015.

[48] D. M. Pozar, *Microwave Engineering*, 4th ed. Hoboken, NJ, USA: Wiley, 2012.

[49] J.-S. Hong, *Microstrip Filters for RF/Microwave Applications*, Hoboken, NJ, USA: Wiley, 2001.

[50] J. W. Bandler, R. M. Biernacki, S. H. Chen, P. A. Grobelny, and R. H. Hemmers, "Space mapping technique for electromagnetic optimization," *IEEE Trans. Microw. Theory Techn.*, vol. 42, no. 12, pp. 2536–2544, Dec. 1994.

[51] J. W. Bandler, R. M. Biernacki, S. H. Chen, R. H. Hemmers, and K. Madsen, "Electromagnetic optimization exploiting aggressive space mapping," *IEEE Trans. Microw. Theory Techn.*, vol. 43, no. 12, pp. 2874–2882, Dec. 1995.

[52] S. Koziel, Q. S. Cheng, and J. W. Bandler, "Space mapping," *IEEE Microw. Mag.*, vol. 9, no. 6, pp. 105–122, Dec. 2008.

Marc Sans was born in Terrassa (Barcelona), Spain, in 1982. He received the B.S. degree in telecommunications engineering–electronic systems in 2006, the M.S. degree in telecommunications engineering in 2008, and the M.S. degree in electronics engineering in 2013 from the Universitat Autònoma de Barcelona (UAB), Barcelona.

In 2008 he started his professional career as an RF Engineer at Sony-FTVE in the RF group focused on the development of TV receivers. In 2010 he started working as an RF Design Engineer at Mier Comunicaciones S.A., where he was in charge of the design of passive and active devices for VHF-UHF broadcasting units. Since December 2015 up to the present, he is working as an Innovation RF Design Engineer at Ampleon. Meanwhile, in 2014 he joined the CIMITEC research group, mainly focused on metamaterial technology development, to start up his Ph.D. degree consisting in the synthesis of microwave devices based on EM optimization techniques.

Jordi Selga (S'11–M'14) was born in Barcelona, Spain, in 1982. He received the B.S. degree in telecommunications engineering—electronic systems, M.S. degree in electronics engineering, and Ph.D. degree in electronics engineering from the Universitat Autònoma de Barcelona (UAB), Barcelona.

Since 2008, he has been a member of CIMITEC-UAB, Bellaterra, Spain. He is currently with UAB, where he is involved in the development of metamaterials, CAD design of microwave devices, EM optimization methods, and automated synthesis of planar microwave components.

Dr. Selga is a Reviewer of IEEE MICROWAVE AND WIRELESS COMPONENTS LETTERS, *IET Microwave, Antennas and Propagation* among others specialized journals in the RF/microwave field. He was a holder of a National Research Fellowship from the Formación de Profesorado Universitario Program of the Education and Science Ministry (Reference AP2008-4707).

Paris Vélez (S'10–M'14) was born in Barcelona, Spain, in 1982. He received the degree in telecommunications engineering, with a specialization in electronics, Electronics Engineering degree, and Ph.D. degree in electrical engineering from the Universitat Autònoma de Barcelona, Barcelona, Spain, in 2008, 2010, and 2014, respectively. His Ph.D. thesis concerned common mode suppression differential microwave circuits based on metamaterial concepts and semilumped resonators.

He is currently with the LAAS-CNRS, Toulouse, France, where he is involved in metamaterials sensors for fluidics detection. His current research interests include the miniaturization of passive circuits RF/microwave and sensor-based metamaterials.

Dr. Vélez was a recipient of a Predoctoral Teaching and Research Fellowship by the Spanish Government from 2011 to 2014. He was the recipient of a TECNIOSpring Fellowship cofounded by the Mari Curie Program. He is a Reviewer for the IEEE TRANSACTIONS ON MICROWAVE THEORY AND TECHNIQUES and other journals.

Jordi Bonache (S'05–M'07) was born in Barcelona, Spain, in 1976. He received the Physics and Electronics Engineering degrees and Ph.D. degree in electronics engineering from the Universitat Autònoma de Barcelona, Barcelona, in 1999 and 2001 and 2007, respectively.

In 2000, he joined the High Energy Physics Institute, Barcelona, where he was involved in the design and implementation of the control and monitoring system of the MAGIC telescope. In 2001, he joined the Department of Electronics Engineering, Universitat Autònoma de Barcelona, where he is currently an Associate Professor. From 2006 to 2009, he was an Executive Manager with CIMITEC, Bellaterra, Spain, where he led research on RFID and antennas. His current research interests include active and passive microwave devices, metamaterials, antennas, and RFID.

Ana Rodríguez (GS'09–M'12) was born in Lugo, Spain. She received the Telecommunications Engineering degree from the Universidade de Vigo, Vigo, Spain, in 2008, and the Master en Tecnología, Sistemas y Redes de Comunicaciones and the Ph.D. degree from the Universitat Politècnica de València (UPV), València, Spain, in 2010 and 2014, respectively.

She participated in the Erasmus Exchange Program, developing her master's thesis at the University of Oulu, Oulu, Finland. Since 2008, she has been with the Institute of Telecommunications and Multimedia Applications, UPV. Her current research interests include the CAD design of microwave devices, EM optimization methods, and metamaterials.

Vicente E. Boria (S'91–A'99–SM'02) was born in Valencia, Spain, in 1970. He received the Ingeniero de Telecomunicación degree (with First-Class Hons.) and Doctor Ingeniero de Telecomunicación degree from the Universidad Politécnica de Valencia, Valencia, in 1993, and 1997, respectively.

In 1993, he joined the Departamento de Comunicaciones, Universidad Politécnica de Valencia, where he has been a Full Professor since 2003. From 1995 to 1996, he was a Spanish Trainee with the European Space Research and Technology Centre, European Space Agency, Noordwijk, The Netherlands, where he was involved in the EM analysis and design of passive waveguide devices. He has authored or co-authored 10 chapters in technical textbooks, 135 papers in refereed international technical journals, and over 180 papers in international conference proceedings. His current research interests include the analysis and automated design of passive components, left-handed and periodic structures, as well as on the simulation and measurement of power effects in passive waveguide systems.

Dr. Boria has been a member of the IEEE Microwave Theory and Techniques Society (IEEE MTT-S) and the IEEE Antennas and Propagation Society since 1992. He is also a member of the Technical Committees of the IEEE-MTT International Microwave Symposium and the European Microwave Conference. He is a Reviewer for the IEEE TRANSACTIONS ON MICROWAVE THEORY AND TECHNIQUES, and *Proceeding of the IET* (*Microwaves, Antennas and Propagation*). He currently serves as an Associate Editor for IEEE MICROWAVE AND WIRELESS COMPONENTS LETTERS and *IET Electronics Letters*.

Ferran Martín (M'04–SM'08–F'12) was born in Barakaldo (Vizcaya), Spain, in 1965. He received the B.S. degree in physics from the Universitat Autònoma de Barcelona (UAB), Barcelona, Spain, in 1988, and the Ph.D. degree in 1992.

From 1994 to 2006, he was an Associate Professor of electronics with the Departament d'Enginyeria Electrònica, UAB, where he has been a Full Professor of electronics since 2007. He is currently the Head of the Microwave Engineering, Metamaterials and Antennas Group, UAB, and the Director of the CIMITEC. He has been involved in different research activities including modelling and simulation of electron devices for high-frequency applications, millimeter-wave and terahertz generation systems, and the application of electromagnetic bandgaps to microwave and millimeter-wave circuits, metamaterials and their application to the miniaturization and optimization of microwave circuits and antennas. He has authored or co-authored over 500 technical conference, letter, journal papers, and book chapters. He co-authored the book on metamaterials *Metamaterials With Negative Parameters: Theory, Design and Microwave Applications* (Wiley, 2008), authored *Artificial Transmission Lines for RF and Microwave Applications* (Wiley, 2015), and he has generated 17 Ph.Ds. He has filed several patents on metamaterials and has headed several development contracts.

Prof. Martín is a member of the IEEE Microwave Theory and Techniques Society (IEEE MTT-S). He is also a member of the Technical Committees of the European Microwave Conference and the International Congress on Advanced Electromagnetic Materials in Microwaves and Optics (Metamaterials). He has been a Fellow of the IET since 2016. He was a recipient of the 2006 Duran Farell Prize for Technological Research. He holds the *Parc de Recerca UAB—Santander* Technology Transfer Chair and two ICREA ACADEMIA Awards (2008 and 2013). He is a Reviewer for the IEEE TRANSACTIONS ON MICROWAVE THEORY AND TECHNIQUES and IEEE MICROWAVE AND WIRELESS COMPONENTS LETTERS, among many other journals, and he serves as a member of the Editorial Board of *IET Microwaves, Antennas and Propagation* and the *International Journal of RF and Microwave Computer-Aided Engineering*. He served as a Guest Editor for three special issues on metamaterials in three international journals. He has organized several international events related to metamaterials, including workshops at the IEEE MTT-S International Microwave Symposium in 2005 and 2007, the European Microwave Conference in 2009, and the Fifth International Congress on Advanced Electromagnetic Materials in Microwaves and Optics (Metamaterials 2011), where he was the Chair of the Local Organizing Committee.

PhD Thesis Author Publications

Journals

[1] M. Sans, J. Selga, A. Rodríguez, J. Bonache, V. E. Boria, and F. Martín, "Design of planar wideband bandpass filters from specifications using a two-step aggressive space mapping (ASM) Optimization Algorithm" *IEEE Trans. Microw. Theory Tech.*, vol. 62, no. 12, pp. 3341–3350, Dec. 2014.

[2] M. Orellana, J. Selga, M. Sans, A. Rodríguez, V. Boria, and F. Martín, "Synthesis of slow-wave structures based on capacitive-loaded lines through aggressive space mapping (ASM)", *Int. J. RF Microw. Comput. Eng.*, vol. 25, no. 7, pp. 629–638, Sept. 2015.

[3] M. Sans, J. Selga, P. Vélez, A. Rodríguez, J. Bonache, V. E. Boria, and F. Martín, "Automated Design of Common-Mode Suppressed Balanced Wideband Bandpass Filters by Means of Aggressive Space Mapping", *IEEE Trans. Microw. Theory Tech.*, vol. 63, no. 12, pp. 3896–3908, Dec. 2015.

[4] M. Sans, J. Selga, P. Vélez, A. Rodríguez, J. Bonache, V. E. Boria, and F. Martín, "Automated design of balanced wideband bandpass filters based on mirrored stepped impedance resonators (SIRs) and interdigital capacitors", *Int. J. Microw. Wirel. Technol.*, vol. 8, no. 4–5, pp. 731–740, June 2016.

[5] A. Rodríguez, J. Selga, M. Sans, F. Martín, and V. E. Boria, "Automated design of bandpass filters based on open complementary split ring resonators (OCSRRs) using aggressive space mapping (ASM) optimization", *Int. J. Numer. Model. Electron. Networks, Devices and Fields*, vol. 30, no. 3–4, May–Aug. 2017.

[6] M. Orellana, J. Selga, P. Vélez, M. Sans, A. Rodríguez, J. Bonache, V. E. Boria, and F. Martín, "Design of Capacitively Loaded Coupled-Line Bandpass Filters with Compact Size and Spurious Suppression" *IEEE Trans. Microw. Theory Tech.*, vol. 65, no. 4, pp. 1235–1248, April 2017.

[7] M. Sans, J. Selga, P. Vélez, A. Rodríguez, J. Bonache, V. E. Boria, and F. Martín, "Compact Wideband Balanced Bandpass Filters with Very Broad Common-Mode and Differential-Mode Stopbands" *IEEE Trans. Microw. Theory Tech.*, vol. 66, pp. 737–750, Feb. 2018.

Conferences

[1] J. Selga, M. Sans, J. Bonache, A. Rodríguez, V. E. Boria, and F. Martín, "Automated synthesis of planar wideband bandpass filters based on stepped impedance resonators (SIRs) and shunt stubs through aggressive space mapping (ASM)", *IEEE MTT-S International Microwave Symposium Digest* (IMS'14), Tampa, FL (USA), June 2014.

[2] A. Rodríguez, V. E. Boria, J. Selga, M. Sans, and F. Martín, "Synthesis of open complementary split ring resonators (OCSRRs) through aggressive space mapping (ASM) and application to bandpass filters" *European Microwave Conference Proceedings* (EuMC'14), Rome (Italy), Oct. 2014.

[3] P. Velez, J. Selga, M. Sans, J. Bonache, and F. Martín, "Design of differential-mode wideband bandpass filters with wide stop band and common-mode suppression by means of multi-section mirrored stepped impedance resonators (SIRs)", *IEEE MTT-S International Microwave Symposium*, (IMS'15), Phoenix, AR (USA), May 2015.

[4] M. Sans, J. Selga, P. Vélez, J. Bonache, A. Rodríguez, V. E. Boria, and F. Martín, "Application of aggressive space mapping (ASM) to the automated design of differential-mode wideband bandpass filters with common-mode suppression", *European Microwave Conference Proceedings* (EuMC'15), Paris (France), Sept. 2015.

[5] J. Selga, P. Vélez, M. Orellana, M. Sans, A. Rodríguez, V. E. Boria, and F. Martín, "Size reduction and spurious suppression in microstrip coupled line bandpass filters by means of capacitive electromagnetic bandgaps", *IEEE MTT-S International Microwave Symposium* (IMS'16), San Francisco, CA (USA), May 2016.

[6] A. Rodríguez, J.V. Morro, J. Selga, M. Sans, J. Ossorio, M. Guglielmi, F. Martín and V.E. Boria, "Robust optimization and tuning of microwave filters and artificial transmission lines using aggressive space mapping techniques", *IEEE MTT-S International Microwave Symposium* (IMS'17), Honolulu, HA (USA), June 2017.

[7] M. Sans, J. Selga, P. Vélez, A. Rodríguez, J. Bonache, V. E. Boria, and F. Martín, “Optimized wideband differential-mode bandpass filters with broad stopband and common-mode suppression based on multi-section stepped impedance resonators and interdigital capacitors”, *IEEE MTT-S International Conference on Numerical Electromagnetic and Multiphysics Modeling and Optimization for RF, Microwave, and Terahertz Applications* (NEMO’17), Seville (Spain), May 2017.

Book Chapters

[1] M. Sans, J. Selga, A. Rodríguez, P. Vélez, V. E. Boria, J. Bonache, and F. Martín, “Unattended design of wideband planar filters using a two-step aggressive space mapping (ASM) optimization algorithm”, Koziel S., Leifsson L., Yang XS. (eds) Simulation-Driven Modeling and Optimization. *Springer Proceedings in Mathematics and Statistics*, vol. 153, pp. 135–159, Feb. 2016.

Acronyms

ASM	Aggressive Space Mapping
CAD	Computer-Aided Design
CMRR	Common-mode Rejection Ratio
CSRR	Complementary Split Ring Resonator
DGS	Defected Ground Structure
EM	Electromagnetic
EMI	Electromagnetic Interference
FBW	Fractional Band-Width
$\mathbf{FBW_{-3dB}}$	FBW defined by the cut-off frequencies at -3dB of the pass band response
$\mathbf{L_{Ar}}$	Chebyshev response passband ripple
OCSRR	Open Complementary Split Ring Resonators
OSRR	Open Split Ring Resonators
SIR	Stepped Impedance Resonator
SIW	Substrate Integrated Waveguide
SM	Space Mapping
SNR	Signal-to-Noise Ratio
UWB	Ultra-Wide Band